



**OPTIMUM MODELLING OF FLUX-PIPE RESONANT COILS FOR
STATIC AND DYNAMIC BIDIRECTIONAL WIRELESS POWER
TRANSFER SYSTEM APPLICABLE TO ELECTRIC VEHICLES**

PhD Report

Student: Mr. Babatunde Olukotun, MSc. (Hons)

Supervisor: Prof. RWG Bucknall

Co-Supervisor: Dr Julius Partridge

Department of Mechanical Engineering

University College London

I, Babatunde Olukotun confirm that the work presented in this thesis is my own. Where information has been derived from other sources, I confirmed that this has been indicated in the thesis.

February 2020

Abstract

Wireless power transfer (WPT) technology enables the transfer of electrical power from the electric grid to the electric vehicles across an airgap using electromagnetic fields with the help of wireless battery chargers. WPT technology addresses most problems associated with the “plug-in” method of charging EVs like vandalization, system power losses, and safety problems due to hanging cables and opened electrical contact in addition to the flexibility of charging electric vehicles while in a static or dynamic mode of operation.

Significant research has been undertaken over the years in the development of efficient WPT topologies applicable to electric vehicles. A preliminary review of these revealed that the ferrite core WPT is a promising and efficient method of charging electric vehicles. The charging method is suitable for wireless charging of electric vehicles because of its low cost, high efficiency and high power output. This research proposed the use of the flux-pipe model as a suitable ferrite core, magnetic resonance coupled-based WPT system for the charging of the electric vehicle. The traditional flux-pipe model has some specific benefits which include high coupling coefficient, high misalignment tolerance and high efficiencies under misalignment conditions. However, it has a major drawback of low power output due to the generation of an equal amount of useful and non-useful fluxes.

A set of governing equations guiding the performance output of a WPT system was presented. It was identified that the losses in the WPT system can be minimized by reducing the value of the maximum magnetic flux density while the power output and efficiency can be increased by increasing the value of the coupling factor and quality factor. Based on these findings, 3-D finite element modelling was employed for the optimal design and analysis of a typical flux-pipe model for higher coupling strength, high power output and low losses. The magnetic coupling performance of flux-pipe resonant coils was enhanced with an increased number of turns along the core length relative to increasing the width of each coil turns along the coil width. The high power transfer and efficiency was attained by splitting of the coil windings into two in order to reduce intrinsic coil resistances; copper sheet was employed as a shielding material in order to reduce the eddy current losses and finally, an air gap was introduced in the ferrite core in order to reduce the core losses and invariably increased the amount of excitation current required to drive the core into saturation.

The proposed optimization methodology results in the creation of two models for application in static and dynamic charging operations respectively. From the simulation results presented, the model designed for static charging operations can transfer up to 11 kW of power across the airgap at a coil-to-coil efficiency of 99.12% while the model design for dynamic charging of electric vehicles can transfer up to 13 kW of power across the airgap at a coil-to-coil efficiency of 98.64% without exceeding the average limit specified for the exposure of human body to electromagnetic fields.

Impact of Research Work

In this thesis, a system-level engineering and simulation-based approach is presented and employed for the engineering design of novel coils for wireless charging systems. The methodology comprises an initial validation of model designs obtained from published literature. These are then subjected to an iterative simulation process to fine-tune designs in order to achieve an optimal specification for the present application. Wherever possible, the modelled operation is compared with published practical results in order to ascertain the degree of validity of the modelling undertaken. This has enabled the optimization of proposed engineering designs.

A numerical method, finite element modelling (FEM) using Ansys Maxwell 3-D software is chosen and employed for the model designs, analyses, optimization and evaluations. The initial boundary conditions were carefully selected based on the analysis of published designs. FEM as a numerical method is employed because it can easily handle very complex geometry involving an infinite degree of freedom cutting across a wide range of engineering context such as dynamics, solid mechanics, fluids, heat flows, electrostatic, and electromagnetics. For this research, FEM methodology was applied for the optimal design and analysis of ferrite core, magnetic resonance coupling-based wireless power transfer systems.

The research and modelling methodology applied in the present work resulted in the creation of two ferrite-cored flux-pipe models with high power transfer capability and low losses. The optimal model designs still retain the inherent high coupling capability associated with typical flux-pipe coil designs. The two models also have potential application in the bidirectional transfer of wireless power for static and dynamic operations at very high coil-to-coil efficiencies. The model design for dynamic charging is best suited for segmented coil array systems which come with benefits of low electromagnetic exposure and a low number of compensation capacitors. With eventual creation of prototype designs and practical demonstrations, the models offer a cost-effective wireless power transfer systems with additional capability for vehicle-to-grid integration.

The system-level engineering and simulation-based design approach employed in this research could be deployed for optimal model designs and optimizations in other areas of engineering. The methodology reduces the high cost involved in the production of numerous prototypes using the traditional iterative process by creating numerous virtual prototypes in the modelling and simulation stage. The majority of the iterative optimization and testing process is undertaken at the model design and simulation stage, thus, significantly reducing the number of prototypes production at the fabrication stage.

Acknowledgements

I wish to acknowledge the supervisory roles of my main supervisor Prof. RWG Bucknall for his invaluable academic guidance, advice and support with regard to the concepts, design, development and completion of this research work. I also wish to acknowledge the contribution of Dr Partridge Julius. I must especially thank him for the invaluable hours of discussion on the research gaps and areas of optimization.

I will also like to acknowledge the technical advice and editorial work of Engr. Konrad Yearwood in the course of writing this thesis. His critical review and feedbacks were helpful in ensuring that this report was of high standard and quality in terms of technical contents and thesis structure.

I will also like to appreciate the experts at MDPI Journal of energies for their critical reviews and recommendations in the course of this research, which was helpful in the analysis, validation and evaluations of proposed designs.

Appreciation

I wish to especially express my profound gratitude and sincere appreciation to the almighty GOD the Maker of heaven and earth for the power and grace to successfully complete this research. I wish to also appreciate my parent Rev and Mrs Joseph Olukotun for their financial and moral support throughout the course of my academic career and progress till date. I also wish to appreciate Nigeria former President, Dr Goodluck Ebele Jonathan for his innovation and successful implementation of the Presidential Special Scholarship for Innovation and Development (PRESSID) in which I am a beneficiary.

I also wish to appreciate my scholarship guarantors: Pastor Kelvin Dariya and Mr Micah Olarewaju. I will also not forget my academic guarantors: Prof. Oyetunji and Prof. Bello. A special appreciation goes to my wife, Dorah for her advice and support. I will like to appreciate sons: Jadon and Jaymin and my siblings: Ibukun, Adekunle, Adeniyi, Oluwagbenga and Abigail for all their support towards the progress in my academic career.

Finally, I will like to appreciate my colleagues at the Federal University of Technology, Akure, friends and well-wishers for their prayers, support and encouragement.

Contents

| | |
|--|----|
| Title Page..... | 1 |
| Abstract..... | 2 |
| Impact of Research Work..... | 3 |
| Acknowledgements | 4 |
| Appreciation | 5 |
| List of Figures..... | 11 |
| List of Tables..... | 15 |
| Abbreviations..... | 17 |
| Nomenclatures | 20 |
| CHAPTER 1 Introduction and Background | 22 |
| 1.1 Background..... | 22 |
| 1.2 Aims and Objectives..... | 24 |
| 1.3 Scope of the Research..... | 24 |
| 1.4 Publications | 25 |
| 1.5 Contributions..... | 26 |
| 1.6 Thesis Outline..... | 28 |
| CHAPTER 2 Smart Grid and Review of Wireless Power Transfer..... | 30 |
| 2.1 Introduction | 30 |
| 2.2 The Evolution of Traditional Electric Power Grid into Smart Grid..... | 30 |
| 2.2.1 Vehicle-to-Vehicle (V2V) Technology..... | 34 |
| 2.2.2 Vehicle-to-Home (V2H) Technology | 35 |
| 2.2.3 Vehicle-to-Grid (V2G) Technology..... | 36 |
| 2.3 Review of Plug-in Charging of Electric Vehicles | 37 |
| 2.3.1 Drawbacks in the use of Plug-in Electric Vehicles (PEVs) | 38 |
| 2.4 Theory and Development of Wireless Power Transfer for EVs | 39 |
| 2.5 The Magnetic Gear WPT Technology..... | 41 |
| 2.6 The Capacitive WPT Technology..... | 43 |
| 2.7 The Electromagnetic Field-based WPT Technology..... | 44 |
| 2.8 Performance Parameters for Electromagnetic Field-Based WPT Technology..... | 44 |
| 2.8.1 Coupling Coefficient (k) | 44 |

| | | |
|-----------|---|----|
| 2.8.2 | Quality Factor (Q)..... | 45 |
| 2.8.3 | Power Level..... | 46 |
| 2.8.4 | Power Transfer Efficiency (PTE)..... | 47 |
| 2.9 | The Far Field WPT Technology..... | 48 |
| 2.10 | The Near Field WPT Technology..... | 49 |
| 2.10.1 | The Inductive Power Transfer (IPT) Technologies..... | 49 |
| 2.11 | Magnetic Resonant Coupling WPT Technologies..... | 50 |
| 2.11.1 | Air-Core Magnetic Resonant Coupling WPT Technologies..... | 51 |
| 2.11.2 | The Air Core Low MRC model..... | 52 |
| 2.11.3 | The Air Core Medium MRC model..... | 53 |
| 2.11.4 | The Air Core Strong MRC model..... | 54 |
| 2.11.5 | Ferrite Core Magnetic Resonant Coupling WPT Technologies..... | 58 |
| 2.12 | Review of Static and Dynamic Charging of EVs..... | 59 |
| 2.12.1 | Static Wireless Charging of Electric Vehicles..... | 59 |
| 2.12.2 | Dynamic Wireless Charging of Electric Vehicles..... | 60 |
| 2.13 | Investigation into Bidirectional Wireless Power Transfer Topology for Electric Vehicle..... | 63 |
| 2.14 | Research Gaps in the Development of Bidirectional WPT for EV Application..... | 65 |
| 2.14.1 | Power Electronic Controls for Electric Vehicle Bidirectional WPT Applications..... | 66 |
| 2.14.2 | Electric Circuit Design for Electric Vehicle Bidirectional WPT Applications..... | 68 |
| 2.14.3 | Electromagnetic Design for Electric Vehicle Bidirectional WPT Applications..... | 68 |
| 2.15 | Summary..... | 69 |
| CHAPTER 3 | Analysis and Evaluation of Ferrite-Core MRC-based Coils..... | 71 |
| 3.1 | Introduction..... | 71 |
| 3.2 | Environmental Factors Affecting Ferrite-Core MRC-Based Coil Topologies..... | 71 |
| 3.3 | Circuit Designs for Ferrite-Core MRC-Based Coil Topologies..... | 72 |
| 3.3.1 | Frequency Specification for WPT Systems..... | 72 |
| 3.3.2 | Converter Design for MRC Wireless Power Transfer System..... | 74 |
| 3.3.3 | Compensation Circuit Designs for WPT Systems..... | 76 |
| 3.4 | Impact of Coil Alignment on Ferrite-Core MRC-Based Coil Topologies..... | 80 |
| 3.4.1 | Angular Misalignment Resonant Coils..... | 80 |

| | | |
|---|---|-----|
| 3.4.2 | Lateral and Longitudinal Misalignment of Resonant Coils | 81 |
| 3.4.3 | Airgap Variation of Resonant Coils | 82 |
| 3.4.4 | Coil Design for MRC Wireless Power Transfer System..... | 83 |
| 3.5 | Coil Designs for Ferrite-Core MRC-Based Coil Topologies..... | 84 |
| 3.5.1 | Geometric Specifications of Coil Designs..... | 84 |
| 3.5.2 | Coil Size Specifications | 87 |
| 3.5.3 | Coil Material Specifications | 88 |
| 3.6 | Summary..... | 91 |
| CHAPTER 4 Finite Element Modelling and Design Validation..... | | 93 |
| 4.1 | Introduction | 93 |
| 4.2 | The Overall Wireless Power Transfer System Design Specification..... | 93 |
| 4.3 | Finite Element Modelling and Analysis | 95 |
| 4.3.1 | FEM Magnetostatic Analysis | 98 |
| 4.3.2 | FEM Eddy Current Analysis..... | 99 |
| 4.3.3 | Mathematical Analysis of Equivalent Circuit Model | 101 |
| 4.3.4 | Circuit Analysis of Reduced-Order Model (ROM) of WPT Coils | 107 |
| 4.4 | Specification of Initial and Boundary Conditions..... | 111 |
| 4.4.1 | Planar Coil Design Systems..... | 111 |
| 4.4.2 | Double D Coil Design Systems..... | 113 |
| 4.4.3 | Double D and Solenoid Coils Combination Design | 115 |
| 4.5 | Validation of a Circular MRC Coil-to-Coil Design Model..... | 118 |
| 4.6 | Summary..... | 119 |
| CHAPTER 5 Selection and Analysis of Coil Models..... | | 121 |
| 5.1 | Introduction | 121 |
| 5.2 | Selection of Proposed Coil Topology and Design Specification..... | 121 |
| 5.3 | Magnetostatic Analysis of Resonant Coils..... | 123 |
| 5.3.1 | Magnetic Flux Density Distribution in Ferrite Cores..... | 124 |
| 5.4 | Parametric Analysis of the Resonant Coil Designs | 128 |
| 5.4.1 | Performance Analysis of Lateral Misalignment of Resonant Coils..... | 128 |
| 5.4.2 | Performance Analysis of Longitudinal Misalignment of Resonant Coils | 130 |

| | | |
|-----------|---|-----|
| 5.4.3 | Performance Analysis of Resonant Coils with Variation in Airgap | 132 |
| 5.5 | Further Analysis of Conventional Flux-Pipe Topology | 134 |
| 5.6 | Magnetic Flux Distribution for Flux-Pipe Resonant Coil Designs | 137 |
| 5.7 | Parametric Analysis of Flux-Pipe Resonant Coil Designs | 139 |
| 5.7.1 | Lateral Misalignment Performance of Flux-Pipe Resonant Coils..... | 139 |
| 5.7.2 | Longitudinal Misalignment Performance of Flux-Pipe Resonant Coils | 140 |
| 5.7.3 | Performance of Flux-Pipe Resonant Coils under Airgap Variation | 141 |
| 5.8 | Eddy Current Analysis of Resonant Coils..... | 142 |
| 5.9 | Circuit Analysis of Resonant Coils..... | 145 |
| 5.9.1 | Impact of Load Resistance for S-S Compensation Topology. | 147 |
| 5.9.2 | Impact of Load Resistance in S-P Compensation Topology..... | 149 |
| 5.9.3 | Impact of Misalignment on the Efficiency of Coil Designs..... | 153 |
| 5.10 | Summary..... | 154 |
| CHAPTER 6 | Design Optimization of Flux-Pipe Model | 157 |
| 6.1 | Introduction | 157 |
| 6.2 | Performance Limitation of Traditional Flux Pipe Design | 157 |
| 6.3 | Governing Equations for Losses in Flux-Pipe Resonant Coil System..... | 159 |
| 6.4 | Optimal Selection of Shielding Material | 160 |
| 6.5 | Optimization of Coil Windings..... | 162 |
| 6.6 | Geometric Modification of Ferrite Core..... | 164 |
| 6.7 | Optimal Selection of Supporting Material | 165 |
| 6.8 | Modification of Optimal Flux-Pipe Design for Dynamic Operations..... | 166 |
| 6.9 | Validation of Coil Winding Specification..... | 168 |
| 6.10 | Magnetostatic Analysis of Optimal Flux-Pipe Resonant Coils..... | 169 |
| 6.10.1 | Magnetic Flux Density Distribution in Ferrite Cores..... | 170 |
| 6.11 | Parametric Analysis of the Resonant Coil Designs | 173 |
| 6.11.1 | The Parametric Misalignment Performance of Resonant Coils | 174 |
| 6.12 | Eddy Current Analysis of Resonant Coils..... | 175 |
| 6.13 | Circuit Analysis and Performance..... | 177 |
| 6.13.1 | Performance Characteristics of Optimal Flux-Pipe Resonant Coil in an S-S Compensation Topology..... | 179 |

| | | |
|-----------|---|-----|
| 6.13.2 | Performance Characteristics of Optimal Flux-Pipe Resonant Coil in an S-P Compensation Topology..... | 183 |
| 6.13.3 | Impact of Misalignment on the Efficiency of Coil Designs..... | 186 |
| 6.14 | Electromagnetic Field Radiation Analysis..... | 188 |
| 6.15 | Summary..... | 189 |
| CHAPTER 7 | Conclusion and Recommendations..... | 191 |
| 7.1 | Conclusion from Research..... | 191 |
| 7.2 | Research Limitations..... | 192 |
| 7.3 | Future Work..... | 193 |
| | References..... | 195 |
| | Appendices..... | 207 |

List of Figures

| | |
|---|----|
| Figure 2.1: Smart Power Grid Infrastructure integrating the Traditional Power with Distributed Energy Sources(Adapted from Vogilitsis .D. [20])..... | 32 |
| Figure 2.2: Illustration of the V2V, V2H and V2G Technologies and Integration[42]..... | 34 |
| Figure 2.3: Practical Implementation of Plug-in Charging Method for PEVs. (a) Plug-in Hybrid Charging Infrastructure[58]. (b) A Commercial Charger for PEVs[59]..... | 38 |
| Figure 2.4: Categories of Different WPT Technologies[45]..... | 41 |
| Figure 2.5: Schematic of Magnetic Gear WPT Application for EVs[45]..... | 42 |
| Figure 2.6: Working Principle of Capacitive WPT Technology..... | 43 |
| Figure 2.7: (a) Divergent Nature of Magnetic Flux and Fields as they travel in Space (b) Circuit Representation[11]..... | 45 |
| Figure 2.8: (a) Setup and Equivalent Circuit Model Diagram of Traditional IPT Technology[45]. (b) Charging pad of a Typical IPT Technology[96]...... | 49 |
| Figure 2.9: Model Diagram and Equivalent Circuit Diagram of Low MRC[45]..... | 52 |
| Figure 2.10: Model Diagram and Equivalent Circuit Diagram of Medium MRC[45]..... | 53 |
| Figure 2.11: Model Diagram and Equivalent Circuit Diagram of Strong MRC[45]..... | 54 |
| Figure 2.12: Overview of Charging Structure of MRC system for EV Application (Source: Qiu et al [45])56 | |
| Figure 2.13: The Transformer Model for the Strong MRC WPT System..... | 57 |
| Figure 2.14: Coupling Inductor Model for the Strong MRC Wireless Power Transfer System..... | 57 |
| Figure 2.15: Typical Illustration of Static Mode of Wireless Charging of an EV[40]..... | 59 |
| Figure 2.16: Typical Illustration of Dynamic Mode of Wireless Charging of an EV[36]..... | 61 |
| Figure 2.17: Typical Illustration of Segmented Coil Array for Dynamic Wireless Charging of Electric Vehicle[40]...... | 62 |
| Figure 2.18: Typical Subsystems for Bidirectional WPT System[20]..... | 66 |
| Figure 2.19: ICNIRP Standard Limit for Human Exposure to Magnetic Field[127]..... | 69 |
| Figure 3.1: Effect of Coupling Coefficient and Resonant Frequencies on the PTE of Ferrite-Cored WPTCoils[43]..... | 73 |
| Figure 3.2: Compensation Topologies Used for Strong MRC Wireless Power Transfer Systems [149]. | 77 |
| Figure 3.3: Alternative Compensation Topologies. (a) PPS Topology. (b) SPS Topology..... | 79 |
| Figure 3.4 (a) 3-D Misalignment Representation. (b) X-axis: Lateral Misalignment, Y-axis: Longitudinal Misalignment[93]. (c) Z-axis: Airgap Variation. (d) Angular Misalignment at an Angle (theta) [93].80 | |
| Figure 3.5: Commonly Used Coil Shape Design. (a) Circular Shaped Coil. (b) Rectangular Shaped Coil[134]..... | 84 |
| Figure 3.6: Flux Path Distribution for Circular/Rectangular Coil Designs. (a) Flux Path in a perfectly aligned Condition. (b) Flux Path Distribution in a Misaligned Condition(Source: Budhia et al [99]) . | |
| | 85 |
| Figure 3.7: Flux-Pipe and Rectangular Bipolar Coils..... | 86 |
| Figure 3.8: Shapes and Sizes of Commercially Available Litz Wires[171]. | 88 |

| | |
|--|-----|
| Figure 3.9: Effect of Ferrite Material on Emitted Magnetic Field. (a) Magnetic Orientation in Ferrite Sheet. (b) Effect on Mutual Inductance between Coils[144]..... | 89 |
| Figure 3.10: Effect of Aluminum as Shielding Material for Leaked Magnetic Field. (a) Magnetic Orientation in Aluminum Sheet. (b) Effect on Mutual Inductance between Coils [116]..... | 90 |
| Figure 4.1: Overview of Optimized System-level Engineering and Simulation-based Design. | 94 |
| Figure 4.2: Flowchart Algorithm for Finite Element Modeling and Analysis in Ansys Maxwell 3D..... | 97 |
| Figure 4.3: Magnetostatic Solution Process for Ansys Modelling Software[177]..... | 99 |
| Figure 4.4: Eddy Current Solution Process for Ansys Modelling Software [[177]]..... | 100 |
| Figure 4.5: Equivalent Circuit for an S-S Compensation Topology..... | 102 |
| Figure 4.6: Equivalent Circuit for an S-P Compensation Topology..... | 104 |
| Figure 4.7: Implementation of the Reduced Order Model for Circuit Analysis..... | 108 |
| Figure 4.8: Simplorer® Maxwell ROM Design Implementation for S-S Compensation Topology..... | 109 |
| Figure 4.9: Simplorer® Maxwell ROM Design Implementation for S-P Compensation Topology..... | 110 |
| Figure 4.10: Proposed FEM Simulation Design and Design of Planar Resonant Coils Taken from Literature [11]..... | 112 |
| Figure 4.11: Proposed FEM Simulation Design and Physical Design of a Pair of Double-D Resonant Coils Taken from Literature[11]..... | 114 |
| Figure 4.12: FEM Simulation Design and Physical Design of a Pair of Double-D and Solenoid Resonant Coils Taken from Literature[11]..... | 116 |
| Figure 5.1: The Different Coil Design Topologies. (a) The Circular Resonant Coil Design (b) The Rectangular Resonant Coil. (c) The Flux Pipe Resonant Coil Design..... | 122 |
| Figure 5.2: The B-H Curve for FDK 6H40 Ferrite Core..... | 125 |
| Figure 5.3: Magnetic Flux Distribution in Coil Designs at Excitation Current of 50 A..... | 126 |
| Figure 5.4: Magnetic Flux Distribution in Ferrite Cores with Variation in Excitation Current. (a) Flux Distribution at 150mm Airgap. (b) Flux Distribution at 200mm Airgap..... | 127 |
| Figure 5.5: 3-Dimensional Positional Arrangement for Airgap, Lateral Misalignment, and Longitudinal Misalignment..... | 128 |
| Figure 5.6: Lateral Misalignment Parametric Analysis of Resonant Coils..... | 129 |
| Figure 5.7: Magnetic Field Distribution around Coil Designs at Different Lateral Misalignment..... | 130 |
| Figure 5.8: Longitudinal Misalignment Parametric Analysis of Resonant Coils..... | 131 |
| Figure 5.9: Magnetic Field Distribution around Coil Designs at Different Longitudinal Misalignment.... | 131 |
| Figure 5.10: Airgap Variation Parametric Analysis of Resonant Coils..... | 132 |
| Figure 5.11: Magnetic Field Distribution around Coil Designs at Different Airgaps..... | 133 |
| Figure 5.12: Dimension Parameters Specification of the Flux-Pipe Resonant Coil..... | 134 |
| Figure 5.13: Physical Design Variations of Proposed Flux-Pipe Resonant Coil..... | 136 |
| Figure 5.14: Magnetic Flux Distribution in Ferrite Cores for Flux-Pipe Resonant Coils..... | 137 |
| Figure 5.15: Variation of Magnetic Flux Density with Current Excitation. (a) Variations at Airgap of 150mm. (b) Variations at Airgap of 200mm..... | 138 |
| Figure 5.16: Lateral Misalignment Parametric Analysis of Flux-Pipe Resonant Coils..... | 139 |

| | |
|--|-----|
| Figure 5.17: Longitudinal Misalignment Parametric Analysis of Flux-Pipe Resonant Coils..... | 140 |
| Figure 5.18: Airgap Variation Parametric Analysis of Flux-Pipe Resonant Coils | 141 |
| Figure 5.19: Losses in Coil Models due to Variation in Excitation Current. (a) Core Losses. (b) Eddy Current Losses (c) Ohmic Losses | 143 |
| Figure 5.20: Losses in Coil Models due to Variation in Frequency. (a) Core Losses. (b) Eddy Current Losses (c) Ohmic Losses | 144 |
| Figure 5.21: Relationship between Maximum efficiency and the Parameter $kQps$ over a range of Frequencies. | 146 |
| Figure 5.22: Effect of Load Resistance on the Performance of Resonant Coils for S-S Compensation Topology. (a) Effect on Efficiency. (b) Effect on Power Output..... | 147 |
| Figure 5.23: Effect of Load Resistance on the Performance of Resonant Coils for S-P Compensation Topology (a) Effect on Efficiency. (b) Effect on Power Output..... | 150 |
| Figure 5.24: Misalignment Performance of Resonant Coil Designs for S-S Compensation Topology..... | 153 |
| Figure 5.25: Misalignment Performance of Resonant Coil Designs for S-P Compensation Topology..... | 154 |
| Figure 6.1: Magnetic Field around a Flux-pipe Resonant Coil..... | 157 |
| Figure 6.2: Magnetic Flux Distribution around an Unshielded Flux-Pipe Resonant Coil | 158 |
| Figure 6.3: Magnetic Flux Distribution around Shielded Flux-Pipe Resonant Coils | 159 |
| Figure 6.4: Common Losses encountered in WPT Systems with Conductive and Magnetic Shield..... | 162 |
| Figure 6.5: Optimal Coil Winding Implementation using Parallel Aiding Configuration. (a) Circuit Representation (b) Finite Element Modeling in Ansys Maxwell 3D..... | 163 |
| Figure 6.6: Modification of Ferrite Core Geometry for Optimal Performance. (a) The Model_4 Design Topology. (b) The Ungapped-core Model 4 Design Topology | 165 |
| Figure 6.7: The Finite Element 3-D Model of the Ungapped-core Model 4 Flux-Pipe Resonant Coil Topology..... | 166 |
| Figure 6.8: Modification of the Ferrite Core for Dynamic Charging. (a) Optimized Model_4 with air gap in the Core. (b) Hysteresis Curve for Gapped and Ungapped Ferrite Core. | 167 |
| Figure 6.9: The Finite Element 3-D Model of the Gapped-core Model 4 Flux-Pipe Resonant Coil Topology | 167 |
| Figure 6.10: Finite Element Modelling of Split of Coil Windings | 168 |
| Figure 6.11: The B-H Curve for FDK 6H40 Ferrite Core | 171 |
| Figure 6.12: Magnetic Flux Distribution in Flux-Pipe Resonant Coils Designs at Excitation Current of 50 A | 171 |
| Figure 6.13: Magnetic Flux Distribution in Ferrite Cores with Variation in Excitation Current for Flux-Pipe Models (a) Flux Distribution at 150mm Airgap. (b) Flux Distribution at 200mm Airgap | 172 |
| Figure 6.14: 3-Dimensional Positional Arrangement for Airgap, Lateral Misalignment, and Longitudinal Misalignment. | 173 |
| Figure 6.15: Misalignment Parametric Analysis of Flux-Pipe Resonant Coils. (a) Lateral Misalignment (b) Longitudinal Misalignment (c) Airgap Variations..... | 174 |

| | |
|--|-----|
| Figure 6.16: Losses in Coil Models due to Variation in Excitation Current. (a) Core Losses. (b) Eddy Current Losses (c) Ohmic Losses | 176 |
| Figure 6.17: Losses in Flux-Pipe Coil Models due to Variation in Frequency (a) Core Losses (b) Eddy Current Losses (c) Ohmic Losses | 177 |
| Figure 6.18: Relationship between Maximum efficiency and the Parameter $kQps$ over a range of Frequencies. | 179 |
| Figure 6.19: Effect of Load Resistance on the Performance of Resonant Coils for S-S Compensation Topology. (a) Effect on Efficiency. (b) Effect on Power Output..... | 182 |
| Figure 6.20: Effect of Load Resistance on the Performance of Resonant Coils for S-P Compensation Topology (a) Effect on Efficiency. (b) Effect on Power Output..... | 183 |
| Figure 6.21: Misalignment Performance of Flux-Pipe Resonant Coil Designs for S-S Compensation Topology..... | 186 |
| Figure 6.22: Misalignment Performance of Resonant Coil Designs for S-P Compensation Topology..... | 187 |
| Figure 6.23: Magnetic Field Radiation of Proposed Optimal Flux-Pipe Models. (a) Ungapped-core Model 4. (b) Gapped-core Model 4..... | 188 |

List of Tables

| | |
|--|-----|
| Table 2.1: Basic Difference between Traditional Power Grid and the Smart Power Grid[27]..... | 31 |
| Table 2.2: The Power Level Type and Expected Power Ratings Defined by SAE J1772 | 47 |
| Table 2.3: List of Some Selected Static Wireless Charging Projects for Electric Vehicles..... | 60 |
| Table 2.4: List of Some Selected Dynamic Wireless Charging Projects for Electric Vehicles | 63 |
| Table 3.1: Resonant Frequencies of Some MRC-based WPT Models | 73 |
| Table 3.2: Various Types of Converter Topologies used for WPT Technologies | 75 |
| Table 3.3: Performance Metrics of Some Selected WPT Models at Different Airgaps..... | 83 |
| Table 3.4: Table of Coil Shapes, Dimensions, and Performances of Some Research Works..... | 87 |
| Table 4.1: Physical Parameter Specification for the Planar Coil Designs. | 112 |
| Table 4.2: Physical Parameter..... | 112 |
| Table 4.3: Comparison of FEM Simulated Result of Planar Resonant Coil Design with Experimental Result Taken from Literature. | 113 |
| Table 4.4: Physical Parameter Specification for a Pair of Double-D Coil Designs..... | 113 |
| Table 4.5: Comparison of FEM Simulated Result with Experimental Result for Double-D Resonant Coil Design Taken from Literature..... | 115 |
| Table 4.6: Physical Parameter Specification for Double-D Coil and Solenoid Coil Designs..... | 116 |
| Table 4.7: Comparison of FEM Simulated Result with Experimental Result for Double-D and Solenoid Resonant Coil Design Taken from Literature. | 117 |
| Table 4.8: Comparison of Simulation Results of (k/T) for Different Values of Cross-Sectional Radius at 0.5m Coil Radius | 118 |
| Table 4.9: Comparison of Simulation Results of (k/T) for Different Values of Cross-Sectional Radius at 1m Coil Radius | 118 |
| Table 4.10: Comparison of Simulation Results of Efficiency Values for Different Values of Cross-Sectional and Circular Coil Radius..... | 119 |
| Table 5.1: Table of Parameter Specifications for Simple Coil Designs..... | 122 |
| Table 5.2: Evaluated Circuit Parameters for Coil Model Designs without Ferrite Cores | 123 |
| Table 5.3: Evaluated Circuit Parameters Coil Model Designs with Ferrite Cores..... | 124 |
| Table 5.4: Model Designs of Flux-Pipe Topology with Variation in Length and Width | 135 |
| Table 5.5: Evaluated Circuit Parameters for Flux-Pipe Resonant Coil Models..... | 136 |
| Table 5.6: Coil Parameters and Loss Evaluation of Resonant Coil for 8 kW Power Application..... | 143 |
| Table 5.7: Circuit Parameters of Resonant Coils from Eddy Current Solution | 145 |
| Table 5.8: Summary of Performance Characteristics of Resonant Coil Models..... | 148 |
| Table 5.9: Performance Characteristics of Resonant Coil Models Based on SAE J2954 standard for the S-S Compensation Topology..... | 149 |
| Table 5.10: Performance Characteristics of Resonant Coil Models for the S-P Compensation Configuration | 151 |

| | |
|--|-----|
| Table 5.11: Performance Characteristics of Resonant Coil Models Based on SAE J2954 standard for S-P Compensation Configuration | 152 |
| Table 6.1: Eddy Current Loss per unit mass for Different types of Conductive Shields | 161 |
| Table 6.2: Performance Characteristics of Flux-Pipe Resonant Coils with Different Shield Materials | 161 |
| Table 6.3: Coil Parameters and Loss Evaluation of Resonant Coil for 8 kW Power Application | 169 |
| Table 6.4: Evaluated Circuit Parameters of Flux-Pipe Resonant Coil Models | 170 |
| Table 6.5: Coil Parameters and Loss Evaluation of Flux-pipe Coils for 8 kW Power Application | 175 |
| Table 6.6: Circuit Parameters of Resonant Coils from Eddy Current Solution | 178 |
| Table 6.7: Summary of Performance Characteristics of Resonant Coil Models for S-S Configuration | 180 |
| Table 6.8: Performance Characteristics of Flux-pipe Coil Models Based on SAE J2954 standard for the S-S Compensation Topology | 181 |
| Table 6.9: Summary of Performance Characteristics of Resonant Coil Models for S-P Configuration | 184 |
| Table 6.10: Performance Characteristics of Flux-pipe Coil Models Based on SAE J2954 standard for the S-P Compensation Topology | 185 |

Abbreviations

| | |
|--------|---|
| BEM | Boundary Element Modelling |
| BEVs | Battery Electric Vehicles. |
| CPT | Contactless Power Transfer |
| DC | Direct current |
| DOF | Degree of Freedom |
| EMC | Electromagnetic Compatibility |
| EV | Electric Vehicle |
| EVSE | Electric Vehicle Supply Equipment |
| FCEVs | Fuel-Cell Electric Vehicles |
| FDM | Finite Difference Modelling |
| FEA | Finite Element Analysis |
| FEM | Finite Element Modelling |
| FVM | Finite Volume Modelling |
| HEVs | Hybrid Electric Vehicles |
| ICEs | Internal Combustion Engines |
| ICNIRP | International Commission on Non-Ionizing Radiation Protection |
| ICCG | Incomplete Choleski Conjugate Gradient Method |
| IPT | Inductive Power Transfer |
| kWh | kilowatt-hours |

| | |
|-------|---------------------------------------|
| MM | Meshless Method |
| MRC | Magnetic Resonant Coupling |
| OEMs | Original Equipment Manufacturers |
| PEC | Power Electronics Converter |
| PEV | Plug-in Electric Vehicle |
| PFC | Power Factor Corrector |
| PHEVs | Plug-in Hybrid Electric Vehicles |
| PM | Permanent Magnet |
| PP | Parallel-parallel compensation |
| PPS | Parallel-parallel-series compensation |
| PS | Parallel-series compensation |
| PTE | Power Transfer Efficiency |
| PWM | Pulse Width Modulation |
| RES | Renewable Energy Sources |
| RF | Radio Frequency |
| ROM | Reduced Order Model |
| SAE | Society of Automotive Engineers |
| SoC | State of Charge |
| SPG | Smart Power Grid |
| SP | Series-parallel compensation |

| | |
|------|-------------------------------------|
| SPS | Series-parallel-series compensation |
| SS | Series-series compensation |
| V2G | Vehicle-to-Grid |
| V2H | Vehicle-to-Home |
| V2V | Vehicle-to-Vehicle |
| WPT | Wireless Power Transfer |
| ZEVs | Zero-emission Electric Vehicles |
| ZPA | Zero Phase Angle |

Nomenclatures

| | | |
|-------------|-----------------------------------|----------------------|
| \vec{B} | Magnetic flux density | (T) |
| B_{max} | Maximum Magnetic flux density | (T) |
| C_p | Primary compensation capacitor | (F) |
| C_s | Secondary compensation capacitor | (F) |
| D | Density of Material | (kg/m ³) |
| f_o | Resonant Frequency | (Hz) |
| H | Magnetic field intensity | (A/m) |
| J | Current density | (A/m ²) |
| L_{lkt} | Primary leakage inductance | (H) |
| L_{lks} | Secondary leakage inductance | (H) |
| L_m | Mutual Inductance | (H) |
| L_p | Primary Coil self-inductance | (H) |
| L_s | Secondary coil self-inductance | (H) |
| k | Coupling Coefficient | - |
| K_{df} | Coil dimension factor | - |
| P_{core} | Core Losses | (W) |
| P_{eddy} | Eddy Current Losses per unit mass | (W/kg) |
| P_{ohmic} | Ohmic Losses | (W) |
| P_{out} | Power output | (W) |
| P_{in} | Power input | (W) |

| | | |
|-------------|--|----------------|
| Q_p | Primary Quality factor | - |
| Q_s | Secondary Quality factor | - |
| R_{ac} | A.C Resistance of coil Windings | (Ω) |
| R_p | Intrinsic resistance of the primary coil | (Ω) |
| R_s | Intrinsic resistance of the secondary coil | (Ω) |
| R_L | Load resistance | (Ω) |
| r_t | Radius of circular transmitter coil | (m) |
| r_r | Radius of circular receiver coil | (m) |
| V_s | Source voltage | (V) |
| V_{in} | Input voltage | (V) |
| V_{out} | Output voltage | (V) |
| X_{cp} | Primary capacitive reactance | (Ω) |
| X_{cs} | Secondary capacitive reactance | (Ω) |
| X_{lp} | Primary inductive reactance | (Ω) |
| X_{ls} | Secondary inductive reactance | (Ω) |
| X_m | Mutual inductive reactance | (Ω) |
| Z_{Total} | Total impedance | (Ω) |
| ρ | Resistivity of a Material | (Ωm) |
| ω_o | Resonant Frequency | (rad/s) |

CHAPTER 1 Introduction and Background

1.1 Background

The instability of oil prices and the high demand for imported fossil fuels by most developed countries has driven research towards the utilization of alternative energy sources[1]. In the same vein, in order to combat the effect of global warming due to the emission of greenhouse gases like carbon dioxide (CO₂) from the combustion of fossil fuel, there has been a rapid technological development towards the production of low and zero-emission vehicles[2]. These vehicles serve as suitable alternatives to vehicles powered by internal combustion engines (ICEs). Products of these technological advancements include the commercial production and deployment of electric vehicles such as Fuel-Cell Electric Vehicles (FCEVs), Hybrid Electric Vehicles (HEVs), Plug-in Hybrid Electric Vehicles (PHEVs) and Battery Electric Vehicles (BEVs)[3][1].

The HEVs and PHEVs have similar propulsion systems as they are both propelled by an ICE and an electric motor[4], [5]; the major difference between the two types of electric vehicles is that PHEV has a larger battery pack and can be charged externally from the electric power grid while the battery pack of the HEV is smaller and can only be efficiently charged through regenerative braking; a mechanism of converting the kinetic energy of the car into chemical energy that is stored in the battery[1], [6]–[8]. Similarly, the BEV has a much larger battery pack than the PHEV and is solely dependent on the electrical power stored in the battery pack installed in the vehicle to provide the necessary propulsion, air conditioning, stability and lighting requirements[1], [6].

In addition to the above-stated advantages of EVs, a further benefit of EVs over conventional ICE vehicles include a significant reduction in vehicular noise, relatively low maintenance cost and the presence of relatively low cost and high-efficient electric motors. As a result, there has been a significant increase in the sales of EVs and market penetration worldwide; which is over 5 million in 2019 and expected to reach 44 million per year in 2030 [9].

In numerous cases, the batteries of EVs are charged using the ‘plug-in’ method whereby the battery is charged from a public power utility by plugging a charging cable into an electrical outlet at private residences or charging stations. This type of charging method raises concerns and problems which include vandalization[10], system power losses, voltage drops, the creation of harmonics, phase unbalancing, equipment overloading, grid instability and safety problems due to hanging cables and opened electrical contacts[11]–[13].

Consequently, there is a need to design and develop alternative charging system that is efficient, reliable, automatic and safe; with the ability to implement robust energy supply/demand management algorithms as well as efficient use of alternative energy sources. This is attainable through a technology known as wireless power transfer (WPT). The WPT technology enables the transfer of electrical power

from the electric grid to the EVs across an airgap using electromagnetic fields with the help of wireless battery chargers. The WPT technology addresses most problems associated with the “plug-in” method of charging EVs in addition to the flexibility of charging the EVs while in a static or dynamic mode of operation.

With added capabilities for wireless bidirectional power flow between the grid and the EVs, most electric vehicles can be taken off the grid especially during the peak demand period. In addition, the bidirectional flow of energy between EVs and the grid provides the prospect of using EVs as mobile energy storage devices. By the year 2020, if there are a million cars equipped with the Vehicle-to-Grid (V2G) technology in the United Kingdom, they can generate up to 10 gigawatts (GW) of electricity [14], but as of December 2019, approximately 265,000 plug-in cars are registered in the U.K.[15] with the theoretical potential of generating just little over 2.6GW at the moment. But, a significant increase in market penetration will pave the way for easy integration of future smart grid technologies with an aggregation of EVs.

Fundamentally, WPT technology with smart grid capabilities is divided into three basic subsystems: the power electronics control, electrical circuit design and the magnetic subsystem. The magnetic subsystem covers the design of resonant coils and associated circuitry as well as electromagnetic shielding. The magnetic subsystem is the part where the transfer of electrical power across the airgap actually occurs and very critical for an efficient power transfer process. The other two subsystems deal with the conditioning of the electrical power signals.

Much previous research has been undertaken in the optimization of the electrical circuitry and power electronics controls for wireless power transfer systems with reported significant improvement[16]–[19]. Similarly, different wireless power technologies have been investigated ranging from magnetic mechanical force to capacitive power transfer and electromagnetic field technology.

Significant works has been reported on electromagnetic field technology with a major focus on power electronics and magnetic subsystems. But despite studies undertaken in order to improve the performance of the magnetic subsystem, it has been reported in many works of literature that there is a need for further optimization[20][19].

In order to move forward, efforts needs to the expended on the optimization of the magnetic subsystems of wireless power systems, based on the electromagnetic field technology. Thus, the focus of this research will be the design and optimization of the magnetic subsystem of a WPT technology for the bidirectional transfer of wireless electrical power between the electric grid and EVs.

1.2 Aims and Objectives

This project aims to design and develop optimal flux-pipe WPT coils models for the efficient charging of electric vehicles with added the capability for bidirectional flow of power between the vehicle and the electric grid. The research aims to create flux-pipe WPT models with a power rating in the range of 8 kW for static charging operations and up to 11 kW for dynamic charging operations.

The objectives of the research include:

1. The investigation into the prospects and applicability of different wireless power transfer (WPT) technologies for the charging of EVs.
2. Identification of potential viable WPT coil design topologies and shielding models applicable to the charging of electric vehicles
3. Design, modelling and optimization of commercially viable wireless power transfer resonant coil with high power transfer capability and efficiency for static bidirectional WPT operations.
4. Optimal remodelling of the proposed design of static bidirectional WPT model for dynamic bidirectional WPT operations.
5. Statistical analysis of coil design performance parameters like coupling factor, power transfer efficiency and power level in relation to the increase in current, variations in airgap and variations in coils' misalignment.

1.3 Scope of the Research

The research will limit its scope to emerging WPT technology applicable to EVs. The research begins with a review of the different types of WPT designs currently in circulation and their inherent challenges and limitations. It will further aim to model and optimise viable existing WPT system model designs for higher power transfer and efficiency while incorporating the capabilities for bidirectional WPT between EVs and the grid.

The overall system design will only take into consideration the finite element modelling and analysis of the proposed optimal resonant coil design model in order to establish the level of improvement and performance.

1.4 Publications

In the course of the research work, the conference and journal publication was generated.

❖ Published Journal Article

1. Olukotun, B.; Partridge, J.; Bucknall, R. *Finite Element Modelling and Analysis of High Power, Low-loss Flux-Pipe Resonant Coils for Static Bidirectional Wireless Power Transfer*. Energies 2019, 12, 3534. doi: 10.3390/en12183534

❖ Published Conference Articles

1. B. Olukotun, J. S. Partridge and R. W. G. Bucknall, "Impact of Coil Turns on Losses, Output power and Efficiency Performance of Flux-Pipe Resonant Coils," 2019 IEEE PES Innovative Smart Grid Technologies Europe (ISGT-Europe), Bucharest, Romania, 2019, pp. 1-5. doi: 10.1109/ISGTEurope.2019.8905677
2. B. Olukotun, J. S. Partridge and R. W. G. Bucknall, "Loss Performance Evaluation of Ferrite-Cored Wireless Power System with Conductive and Magnetic Shields" 2019 IEEE PES Innovative Smart Grid Technologies Europe (ISGT-Europe), Bucharest, Romania, 2019, pp. 1-5. doi: 10.1109/ISGTEurope.2019.8905437
3. B. Olukotun, J. S. Partridge and R. W. G. Bucknall, "Optimal Finite Element Modelling and 3-D Parametric Analysis of Strong Coupled Resonant Coils for Bidirectional Wireless Power Transfer," 2018 53rd International Universities Power Engineering Conference (UPEC), Glasgow, 2018, pp. 1-6. doi: 10.1109/UPEC.2018.8541867

❖ Journal Article in the Process of Publication

1. *Finite Element Modeling and Analysis of Flux-Pipe Resonant Coils for Segmented Transmitter Coil Array Systems Applicable for Dynamic Wireless Charging of Electric Vehicles*. To be published in IEEE Transactions on Transportation Electrification

1.5 Contributions

The major contributions of this research work are enumerated as follows:

1. **Review of the Evolution of Electric Grid into Smart Grid**

A comprehensive literature review of the electric grid has been conducted in order to understand the current status of infrastructural development and operations. The evolution of the traditional electric grid into a smart grid has been identified and the possible integration of electric vehicles with the smart grid was identified and presented. Finally, the modes of interaction of electric vehicles with the future smart grid were identified and discussed.

2. **Review of the Different Modes of Charging an Electric Vehicle**

The different modes of charging an electric vehicle were studied in order to understand and identify the most viable and optimal mode required for efficient integration with the smart grid. Two modes of charging an electric vehicle were identified- the plug-in mode and the wireless power transfer (WPT) mode. The advantages and disadvantages of the two modes were discussed and the WPT model was chosen over the plug-in mode due to added advantages like automation, safety, reliability and flexibility.

3. **Adaptation of Appropriate WPT Topologies.**

A broad review of available media for WPT technology was studied with the goal of adopting the appropriate media for electric vehicle applications. The magnetic gear, electric field and electromagnetic field technology were discussed. The ferrite-core coupled magnetic resonance topology was identified and adopted as the most suitable topology for effective and efficient charging of electric vehicles.

4. **Adoption of Flux-Pipe Resonant Coil Model for WPT**

Three common models of ferrite-core magnetic resonance topology were acknowledged- they are circular, rectangular and flux-pipe resonant coil model. The three models were designed and a finite element analysis was applied to each of the models to determine their coupling strength, misalignment tolerance, power level and power transfer efficiency. The flux-pipe model was chosen over the other two because of its performance in terms of high coupling strength and robust misalignment tolerance. However, the power transferred across the airgap was quite low when compared with the circular and rectangular models of the same design specifications.

5. **Optimal Modelling of Flux-Pipe Resonant Coil for WPT**

The selected flux-pipe model was further optimized by changing the number of turns with corresponding variations in the length and breadth of the model. Five different models were created with a varying number of turns. The five models were subjected to finite analysis to determine the most suitable model. It was revealed that increasing the number of turns for a flux-pipe resonant coil model increases its coupling strength and misalignment performance using the same amount modelling materials; thus the model with the highest number of turns provided the best performance in terms of coupling strength and misalignment tolerance.

6. **Optimization of Flux-Pipe Model for Static and Dynamic Operations.**

The initial optimal flux-pipe model was chosen based on having the highest number of turns. The model was further optimized in order to reduce the amount of power loss associated with the model. Sets of mathematical equations were developed to identify the critical physical and electrical parameters responsible for the high losses common with the traditional flux-pipe models. A physical reconfiguration of the winding turns, ferrite core geometry and the use of copper as a shielding sheet instead of aluminium was applied to the initial optimal flux-pipe model. As a consequence, three models were designed and proposed: the first model was designed for static operation. The model was designed with capability for high efficiency but with medium power output (around 11kW) at an operating frequency of 50 kHz and coil-to-coil efficiency of 98.44%. The second and third model was designed for dynamic charging operations. One of the models known as the gapped-core model 4 was optimized for high power operation (typically around 19kW) at an operating frequency of 60 kHz and coil-to-coil efficiency of 98.55%. The third model was optimized to bridge the gap between efficiency and power output of the WPT system. This hybrid model known as gapped/ungapped model 4 consists of the primary coil which is gapped model 4 and the secondary coil which is the ungapped model 4. The power output of the hybrid system is around 15kW at an operating frequency of 55 kHz and coil-to-coil efficiency of 98.73%. The three models were subjected to a finite element analysis in order to evaluate the level of their individual system performance.

1.6 Thesis Outline

The thesis is divided into 7 chapters:

Chapter 1. This chapter presents a background introduction to the reasons for the research. It gives a brief evolution of the automobile vehicles from the use of internal combustion engines (ICE) into electric vehicles powered by electric motors. The advantages and disadvantages of the three different modes of charging an EV were discussed. The research aims and objectives, scope, publications, contributions and thesis outline are presented.

Chapter 2. This chapter gives a detailed literature review of the vehicle-to-grid technology associated with future smart grids and the different modes of integration with electric vehicles. A brief discussion of the drawbacks associated with the plug-in method of charging EVs was presented and a viable alternative charging system involving the use of wireless power transfer technology was presented and discussed.

Chapter 3. In this chapter, an exhaustive analysis of ferrite-core, MRC-based coils were presented. Impact factors affecting the power level and efficiency were also discussed. The various resonant frequencies adopted, power electronic converter schemes used and compensation topology commonly used by researchers and engineers were discussed. The common models associated with the ferrite-core model was presented highlighting their advantages, limitations and a summary of the research gaps common with the selected model designs was discussed.

Chapter 4. This chapter gives a brief background, advantages and limitation of the finite element modelling (FEM) numerical method used for simulation and analysis of all model designs in this research. The adequate steps that were taken to arrive at an accurate solution and simulation were presented and validated against existing works of literature. The level of accuracy was evaluated and presented. The validated initial and boundary conditions used was subsequently adopted for all model designs and simulations.

Chapter 5. In this chapter, a selection of three appropriate models design was modelled with the same amount of materials and simulated using Ansys Maxwell 3-D finite element modelling software. Initial performance analysis and evaluation of the three models were executed. The flux-pipe model was selected and five models were created by varying the length, breadth and number of turns of the initial flux-pipe model. Further analysis was done to select the optimal and best-performing model among five flux-pipe model designs.

Chapter 6. This chapter presents the optimal remodelling of the best-performing flux-pipe model from chapter 5 resulting in the creation of two flux-pipe resonant coil design for static and dynamic charging of EVs respectively. An additional model was created comprising of a coil each from the flux-pipe designs for static and dynamic wireless charging. Related mathematical equations guiding the

optimization procedures were presented. The resulting optimal models were subjected to finite element analysis to establish their individual performance under different current values, frequency variations, load resistance, and misalignment conditions. The level of ohmic losses, eddy current losses, core losses, power output, and coil-to-coil efficiency for each model was calculated and presented. The results indicated that the proposed optimization method employed in the research was justified.

Chapter 7. A brief conclusion of the research work implemented in this thesis was presented. The level of improvement was discussed, limitations encountered in the research was presented and suggestion for future research works outlined.

CHAPTER 2 Smart Grid and Review of Wireless Power Transfer

2.1 Introduction

A proper understanding of the background and challenges of traditional electric grid, the evolution of the traditional grid into smart grid, impact of using “plug-in” method of charging electric vehicle, a review of alternative wireless charging technologies currently being developed and deployed is very essential in the search for the design and development of viable and optimal WPT topology applicable to EVs.

Thus, the literature review of this research focuses on four main categories namely: 1) Theory and development of Vehicle-to-Grid Technology for EVs, 2) Review of the Plug-in EVs in a power system network, 3) Theory and development of wireless power transfer for EVs, and 4) Review of Bidirectional wireless power transfer systems for electric vehicles.

The literature review was undertaken through the synthesis of a variety of sources. These include a diverse range of literature such as published theses, reports, conference proceedings and company reports. Additional information was obtained from sources such as books, news articles, journals and some government publications.

2.2 The Evolution of Traditional Electric Power Grid into Smart Grid

The electrical power systems are one of the fundamental infrastructures of modern society as electric grids and distribution networks are visible in almost every home, office, factory and institution. According to Amin. M. and J. Stringer[21], the electrical power grid is defined as “the entire apparatus of wires and machines that connects the power plants which are the major sources of electricity with the consumers and their numerous needs.”

The electrical power grid encompasses both the generation plants, the electrical transmission system as well as the distribution facilities. The distribution aspect is responsible for the movement of electrical power from the substation to the individual consumers[22]. Consequently, the distribution facilities are majorly responsible for the charging of electric vehicles. The distribution aspect is composed of a tree network consisting of medium voltage (1-100kV) and low voltages (110-115V in the USA or 220-240V in the UK) which can be connected to small generators, medium-sized customers and local low-voltage networks.

A fundamental feature of the traditional power grid is the presence of one-way communication structure. The feature is basically realized by carrying power to a large number of consumers from a few centralized generators[23][21]. The operation made use of an electromechanical method for control which is limited in nature. Similarly, for most power system networks, there are only a few sensors available. The sensors are only capable of manual implementation of system monitoring and

restoration[24]. The use of such a method of system monitoring and restoration is grossly inefficient as evident from the cases of blackouts and failures in the power systems. The traditional electric grid structure is limited to very few consumer interaction choices with the power system[23][25].

But the smart power grid (SPG) largely reduces most of these challenges and drawbacks by offering two-way information and communication strategies in addition to employing the use of the modern digital method for controls and coordination. The SPG also implements a method of self-healing and self-monitoring in the power system by relaying information from the numerous network sensors installed throughout the power system network[26][27]. The major difference between the traditional power grid and smart grid are summarised in Table 2.1[27].

Table 2.1: Basic Difference between Traditional Power Grid and the Smart Power Grid[27]

| Traditional Power Grid | Smart Power Grid |
|---|--|
| Uses electromechanical sensors | Employ the use of digital sensors |
| Uses one-way communication | Uses two-way communication |
| Power generation is centralized | Power generation is distributed |
| Employs the use of a few sensors | Employs the use of numerous sensors |
| Blind to systems' performance | Self-Monitoring of system performance |
| Manual method employed for system restoration | Self-Healing employed for system restoration |
| High number of blackouts and failures | Low number of blackouts and failures |
| Test/Checks are manually implemented | Test/Checks can be remotely implemented |
| System controls are limited | Wide range of control capabilities |
| Allows few consumer choices and interaction | Allows numerous consumer choices/Interaction |

However, most of the challenges and problems encountered in the power system do occur at the electrical distribution system level. As a result, the gradual transformation of the existing traditional grid into SPG will begin at the distribution level[27]. Another important feature at the distribution level in the power sector is the ability of the consumer to interact with the grid[21]. The SPG technology will afford electricity consumers the opportunity to access information regarding electricity tariff, usage and incentives in real-time; this feature will help the consumers control and coordinate their preferences and electricity usage which will in turn balance electricity demand and supply[26][28].

The SPG also employs the use of numerous distributed generation sources ranging from the use of existing thermal/hydro/nuclear power stations to the use of renewable energy sources (RES) and the capability to integrate with EVs[29]. The EVs can act as both mobile energy consuming and storage devices. The presence of many distributed energy sources reduces the risks against natural disasters and attack; thus, increasing the power system reliability and security[30][31][28].

The system infrastructure of the future smart grid integrating RES, the traditional grid, consumer loads, and electric vehicles was presented in the research works of Voglitsis .D.[20], and it is reproduced in Figure 2.1.

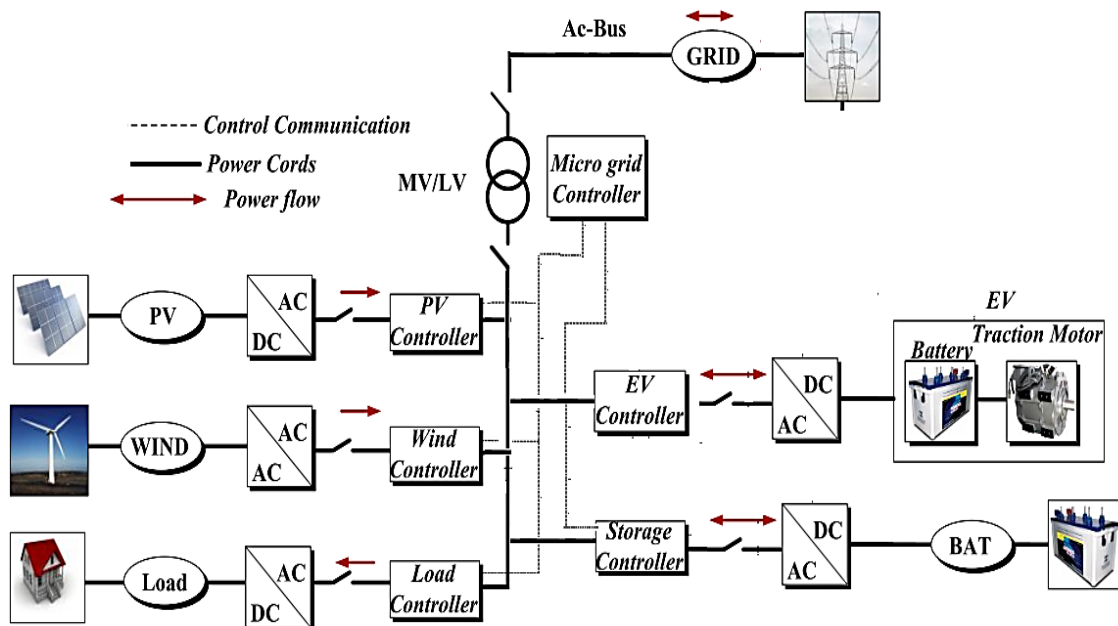


Figure 2.1: Smart Power Grid Infrastructure integrating the Traditional Power with Distributed Energy Sources (Adapted from Voglitsis .D. [20])

The electric grid, electric vehicles and battery storage system are capable of bidirectional power flow while the photovoltaic cells and wind turbines can only allow one-way power flow[32]. The presence of controllers for each of the distributed energy generation sources is to ensure intelligent communication with the microgrid controller for efficient and robust power flow in the microgrid power system[33].

The RES basically utilises energy from the wind and the sun, which offers a source of power that is emission-free and clean[34]. However, there are drawbacks; the variations in solar radiation and wind speed creates an intermittent generation of electrical power by the photovoltaic cells and wind turbines; these setbacks are responsible for the current low level of deployment[28].

Many research has been undertaken to reduce the impact of an intermittent generation of energies by RESs. For example, research work undertaken by Mwasilu .F. et al [35] focused on the design and development of stationary energy storage systems capable of supplying electrical energy during a period of low power generation and also absorbing excess power generation during a period of excess power generation. But the major drawbacks to this solution is the high cost of investment, as a result, commercial deployment of the proposed solution has been very slow.

Alternatively, the EVs can act as good alternatives to the stationary energy storage system. This is because the batteries of most EVs which ranges between 10 kWh and 110 kWh are capable of storing a significant amount of electrical energy. With high numbers of EVs equipped with V2G technology,

they are capable of storing the excess electrical energy from RESs[36][37] on a large scale when connected to smart grid infrastructure. The high performance was possible because EV batteries have undergone remarkable technological changes and development in recent years; starting with the lead-acid battery, other battery models like nickel-metal hydride, ZEBRA model have been developed[28][4]. The lithium-based batteries are currently the most common battery model adopted for use in EVs. These lithium-based batteries are light in weight, non-toxic, cheap and have very high energy and power densities[28][38]. Due to these essential features, batteries of EVs are considered for use as reliable energy storage devices. With the addition of bidirectional power transfer capabilities between the EVs and the grid, the excess energies stored in the batteries can be discharged back to the grid or microgrids when needed, especially during the peak demand period[39].

The bidirectional capabilities are only possible through a technology known as Vehicle-to-Grid technology (V2G) [28][29], [40]. Though the V2G technology is currently in its developmental stage, the traditional grids are fundamentally designed to support unidirectional communication with EVs (i.e. efficient power flow from the electric grid to EVs). The added features and functionalities present in the smart power grid infrastructure enables the use of V2G technology in the control of the battery charging rate based on a good incentive system or specific scheduling algorithms[28][41].

The increase in consumer participation in SPG networks due to its capability for two-way communication increases V2G technological capabilities of implementing bidirectional management and control of energy exchange between the EVs and power grid. Also, the V2G technology application in smart power grid affords users the incentive of charging their EVs during the off-peak period at lower cost through an efficient control mechanism. The SPG is also configured to allow the discharging of electrical power from the batteries back to the grid during peak periods depending on the state of charge (SoC) of the battery; the possibility of such users' interactions provides a potential for an added source of income to electricity customers. This will help to a large extent in levelling the load demand throughout the day as it reduces power losses and it is cost-effective [28].

With the gradual progress and developmental evolution of the electric grid into SPG, the ultimate goal of the V2G technology will be to ensure the bidirectional flow of electrical energy between the EV and the grid; thus, the term V2G will be known as bidirectional V2G technology henceforth. The bidirectional flow of electrical power between EVs and the grid has been further enhanced by the development and deployment of bidirectional EV chargers. However, only the plug-in charger is commonly used for such purpose at the moment.

Based on the scale fleet of the EVs, The V2G technology can be categorized into Vehicle-to-Vehicle (V2V), Vehicle-to-Home (V2H) and Vehicle-to-Grid (V2G)[42][43]. A basic illustration of the V2V, V2H and V2G is shown in Figure 2.2[42].

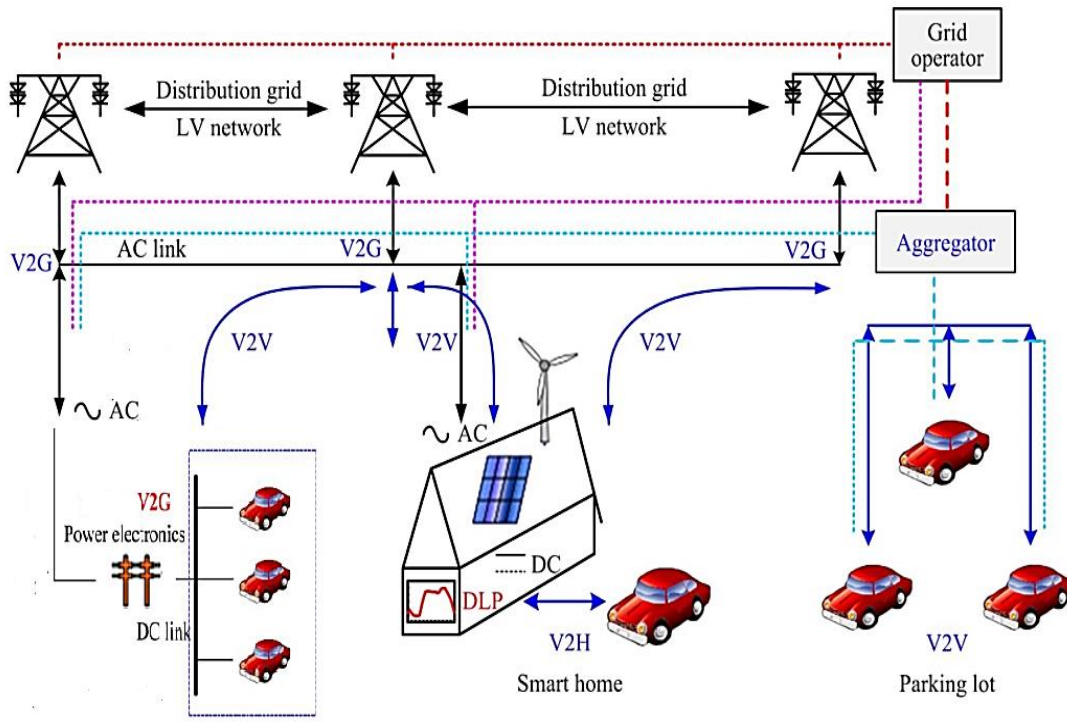


Figure 2.2: Illustration of the V2V, V2H and V2G Technologies and Integration[42]

2.2.1 Vehicle-to-Vehicle (V2V) Technology

The V2V technology employs the use of a controller called an aggregator to distribute electrical power among the EVs. The aggregator makes it possible by connecting the EVs between each other and ensuring interaction between the vehicles and the electrical grid. This is achieved by using a bidirectional transfer of energy through the local grid which is then distributed among the EVs[42][35].

Key features of the V2V[35] technology include the use of multiple vehicles equipped with grid integration capabilities. The interaction between the community of electric vehicles and the electric grid occurs at the low voltage distribution level[42]. The exchange of electrical power can be achieved using simple infrastructure with little losses in the system.

But there are factors affecting the use of V2V technology with the smart grid power networks. The major factor affecting the successful operation of V2V technology is the aggregator's requirement for charging and discharging operations[42]. For some design, the aggregator is optimized for charging operations than for discharging operations. Also, another factor is the total number of vehicles available in the fleet. Another factor affecting the V2V technology is the characteristics of the battery capacity and the type of battery. Some battery types are more efficient for V2V technology than others[32][42]. Similarly, the capacity of the battery of an EV determines to a large extent the role they can play in the V2V technology. EVs with bigger battery capacity like the ones installed in buses has more capacity for discharging operations for the charging of medium electric vehicles. Other factors

affecting the use of V2V technology are prices of electrical energy, state of charge of the batteries, the driving habit of the user and the time of arrival and departure of the user of the technology[42][44]

In summary, the major function of the V2V technology include the provision of electric energy for electric vehicles, increasing the efficiency of electric vehicles for discharging and charging operations, power trading within the local grid for reduction of the tariff, support for reactive power, and control coordination of grid-enable electric vehicles[42][28].

2.2.2 Vehicle-to-Home (V2H) Technology

The V2H technology employs the use of bidirectional chargers which can be off-board or on-board in the discharging/charging of the EVs to or from the home through a control scheme[45]. The control scheme is implemented using a controller that synchronises the public power utility, and any renewable energy source at home with the electric vehicle[43].

Key features of the V2H technology include the use of a lone vehicle equipped with grid integration capability. The V2H infrastructure is relatively simple in design with negligible losses in the course of transmission. The V2H is also very easy to install as it is limited only to the grid operation at a particular household[42].

But there are factors affecting the use of V2H technology with the smart grid power networks. The major factor affecting the successful operation of V2H technology is the day-to-day load profile of electric devices at home[35]. For some homes, the majority of the energy supply is consumed by electric devices with high power ratings like washing machines, dryers, fridges and heating elements. Also, another factor is the requirement for support of reactive power in the home. Another factor affecting V2H technology is the characteristics of the battery capacity and the type of battery. Some battery types are more efficient for V2H technology than others[42][4]. Similarly, the capacity of the battery of an EV determines to a large extent the role they can play in the V2H technology. EVs with bigger battery capacity has more capacity for discharging operations for the supply of electrical energy to the home. Other factors affecting the use of V2H technology are prices of electrical energy, state of charge of the batteries, the driving habit of the user and the time of arrival and departure of the user of the technology[46][42].

In summary, the major function of the V2H technology includes the provision of electric energy for home use by acting as a back-up generator. With the appropriate scheduling operation, the V2H technology can synchronize with the electric devices for the shifting of loads. The electric vehicle can be charged at off-peak periods when electricity is less expensive and then discharge back to the grid during peak period at a profit. The electric vehicle used in V2H technology can be used to store excess energy from home-built photovoltaic cells and wind turbines which is then sold to power companies[42][47], [48].

2.2.3 Vehicle-to-Grid (V2G) Technology

The V2G technology employs the use of a fleet of EVs for the bidirectional transfer of electrical energy between the vehicles and the grid. Just like the V2V technology, the aggregator is employed for the grouping of the EVs for discharging/charging operation and it is also used for grid integration and regulation[45][24], [49].

The major features of the V2G are the large fleet of cars involved. These cars are the accumulated total of electric vehicles from V2H, V2V and electric vehicles connected directly to the grid at commercial charging/discharging stations. The major source of power is the power grid[42]. Because of the large scale of operations, the technology employs complex control schemes for the discharging/charging coordination of the connected electric vehicles[30]. Accommodation of a large number of electric vehicles will require big and complex infrastructure. The transmission losses recorded in the course of charging/discharging operations is significantly high[6], [50].

Just like V2H technology, there are similar factors affecting the use of V2G technology with smart grid power networks. The major factor affecting the success of the operation of the V2G technology is the number of aggregators required for a particular number of electric vehicles connected to the grid for charging and discharging operations. For some design, a particular aggregator is optimized for charging operations/discharging operations of electric vehicles that are less than 100 in number[22]. Also, another factor is the level of power flow in the electric grid. Depending on the time of the day, the flow of power in and out of the electric grid varies depending on the number of EVs undergoing discharging or charging operations. Thus, in order to avoid grid instability, the grid operators implement some control and regulation schemes to limit the number of cars for charging/discharging operations at a particular location[23], [25], [51]. Another factor affecting the V2G technology is the characteristics of the battery capacity and the type of battery. Some battery types are more efficient for V2G technology than others[42]. Similarly, the capacity of the battery of an EV determines to a large extent the role they can play in the V2G technology. EVs with bigger battery capacity like the ones installed in buses has more capacity for discharging operations for the charging of medium electric vehicles, thus, are normally connected to the grid at peak periods for discharging operations. Other factors affecting the use of V2G technology are prices of electrical energy, state of charge of the batteries, the driving habit of the user and the time of arrival and departure of the user of the technology[42][52].

In summary, the major function of the V2G technology includes the provision of electric energy to the grid supplementary services by acting as back-up energy generation sources. With the appropriate scheduling operation, the V2G technology can synchronize with the electrical devices for the shifting and controlling of electrical loads in the power system. The electric vehicle can be charged at the off-peak periods when electricity is less expensive and then discharge back to the grid during peak period at a profit. The electric vehicle used in V2G technology can be used to provide electrical energy for

private and business premises to save cost[6][42]. It also allows for synchronization of renewable energies with the traditional grid, support for reactive power and the short-term stabilization of the electric grid.

2.3 Review of Plug-in Charging of Electric Vehicles

For most research applications, EVs is a term used to describe any type of vehicles employing the use of electric motors for propulsion. Three types of such vehicles are currently being developed, and in operations currently. They are the Fuel-Cell Electric Vehicles (FCEVs), Hybrid Electric Vehicles (HEVs), Plug-in Hybrid Electric Vehicles (PHEVs) and Battery Electric Vehicles (BEVs)[1][4], [38].

The FCEVs uses a fuel-cell as a source of energy storage and conversion[53][54]. The fuel source can be in gaseous or liquid form. The gaseous form can employ the use of natural gas or hydrogen while the liquid form employs the use of methanol[53]. Hydrogen fuel-based FCEVs is known as Zero-emission EVs (ZEVs) while the ethanol-based and natural gas-based EVs are known as low emission vehicles. One common feature of FCEVs is the absence of batteries and thus, it is currently not designed for application with V2G technology[53][55].

The BEVs, PHEVs and HEVs, on the other hand, are capable of using batteries for the storage of electricity. If an electric vehicle has the dual capabilities of a battery and ICEs, it is known as a PHEV, or HEV while if there is an absence of an ICE, it is known as BEV. The HEV has a small battery capacity that can be as small as 36 Ah[56]. Due to its small capacity, the batteries of an HEV can be charged efficiently using the internal regenerative braking of the vehicle; and in most cases, it is not designed for the charging of the batteries using external energy sources. Thus, the HEV is not currently adapted for use with the V2G technology.

The PHEV, on the other hand, has a bigger battery capacity which can be as big as 16 kWh for a typical vehicle and 50 kWh for a bus[29]. Due to its bigger battery capacity, the vehicle is equipped with the necessary interface for the battery to be charged from an external energy source from where it derived the name “plug-in” HEV. Due to the capability of the PHEV to interact with the electric grid, the vehicle charging system can easily be modified for V2G technology through an efficient WPT system[23], [47], [57].

Finally, the BEV only uses batteries for the storage of electrical energy used for the propulsion of the vehicle. The battery capacity of the BEV is quite bigger than that of the PHEV and can be as big as 56 kWh for a typical vehicle and up to 100 kWh for a bus[6]. For the BEV, the only interface available for the charging of the battery on a big scale is the use of a dedicated public power supply utility. Due to its design and operation, it can be easily modified for use with V2G technology.

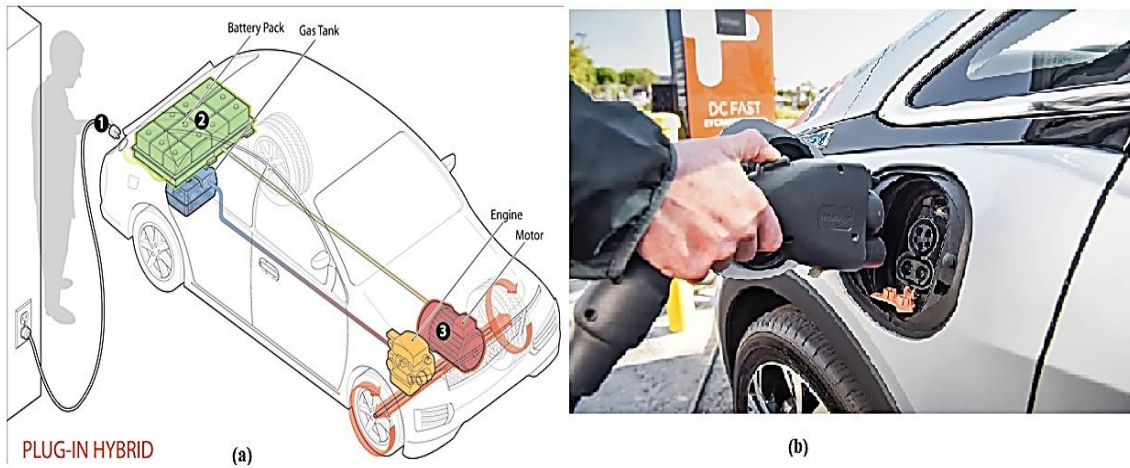


Figure 2.3: Practical Implementation of Plug-in Charging Method for PEVs. (a) Plug-in Hybrid Charging Infrastructure[58]. (b) A Commercial Charger for PEVs[59].

For most practical applications, the BEV and PHEV are known as plug-in electric vehicles because they are mostly charged using dedicated charging cables connected to a power utility[3], [35], [50]. This is illustrated in Figure 2.3. These BEVs and PHEVs are increasingly becoming popular because of some benefits they offer the consumers, which will be discussed in the next section. However, both BEV and PHEV are currently designed for plug-in charging operations; they will be jointly referred to, as Plug-in electric vehicles (PEVs) for simplicity and analysis in this chapter.

2.3.1 Drawbacks in the use of Plug-in Electric Vehicles (PEVs)

Despite the common advantages of using PEVs, there are potential and practical drawbacks in its wide adaptability and acceptance. The most common disadvantage is the cost of PEV batteries. For example, it was reported in the year 2018 that a high-volume battery of a PEV cost an average of \$190 per kWh for Tesla's Model 3 battery pack while General Motors' 2017 Chevrolet Bolt Battery pack is estimated at about \$205 per kWh[60]. Thus, the cost of an electric vehicle can go as high \$40,000 and the minimum cost for a new PEVs is normally not less than \$35, 000[47].

As a result of the high cost of the batteries for PEVs, most customers typically buy a mid-range vehicle with 30 kWh capacity capable of travelling a cumulative distance between 125 km and 150 km [47][36], [61].

Another drawback is the cost of recharging infrastructures. For most owners of electric vehicles, their PEVs are charged at dedicated parking locations equipped with electric charging cables[62]. This is because of the amount of electrical energy required for the full charging of the batteries. The installation of a private charging outlet at home will require massive investment in the alteration of household electrical systems which comes at an exorbitant cost, coupled with the fact that it can mostly accommodate slow and low charging power ratings[51]. The charging operations are most efficient when done overnight.

Another common setback is the limitation of the current PEV is the charging capabilities. PEVs are limited to the static mode of charging due to the short length of the charging cable[11] and this is the major reason why the driving range of EVs is limited to short distances (typically less than 80 miles)[29], [63]. The setback can be overcome through the modification of power electronics circuitry and the addition of coil plates for wireless power transfer.

Other common challenges associated with charging operations of PEVs is the risk of vandalism, safety issues as a result of hanging cables and open contacts, manual mode of operation from the user, the presence of galvanic actions and creation of harmonics[64][28][11].

In order to minimize some of the drawbacks of plug-in charging method associated with PEVs, a wireless charging alternative was proposed which addresses some of these challenges[11][20]. The development and adoption of an optimal wireless power transfer technology applicable to electric vehicles will reduce if not eliminates the majority of these drawbacks[40], [65]. A review of various wireless power technologies, their feasibility studies and potential suitability for electric vehicles are discussed in the next section.

2.4 Theory and Development of Wireless Power Transfer for EVs

Electricity as a reliable energy source can be used to power the automobile transportation systems especially cars and trains; thus, reducing the demand and consumption of fossil fuels. For personal electric transportation, there are already vehicles which can be plugged into the grid and off-board energy-storage systems comprising of batteries; these off-board batteries can be recharged using clean and renewable electricity[66]. It has also been observed that the charging process can be optimally utilised by charging the EVs at night when there is low consumer demand on the electrical power grid; thus, reducing strain on the grid and the need to add any major generation and transmission infrastructure [62].

In order to reduce the strain on the electrical power grid as well as providing a convenient means to charge EVs at any time of the day; an alternative charging technology known as Wireless Power Transfer (WPT) technology was proposed. This is a process in which wireless or contactless power is transferred through the process of induction or resonance [1][67]–[69]. It has been reported that connecting PEVs to the grid to charge the batteries creates issues like harmonics and galvanic actions[11]; in addition, there is also a limitation in battery performance due to the state-of-the-art technology of the lithium-ion (Li-ion) batteries which are the commonly used energy-storage device for PEVs. The problems includes the environmental cost of disposing of the batteries, degradation which once limits the market acceptance, and the charging limit due to the chemistry of the chemical components, to their low energy density [1] when compared with the energy density of fossil fuels.

With the limitation of the onboard energy storage to a few miles, swapping of car batteries at intervals and hybridization of the drive-train became a viable alternative option[4], [62]. The WPT concept was

proposed as a hybridization concept because of the possibility of extending the capabilities of PEVs for the exchange power between the vehicle and the grid when the vehicle is in stationary mode or in dynamic mode (in motion). Charging the EVs while they are stationary is known as static charging and has three applications vis-a-vis: WPT-powered parking lots, WPT-powered home parking lot, a WPT-powered bus stops and a WPT-powered area close to a traffic light or traffic-congested areas in an urban area[28][62].

Charging the PEVs while in motion in some literature is referred to as roadway powered EVs, others termed it as dynamic charging, while some calls it move-and-charge. The major application of dynamic charging is a WPT-powered track section on a highway[62], [70]. This has the capability of powering multiple vehicles at once. However, while the static charging is reaching the required industry standardization, the dynamic charging EVs offer the advantage of significantly reducing the size of battery packs of EVs as well as providing automatic charging of the vehicle with little effort from the user[62][61]. The concept requires little maintenance and reduces the act of vandalism while providing safety from sparks and trip hazards.

However, the dynamic wireless charging is in the incubation stage with lots of work currently on-going in the area of research and development[71], [72]; but the adoption of such charging method will help the partial removal of overnight charging by using network-dynamic wireless chargers that are compact which are installed on the road[73]; thus, keeping the batteries of EVs charged at most times. As a result, a small battery can power an EV over a long range of travelling distance.

For the adaption of appropriate WPT topology suitable for EV applications, a review of available media for wireless power transfer is very vital. The media of wireless power transfer adequately gives a better understanding of the existing technological level of efficiency, power output and application restrictions.

From published reports on WPT technology, WPT is basically divided into three: Mechanical force, Electric field and Electromagnetic field [45] as shown in Figure 2.4.

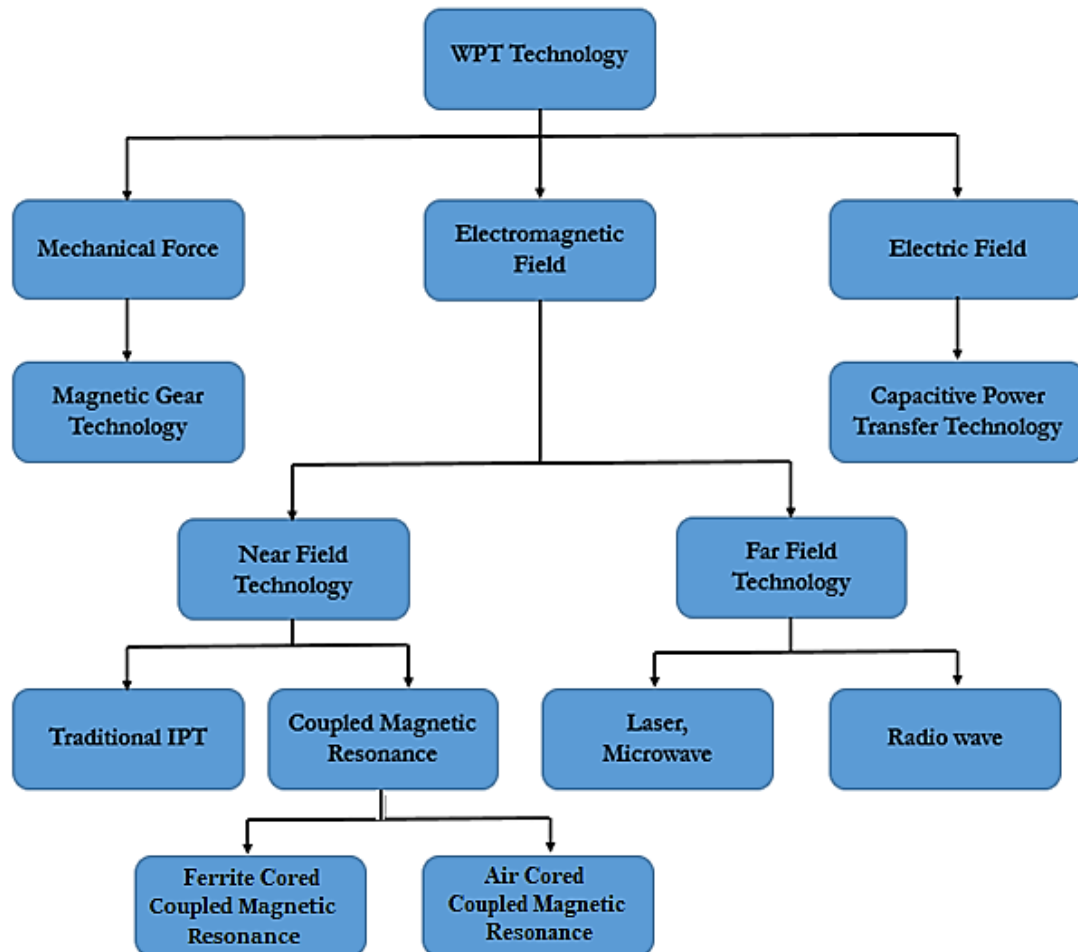


Figure 2.4: Categories of Different WPT Technologies[45].

2.5 The Magnetic Gear WPT Technology

The Magnetic Gear WPT technology works on the basis of the synchronization of two permanent magnets (PMs) in tubular form as the main coupling technology. The two permanent magnets are placed side by side for wireless power transfer application. This is unlike the coaxial configuration designed for application in wind power generation[74]. The typical setup for the magnetic gear WPT technology is shown in Figure 2.5[45].

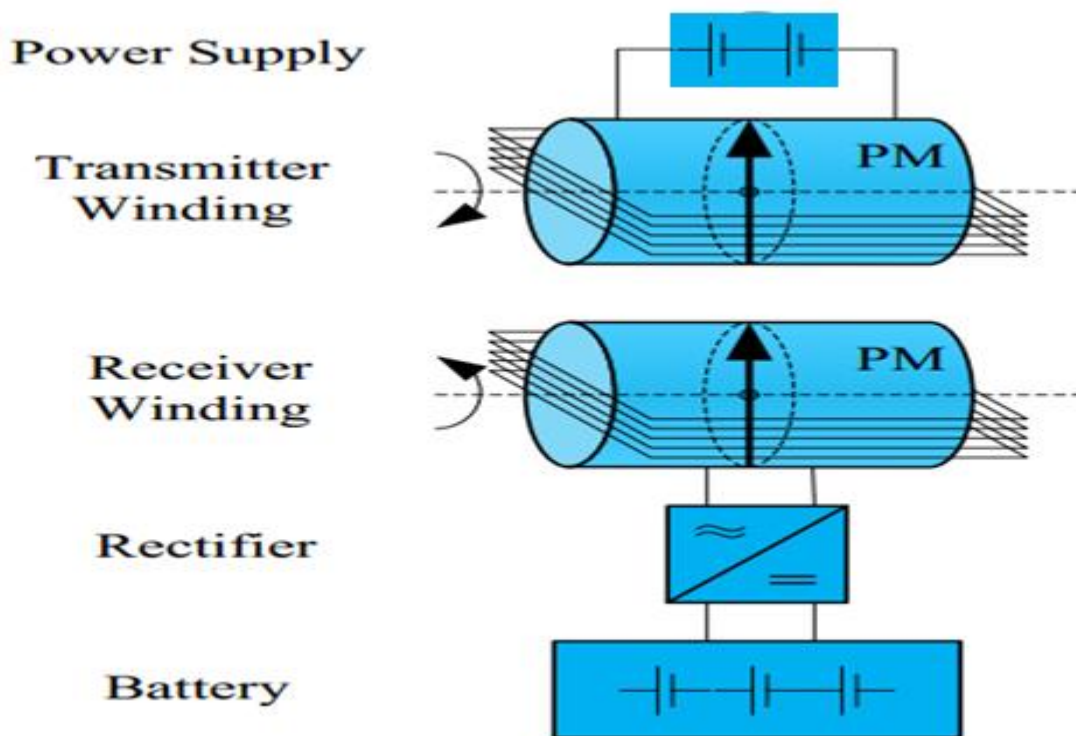


Figure 2.5: Schematic of Magnetic Gear WPT Application for EVs[45].

The basic principles of this technology consist of the production of mechanical torque on the transmitter winding when power is supplied from a DC source; this causes it to rotate. The magnetic field, as a result of the rotation, causes the receiver winding to rotate in synchronism making the receiver work by the mechanism used for an a.c generator, thereby charging the battery via the rectifier[45][74].

It is relevant to state that this technique has been used in medical implants but the power output and air gap are very small[45][75]; mostly less than 100W and 5cm respectively. For example, Matias. R and Cunha.H [76] developed a model magnetic gear WPT system capable of transferring a maximum power of 6.6W. Coincidentally, only 1W of power was generated at a distance of 1cm; possibly due to the limited space available in the human body. Based on the same technique, Lee S.H and Lorenz R.D[75] were able to generate a power of 1.6kW at a distance of 15cm which is high enough to charge an EV, but this comes at a high cost of controlling the speed of the rotators. It was noted that at a frequency of 150Hz, the upper power limit requirement was reached and the synchronization of the rotators becomes significantly degraded. Due to this limitation, the practical application of the technology for high power operations will require the adjustment of the rotator's speed with feedback control from the battery. In addition to the drawbacks mentioned above, there is also an issue with the alignment; this is because the power transfer efficiency (PTE) degrades significantly when the permanent magnets are not properly aligned; making it very unsuitable for dynamic charging of EVs[45]. Another issue with this technology is the decrease in WPT when there is an increase in the axis-to-axis separation of the PMs. Likewise; the wireless power transfer process becomes complicated

due to the small dimension of the PM. For example, a 5cm by 10cm PM is only capable of supplying 1kW of power. Increasing the PM's dimensions for higher power transfer makes it difficult for static charging of EVs[74].

2.6 The Capacitive WPT Technology

This technology made use of an alternating electric field confined between two conductive plates to transfer power wirelessly. The mode of operation is illustrated in Figure 2.6[77]. The capacitive method of WPT technology was developed in order to overcome the need for guiding of magnetic flux and use of shielding component as obtainable using the inductive method of wireless power transfer[77][78].

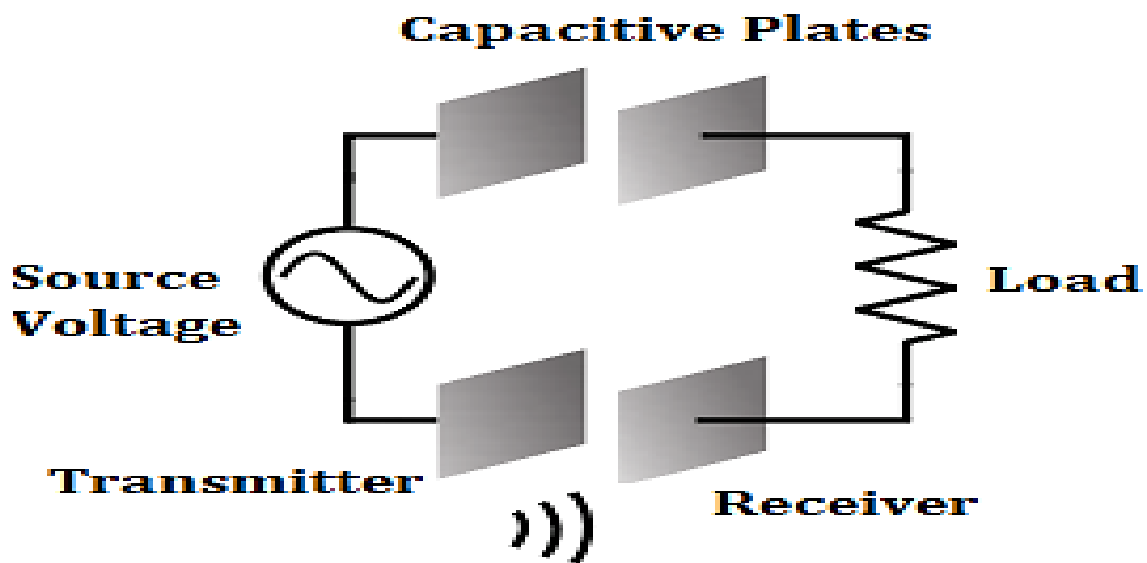


Figure 2.6: Working Principle of Capacitive WPT Technology

The technology is noted for a high PTE of around 90% but operates at a high frequency in the Megahertz range. The high frequency is employed in order to limit the capacitive reactance of capacitive plates. The capacitive WPT technology is known for its low electromagnetic interference (EMI) and the ability to combine both charging and data synchronization over a single interface[77][79]. The capacitive WPT technology is relatively affordable with notable galvanic isolation capabilities[78][80].

Despite these advantages, the coupling capacitance is very small mostly in the microfarad range for most practical applications. This is as a result of the low permittivity of the air/vacuum which is 8.854×10^{-12} F/m. Though the capacitance can be increased by special and costly dielectric materials like BaTiO_3 [68], [81]; the existence of an air gap or displacement of the coupling plates decreases the capacitance of the plates. Another major drawback of this technology is the low power transfer output; in most cases, it is less than 100W and this power ratings is achievable at a very small distance of transmission; typically in the range less than 20 millimetres[45]. For example, in the published work

of Mitchell Kline et al[77], their proposed capacitive WPT model could only transmit 3.7 W of power across the capacitive plates at a maximum efficiency of 80%. Similarly, a variation of the coupling capacitance causes a significant reduction in the operating frequency.

The limitation in transmission distance is as a result of the electric flux being confined within the conductive plate. Under this condition, the magnetic flux tends to make a closed flux loop by spreading in all directions from within the coils. Despite the drawbacks, the capacitive WPT has the ability to transfer electrical power through metal. This is attainable because of the ability of the lower and upper surface of the metal to act as a conductive plate in an electric field. Though this may end up dividing the original electric field into two, it has no effect on the amount of transferred power[45].

There is also the issue of poor displacement tolerance between the conductive plates[45]. A WPT model is said to have poor displacement tolerance if a displacement of 30% of the total length of any of the coil causes more than 50% reduction in the power transferred and more than 25% reduction in efficiency[43]. The WPT technology also requires a complex control of the duty cycle in order to maintain high efficiency of above 70% at light loads.

Due to these limitations, it is impracticable to use the capacitive WPT technology for the charging of EVs; this is due to the minimum practical requirement of the airgap between the transmitting and receiving units (typically 110mm to 200 mm)[11].

2.7 The Electromagnetic Field-based WPT Technology.

This technology is based on a time-varying electromagnetic field. The technology is subdivided into two groups based on the distance of power transfer. They are Near Field WPT technology and Far Field WPT technology. For a proper discussion of these WPT technologies, there are common terms and parameter specifications that need to be defined. The common terms are discussed in the next section.

2.8 Performance Parameters for Electromagnetic Field-Based WPT Technology

In the research and development of WPT, many common terms and terminologies are being used by researchers to measure the performance of a WPT model. The measured performance level gives a degree of suitability and adaptability of the model. Common terminologies used are coupling coefficient, quality factor, power level, power transfer efficiency and loss factor.

2.8.1 Coupling Coefficient (k)

In the case of electromagnetic field-based WPT technology, the receiver and transmitter coils are separated by a large airgap ranging from hundreds of millimetres to thousands of miles. Due to the large distances, most model designs do not have a common magnetic core; this creates a poor or weak magnetic coupling between the coils. The creation of weak magnetic coupling between coils is because

of the divergent nature of magnetic flux as they travel in space. The scenario is depicted in Figure 2.7[11].

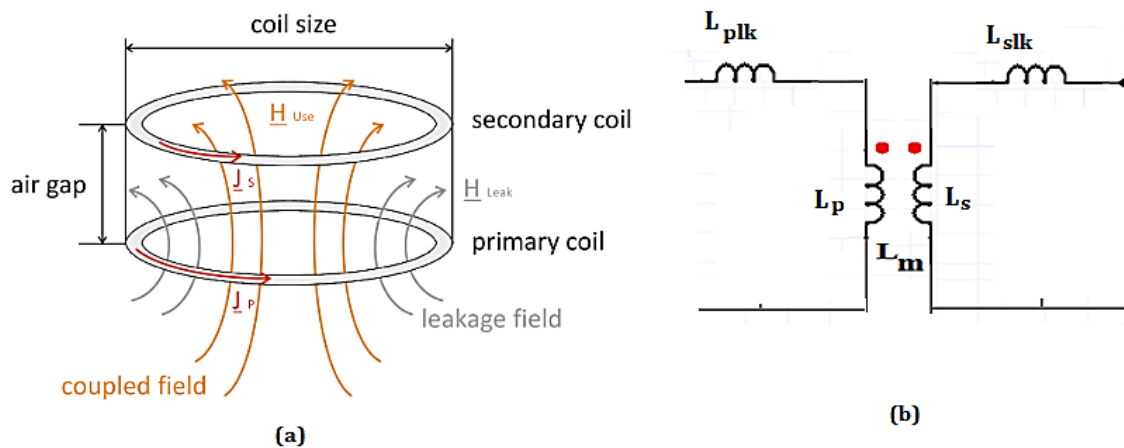


Figure 2.7: (a) Divergent Nature of Magnetic Flux and Fields as they travel in Space (b) Circuit Representation[11].

The extent of this magnetic coupling between the transmitter and receiver coils is defined as the coupling coefficient k and is mathematically represented as:

$$k = \frac{L_m}{\sqrt{L_p * L_s}} \quad 2.1$$

The coupling coefficient is zero and no coupling exists when there is no mutual inductance (L_m) between the transmitter and receiver. The values of L_p and L_s are the self-inductance (H) of the transmitter and receiver coils respectively. For a typical iron core transformer, the coupling coefficient is very close to 1 and thus, have the highest coupling coefficient[43]. When the values of $k \geq 0.5$, they are termed as strongly coupled or tightly coupled and when the values of $k \leq 0.5$, they are termed as poorly coupled or loosely coupled[43]. For most applications, the values of the k is dependent on the magnetic properties of the ferrite core on which the coils are wound, the physical dimensions of the coils, their relative position to each other and the number of turns of each coils[13], [82], [83]. Also during the process of static or dynamic charging, the coupling coefficient decreases with an increase in the vertical and horizontal displacement of the receiver coil known as misalignment[43].

2.8.2 Quality Factor (Q)

According to K. A. Kalwar et al [43], the quality factor gives an indication of the level of inductive properties of resonant coils used for WPT applications. It is the measure of the capacity of the coils to produce a large amount of magnetic field which will be responsible for the transfer of power across the airgap. The intrinsic quality factor for the transmitter and receiver coils is defined mathematically as[43]:

$$Q_p = \frac{\omega_o L_p}{R_p}, \quad Q_s = \frac{\omega_o L_s}{R_s} \quad 2.2$$

Under normal conditions, the WPT system is required to operate at a constant resonant frequency; but changes in system parameters like the airgap, load or capacitance can cause a variation in the resonant frequency and thus, the system's angular frequency is not at the required zero phases [43]. The presence of more than one zero phase angle frequency is known as bifurcation[70][71]. At these different resonant frequencies, the efficiency is quite high and it has been noted [84][86] that the existence of bifurcation in the system is greatly influenced by the value of the quality factors of the coils. Possible solutions have been proffered to avoid this phenomenon. For example, C. Sen Wang et al [86] proposed that the value of quality factor of the transmitter coil must be greater than that of the receiver coil in order to maintain a single zero angle frequency. In addition, it was reported that a greater value of the product of the coupling coefficient and quality factor increases the power transferred efficiency of the resonant coils[87][13].

2.8.3 Power Level

For most WPT applications in the charging of electric vehicle, the power level is dependent on the charging time, cost and locations. These parameters must be adequately accommodated[88] for optimal design. For example, at an operational airgap of between 100mm and 250 mm, power level of 2 kW to 7 kW was proposed for a case of single charging track[43]. The appropriate criteria for the selection of appropriate power levels for selected charging of EVs are based on a number of different standards and codes. Typically, the Society of Automotive Engineers (SAE) J1772 code describes different levels of power requiring a different type of infrastructures[43]. The codes prescribe three categories of the power level for charging operations. They are on-board (level 1, level 2) and an off-board charging (level 3) [89]. The charging level classification prescribed by the SAEJ1772 is applicable in the European Union (EU) and are illustrated in Table 2.2[90]

Typically, the level 1 power level type is supplied by a convenient outlet interface while Level 2 and Level 3 is supplied by a dedicated electric vehicle supply equipment (EVSE). Different Original Equipment Manufacturers (OEMs) produce different equipment with different design specification shown in Table 2.2 and thus, do not follow a particular worldwide standard. The SAE J2954 task force responsible for light-duty PEVs' wireless power transfer proposed [43] a specific power level and frequency to enable the interoperability of charging electric vehicle before commercialization. The resonant frequency proposed for charging of light electric vehicles was 85 kHz and this value lies in between the internationally acceptable frequency band of 81.38 kHz-90 kHz proposed by the SAE J1772 regulation.

Table 2.2: The Power Level Type and Expected Power Ratings Defined by SAE J1772

| Power Level Type | Charging Location | Expected Power Level | Charging Time | Vehicle Technology |
|--|-------------------|----------------------|---------------|--------------------|
| Level 1 230V (A.C.) | On-Board | 1.4 kW (12 A) | 4 - 11 Hrs | PHEVs (5-15 kWh) |
| | 1-Phase | 1.9 kW (20 A) | 11 - 36 Hrs | EVs (16-50 kWh) |
| Level 2 230 V (A.C.) 415 V (A.C.) | On-Board | | | |
| | 1-Phase | 4 kW (17 A) | 1-4 Hrs | PHEVs (5-15 kWh) |
| | 3-Phase | 8 kW (32 A) | 2-6 Hrs | EVs (16-30 kWh) |
| Level 3 (Fast) 280 - 600 V (A.C.) 280 - 600 V (D.C.) | Off-Board | | | |
| | 3-Phase | 50 kW | 0.4 - 1 Hr | EVs (20-50 kWh) |
| | | 100 kW | | |

For the purpose of this research, level 1, level 2, and level 3 will be denoted as low power, medium power and high power level. From the description of the power level types, the expected A.C. power level ranges from 1.4 kW to 50 kW.

2.8.4 Power Transfer Efficiency (PTE)

Power Transfer Efficiency is the ratio of the transferred power across the gap and the input power. This is a crucial parameter in the design of wireless power transfer[36], [62]. The relatively low value of the PTE has been responsible for the slow commercial deployment of WPT technology in the charging of electric vehicles. In addition, there is also the issue of size, cost of new infrastructure and the power level[65]. The measure of PTE can be calculated from the various subsystems of the whole wireless power transfer system. The commonly used term is the overall efficiency which is the measure of the efficiency as a ratio of the power received at the battery to the input power supply. Many WPT models have been developed and the overall system efficiency presented. For example, SangCheol Moon [91] developed a wireless power transfer system employing the use of an intermediate coil between the source coil and receiver coil. The model offered an overall efficiency of 95.57% while transferring 6.6kW of power across an airgap of 200 mm. Similarly, P. Ning et al [92] designed and developed a WPT prototype capable of transferring up to 7 kW of power across an airgap of 200 mm at 90% efficiency.

In another instance, some researchers presented the performance of their WPT models by measuring the coil-to-coil efficiency. The coil-to-coil efficiency does not take into consideration the losses encountered in the power electronic converters and only measure the efficiency as the ratio of power at the transmitter to the power received at the receiver coil. For example, J. M. Miller [63] developed a WPT model capable of transferring 6.6kW at a coil-to-coil efficiency of 91% across an airgap of 75 mm. It was also reported that C. Qiu et al [45] at the Oak Ridge National Laboratory (ORNL) were able to develop three different WPT with the capability of transferring between 2 kW and 7.7 kW of power across a range of airgap between 75 mm and 254 mm with a coil-to-coil efficiencies between the range of 91% and 93%.

Another performance metric known as overall D.C. to D.C. efficiency was proposed by T.D. Nguyen et al [93]. The DC to DC efficiency was measured as a ratio of the power output at the rectifier to the power input at the rectifier of the receiver of their proposed rectangular bipolar pads. An overall DC to DC efficiency of 95.66% was reported when 8 kW of power was transferred across an airgap of 200 mm with zero misalignment.

From all the various efficiencies reported, the fundamental principle was maintained which is the measure of the ratio of the output power to the input power.

2.9 The Far Field WPT Technology

This technique requires the use of microwave frequency power transfer from the transmitter antenna to the receiver's antenna. The technology requires a microwave source, a transmitting antenna, a receiving antenna and a waveguide [16]. Electrical power is first transmitted to the waveguide from the microwave source. The electromagnetic wave is then emitted uniformly from the transmitting antenna. At the receiver's side, the receiving antenna collects the microwave energy using silicon-controlled rectifier diode which is then converted into a direct current by the diode's rectification capability [16].

With the use of laser beams and antennas with high directivity, power can be transferred at high PTE when used with the laser or microwave technology; but there is an issue with maintaining a good alignment at such distance as it requires complicated tracking methods. Subsequently, when omnidirectional antennas are used as is the case with radio waves, the power density is inversely proportional to the square of the distance of transmission. This is why it is mostly used in signal broadcasting applications because the power requirement can be as low as microwatts[45], [91].

The electromagnetic radiation method of power transfer has the advantage of efficient power transfer over long distances but requires a line of sight transmission. Subsequently, as the name suggests, there is a problem of radiation which could be extremely harmful to man and animals when transmitting high power as the required standard for cars and buses. Even when it is used for charging purposes, the antennas are required to be very large so as not to go against safety standards and regulations

[90],[45]. Due to this inherent problem coupled with the high cost of antenna design and development, the technology is not appropriate for the wireless charging of EVs. Thus, this literature review will not cover development in this area of technology.

2.10 The Near Field WPT Technology

This technology is a non-radiative type and capable of transferring energy over a shorter distance in contrast to the far-field WPT technology but not up to a wavelength[45]. This technology is basically divided into Inductive Power Transfer (IPT) and magnetic resonance coupling (MRC) technology.

2.10.1 The Inductive Power Transfer (IPT) Technologies

The traditional IPT method of wireless power transfer employs the basic principle of magnetic field induction. This involves the supply of electric current at a particular frequency into the primary coil which induces a current in the secondary coil through electromagnetic induction. This method is based on near-field transmission method as there are nearly no interference and power loss due to its short distance of transmission. The inductive coupling design is based on the fundamental theories of Biot-Savart's Law and Faraday's Law of Electromagnetic Induction[16].

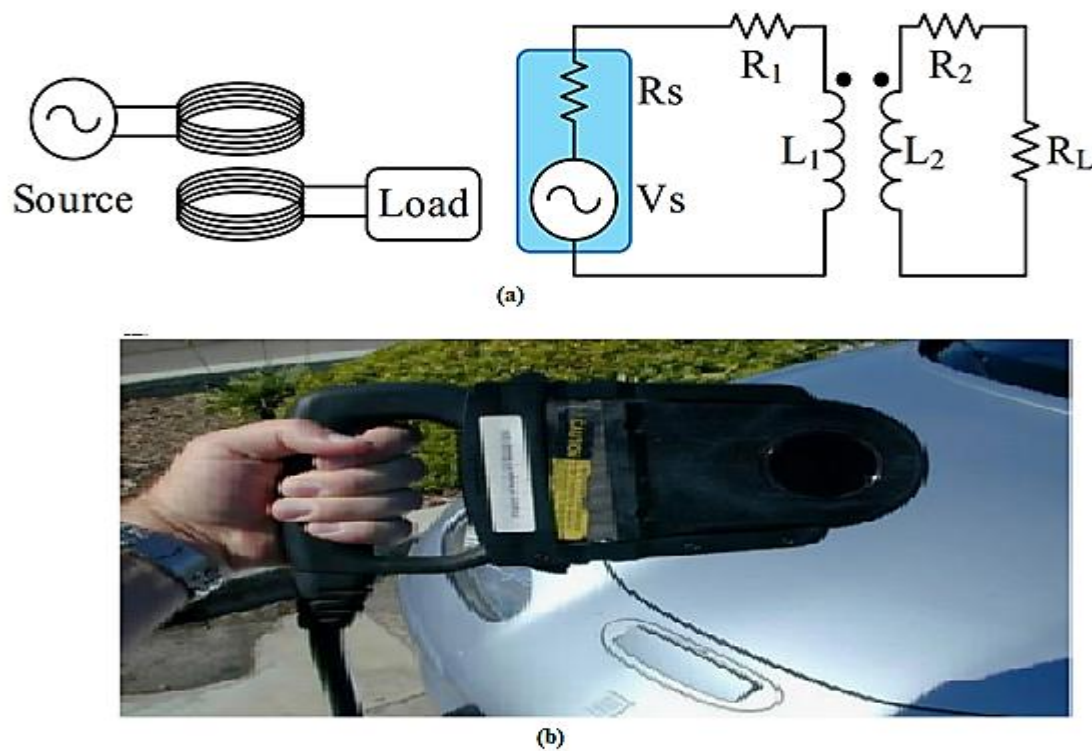


Figure 2.8: (a) Setup and Equivalent Circuit Model Diagram of Traditional IPT Technology[45]. (b) Charging pad of a Typical IPT Technology[96].

The typical setup for IPT technology consists of two coils of wire with their respective resistances and inductances. This is shown in Figure 2.8[45][96].

The inductive coupling based WPT is simple in design and it offers high safety. These advantages contributed greatly to its popularity and applicability, but it has three major setbacks. The technology works best in applications requiring only short transmission distances. It has been observed that the power transfer efficiency is inversely proportional to the cube of the air gap[45]. As a result, high PTE of over 90% is limited to a range of few millimetres; typically less than 20 mm. There is also a significant degradation in the PTE when the transmission and receiver coils are not properly aligned. This is because of the small size of the charger as shown in Figure 2.8(b). A significant increase in displacement between the coils will result in only a small percentage of flux linkage between the transmitter and the receiver. Lastly, due to the small distance of transmission and small power requirement, the technology works best for low power applications as used in the charging of laptops, toothbrush, mobile phones and medical implants[97].

2.11 Magnetic Resonant Coupling WPT Technologies

The basic principle of the magnetic resonance coupling WPT technology employs the principle similar to the operation of the iron core transformer. But unlike the iron core transformer, the primary and secondary windings are separated over an airgap and not linked through a common magnetic core[43][72]. As a result, there is a presence of leakage inductance resulting in the poor magnetic coupling between the primary and secondary coils. The WPT technology typically consists of a utility power supply, transmitter and receiver resonant circuits, high-frequency converters and an electrical load[98][16]. For most practical deployment, the transmitter coil is fixed underneath the ground while the receiver coil is installed underneath the chassis of the electric vehicle.

When the electric vehicle moves over the charging pad in the case of dynamic charging or parked over the charging pad for static charging, an AC voltage at high frequency is applied to the charging pad; which in most cases are buried under the ground. The resulting current flow creates a time-varying magnetic field around the transmitter and by the application of Faraday's law and Ampere's law, a voltage is induced at the terminals of the receiver coil[99]. The receiver coils are linked to the electrical load of the electric vehicle which is the battery and a significant amount of power is transferred[43].

The magnetic resonance coupling WPT technology is divided into two types: the air-core magnetic resonant coupling WPT technology and ferrite core magnetic resonant coupling WPT technology[72]. The major difference between the two types of magnetic resonant coupling WPT technologies is the absence/presence of a ferrite core in the WPT system. The air-core magnetic resonant coupling WPT system consist of only coils of copper wire operated at very high frequencies typically in the megahertz range while the ferrite-core magnetic core resonant coupling WPT system consists of a magnetic ferrite core which is used to boost the magnetic coupling and self-inductance of the resonant coils[16], [72], [95], [100], [101]. The designs and operations of the two types of magnetic resonance WPT are discussed in the next two sections.

2.11.1 Air-Core Magnetic Resonant Coupling WPT Technologies

The air-core MRC wireless power transfer technology consists mainly of two subsystems which offer a better wireless PTE compared to the IPT technology with the same natural resonant frequency for the receiver and transmitter[102]. The technology is illustrated using a typical RLC circuit consisting of a resistor, inductor and a capacitor. The basic manner of operation involves the coupling of the transmitter and receiver coils magnetically when the source electrically excites the transmitter coil[16]. The PTE is determined by two parameters- the mutual coupling strength, M , and the Q-factor of the resonators[16], [103]. The Quality factor (Q-factor) of an inductor indicates the ratio of the reactive reactance of the coil to its resistance. The formula for the mutual inductance of the two coils (L_m) is given by[102]:

$$L_m = k\sqrt{L_p * L_s} \quad 2.3$$

Where k is the coupling coefficient of the coil and L_p, L_s are inductance of the transmitter and receiver coils respectively. The value of k is determined by the transmission distance between the receiver and transmitter coils. For a typical circular coil, k is given by[102]

$$k = \frac{1}{[1 + 2^{\frac{2}{3}}(\frac{D}{\sqrt{r_t * r_r}})^2]^{\frac{3}{2}}} \quad 2.4$$

D is the length of the air gap, while r_t, r_r are the radius of the transmitter and receiver coils respectively. Subsequently, the Q factor is directly proportional to the angular resonant frequency (ω_o) and inductance (L) of the coils and inversely proportional to the intrinsic resistance (R) of the coil [102]. The relationship is further illustrated using the formula:

$$Q = \frac{\omega_o L}{R} \quad 2.5$$

It is noted from equation (2.5) that an increase in the angular resonant frequency (Hz) and increase in inductance (H) at constant resistance (Ω) of the coil increases the value of Q, which will reduce the power losses in transmitting energy across the gap. For most practical applications, an increase in Q is achieved by decreasing the value of R.

The PTE efficiency of the air-cored MRC is also dependent on the strength of the magnetic coupling[104], [105], which also directly affects the range of power transfer of the system typically between 10cm to 50cm. The level of magnetic coupling is divided into three types: air-core low MRC, air-core medium MRC and air-core strong MRC models.

2.11.2 The Air Core Low MRC model

This model consists of two pairs of RLC resonators consisting of a source coil as the transmitter coil mounted underneath the road and the load coil at the receiver coil mounted beneath the vehicle. The circuit setup is illustrated in Figure 2.9[45].

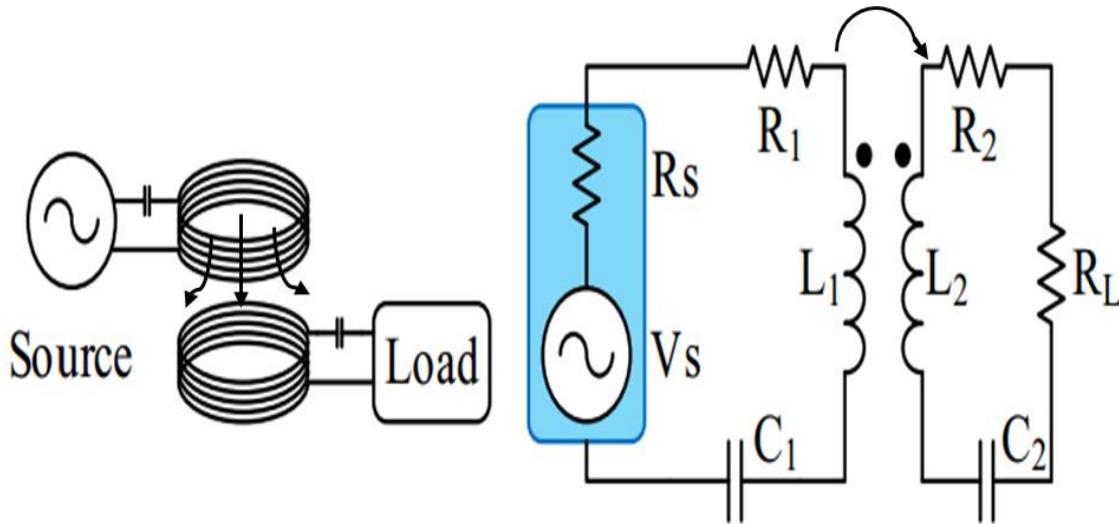


Figure 2.9: Model Diagram and Equivalent Circuit Diagram of Low MRC[45].

The transmitter coil is connected to the source supply, which transmits the electromagnetic field (indicated by 3 arrows pointing downward) to the receiver coil that is connected to the load.

The presence of capacitors C_1 and C_2 is to compensate for the large leakage inductance present in L_1 and L_2 in the model. The MRC based WPT models are loosely coupled WPT systems because only a small percentage of the magnetic flux emanating from the transmitter essentially couples with the receiver. The loss in flux-linkages is due to the presence of the air gap and the divergent nature of the magnetic fluxes.

According to A.K. Sah [106], the model was able to offer an efficiency of 13.46% when using a k value of 0.5 with a resonant frequency of 13.56MHz. In the later work of J. Zhang et al [107], it was noted that the low MRC model tends to exhibit a very low stiffness in efficiency when the resonant frequency is constant and other parameters like coupling factor, Q and airgap are varied. The emission of strayed electromagnetic field (EMF) was observed to be high whenever there is a significant distance variation because of misalignment between the receiver and the transmitter coils. But a significant improvement was attained in the works of SangCheol M. [108], where a low MRC model prototype was built with Silicon carbide (SiC) MOSFETs used as the components for the full-bridge inverter. The design was able to achieve a maximum efficiency of 90.45% at a load of 3.3kW. Consequently, an efficiency of 89.93% was attained at a maximum load of 6.6kW. These efficiencies were attained using a 3-phase 400V power supply at an inverter frequency of 100 kHz. Despite the high PTE, there is room for improvement.

2.11.3 The Air Core Medium MRC model

This model consists of three pairs of RLC resonators. The resonators can be arranged comprising of two coils (source coil and an intermediate or relay coil) at the transmitter side mounted underneath the road and a single load coil at the receiver side mounted beneath the vehicle or vice versa. The typical circuit set up with the source coil and the relay coil together is illustrated in Figure 2.10[45].

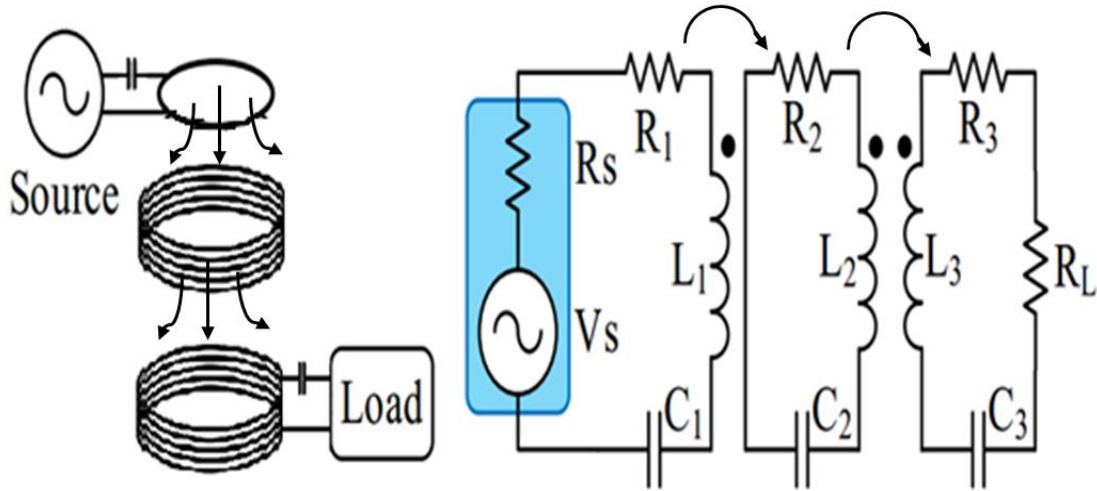


Figure 2.10: Model Diagram and Equivalent Circuit Diagram of Medium MRC[45]

The air-core medium MRC model operations begin with the propagation of the electromagnetic fields from the source coils connected to source supply. The intermediate coil receives the electromagnetic field emanating from the source coil. The purpose of the intermediate coil is to ensure that the input coil is properly loaded for adequate impedance matching as well as ensure that the electromagnetic field is transmitted in a focused manner to the receiver coil that is linked to the load. The source coil and intermediate coil forms an impedance matching network whose major benefit is to ensure efficient switching-amplifier operation while ensuring effective coupling of the source coils with the load coil[109]. The model topology implements magnetic coupling in two stages as shown in Figure 2.10. The first coupling and impedance matching occur between the source coil and the intermediate coil, while the second coupling is responsible for power transfer between the transmitter and receiver occurs between the intermediate coil and receiver coil.

In the work of A.K. Sah [106], his medium MRC model was able to attain an efficiency of 55.20% when using a k value of 0.5 with a resonant frequency of 13.56MHz. This is an additional increase of over 31% when compared with his low MRC model. Subsequently, in the work of J. Zhang et al [107], it was observed that the model tends to exhibit a very high-efficiency stiffness when the resonant frequency is constant and other parameters varied just as the case with the low MRC model.

In contrast to the low MRC model, the electromagnetic field (EMF) emission was observed to be low whenever there is a significant distance variation because of misalignment between the receiver and the transmitter coil, despite the fact that the model offers better performance in terms of PTE when

compared with the low MRC model. However, SangCheol, M. [104] proposed a model with a significant improvement in the PTE by using Silicon (Si) and SiC MOSFETs as the switching devices for the full-bridge inverter installed at the transmitter side. Using a 3-phase 400V supply and at a distance of 20cm, the SiC MOSFET and Si MOSFET powered inverter models were able to achieve prototype efficiencies of 95.04% and 95.57% respectively at a maximum load of 6.6kW using the same switching frequency of 100kHz. However, it comes at a trade-off of operating WPT systems at three different resonant frequencies. This is because as the k increases, a phenomenon known as pole splitting occurs creating three Zero Phase Angle (ZPA) frequencies at the input impedance due to load variations. Thus, operating the model involves complicated design estimations.

In summary, a coupling coefficient of 0.408 at a distance of 8cm was achieved which is an increase of over 250% compared to 0.191 coupling coefficient achieved in the low MRC model prototype. The PTE achieved using this model makes it a suitable option for use in commercial vehicle charging applications, but it comes at a higher cost due to the added intermediate coil. Higher power transfer efficiency can be attained at a higher switching frequency but this is limited due to the coupling strength.

2.11.4 The Air Core Strong MRC model

The strong MRC model consists of four pairs of RLC resonators consisting of two coils (source coil and source resonant coil) at the transmitter side which is normally mounted underneath the road and another two coils (load resonant coil and load coil) at the receiver side which is mounted beneath the vehicle. The circuit setup is illustrated in Figure 2.11[45].

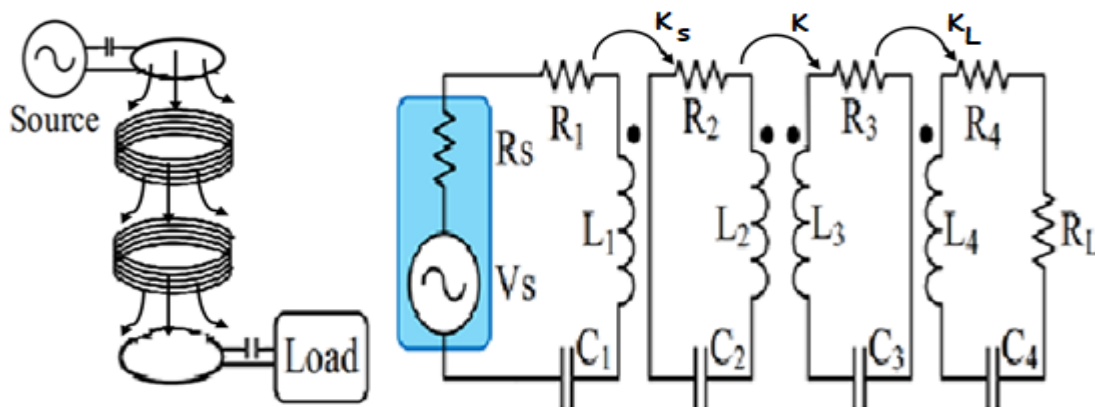


Figure 2.11: Model Diagram and Equivalent Circuit Diagram of Strong MRC[45]

The air-core strong MRC model operations start with the propagation of the electromagnetic fields from the source coils connected to source supply. The source resonant coil receives the field emanating from the source coil. The purpose of the coupling is to ensure optimum tuning of the input coupling as well as to ensure impedance matching of the input coils by adjusting the alignment between the source coil and resonant coils indicated by k_s ; the optimum k_s that gives the desirable input impedance for a given source resonant coil loading is then achieved[109]. Similarly, impedance matching is achieved

at the receiver side by adjusting the value of K_L until an optimum tuning of the output coupling is achieved. Effective wireless power transfer between the transmitter and the receiver occurs between the source and load resonant coils indicated by k . The model topology implements magnetic coupling in three stages as shown in Figure 2.11. The first coupling between the source coil and the source resonant coil is to ensure impedance matching at the input. Subsequently, the second magnetic coupling occurs between the source resonant coil and load resonant coil is to ensure effective wireless power transfer from the transmitter to the receiver, and the third coupling occurs between the load resonant coil and the load coil is to ensure impedance matching at the output.

Due to the absence of source resistance R_S and load R_L in the two resonant coils, the quality factor Q is increased. The implication is that more energy can be transferred to the load with a constant coupling coefficient [45]. The PTE was further enhanced by the elimination of the lumped resonant capacitors, which is replaced with the coils parasitic capacitance C_2 , and C_3 . The parasitic capacitances help in further reducing the power loss because of the presence of resonant coils internal resistance. With the reduction in the internal resistance, the Q -factor increases, which invariably increases the PTE even for low coupling coefficients [45].

A proposed design using the strong MRC model was implemented by Sah A. K. [106]. The model offered an efficiency of 78% when using a k value of 0.5 with a resonant frequency of 13.56MHz. This is an additional increase of over 22% compared with his medium MRC model. Subsequently, in the work of H.C. Son [111], the PTE was calculated based on the formula proposed by Kurs, A. et al [112]. It was discovered that the PTE of the model in the case of the circular coil could be mathematically calculated based on the radius of the resonant coils, the air gap, and radius of the wire at a certain resonant frequency. An optimal radius of both the transmitter and receiver coils was determined and simulations were undertaken for various values of the wire radius at a resonant frequency of 13.56MHz.

At a loop radius of 1m and wire radius of 2mm, a PTE of 88% was attained at a distance of 1.5m. This is a significant improvement. The strong MRC model, according to Moon, S. [104], has a prospect of the higher efficiency of 98% which is higher than the 95.57% efficiency achieved with the Medium MRC model at a higher switching frequency. Also, a trend has been established that there is an increase in power transfer efficiency as the number of intermediate coils increases.

For a unidirectional wireless power system (power transfer from the grid to the vehicle), The major components are PFC (Power Factor Correction) converter, a radio frequency (RF) amplifier, the resonators (coils) where the wireless power transfer occurs and an on-board rectifier. This is illustrated in Figure 2.12 [45].

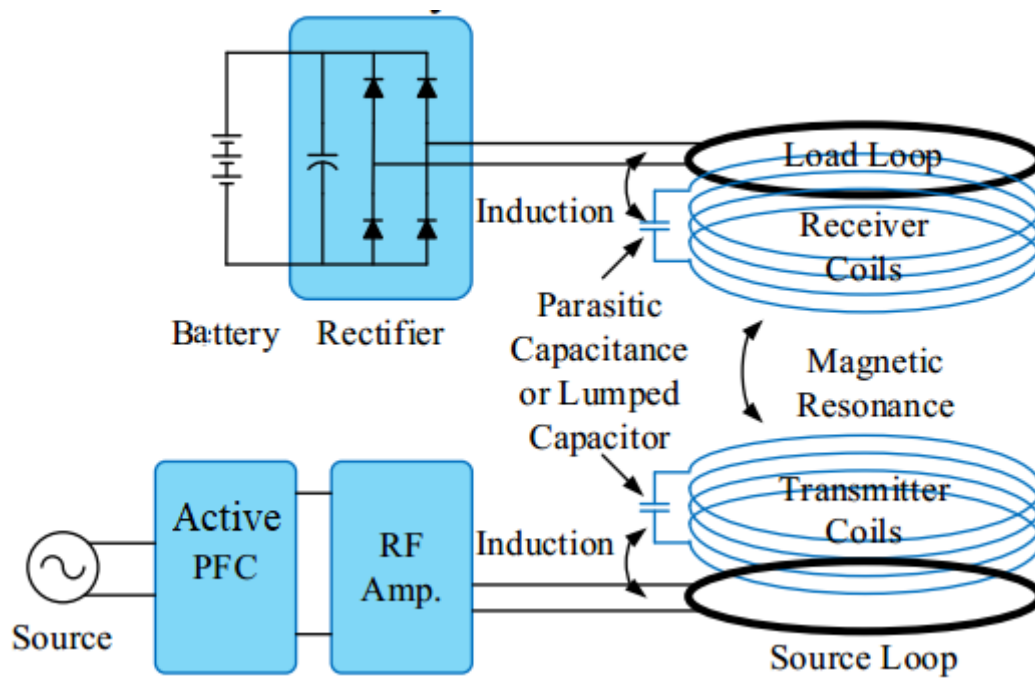


Figure 2.12: Overview of Charging Structure of MRC system for EV Application (Source: Qiu et al [45])

The efficiency of each of these individual stages all contributes to the overall efficiency of the charging systems. For example, an overall 90% efficient systems will require at least 96% coil-to-coil efficiency, the RF amplifier and PFC converter must have not less than 97% efficiency while the rectifier efficiency must be around 99%[45]. In the design of WPT systems, the maximum coil-to-coil PTE is basically affected by four factors namely; the coil design, alignment tolerance, circuit design and environmental factors[16].

From the diagram, the source coil takes electrical power from the power supply, which is then transferred to the primary coil inductively as the source coil, and the primary coil is at close proximity to each other. The power is then transmitted from the primary coil to the secondary coil by strong magnetic resonance coupling at very high resonant frequency.

The four coil WPT system can be modelled in two ways- the transformer model and the coupling inductor model. The transformer model consists of the source and load coils, and the resonators. The source coil takes in the source voltage V_{in} while the load coil gives the output voltage V_{out} . This is illustrated in Figure 2.13 and Figure 2.14.

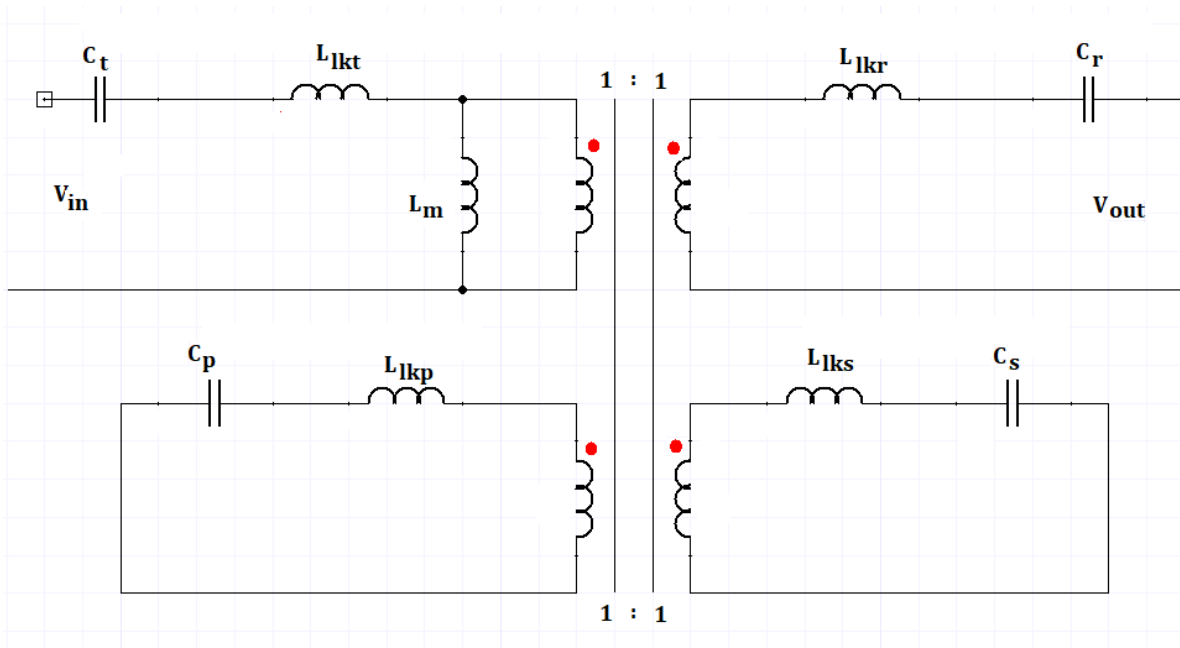


Figure 2.13: The Transformer Model for the Strong MRC WPT System

L_{lkt} and L_{lkr} represent the leakage inductances of the source and load coils respectively while C_t and C_r represent the coupling capacitor to compensate for the leakage inductances of the source and load coils respectively. The L_{lkp} and L_{lks} represent the leakage inductances of the primary and secondary coils respectively while C_p and C_s represent the coupling capacitor to compensate for the leakage inductances of the primary and secondary coils respectively. Since the primary and secondary coils are not connected to an external load resistance, there is a strong coupling between the coil and low losses recorded in the coils.

The inductor coupling model, on the other hand, takes into account the mutual coupling of the four coils. This is illustrated in Figure 2.14.

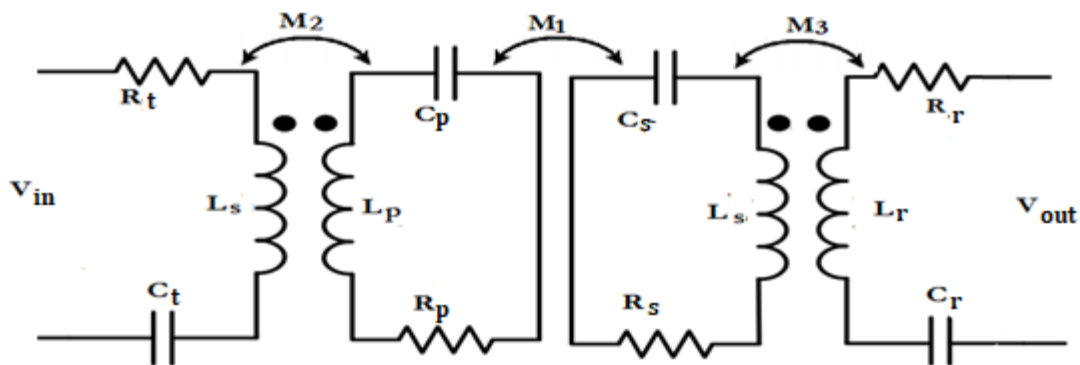


Figure 2.14: Coupling Inductor Model for the Strong MRC Wireless Power Transfer System

The models also take into account the total resistance of each coil. The guiding equation for the resistance, capacitance, and self-inductance for a case study of circular resonant coils was developed and presented by Son, H. C. et al [111]. The L_p and L_s represent the leakage inductances of the primary

and secondary coils respectively while C_p and C_s represent the coupling capacitor to compensate for the leakage inductances of the primary and secondary coils respectively. Maximum magnetic coupling is attained between the primary and secondary coils when the reactance of the compensating capacitors matches the reactance of the leakage inductances and only the intrinsic resistances are present in the coils.

Though there is a high value of PTE with regard to the strong MRC model, it is not widely adopted in the design of WPT systems for the charging of EVs due to the high number of coils needed for efficient operations. The additional two resonant coils in the WPT system increase the cost of infrastructure and maintenance of the system operations.

2.11.5 Ferrite Core Magnetic Resonant Coupling WPT Technologies

There have been series of research carried out on WPT systems with a core (ferrite) in order to achieve optimum, efficient and high power transfer[43]; as a result, many WPT model designs have been proposed[99]. In the course of comparing the ferrite-cored models with the air-cored models, ferrite cored-models were preferred. This is due to the advantage of lower cost and higher coupling factor when compared with the air-cored models. For example, Zhang. Y. et al [113] attained a coupling coefficient of 0.25 at a distance of 80mm, V. Prasanth and P. Bauer [114] on the other hand attained a coupling coefficient of 0.35 at a charging distance of 70mm while Sibue J. R. et al [115] achieved a coupling coefficient of 0.72 at a distance of 6mm. This is in sharp contrast with the air-core WPT model of Shinoraha N [116], which attained a coupling coefficient of 0.16 at a distance of 200mm and the model of Lee S.H. and Lorenz R.D [85], whose air-core WPT model attained a coupling coefficient of 0.05 at a charging distance of 300mm. These research outputs indicate that the ferrite-cored MRC models offer a higher coupling coefficient than those obtainable for most air-cored MRC models.

Consequently, in order to optimize the charging pads of these WPT models, there have been a series of research studies with subsequent publications of the research findings over time; the proposed models employed the use of different shapes of ferrite cores among which are the E cores, U Cores and pot cores but were considered incompatible for charging applications with respect to electric vehicles due to their large thickness[43]. Other alternatives adopted are the circular cores[11], [43], [117], rectangular cores [11], double-sided windings [11], [118], [119] and a polarized coupler known as Double D quadrature (DDQ)[120][11].

With respect to affordability, the ferrite-cored WPT system significant cost is as a result of the ferrite material used which depends on the grade and performance characteristics. Depending on the number of coil turns and the number of resonators, the air-core MRC model can be less or more costly than the ferrite-cored counterparts. The addition of one or two resonators as the case of the medium and strong MRC model respectively can increase the overall cost of the WPT system when compared with ferrite-cored WPT systems of similar size and coil turns.

Due to the numerous advantages the ferrite-cored MRC models have over their air-cored counterparts, further research studies of characteristics performances of viable designs of some ferrite-cored MRC models was discussed in chapter 3.

2.12 Review of Static and Dynamic Charging of EVs

The static and dynamic charging of electric vehicles is one of the essential features of wireless power transfer operations applicable to electric vehicles. The static method of charging an electric vehicle is applicable to both the plug-in and wireless modes of charging an electric vehicle. The charging process is implemented when the electric vehicle is in a stationary mode[62], [70], [73]. The available areas where the static type of wireless charging are normally possible are parking decks, bus stops, and road sections before traffic lights[62], [73]. On the other hand, the dynamic charging is the power exchange between the grid and the electric vehicle while the vehicle is in motion[62], [121].

2.12.1 Static Wireless Charging of Electric Vehicles

In the static mode of wireless charging of electric vehicles, all that is required by the driver is to park the car over a transmitter coil and the charging operation starts automatically[121]. For most WPT models for static charging operations, the primary and secondary coils are designed in a pad form[99], [121], [122]. The early design of WPT coils was made in the form of a simple transformer with a split core. The limitation of these earlier types of WPT system is the very small airgap[121].

In order to meet the large airgap required for wireless charging of electric vehicles, the split core transformer was modified into the magnetic coil types. Numerous research has been undertaken and were presented in the earlier sections. A typical illustration of the static model of charging an electric vehicle was presented by Vilathgamuwa and Sampath [40] and reproduced in Figure 2.15.

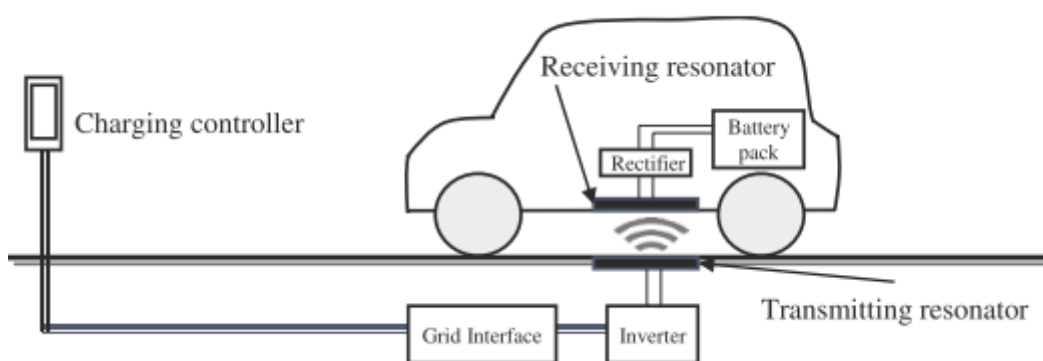


Figure 2.15: Typical Illustration of Static Mode of Wireless Charging of an EV[40]

For static wireless charging of electric vehicles, the cost of infrastructure and operations is relatively cheap when compared with the one obtainable with the dynamic charging[40]. Many projects have been undertaken in the area of static charging of electric vehicles. Few of such projects are presented in Table 2.3 [40][45].

Table 2.3: List of Some Selected Static Wireless Charging Projects for Electric Vehicles

| Institute/ Corporation | Installation Year | Location | Airgap (mm) | Power Ratings | Efficiency |
|-------------------------------------|-------------------|----------|-------------|---------------|------------|
| Auckland University & Qualcomm Halo | 2010 | Auckland | 180 | 3 kW | 85 % |
| ORNL | 2012 | U.S | 200 | 7.7 kW | 93 % |
| MIT Witricity & Delphi | 2010 | U.S | 180 | 3.3 kW | 90 % |
| Evatran | 2010 | U.S | 100 | 3.3 kW | 90% |
| University of Michigan | 2014 | U.S | 200 | 8 kW | 95.7% |

One key feature of the static mode of wirelessly charging an electric vehicle is the low power ratings required; typically less than 10 kW. The low power ratings in such system is because of the limit in the number of electric vehicles involved in the charging operations (typically one).

The overall aim of the static mode of wireless power transfer technology for electric vehicles is the reduction in the complexity of the charging infrastructure[40]. This is achieved by the creation of simple components for efficient and effective charging operations. But there are still outstanding issues like slow charging times and smaller driving range[40].

2.12.2 Dynamic Wireless Charging of Electric Vehicles

In the dynamic mode of wireless power transfer technology for electric vehicles, the transfer of power to the electric vehicle occurs while in motion. Thus, the wireless power transfer system infrastructure of the primary side is installed on the roadway[36]. The basic components of the dynamic wireless power transfer system are the long primary coils installed under the road and the short primary coils installed under the chassis of the electric vehicle. A typical illustration of the static mode of charging an electric vehicle was presented by Theodora-Elli Stamati and Pavol Bauer[36] and reproduced in Figure 2.16.

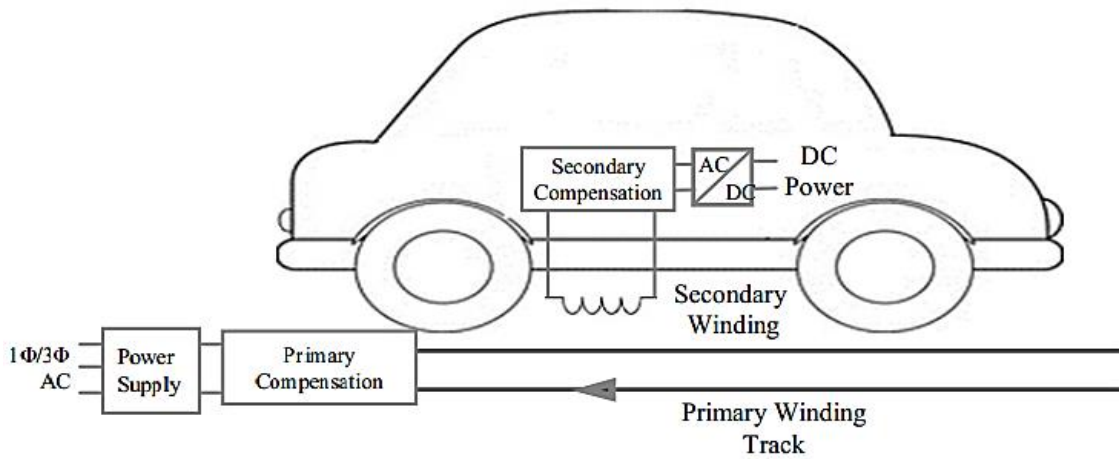


Figure 2.16: Typical Illustration of Dynamic Mode of Wireless Charging of an EV[36]

The application of the dynamic mode of wireless power transfer technology theoretically reduces the problem surrounding the limited range of travel for electric vehicles by extending the driving range in an unlimited manner[40]. The major determining factor limiting the number of electric vehicles the system can accommodate is the power ratings of the system[40]. Other factors are the duration and speed of the electric vehicles within the section of the road equipped with the dynamic wireless power technology[40].

The primary winding track can be designed in two ways: segmented transmitter coil array and single transmitter coil track [40]. The single transmitter coil track consists of a long length of transmitter coils that are connected to a power supply[40] and graphic illustration of such a system is shown in Figure 2.16. The segmented transmitter coil array, on the other hand, consists of a number of short-length transmitter coils each connected to an individual power supply. A typical illustration of the segmented transmitter coil array-type of charging an electric vehicle was presented by Vilathgamuwa and Sampath [40] and reproduced in Figure 2.17.

The long single transmitter coil track offers an advantage of an easier control mechanism as only a single power source is required to power the whole length of the transmitter coil. Another advantage of the long single transmitter coil is the constant value of magnetic coupling along the whole length of the coil[40] as the electric vehicle moves along the transmitter track. But the long single transmitter coil track comes with some limitations and drawbacks. Due to the high power requirement for the single track dynamic wireless charging technology, the emitted electromagnetic field, especially in the uncoupled section of the system, needs to be suppressed in order to limit or eliminate any harmful exposure to humans or animals[40]. The compensation of the leakage inductance along the long length of the transmitter coil will require the installation of quite a high number of compensation capacitors, thus, increasing the cost of in construction and maintenance[40].

Lastly, due to the long length of the transmitter coils which can range from few metres to tens of metre long, the coupling coefficient is usually low which lowers the efficiency of the system[40].

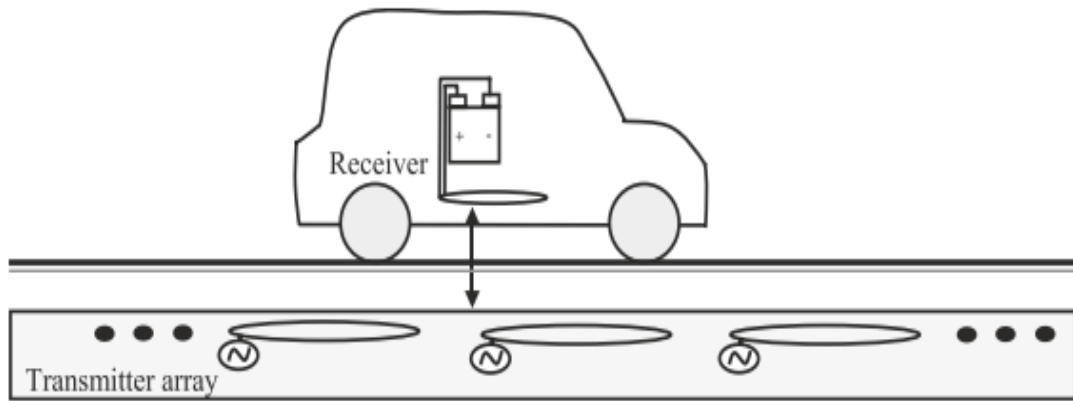


Figure 2.17: Typical Illustration of Segmented Coil Array for Dynamic Wireless Charging of Electric Vehicle[40].

On the other hand, some of the limitations and drawbacks common with the long length transmitter topology for dynamic charging operations are eliminated using the segmented coil array system. For example, the field exposure problem in the long length transmitter topology is eliminated in the segment coil arrays system. Also, the requirement for a high number of compensation capacitors is eliminated while increasing the level of magnetic coupling between the transmitter and receiver coil[40].

But the segment coil array system has some inherent design limitations. For example, there is a need for a tracking mechanism that monitors the movement of the receiver coils installed under the chassis of the electric vehicle in order to switch on the appropriate power source at the transmitter side for the load[40]. Similarly, there is a need to optimize the level of separation between adjacent transmitter coils. For example, there is a sharp reduction in efficiency when the receiver coils move away from the transmitter and the transmitter coils are too far apart from each other. Also, due to the generation of negative mutual inductance between adjacent transmitter coils for neighbouring transmitter coils; keeping adjacent transmitter coils close to each other creates negative current stress on the transmitter coil[40].

There has been an issue with the design cost of the segmented coil arrays system. This is because of the cost of installing numerous transmitters along with a given length of primary coil track. Another design issue is the powering of multiple coils with many source converters[40]. Solution proffered for this type of problem is either to connect a single power converter to numerous transmitter coils or a single converter is connected to a single transmitter coil. Whatever be the choice of design implementation, there is high complexity in the power flow control.

Despite the challenges and limitations with the dynamic type of wirelessly charging an electric vehicle, many projects have been undertaken in the area of dynamic charging of electric vehicles through WPT technology. Few of such projects are presented in Table 2.4[40][45]

Table 2.4: List of Some Selected Dynamic Wireless Charging Projects for Electric Vehicles

| Institute/ Corporation | Installation Year | Location | Airgap (mm) | Power Ratings | Efficiency |
|-------------------------------|-------------------|-------------|-------------|---------------|------------|
| KAIST | 2012 | S. Korea | 200 | 100 kW | 75% |
| ORNL | 2010 | U.S | 200 | 4.2 kW | 92 % |
| KAIST | 2010 | S. Korea | 130 | 130 kW | 74% |
| The Delft University of Tech. | 2013 | New Zealand | - | 90 kW | 80% |
| KAIST | 2009 | S. Korea | 170 | 17 kW | 71% |

One key feature of the dynamic WPT systems is the high power requirement of the system. Since the system is designed for high power applications, the efficiency of the system is mostly not an issue. The minimum efficiency recorded based on Table 2.4 is 71% while the maximum efficiency recorded was 92%. Increasing the power output of the system leads to higher losses and more expensive power converters. As a result, there is a trade-off between cost and power ratings in the practical design of dynamic WPT systems.

In summary, the overall aim of the dynamic mode of wireless power transfer technology for electric vehicles is the increase in the travel range[40] by powering as many electric vehicles on the road as much as possible. Because the batteries of electric vehicles can be charged continuously, the need for a large battery for EV is eliminated which causes a significant reduction in the price of the electric vehicles[40].

2.13 Investigation into Bidirectional Wireless Power Transfer Topology for Electric Vehicle

Several research works have been undertaken for the design and development of unidirectional wireless power transfer charging of electric vehicles. The unidirectional approach involves a one-way flow of electrical energy from the electrical source to the battery bank of the electric vehicle via a contactless transmitter and receiver coils. As highlighted earlier in the literature review, the unidirectional approach has been implemented in the traditional IPT and magnetic resonance coupling WPT schemes.

With technological advances and gradual evolution of the electrical power grid into smart grids; there has been gradual addition of dynamically interconnected microgrids comprising of distributed renewable energy sources and storage units. As the distributed energy generation sources gain deeper

integration with the electric grid, the sustainability of the emerging technology can be enhanced using EVs. Since the interconnection of the EVs, storage devices and the renewable energy source is achieved at the low voltage distribution level [20], the battery bank of the EVs can act as an energy storage unit with the help of a microgrid controller which controls the energy flow.

In order to achieve an efficient grid integration of EVs, there was need to design and develop a high efficient bidirectional wireless power transfer systems with additional capabilities of low harmonic distortions of electric currents injected into the grid, flexible system control and high power factor[20]. The bidirectional wireless power is becoming the trend of many power system infrastructure because of the increasing amount of electric grid integration with distributed energy generation sources.

The integration of the electric grid with distributed energy generation sources comes with its own inherent problems due to the unpredictable nature of power generations. For example, It was reported in Germany on the 8th day of May 2018 that excess renewable energy generation outgrown demand to an extent that energy companies were offering consumers financial rewards for increasing consumption of electrical energy to prevent a total collapse of the electric grid[123]. In such a situation, connecting a high number of electric vehicles to the grid will absorb the excess electrical power generated in the grid and the electric vehicle owners could act as a mobile energy generation sources during the period of low power generation for their private residences or sell the electrical energy to the electricity companies at a profit.

Many research has been undertaken in order to create an optimal model for bidirectional transfer of electrical power. For example, G. Lempidis [11] proposed topology for a multi-functional charging system making use of wired and wireless charging technology. A bidirectional resonant inductive charging system was designed, simulated and validated experimentally. The system consists of two parts: the resonant converter and the coil system. A combination of double D coils and solenoid coils were employed in the coil system while a bi-directional full bridge resonant LLC converter was built. The system was controlled such that it was operated as half-bridge converter at partial load and a full-bridge converter at full load in order for the system to operate between 93% to 95% efficiency for a maximum power output of 4.2kW.

Similarly, a bidirectional inductive wireless power transfer system was designed and built using a multiphase resonant converter by Bojarski M. et al [17]. In the proposed system, a DC/DC converter was used as the link between the inverter and the resonant coil. In order to achieve a high-efficient system, a hybrid phase-frequency control method was adopted. The phase-shift control aspect is to ensure the power output is regulated and kept constant. The frequency control aspect ensures that the WPT system operates at a frequency close to the resonant frequency throughout the duration of the operation. From the presented experimental result, the hybrid phase-frequency control methodology was chosen to be a better alternative than the use of the frequency-controlled converter as the range of operating frequency was significantly reduced. Also, the output power was well regulated from the

minimum to the maximum design value while increasing the frequency of the converter. The added control scheme causes an increase in the overall efficiency of the WPT system.

For effective grid-to-vehicle(G2V) and vehicle-to-grid(V2G) integration of wireless power transfer technology, a bidirectional inductive WPT topology was proposed by S. Samanta and S. Member [124] using a half-bridge current fed converter. From the presented experimental results, it was noted that during the grid-to-vehicle (G2V) operation, an almost pure sinusoidal current and voltage was delivered to both the transmission and receive coils. Subsequently, the power factor at the transmitter side was seen to be slightly lagging which provides for the zero voltage, turn-off switching of the converter switches. In the vehicle-to-grid (V2G) operations, an almost harmonic-free current and voltages were injected into the grid even as switch voltage stress on the converter switches was significantly reduced. The proposed topology was quite effective as the G2V and V2G of the system operation was kept constant despite changes in the load. Nevertheless, despite the advantages the proposed system offers; it was only suitable for medium power applications. This was deduced from the presented experimental results.

Further research work has been undertaken in the design and development of a bidirectional WPT charger for electric vehicles using self-resonant pulse width modulation (PWM) by J. Y. Lee and B. M. Han [125]. Since bidirectional wireless chargers work in two modes only; discharging and charging modes, a controller was designed and implemented at the primary and secondary coils to controls these modes. The proposed system design was simple as there was no need for the addition of a current chopper and power was transferred efficiently at a constant frequency pulse width modulation.

From the results generated from the experimental analysis, the maximum charging current of 50A was attained under the bidirectional operation with ease of operation even at an air-gap of 12cm to 20cm. The proposed design was able to maintain the same waveform for the current at the transmitter side irrespective of the load condition and the resonant frequency; even when there were fluctuations in the airgap. The proposed topology was able to operate optimally even with the presence of coil misalignment as it is evident in the high power transfer efficiency obtained through measurements; which were in the range of 88.1% to 95.3% under full load conditions.

But despite the improvements achieved with this topology, the power transfer efficiency was quite low (less than 70%) at partial load and the model works efficiently only in applications requiring constant switching frequency.

2.14 Research Gaps in the Development of Bidirectional WPT for EV

Application

Despite the progress made in the design and development of efficient bidirectional wireless power transfer systems for EV applications, there is room for further investigation, development and optimisation. The aspects requiring further investigation are divided into three main aspects; power

electronic control, electrical circuit design and the electromagnetic aspect. This is further illustrated in Figure 2.18

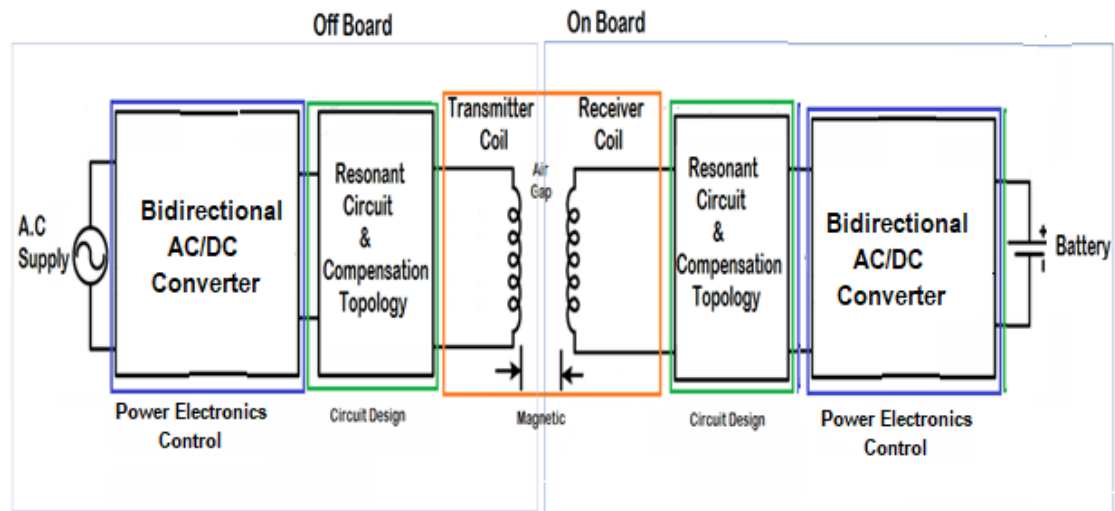


Figure 2.18: Typical Subsystems for Bidirectional WPT System[20].

The power electronics control deals with the control of the switches responsible for the efficient operations of the converters (rectifiers and inverters). The circuit design aspect is where the necessary compensation and resonant circuitry optimizations are implemented. This ensures the correct utilization of resonant frequency and reactive power compensation. The magnetic aspect deals with the coil designs for efficient and optimal wireless power transfer.

2.14.1 Power Electronic Controls for Electric Vehicle Bidirectional WPT

Applications

The control of the semiconductor switches for the efficient operation of the low-frequency and high-frequency converter operations. For each of the design topologies reviewed in the literature, a corresponding control method was adopted for efficient operation. For example, in the design of the self-resonant PWM wireless charger [125]. A primary and secondary controller was added to the system to coordinate the charging and discharging operations of the system respectively. The primary switches are normally located at the transmitter unit and responsible for the charging control implemented by the primary controller whereas the charging current is located at the receiver unit; thus, the input charging current is calculated using the battery voltage and the control was optimized with the delay in the wireless communication from the secondary side taken into account. As a result, the PWM control can easily control the battery charging current.

In discharging mode operation, the battery voltage and current are not constant over the whole SoC of the battery due to the nature and chemical properties of the battery. In order to ensure a stable bidirectional mode of operations, the resonant capacitor needs to be selected through superimposition in the design calculation. The design must take into consideration the battery current, mutual

inductance of the coils and the input voltage. Subsequently, there are many assumptions in the proposed design which can significantly affect the overall system efficiency. For example, the PWM frequency is assumed to be the same as that of the self-resonant frequency; but in actual practice, they are not the same as the self-resonant frequency is chosen based on the calculated values of the resonant capacitance and inductance of the coils while the switching frequency is dependent on the duty ratio. In addition, the presence of harmonics was not adequately identified and reduced in the proposed design.

For multiphase resonant inverter control for a bidirectional WPT system, the conventional approach is to control the operating frequency to operate very close to the resonant frequency. This was to ensure proper current and voltage regulation or phase shift control to ensure the output power is constant. But Bojarski M. et al [17] was able to combine the two conventional control method to achieve a phase-frequency control of the WPT system.

In the course of experimental validation, it was noticed that the load resistance varies with the fluctuation of the output power despite the stable nature of the load voltage. As a result, the expected quality factor was altered which significantly affected the transfer function of the converter. This is a major setback, as it will require a precise frequency tuning in order to maintain effective control since the operating frequency does not change, despite the change in the power level.

Another obvious limitation of the proposed design is the reduced efficiency of the converter at partial load as shown in the experimental results. This is due to the narrow range of the operating frequency, thereby giving rise to a significant amount of circulating current in the system. On a positive note, the system was designed to handle the presence of harmonics that may arise as a result of the converter switching operations. There were suggestions that the proposed design can be improved upon by the addition of a controller at the receiver's unit. This was to ensure the secondary side rectification is in synchronism with the primary side in order to reduce conduction losses while the converter efficiency is improved.

In conclusion, in the work of Voglitsis D [20], phase control and magnitude control was adopted in order to achieve a higher overall system efficiency of a proposed bidirectional WPT system. While the magnitude control was able to ensure the presence of unity power factor and low power losses in the system, the phase control was able to ensure the simplicity of power regulation as well as ensure a faster system response to the change in the power level. But there was a major gap in the control of both the high-frequency and low-frequency components of the overall WPT systems. There is need to integrate both subsystems using a unique and novel control strategy. In addition, the control system also requires a more efficient algorithm in order to significantly reduce the presence of total harmonic distortion especially for low-frequency converters (DC-DC and AC-DC converters). This would further improve the efficiency of the WPT system.

2.14.2 Electric Circuit Design for Electric Vehicle Bidirectional WPT Applications

In addition to the arrangement of the capacitors in four different modes to give capacitive compensation for the WPT system for the MRC model, other modes exist which can offer a better WPT capability. In the work of D. Voglitsis [20], the series-series (SS) topology was noted to have a major problem in maintaining a constant current when there was load variation and when there are alterations in the magnetic coupling. Similarly, the parallel compensation topology is incapable of maintaining the resistive value of the reflected impedance at the primary side. Thus, an LCL compensation topology was adopted which offers a constant current source at resonance even at fluctuating loads. The model was able to regulate the bidirectional power flow with additional features of controlling multiple EVs. But the major issue is the limitation of the compensation topology for low Q (quality factor) and high power applications [126].

In another research work, G. Lempidis [11] employed a different topology to achieve a bidirectional WPT system for EVs. The topology made use of the LLC compensator topology while integrating it into the resonant converter of the proposed system. The modification was able to reduce significantly the switching losses because the leakage inductance of the resonant coils was utilised as a resonant inductor. Despite the improvement, significant losses occurred in the system especially at higher output power greater than 4kW.

Thus, an improved compensation topology is required to handle high Q and high power applications as well as reducing the amount of power loss in the system.

2.14.3 Electromagnetic Design for Electric Vehicle Bidirectional WPT Applications

The electromagnetic aspect of bidirectional WPT is the most important aspect of the overall wireless system requiring optimization. This component implements the actual transfer of power from the transmitter coil to the receiver coil across the air gap.

In most of the research studied [11], [17], [20], [113], [124], [125], only the air-cored MRC and the traditional IPT technology was used in the modelling of each of the bidirectional WPT transfer design models. Since the ferrite-cored MRC model offers better coil-to-coil efficiency, it is worth designing an optimal bidirectional WPT system using such a model.

For many research works on bidirectional WPT system for EV application, there was always a suggestion on the need to develop a better physical design for resonant coils. While Voglitsis D. [20] suggested the need to model different coil configuration and geometries which can best match up any of the compensation topologies. A researcher by the name Lempidis G [11], suggested the need for generic coil system configurations which can suit the wide range of different compensation topologies. This is essential in order to correctly shape the magnetic fields between the transmitter and receiver coils to ensure better coil-to-coil efficiency. This can be achieved by either 2-dimensional or 3-dimensional finite element analysis (FEA) [20]. The coil design also needs to take into consideration

the standard electromagnetic compatibility (EMC) requirement during the design and investigation process in order to avoid any legal actions or sanctions that may emanate from the refusal to adhere to strict guidelines.

The nature of the strict guidelines as proposed by International Commission on Non-Ionizing Radiation Protection (ICNIRP), are basically limited to two specifications[127]: 1) the body must not be exposed beyond an absolute maximum magnetic field of $27.3 \mu\text{T}$ and 2) the measured average electromagnetic field strength at the knees, groin, chest and head must be less than $6.25 \mu\text{T}$. The specification was illustrated diagrammatically by Wu H.H et al[127] and reproduced. The diagram is shown in Figure 2.19

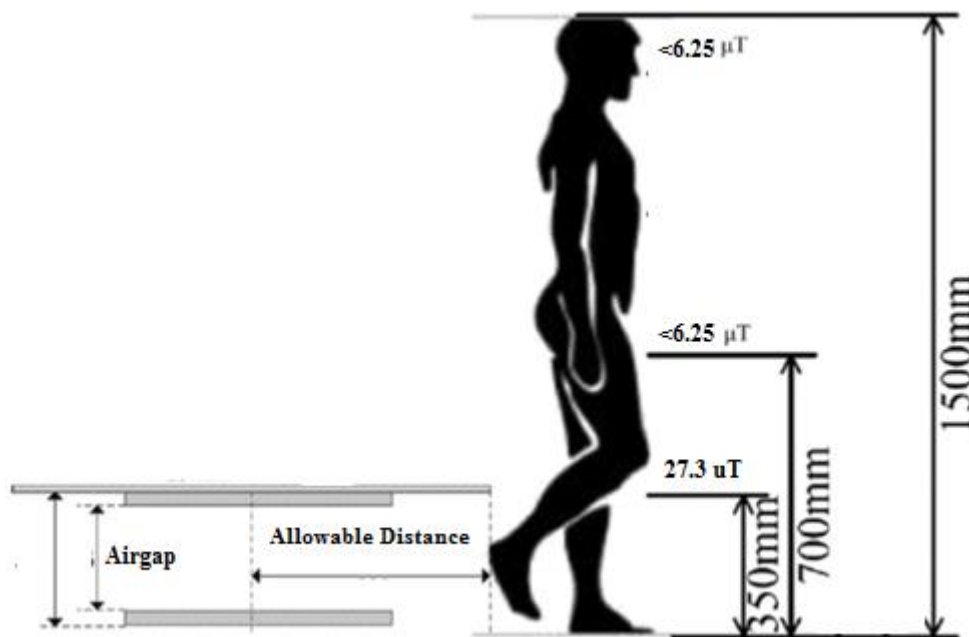


Figure 2.19: ICNIRP Standard Limit for Human Exposure to Magnetic Field[127].

In summary, the coil designs are primarily the aspect limiting the optimal development and deployment of bidirectional WPT technologies applicable to the electric vehicles and it is the focus of research for most commercial design and development of WPT technologies. As a result, this research will focus majorly on this aspect while considering impact of parameters like misalignments and airgap in order to achieve an optimal model.

2.15 Summary

In this section, a literature review of the evolution of the traditional grid into a smart power grid was undertaken. The evolution into the smart grid will allow for easy integration of EVs with the smart grid known as V2G. The interaction of the EVs with the grid can take the form of Vehicle-to-Grid, Vehicle-to-Home and Vehicle-to-Vehicle interface. The various form of interaction was discussed together with

their operating conditions. It was concluded that the integration will increase the potential for bidirectional flow of energy between the grid and the electric vehicle.

A literature review of plug-in electric vehicles (PEVs) was undertaken to highlight their advantages and drawbacks. The advantages of PEVs reduction in the emission of greenhouse gases, low maintenance and running cost and the potential of integration with the electric grid through the V2G technology. The drawbacks include the high cost of the battery, the risk of vandalism, safety issues as a result of hanging cables and open contacts, and the impossibility for dynamic charging operations. It was concluded that most of the issues with plug-in charging can be minimized through wireless power transfer technology.

Subsequently, a review of the wireless power technology was undertaken. Three media of operations was identified: mechanical force, electric field and magnetic field. The mechanical force and electric field mode of wireless power transfer were discussed and it was noted that they are not viable for electric vehicle charging applications because of their low power output and poor misalignment tolerance. During the review of the magnetic field mode, it was concluded that the ferrite core MRC wireless power systems offer the best performance for the charging of electric vehicles because of its potential for high power transfer, high power transfer efficiency and good misalignment tolerance.

A literature review of static and dynamic mode of charging electric vehicles was undertaken. The static charging process is implemented when the electric vehicle is in a stationary mode and the available areas where the static type of wireless charging are normally implemented are parking decks, bus stops, and road sections before traffic lights. On the other hand, the dynamic charging is the power exchange between the grid and the electric vehicle while the vehicle is in motion. The key features of static WPT technology are the low power ratings (less than 10kW) and high efficiency while the key features of dynamic WPT technology are the high power ratings (greater than 10 kW) and medium efficiency. In the areas of applications, the overall aim of the static mode of wireless power transfer technology for electric vehicles is the reduction in the complexity of the charging infrastructure. This is achieved by the creation of simple components for efficient and effective charging operations. Similarly, the overall aim of the dynamic mode of wireless power transfer technology for electric vehicles is the increase in the travel range by powering as many electric vehicles on the road as much as possible. Because the batteries of electric vehicles can be charged continuously, the need for a large battery for EV is eliminated which causes a significant reduction in the prices of the electric vehicles

Finally, a review of the mode, benefits, and research gaps for bidirectional wireless power transfer system was undertaken. Benefits of bidirectional wireless power transfer include the flexibility of power exchange in dynamic mode and the increase in travelling range. The key recharge gap was the need for the optimal design of resonant coils for high coil-to-coil efficiency while adhering to safety regulations.

CHAPTER 3 Analysis and Evaluation of Ferrite-Core MRC-based Coils

3.1 Introduction

The ferrite-cored MRC based WPT systems have been deployed successfully for use in a number of commercial products ranging from charging of electronic toothbrush to the charging of mobile phones and the wireless charging of electric vehicles. Despite the success rate, there are many aspects of WPT technologies requiring improvement and optimization[16]. In view of this, there are many impact factors affecting the power level, the power transmission efficiency (PTE) and the transmission distance. The four major impact factors are Environmental factors[50], [128], circuit designs[128], [129], coil alignment[114], [130], [131] and coil designs[132]-[134]. These impact factors will be discussed in order to ascertain the role they play in affecting the performance metrics of WPT in terms of coupling factor, PTE, and the amount of power transferred.

3.2 Environmental Factors Affecting Ferrite-Core MRC-Based Coil Topologies

The environmental factors of humidity and temperature do affect the PTE of the WPT systems[102]. In the research work of Jonah. H [102], an investigation was made to ascertain the impact of humidity on the performance of strongly coupled magnetic resonance models deployed for wireless sensors embedded in concrete. The focus was on the optimal designs of transmitter/receiver system for better efficiency operating within the air and concrete boundary. From the research result presented, it was noted that the system's efficiency reduces as the humidity level of the air increases. This was true for each variation of the airgap and diameter of the resonant coils used. The reduced performance of the resonant coil was attributed to increased conductivity of the concrete with increasing humidity. The conductivity of concrete creates a detuning of the resonant frequency of the receiver coil and load coil inside the concrete[102]. A practical way to reduce the impact of humidity on the performance of the resonant coils was to increase the cross-sectional radius of the wire-coils used in the proposed model. The proposed coil designs were analysed using a finite element analysis.

In a related development, Kurschner D. et al [128] investigated the sensitivity of some semiconductors to temperature. It was submitted that high temperature limits the level of power transfer in WPT systems. The rise in temperature causes quite a significant amount of thermal stress on the semiconductors. In addition, the rise of temperature impact on the performance of the ferrite cores. This causes the ferrite to suffer some level of demagnetisation. If the temperature rise is closed to the Curie temperature (above 180°C), the ferrite cores may begin to suffer permanent demagnetisation which limits the coupling performance of the WPT coil designs. For most finite element modelling of WPT coils, the heat-flow analysis gives reliable information on the level of temperature in the WPT

systems[135] over a particular time frame. Also, it was reported that below a temperature of 0°C, ferrite cores are less effective and will naturally display a reduction in their pull force and the degree to which this behaviour is exhibited is dependent on the size and the shape[136].

3.3 Circuit Designs for Ferrite-Core MRC-Based Coil Topologies

Design and development of highly efficient WPT systems involve the selection of optimal operating frequency[16][129], and good compensation systems[137], [138]. The power electronic converters are responsible for the production of the optimal resonant frequency in the system and there is need to use converters with low switching and conduction losses as the overall losses of the converters significantly impact on the overall losses of the WPT systems[88], [139], [140].

3.3.1 Frequency Specification for WPT Systems

The ferrite-core MRC wireless power transfer system is also affected by the resonant frequency[106], [111]. It is generally observed that a higher PTE in the range of 95% and above is possible at higher frequencies (above 200 kHz); However, issues such as the skin and proximity effect which increases the winding resistance[16]. Prototypes with high PTE have been developed at frequencies around 100kHz[104]. For ultrahigh frequencies application, an optimal resonant frequency of 13.56MHz was utilised in the work of SangCheol M. [104]. However, for such high frequencies, there is a significant presence of skin and proximity effect [16].

For a typical WPT, the PTE directly varies with the resonant frequency. Also, for most WPT model, there is an optimum frequency for a given load resistance at certain bandwidth of optimum frequencies[43]. At other frequencies outside the range of the bandwidth, the amount of power transfer drops significantly. However, for a typical, ferrite-cored MRC model, the range of resonant frequencies lies between 20-200 kHz[43].

In the selection of the appropriate optimal frequency, there is both the advantages and disadvantages of increasing or decreasing the resonant frequencies. A very high resonant frequency increases the PTE and after a threshold frequency, the efficiency becomes independent of the load and remain constant but comes at a higher cost of the inverter[36]. Also, a decrease in the resonant frequency reduces the switching losses but comes with a trade-off of the PTE; the PTE becomes significantly dependent on the load.

In addition, a combination of the coupling coefficient and optimal resonant frequency greatly impacts the PTE of the WPT model. This is illustrated in Figure 3.1[43]

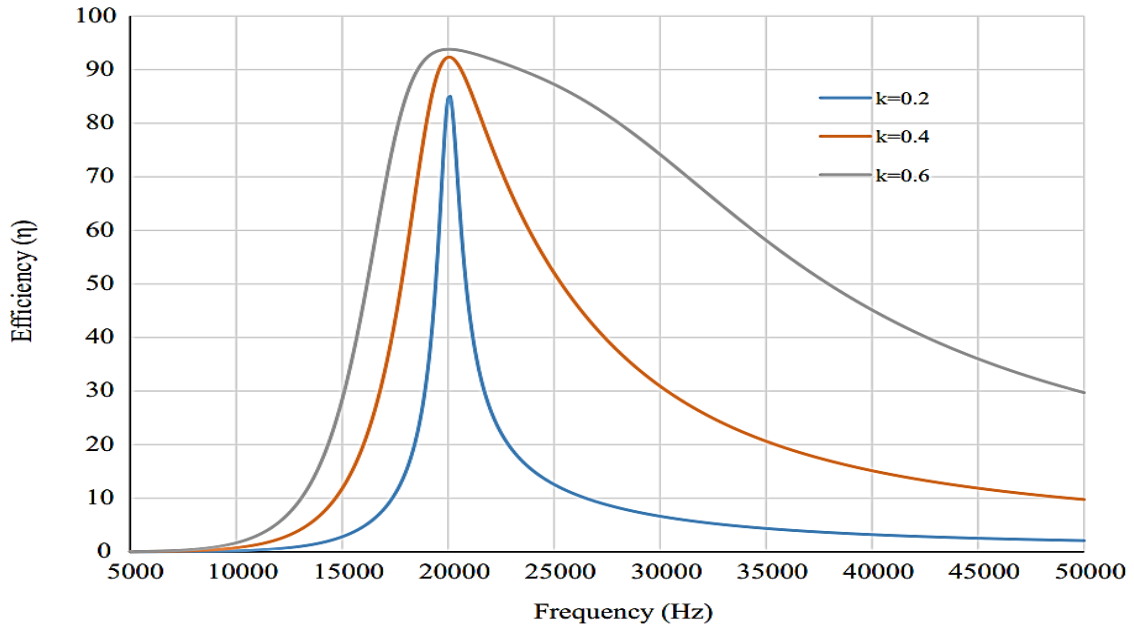


Figure 3.1: Effect of Coupling Coefficient and Resonant Frequencies on the PTE of Ferrite-Cored WPT Coils[43].

At a constant resonant frequency, an increase in the coupling coefficient increases the PTE. This is due to an increase in the magnetic flux linkage between the transmitter and receiver coil and also an increase in the self-inductance of the resonant coils which greatly impacts the quality factor[141].

A comparison of adopted resonant frequencies for various research outputs of some selected ferrite-cored MRC-based models and their corresponding coupling coefficient, power ratings, and efficiency are presented in Table 3.1

Table 3.1: Resonant Frequencies of Some MRC-based WPT Models

| Ref. no | Resonant Frequency | Coupling Coefficient | Power Ratings | Maximum Efficiency |
|---------|--------------------|----------------------|---------------|--------------------|
| [11] | 146 kHz | 0.24 | 3.3 Kw | 95 % |
| [142] | 20 kHz | 0.27 | 5 Kw | 94 % |
| [118] | 30 kHz | 0.33 | 3 kW | 97.9 % |
| [143] | 50 kHz | 0.18 | 3 Kw | 97.1 % |
| [118] | 20 kHz | 0.38 | 1.5 Kw | 95 % |
| [119] | 20 kHz | 0.16 | 1.5 kW | 95 % |

The results shown in Table 3.1 covers a wide range of cored-based WPT systems but gives an idea about the balance of resonant frequency and power ratings and efficiency as well as the range of frequencies applicable to most ferrite-core MRC wireless power transfer systems.

For most of the results presented, the frequency range lies between 20 kHz and 150 kHz. The low-frequency range is majorly due to the use of ferrite core, which boosts the self-inductance of the

resonant coil. It has been reported by Ahn .H. et al [144] that the use of ferrite core can boost the self-inductance of a coil by more than 30 %.

3.3.2 Converter Design for MRC Wireless Power Transfer System

Converters are power electronic devices capable of converting electrical power from one form to another. The conversion can be from DC to AC, AC to DC or changing of frequency or voltage level or any combination of these.

Typically, the primary side of the WPT system receives the normal grid voltage, current and frequency. The frequency is further conditioned by the use of high-power switching elements and converters. Most topologies make use of the common ac-dc-ac conversion topology, which is implemented using a two-stage conversion process. But there is the possibility of a direct ac-ac conversion process through the use of matrix converters[62]. In order to reduce the presence of harmonics and high reactive power, some systems employ the use of filters on the three-phase lines or the use of a power factor corrector which ensures a unity power factor at the primary side[62].

At the secondary side, the high-frequency output of the primary side is converted to dc for input into the battery. The process involves rectifying the high-frequency AC power from the primary side using diodes which are then filtered to remove any harmonic components before using it in the charging of the battery[145].

In the research work of Covic .G. and J. Boys [139], investigations into some viable resonant converters suitable for WPT operations were conducted. They employed the use of mathematical analysis, computer simulations and experiments in the design and optimization of commonly used resonant converters. Among the commonly used resonant converters optimized are the current-fed parallel resonant converters and the voltage-fed series quasi-resonant converters.

The current-fed parallel resonant converter is well known for its high efficiency and production of good current and voltage waveforms. But it has a drawback in terms of power level and length of track coils it can tolerate in addition to the presence of frequency variation if the pick-up loads and resonant circuit are not properly designed. For most practical applications, it is deployed for low power and short tracks applications in the charging of electric vehicles using wireless power transfer[139].

In order to achieve better control of the frequency as well as the capacity to operate over a longer track length of resonant coils, the voltage-fed series quasi-resonant converter was developed and deployed[139]. Also, it has the capability to operate at high efficiencies with soft switching. The converter topology contains a significant amount of harmonics in both its current and voltage waveforms and the optimal efficiency achieved with soft switching is significantly dependent on the compensations employed on the tracks; because most of the time, it is difficult to perform soft switching optimally during the start-up and shut-down transient periods. As a result, for most practical

purposes, the voltage-fed series quasi-resonant converter is deployed for medium power level and track lengths applications[139]

In order to overcome the limitations of the above named converters, a novel converter topology was proposed by Covic .G. and J. Boys [139]. The model developed has a significant improvement over the performance of both the current-fed and voltage fed converters. The proposed converter is based on energy injection control and free oscillations capable of producing low cost and high A.C power at low switching frequencies. The practical implementation of the proposed topology was realised using a self-sustained oscillation in the absence of an external controller operating at low voltages. The design has the advantages of longer track length, high frequencies and high track current. Other added advantages include resistance to start-up transient common with most resonant converters.

In addition to the above resonant converters, other common converter topologies are being developed and deployed and are tabulated in Table 3.2

Table 3.2: Various Types of Converter Topologies used for WPT Technologies

| Resonant Converter Type | Resonant Frequency | Power Ratings |
|---|---------------------------|----------------------|
| LLC Resonant Converter [19] | 146 kHz | 3.3 kW |
| ZCS LCC-Compensated Resonant Converter[140] | 40 kHz | 0.75 kW |
| ZCS LCC-Compensated Resonant Converter[140] | 40 kHz | 0.75 kW |
| Self-Resonant PWM [125] | 20.3 kHz | 6.6 kW |
| Two-Phase Series Resonant Converter[17] | 160 kHz | 1 kW |
| LCL Resonant Converter[142] | 20 kHz | 5 kW |

Among the listed resonant converters, the LCL, LLC and self-resonant PWM are the most commonly used. Recently, many research has been undertaken to further improve on their individual performances. For example, in the research work of Lempidis G. [11], a full bridge LLC resonant converter capable of working as half-bridge converter was used. In order to improve the overall efficiency of the converter across a range of power level, a half-bridge control topology was adopted at low power level typically below 1.5kW and a full-bridge control was implemented at high power outputs above 2.5kW.

For a typical bidirectional converter topology, two choices of a front-end DC/DC converter have been proposed: PWM converter and LLC resonant converter.

According to Stielau H. O. and Covic G. A [146], it was noted that PWM converters perform better with lower primary conduction losses when the input voltages are less than 320V. In contrast, LLC resonant converters have lower losses at higher voltages above 320V and are normally the operating condition for most of this type of converters. It is also reported that PWM has more switching losses than that

obtainable for the LLC converters at given switching frequency [146]. In some cases, it can be greater than 40% for the same operating frequency and power input.

In general, it was reported that LLC resonant converters are capable of providing better efficiency values for a wide range of input voltages when compared with the PWM converter under the same operating conditions. These capabilities made it the preferred choice for their proposed bidirectional converter.

For efficient performance of an LLC resonant converter, the choice of the resonant frequency ultimately determines the efficiency of conversion. According to the research report by Covic G.A and Stielau O.H. [146], operating a given LLC converter design at different frequencies produce different efficiency results. For example, when a given LLC resonant converter was operated at different frequencies of 200 kHz and 400 kHz, maximum efficiency values of 96% and 94% were obtained respectively.

3.3.3 Compensation Circuit Designs for WPT Systems

One of the major challenges in attaining a high PTE is the issue of leakage inductances. Due to the increase in the airgap between two inductive resonant coils, there is a corresponding increase in the magnetizing current and leakage inductance which weakens the magnetic coupling between the two coils[72]. When the leakage inductance is much larger than the magnetising inductance (typically greater than 65%), a loosely coupled system is created. Ferrite-core MRC is an example of such a system. One solution to the problem is ensuring that the transmitter coil receives its rated current while making the voltage a function of the load[147]. But the proposed solution is inadequate; resulting in a more effective solution of compensating the leakage inductance by the addition of coupling capacitor[45].

The solution is proffered because a loosely coupled and uncompensated system creates a lag between the voltage and the current; thus, creating significant reactive power in the system[148]. The presence of such a significant amount of reactive power lowers the power factor in the circuit.

The resultant effect of applying the appropriate capacitance to the circuit drives the circuit into resonance. At the appropriate resonant frequency, the coupling coefficient is strengthened and significant compensation for the leakage inductance[149][137] is achieved.

According to the reports by Huang C.Y et al [149], it was noted that the apparent power rating of the input power can be minimized by compensating the transmitter coil. Similarly, the receiver coil capability to pick up the transmitted power across the airgap can be significantly increased by applying the appropriate compensation scheme to the transmitter coils.

In this regard, many compensation schemes have been adopted in the wireless power system sector; notable among such schemes is the use of power factor correction capacitors to reduce reactive power. It has been noted that series compensation is also used on long transmission lines[147].

When dealing with the issue of leakage inductances, the level of compensation and the topology to be used are critical to the optimal solutions. Unlike what is obtainable for power systems, reactive power can be as large as 70% of the active power for uncompensated WPT systems. There are two basic compensation topologies utilised in the MRC wireless power transfer system- series and parallel (shunt) compensation[147]. The series compensation involves placing the capacitor in series with either coil while the parallel compensation is done by placing the capacitor in parallel to the coil. Thus, there are four possible compensation topologies that can be created at the transmitter and receiver coils. This is illustrated in Figure 3.2 [149][43].

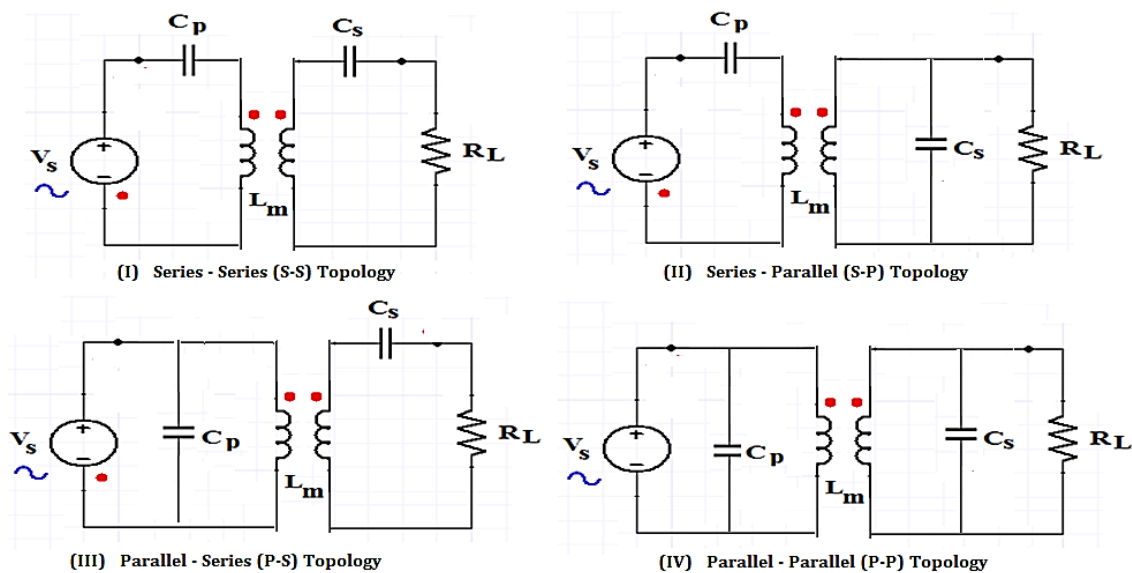


Figure 3.2: Compensation Topologies Used for Strong MRC Wireless Power Transfer Systems [149].

The possible arrangement of the capacitors do results in four combinations namely: series-series, series-parallel, parallel-series and parallel-parallel compensation topology. The adoption of any of the series or parallel compensation at the transmitter or receiver side comes with different merits and demerits. Whatever be the case, the performance of the system is maintained when the operating frequency is kept at zero phase angle and it can only be achieved through compensation.

For most design schemes, series compensation is utilized at the transmitter side when the optimal system performance requires the reduction of power supply voltages to tolerable levels; especially during dynamic charging operations. In contrast, applications requiring large currents at the transmitter normally utilize the parallel compensation topology[147] at the transmitter side.

Similarly, compensation at the receiver side largely depends on the type of application. For systems with voltage source characteristics, series compensation is mostly used. An application utilizing an

intermediate DC where a constant voltage is required uses the series compensation topology [45]. When a constant current source is required as in the case of charging the battery of an electric vehicle, a parallel compensation is preferred[147].

Beyond the required performance of the compensation topology at the receiver and transmitter side, a combination of any of the series and parallel compensation comes with characteristic performance metrics.

For example, a series-series combination is considered to be the most suitable for charging of electric vehicle[149], [150] because of the ability to act as a voltage source which is independent of any changes in the receiver's capacitance and offers a very high efficiency and power factor at small airgap[43]. In addition, the capacitances at the receiver and transmitter sides are unaffected by changes in the load and magnetic coupling. In addition, it is capable of acting as a constant current source.

The parallel-parallel combination, on the other hand, acts as a current source independent of any changes in the transmitter's capacitor with high efficiency and very high power factor at large airgap[43], but offer a high impedance at resonance.

The parallel-series combination offers a medium efficiency with high power factor at large airgap, also produces a high impedance at resonance while acting as voltage source independent of changes in the transmitter's capacitance.

The series-parallel combination also offers a medium efficiency (between 60 % and 90 %) and high power factor (above 0.8) at small airgap while acting as current source independent of changes in receiver's capacitance[43].

Based on the circuit configurations, the series-series and parallel-parallel configurations are capable of bidirectional wireless power transfer, as the performance and configuration remain the same irrespective of the resonant coils that act as transmitter or receiver.

In contrast, the series-parallel and parallel-series compensation configuration is most suitable for unidirectional power transfer. For example, when the direction of power flow is reversed for series-parallel circuit compensation, the circuit becomes parallel-series circuit compensation with different performance metrics as listed above.

A special series-parallel LCL design was presented by Moradewicz A. J. and Kazmierkowski, M. P. [151] which has a limitation of reflecting the reactive power back to the source at the transmitter side. But, offers smooth power transitions during switching while transmitting uninterrupted power across the airgap[152]. The model design is also noted to require a high value of capacitance (in the millifarad range) in order to have strong coupling coefficient[153].

In addition to the four common compensation highlighted above, other viable alternate compensation topologies have been designed and presented[86], [140], [149], [154]. A good design topology was presented by Huang, C.Y. et al [149], which has the performance capability of significantly reducing the negative effect of frequency variation responsible for low magnetic coupling when compensation is done only the transmitter circuit. Consequently, a parallel-parallel-series (PPS)[150] and series-parallel-series[137] (SPS) was proposed and developed and the circuit diagrams are shown in Figure 3.3

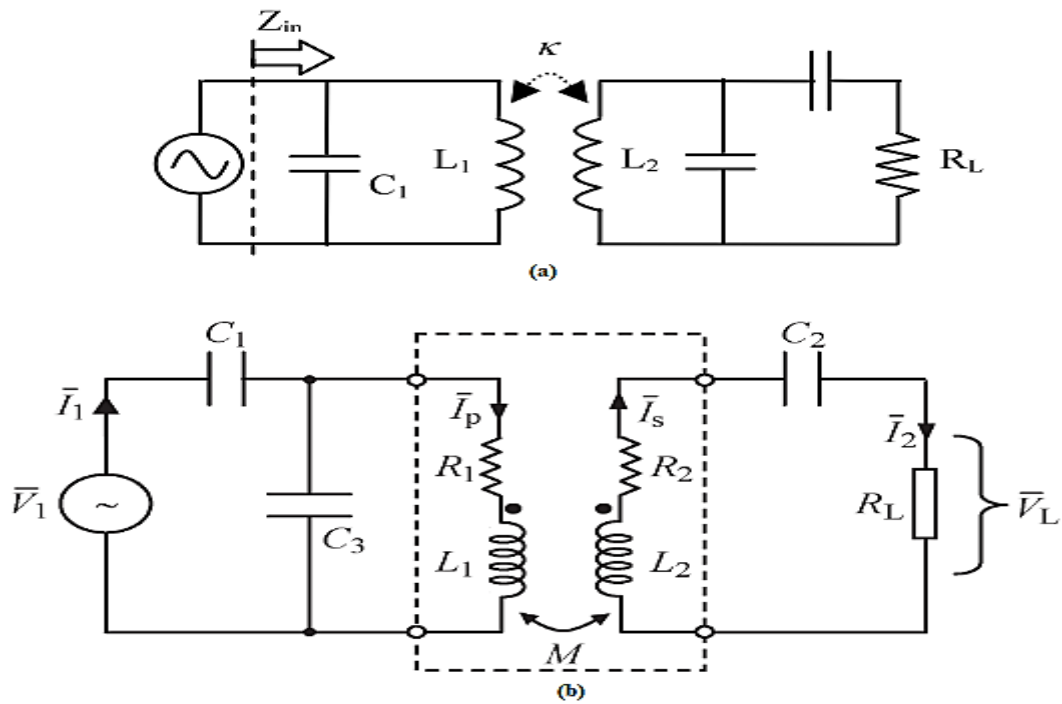


Figure 3.3: Alternative Compensation Topologies. (a) PPS Topology. (b) SPS Topology.

The PPS topology offers higher efficiency than the PP at the same airgap and load of 50mm and 1 ohm respectively. For smaller misalignment between coils (mostly less than 5cm), the PP offers better performance than the PPS but the PPS gives a higher power factor at the converter in relation to that of the PP[137].

The SPS, on the other hand, offers better efficiency and misalignment tolerance when compared to any of the four basic compensation topologies at a given load of 1.25 ohms at a power transfer of 2 kW. Thus, the selection of the SPS and PPS topologies is usually made based on the required application as SPS can be very useful where little misalignment is allowed while PPS will perform poorly under the same physical condition and environment.

Also worthy of note is the design of an inductive coupler by Richardson K. et al [155] which offers a low leakage inductance while providing significantly high self-inductance. The model was capable of transferring 8.3kW of power across an airgap of 3 mm at an overall efficiency of 97%.

In summary, the transmitter side is compensated so as to increase the active power but with a trade-off of lowering the apparent power (VA) of the power supply, thereby lowering the reactive power. Likewise, the receiver side is compensated to enhance the power transfer performance by transferring much of the active power to the load (battery)[45]

3.4 Impact of Coil Alignment on Ferrite-Core MRC-Based Coil Topologies

Coil alignment is also another issue that affects the PTE of wireless power transfer systems. According to Kürschner .D. et al [134], there are basically two types of misalignments- angular misalignment and lateral misalignment. The lateral misalignment occurs when there is both a shift in either the horizontal or the vertical distance between the transmitter and receiver coils. The lateral misalignment can be further divided into airgap variation also known as vertical misalignment[93], door-to-door misalignment and front-to-rear misalignment[93]. For the purpose of this research, the vertical misalignment will be referred to as airgap variations while the door-to-door misalignment and front-to-rear misalignment will be termed as lateral misalignment and longitudinal misalignment respectively. When any of these misalignment occurs, the link efficiency between coils is reduced. A graphic illustration of the various misalignments are shown in Figure 3.4[93]

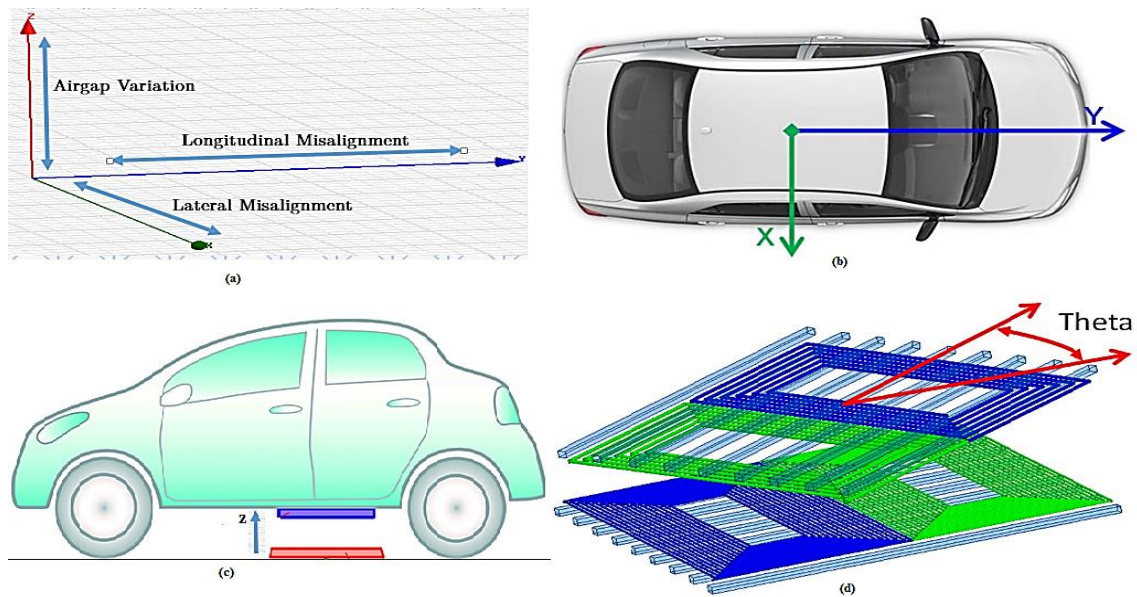


Figure 3.4 (a) 3-D Misalignment Representation. (b) X-axis: Lateral Misalignment, Y-axis: Longitudinal Misalignment[93]. (c) Z-axis: Airgap Variation. (d) Angular Misalignment at an Angle (θ) [93].

3.4.1 Angular Misalignment Resonant Coils

The angular misalignment involves the change in the magnetic field with respect to the level of tilting of the receiver coil. This occurs when the plane of a receiver coil is tilted at an angle of θ and the axes of the receiver pass through the centre of the transmitter[95]. The magnetic field is maximised when the angle of tilt is zero while the magnetic field is minimum when the receiver coil is

perpendicular to the transmitter coil[156]. For most practical scenarios, the angular displacement is not common, but there is a possibility for both the angular and lateral/longitudinal misalignment. According to Budhia .M. et al[157], the angular misalignment dominates at a small lateral/longitudinal misalignment (typically less than 5 cm) but the lateral/longitudinal misalignment dominates over the effect of angular misalignment for at large lateral/longitudinal displacement (typically above 15cm).

Though there is the possibility of lateral and angular misalignment occurring simultaneously, much work is yet to be done on the particular scenario to determine the impact it will have on the PTE. But research has shown that the lateral misalignment is more common than the angular misalignment for most EV application[134], but the latter has a greater effect on the PTE when compared to the former. Subsequently, analysis of angular misalignment is not covered in this research.

3.4.2 Lateral and Longitudinal Misalignment of Resonant Coils

The lateral/longitudinal misalignment occurs when the centre of the receiver's coil is not perfectly aligned with the centre of the transmitter coil. The horizontal movement of the receiver's coil can occur in two dimensions as shown in Figure 3.4

The lateral misalignment occurs when the horizontal movement goes towards the direction of either of the car's doors while the longitudinal misalignment occurs when the horizontal movement goes in the direction of either the front or rear end of the car. For appropriate analysis of the lateral/longitudinal misalignment, many researchers assigned different nomenclatures for the phenomenon. For example, Kalwar, K. A. et al [33], and Budhia, M. et al [107] refers to it with the general term lateral misalignment. Similarly, Chigira M. et al [64], Budhia, M et al[66], and Klontz, K. W. et al [90] refers to lateral or longitudinal misalignment as horizontal misalignment.

Many research has been undertaken to study the effect of lateral and longitudinal misalignment on the performance of resonant coils. For example, in the work of Prasanth, V. and Bauer, B. [114], it was noted that an increase in longitudinal and lateral misalignment causes a reduction in the mutual inductance between the coils. The effect of the drop in mutual inductances was observed to vary based on the number of coils turns.

The experimental investigation was carried out using a single turn, double turns, four turns and five rectangular turns of loop wire. From the experimental results, the single turns and double turns loop wire shows a small variation in mutual inductance with an increase in misalignments while the four turns and five turns loop wire shows a drastic reduction in mutual inductance with an increase in misalignments. Thus, in summary, the reduction in mutual inductance as a result of variation in misalignment increases with increase in wire turns.

Also in the works presented by Huang, C.Y et al [150], a horizontal misalignment analysis was done on the ferrite-core circular coil and it was shown that an increase in horizontal misalignment causes a

drastic decrease in the coupling coefficient between the resonant coils. Interestingly, the effect of misalignment on the power factor was investigated for PP and PPS compensation of the circular coils. From the experimental results, it was noted that the increase in horizontal misalignment causes a drastic decrease in the power factor, though the power factor of the PPS is significantly higher than the PP at zero misalignments.

Finally, an analysis of misalignment on the power transfer efficiency over a horizontal range of 100mm was undertaken and it was noted that PPS compensation topology has a relatively stable PTE over the range of misalignment values while the PP compensation topology performance began to drop significantly at horizontal misalignment of 60mm.

A similar result was presented by Nguyen T. D. et al [93], an 8kW WPT model prototype was developed. At an airgap of 200mm, a horizontal misalignment of 300mm was tested and about 18.8% to 31.1% of the zero-misalignment coupling coefficient was maintained with a D.C.-to-D.C. efficiency of 95.39%. The experiment was implemented using a bipolar pad known as double D coils in [11]

Generally, from the research works of Fuller. M [28], Son, H.C [57], Shinohara [62], Hu, A. P [85], employing different compensation topologies, it was noted that an increase in either or both of the lateral or longitudinal misalignment causes a reduction in the coupling coefficient, power output, power transfer efficiency and some rare cases bifurcation, i.e. the presence of more than one resonant frequency in a WPT systems [49], [88]–[90].

3.4.3 Airgap Variation of Resonant Coils

In the development of EV charging, the presence of large airgap has been the major point of consideration[43]. This is because there is always need for a good ground clearance between the charging pad fixed in the ground and the chassis of the electric vehicle[43]. The ground clearance is known as the airgap and an airgap of a few centimetres is appropriate for application in EV charging[117]. According to the required regulation in the European Union, an airgap between 11cm and 20cm is the standard for most WPT systems applicable to EVs[11]. For this range of airgap, the value of the coupling coefficient ranges between 0.30 and 0.60[149], [161].

For a particular WPT model, a variation in the airgap affects its performance metrics which includes coupling coefficient, power transferred and efficiency. In the presented works of Takanashi, H. et al [87], a 3-kW flux-pipe model operating at a resonant frequency of 50 kHz were developed and its performance at different airgap analysed and evaluated. At an airgap of 160mm, the system achieved a coupling coefficient of 0.18 at a maximum efficiency of 97.1%; when the airgap was increased to 200mm, the coupling coefficient and maximum efficiency dropped to 0.12 and 95.5% respectively.

In the research work presented by Chigira M. et al [158], a parametric sweep of the airgap was performed in order to analyse the performance of their H-shaped ferrite cored model. It was noted

that the self-inductance of the receiver was relatively constant while the coupling factor, power transferred across the airgap and efficiency decreases with increase in the airgap; with the coupling coefficient mostly affected by the increase in the airgap ranging between 40 mm and 130 mm.

In addition to the above research works, other research works and model design performance metrics at different airgaps are presented in Table 3.3

Table 3.3: Performance Metrics of Some Selected WPT Models at Different Airgaps

| Ref. no | Airgap | Coupling Coefficient | Power Ratings | Maximum Efficiency |
|---------|--------|----------------------|---------------|--------------------|
| [117] | 300 mm | - | 1 kW | 80 % |
| [101] | 200 mm | - | 2 kW | - |
| [162] | 250mm | - | 25 kW | - |
| [137] | 150 mm | - | 2 kW | 95 % |
| [93] | 200 mm | 0.32 | 8 kW | 95.66 % |
| [127] | 175 mm | - | 5 kW | 90 % |
| [84] | 300 mm | 0.05 | 3 kW | 95 % |
| [11] | 200 mm | 0.24 | 3.3 kW | 95 % |
| [163] | 300 mm | - | 1 kW | 88% |

From the achievements in research shown in Table 3.3, the research model of Nguyen T. D. et al [93] and Lempidis, G [11] involving the development of bipolar pads or Double-D coils respectively seems to be very promising in the development of ferrite-cored WPT models for EVs.

3.4.4 Coil Design for MRC Wireless Power Transfer System

This is by far the most important factor affecting the PTE of WPT systems. For example, Li .Y. et al[164] was able to show that the use of a high Q structure planar-litz coil can deliver up to 28% efficiency increase compared to the use of the traditional copper coils. A further improvement was achieved by Mizuno .T. et al[165] through plating a copper wire with a thin magnetic film to increase the quality factor. The use of the magnetic film-coated copper for the coil design resulted in a transmission efficiency improvement of more than 8%.

In the work of Pantic .Z. and Lukic .C. [66], an analytic model was designed for a multi-turn, multi-layer hollow and a tubular resonant coil which takes care of the proximity effect. The proximity effect arises when an alternating current flows in more than one nearby conductors that are closely wound together resulting in the constraint of current distribution to smaller regions in the first conductor. According to Ishizaki .T. et al [132], the larger the diameter of the transmitter coil, the longer the range and wider the 2-Dimensional free-access area. Subsequently, spiral coils with a larger cross-sectional area have a higher Q factor. In the work of Kilinic, G. et al[134], coils with different geometries were studied

which includes amongst others, flat coils, square coils, spiral coils and circular coils. The simulation work shows that a square coil produces a larger power transfer than circular coils. The self-inductance also increases with an increase in the number of turns of the coil.

3.5 Coil Designs for Ferrite-Core MRC-Based Coil Topologies

For ferrite-core MRC based coil topology, the WPT consists of only two coils, a transmitter coil and a receiver coil[144]. The basic method of operation is the generation of an electromagnetic field from an alternating current in the transmitter coil. The magnetic field then induces an alternating voltage in the receiver coil[144]. The induced voltage is then rectified and used to charge a battery or power a mobile device. The major components of the coil designs are the coil windings, the ferrite core and the shielding design topology. The coil windings create and propagate the magnetic field, the ferrite core enhance the boosting of the magnetic flux and the shielding topology helps in protecting humans and animals from electromagnetic radiation by absorbing most of the leaked magnetic flux from both the transmitter and the receiver coil[166][16].

In this section, a literature review of coil geometric shapes, coil sizes and coil material types used for modelling of different coil topologies will be discussed. A proper discussion of current trends will help in the proper selection and optimization of proposed coil models.

3.5.1 Geometric Specifications of Coil Designs

Kilinc G. et al [134] in their research work investigated the impact of coil geometry on the PTE of coil models. Different coil models were designed and analysed.

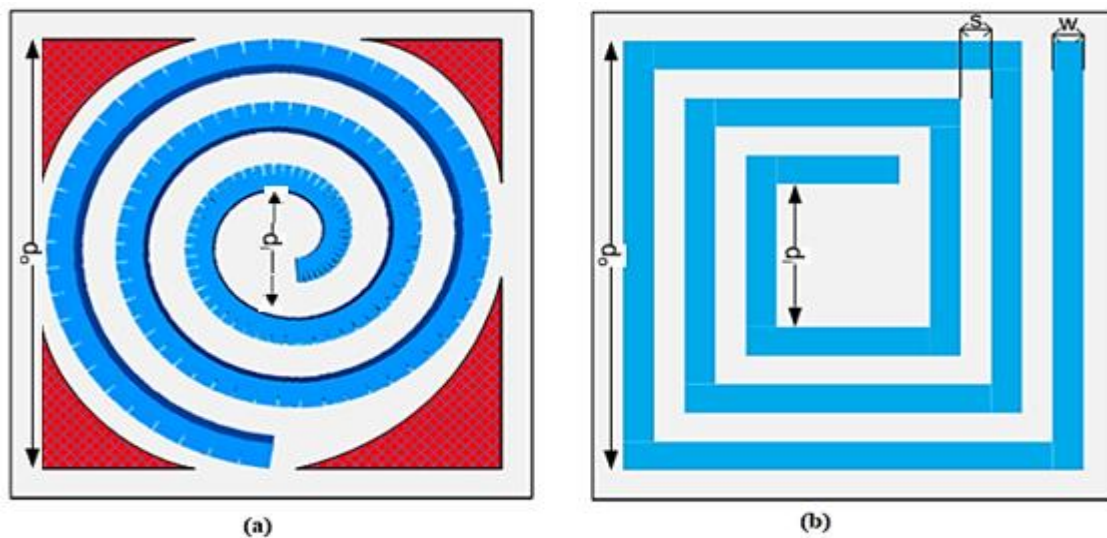


Figure 3.5: Commonly Used Coil Shape Design. (a) Circular Shaped Coil. (b) Rectangular Shaped Coil[134].

In the study, flat coil, square coil, spiral coil, and circular coils performance were analysed and different PTE was reported for each of the coil shapes. Examples of the various shapes investigated are shown in Figure 3.5. Many researchers adopted the circular and rectangular geometric designs in their

proposed models. Budhia M et al[120] and Saeed H. et al [167] used the circular geometry in their model designs. Similarly, researchers like Daniel. O, et al [168] and Al-Saadi et al [169] adopted the rectangular geometry in one of their model designs. From the performance analyses of the various rectangular and circular models designed; it was noted that despite having the capabilities to transfer high power, they have a poor misalignment tolerance as their PTE decreases significantly at a horizontal misalignment of above 12.5cm[119][132]. In fact, it has been noted that a horizontal misalignment of about half of the coil diameter will lead to zero magnetic coupling between the transmitter and the receiver[120].

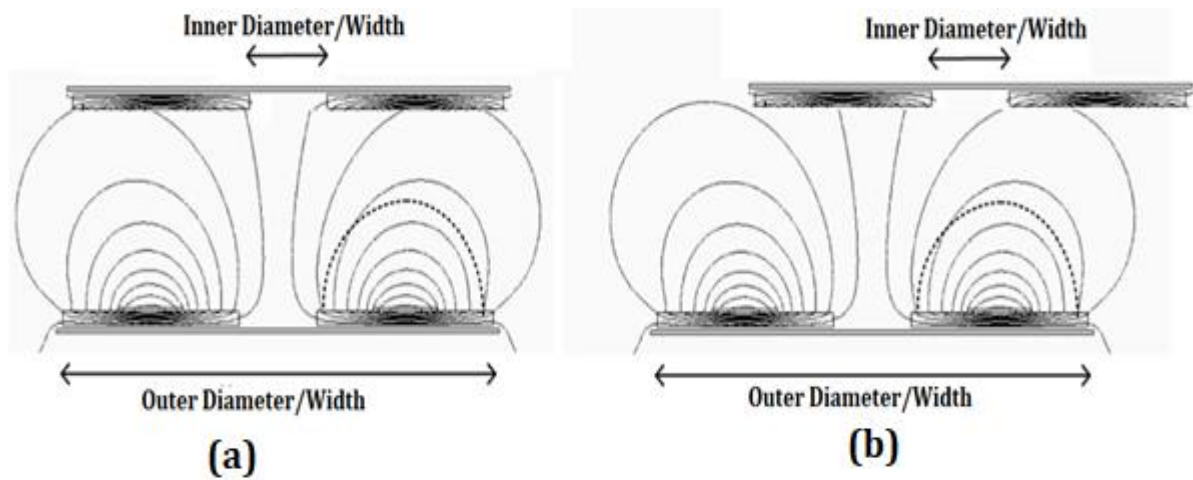


Figure 3.6: Flux Path Distribution for Circular/Rectangular Coil Designs. (a) Flux Path in a perfectly aligned Condition. (b) Flux Path Distribution in a Misaligned Condition (Source: Budhia et al[99]).

The reason for such performance characteristics of circular and rectangular coils is the relatively static nature of the fundamental flux paths irrespective of the optimization techniques applied in its design process[99]. The coupling strength between the transmitter and receiver coils is determined by the flux path height above the transmitter. In order to increase the flux path height, the coil's diameter, or length need to be wider or longer depending on the coil geometry[99]. At perfectly aligned condition (shown in Figure 3.6(a)), each of the two flux paths from the transmitter optimally reaches the receiver, and high power can be transfer. Nevertheless, when there is a misalignment (shown in Figure 3.6(b)), only one of the two available flux paths from the transmitter optimally reaches the receiver. A significant amount of the flux from the left side get leaked to the air while a small portion of the flux from the right side get leaked to the space denoted by the inner diameter/width.

Because of the limitations of the circular and rectangular shape designs, other shape designs have been modelled and adopted and are illustrated in Figure 3.7. The design and development of the flux-pipe coil and the rectangular bipolar coil is essential aimed at reducing the leakage flux at the inner diameter/width section of the circular/rectangular coil designs.

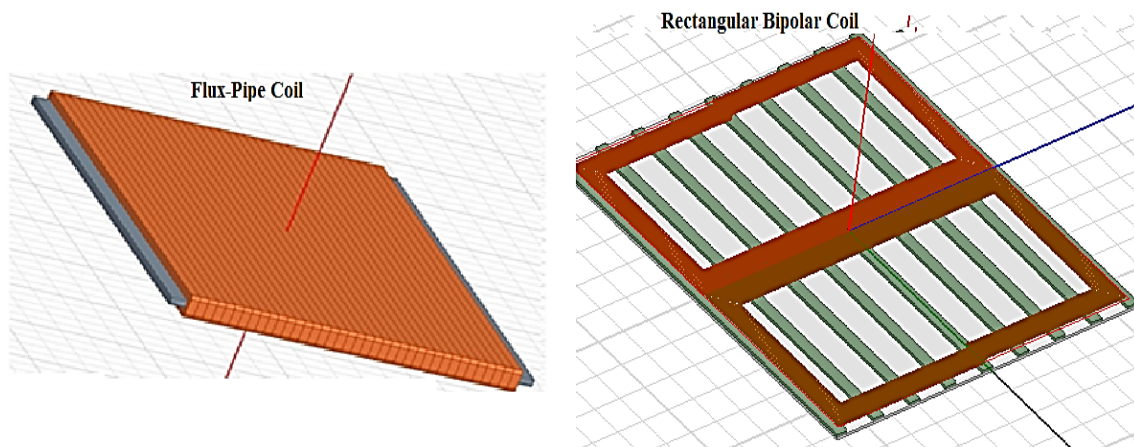


Figure 3.7: Flux-Pipe and Rectangular Bipolar Coils

The flux-pipe coil design also known as double-sided windings by Nagatsuka Y. et al [119]. The flux pipe model is designed by winding a copper wire around a ferrite core as shown in Figure 3.6. From the result presented by Nagatsuka .Y. et al, it was noted that the flux pipe model has a better magnetic coupling and misalignment performance compared to the circular and rectangular models. But the downside of the model is that it can only transfer a low amount of power across the airgap (typically less than 3 kW). This is a result of the “double-sided flux (DSF) path. For a single flux-pipe resonant coil design, there are equivalent amounts of useful and “non-useful” flux created at the upper and lower sides of the resonant of both the transmitter and receiver coil. While the beneficial flux at the top side of the transmitter coil couples with the proportion of useful flux generated in the receiver coil, the “non-useful” flux generates eddy currents in the aluminium shielding installed at the back of the coils. In fact, their flux-pipe model was capable of transferring a maximum of 1.5 kW across the airgap at an efficiency of 95.3 %.

In order to bridge the gap in performance between the flux-pipe model and the circular/rectangular model, a rectangular bipolar coil geometric design was proposed by Nguyen C. et al [93] and a similar model was designed by Lempidis G[11] which was termed the double-D coils. The rectangular bipolar type resonant coil designs consist of two rectangular coils placed side by side over a series of ferrite bars as shown in Figure 3.7.

From the experimental results obtained the model developed was able to transmit up to an optimum power of 8 kW over a 20 mm airgap at a DC to DC efficiency of 95.66 % when both the primary and secondary coils are perfectly aligned. A power transfer of 4 kW at a D.C. to D.C. efficiency of 95.39 % across the gap was also noted when the coils are set with a 30cm lateral misalignment.

Despite the performance improvement of the rectangular bipolar coil over the circular, rectangular and flux-pipe resonant coils, the design model has a significantly higher weight and size when compared to the power output and efficiency obtained. Also, there is a noticeable decrease in power output across the airgap with an increase in lateral misalignment.

3.5.2 Coil Size Specifications

An interesting relationship between the transmitter coil diameter and the transmitting distance (airgap) has been established by Kurschner .D. et al[128]. They investigated the relationship between the ratio of the transmitter coil and airgap as it affects the PTE.

In their submission, it was presented that at constant Q-factor, the ratio of the airgap (Z) and the diameter of the (D) of the coil has a significant effect on the power transfer efficiency. For example, it was noted that the efficiency of more than 80 % can be achieved if the ratio $Z/D < 0.5$. In addition, a coil-to-coil efficiency of up to 90 % can be achieved if the ratio $Z/D < 0.25$. In essence, for an airgap of 200 mm, a coil-to-coil efficiency of 90% can be achieved with a minimum transmitter's diameter of 800 mm. This condition mostly applies to circular, rectangular and rectangular bipolar coils. For most applications, the diameter of the transmitter coils is limited by the width of electrical vehicles which varies between 1.2m to 1.8m. A table of coil size specifications of published research works and their performance in terms of airgap, maximum power transferred and PTE efficiency is shown in Table 3.4.

Table 3.4: Table of Coil Shapes, Dimensions, and Performances of Some Research Works

| Ref. no | Coil Shape | Airgap (mm) | Coil Dimension (L (mm) x B(mm)) | Power Ratings | Maximum Efficiency |
|---------|---------------------|-------------|---------------------------------|---------------|--------------------|
| [100] | Circular Coil | 150 | Diameter = 542 | 20 kW | 97 % |
| [134] | Rectangular Coil | 30 | 230 by 160 | - | 66.7 % |
| [119] | Flux-Pipe | 70±20 | 240 by 250 | 1.5 kW | 95 % |
| [93] | Rectangular Bipolar | 200 | 600 by 800 | 8.0 kW | 95.66% |
| [143] | Flux-Pipe | 200 | 320 by 300 | 3.0 kW | 95% |
| [167] | Circular Coil | 200 | Diameter = 400 | - | 67 % |
| [158] | Rectangular | 70 | 240 by 250 | 1.5 kW | 96.6 % |
| [11] | Rectangular Bipolar | 200 | 580 by 580 | 3.3 kW | 95 % |
| [158] | Flux-Pipe | 70 | 240 by 300 | 1.5 kW | 94.5 % |
| [71] | Rectangular Bipolar | 200 | 540 x 800 | 2.0 kW | - |

From the information presented in Table 3.4, it is noted that the circular and rectangular coil models offer the least power transfer efficiency. This is as a result of poor coupling between coils.

The rectangular coil also has the potential of transferring up to 1.5kW of power at 96.6% efficiency, but can only be achieved at a lower airgap. The performance characteristics are similar to that of the circular coil topology.

The bipolar rectangular coils offer high power transfer efficiency of more than 95% and high power transfer of 3.3 kW and above but mostly achieved such performance with larger dimensions and thus for most practical applications, they tend to be much heavier.

The flux-pipe topology usually has smaller dimensions and higher efficiency but are limited in the amount of power they can transfer mostly less than 2 kW. This is as a result of the double flux problem as a significant amount of power generated is wasted as eddy current losses on the shield sheets. Optimal design of the flux-pipe topology aimed at reducing the eddy current losses in the coil will enhance the power transfer capability and that will be the focus of this research.

3.5.3 Coil Material Specifications

For most practical applications of ferrite core MRC coils, there are three material requirements for most of the designs. They are coil windings, ferrite core and shielding topology.

3.5.3.1 Coil Winding Specifications

The coil windings material used for most design is a copper wire. Initially, solid copper wire of radius between 1mm to 6mm can be used, but not practically possible because of the resistance of copper wire increases at higher frequencies[170] due to the skin and proximity effects. As a result, most researchers employ the use of a special type of wire called Litz wire. The various shapes and size of commercially available Litz wire designs by Osco[171] are shown in Figure 3.8.



Figure 3.8: Shapes and Sizes of Commercially Available Litz Wires[171].

The Litz wire consists of thin strands of copper wire with an insulation layer on each of the strands which are twisted to form a bundle. This type of wire has been the preferred type for copper coils used for most practical designs[66], [143], [158], [170] because of its performance at high frequencies above 1kHz. The losses at these high frequencies are significantly reduced and thus, enable its adaptability for wireless power transfer coil designs. Because it is the current choice for most researchers, it was adopted modelled in this research.

3.5.3.2 Ferrite Core Selection

The ferrite core material is also very important in the design of efficient wireless power transfer systems because of its ability to provide low reluctance path for the emitted magnetic field and

converting them into a transverse magnetic field that radiates towards the receiver. The mode of operation of a ferrite shield is correctly illustrated in Figure 3.9(a)[144]. Ferrite material is able to achieve this performance because of their high permeability characteristics; mostly a few thousand times higher than that of air.

Similarly, it was reported by Seugnyoung, A. et al [144] that the addition of ferrite material to a coil design increases the mutual inductance between the transmitter and the receiver which in turns increases the magnetic coupling between them. The increase in mutual inductance can be as high as over 500%. This is illustrated in Figure 3.9(b) [144].

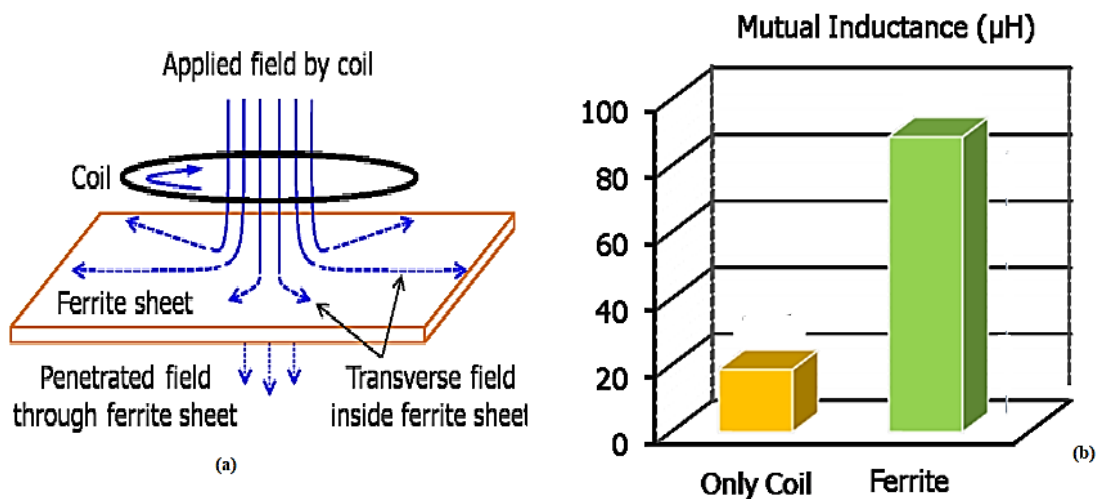


Figure 3.9: Effect of Ferrite Material on Emitted Magnetic Field. (a) Magnetic Orientation in Ferrite Sheet. (b) Effect on Mutual Inductance between Coils[144]

From the publications of many research works, there are numerous types of ferrite material used by researchers. The common types are the FDK 6H45, FDK 6H40, TDK PC44, and the TDK PC47 [64], [65], [79], [123]. For most literature studied in this research, the FDK 6H40 is the most common. In fact, some researchers like Mostak, M. et al [131] were able to calculate the coefficients of core loss equations for the FDK 6H40 ferrite core.

Due to the significant improvement in performance as a result of adding ferrite core to a coil winding, the methodology, as well as the FDK 6H40 ferrite core, will be adopted and modelled in this research.

3.5.3.3 Shielding Topology

Shielding in the design of wireless power transfer system is an important requirement because of the safety standard specified by the International Commission on Non-Ionizing Radiation Protection (ICNIRP). For most practical applications of WPT systems, there is always a significant amount of leakage flux. The leakage flux is as a result of low magnetic coupling common with most WPT systems. The leakage flux poses a serious problem to the health and wellbeing of the users[143]. As the magnetic coupling factor decreases due to an increase in the airgap, the impact of the external electromagnetic flux linkage poses a lot of danger to humans[143].

A practical approach to minimize the number of electromagnetic flux leakages was to introduce a shielding material at the transmitter and receiver of the WPT systems. Typically, there are two types of magnetic field shielding techniques: one uses magnetic material and the other uses conductive materials[144].

The use of magnetic shielding involves the use of magnetic materials. Because of the high permeability of these magnetic materials with respect to air, they tend to concentrate most of the leaked electromagnetic flux into the material. Two types of magnetic materials are normally used- the metallic oxide or ceramics or metallic ones. The metallic magnetic materials like iron and steel are not normally used because of their high conductivity. Their high conductivity results in significant losses at high frequencies in the kilohertz ranges[144].

The use of ceramic materials known as ferrites is another alternative but are mostly not employed because they are better suited for boosting the electromagnetic flux from the transmitter to the receiver.

The use of conductive materials employs the process of electromagnetic induction in the cancellation of leaked magnetic flux. The induced electric current produced creates an eddy current which opposes the applied magnetic field generating the required shielding effect. For virtually all the research work studied, aluminium was used as the shielding material[99], [128], [135], [144], [173]. This is illustrated in Figure 3.10(a). The choice of aluminium is because of its flexibility, conductivity and low weight.

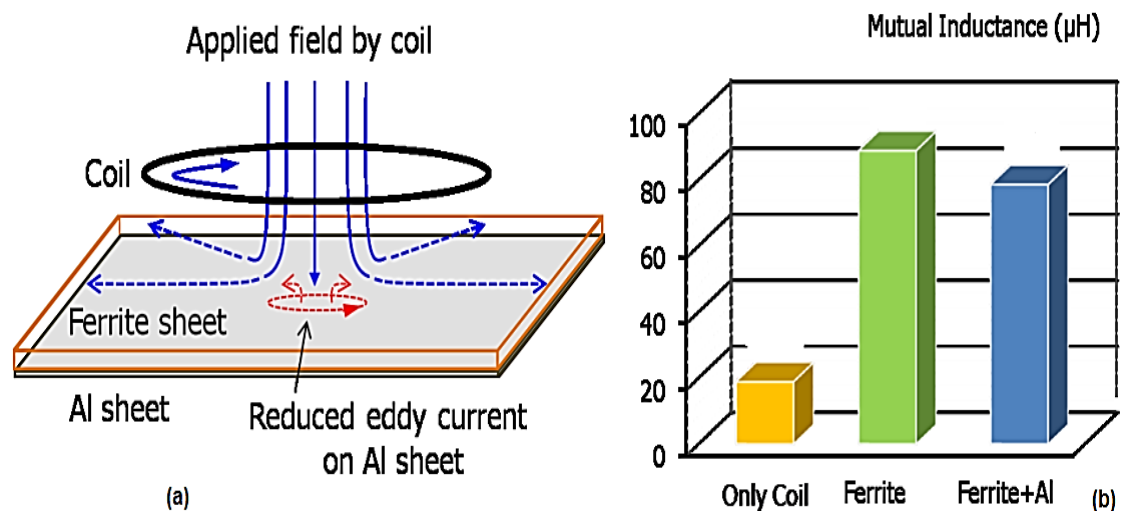


Figure 3.10: Effect of Aluminum as Shielding Material for Leaked Magnetic Field. (a) Magnetic Orientation in Aluminum Sheet. (b) Effect on Mutual Inductance between Coils [116]

The consequence of using conductive shields like aluminium is the slight reduction in the mutual inductance and invariably the magnetic coupling factor. Despite the reduction in performance, the shielding topology is widely used by researchers in their designs. Nevertheless, there are other non-magnetic but conductive shielding materials. The commonly used ones are copper, tin and zinc[174].

This research will include investigations into the viability and suitability of the above-mentioned conductive shielding materials.

3.6 Summary

In this section, a detailed analysis of common impact factors affecting the optimal performance of wireless power transfer systems was presented. The impact factors identified are an environmental factor, circuit designs, coil alignments and coil designs.

Elements of the environmental factor affecting the performance of WPT systems are humidity and temperature. It was noted that the system's efficiency reduces as the humidity level of the air increases while temperature affects the performance of the semiconductors in the power conversion subsystem. In the circuit design, parameters such as operating frequency, compensation scheme and converter design were identified as the key circuit parameters affecting the optimal design of the WPT system. It was noted that the higher the operating frequency the higher the efficiency but the lower the power transfer. For efficient and effective WPT system, the transmitter side is compensated so as to increase the active power by lowering the reactive power but with a trade-off of slight lowering of the apparent power (VA) of the power supply. Likewise, the receiver side is compensated to enhance the power transfer performance by transferring much of the active power to the load (battery).

With regards to coil alignments, it was noted that there are two main two types of misalignments- angular misalignment and horizontal misalignment. Research has shown that the lateral misalignment is more common than the angular misalignment for most EV application, but the latter has a greater effect on the PTE when compared to the former. It was also noted that an increase in the horizontal misalignment causes a reduction in the coupling coefficient, power output, power transfer efficiency and some rare cases bifurcation. From the comprehensive review of the literature, the major components of the coil designs identified are the shape of coil windings, size of coil models, the ferrite core and the shielding design topology. The relationship between the ratio of the transmitter coil and the airgap and the efficiency of the WPT system was identified. It was noted that the efficiency of more than 90% can be attained if the ratio of the airgap and coil diameter is less than 0.25. In essence, for an airgap of 200 mm, a coil-to-coil efficiency of 90% can be achieved with a minimum transmitter's diameter of 800 mm.

Coil design topology was identified as the most important impact factors affecting the performance of WPT systems. Evaluation of common ferrite-core model designs like circular coils, rectangular coils, flux-pipe coils and rectangular bipolar coils was presented. Flux pipe coils were identified as the model design with the best performance in terms of magnetic coupling and misalignment tolerance, but have a limitation in the amount of power that can be transferred across the airgap due to the double-flux problem.

The impact of coil size, ferrite material and shielding methodology on the coupling factor, power transfer efficiency and power transferred was discussed. It was reported that optimal efficiency of coil designs can be achieved if the transmitting coil diameter for a circular or rectangular coil is 4 times larger than the airgap. Similarly, it was noted that the addition of ferrite material to the coil design can increase the self-inductance and mutual inductance of the resonant coils by a factor of more than 4.

Finally, it was noted that every WPT coil design must be equipped with efficient shielding design to protect human and animals from electromagnetic radiation according to safety regulations. For most presented work of literature, the aluminium sheet was used as the preferred due to its lightweight and high conductivity. For reported works on the design of flux-pipe resonant coils, it was noted that a significant amount of eddy current losses was recorded for designs using aluminium sheets as an electromagnetic shield. As a result, this research includes an investigation into more low-loss shielding designs for WPT systems.

CHAPTER 4 **Finite Element Modelling and Design Validation**

4.1 Introduction

In order to accurately design and model an optimal wireless power system, there is a need to develop an efficient algorithm for the design process. For this research, the system-level engineering and simulation-based design were adopted due to its ability to create an optimal prototype using practical engineering specifications and simulations. The computer simulation is required to ascertain the potential performance of the proposed model. In this research, finite element modelling was used for the design and simulation of modelled designs. The initial and boundary conditions were carefully selected and published model designs were replicated and simulated based on those initial and boundary conditions. The simulation results were compared to the published experimental results and the accuracy of the proposed modelling methodology was evaluated.

4.2 The Overall Wireless Power Transfer System Design Specification

A typical WPT system for charging of electric vehicle can be designed in two ways- unidirectional WPT or bidirectional WPT. The unidirectional WPT systems allows electrical power flow in one direction only, basically from the grid or power source through the various power electronics components which is then wirelessly transferred from the primary coils to the secondary coils which is further conditioned electrically before finally being transferred to the battery pack of the electric vehicle through a charging process.

The unidirectional WPT system can be further modified to allow a two-way electrical power flow to create a bidirectional WPT system. The bidirectional WPT systems allow power to flow from the grid to the battery of the EV through the charging process while also having the capability to allow power flow from the battery pack to the electric grid through the discharging process. The capability of a WPT system to allow the bidirectional flow of electrical power is particularly useful in a smart grid network as the EV can be seen as a mobile distributed energy generation source.

The major component of wireless power transfer (WPT) technology for application with electric vehicles is the selection of an appropriate design model in order to achieve the optimum coil-to-coil efficiency of the system. An extensive literature review has been undertaken in that regard and the optimum choice of the strong magnetic resonant coupling WPT topology was deemed appropriate as part of the overall system configuration.

In order to achieve an overall optimum and efficient system design, modelling of the interaction between the components parts is required. In the development of optimized engineering systems, the use of the traditional method of design is inefficient. Thus an optimized system-level engineering simulation-based approach is proposed in order to design an optimized system.

The optimization of an electrical wireless power transfer (WPT) charging system mostly take into cognizance the efficiency of each of the component parts in order to establish the overall power transfer efficiency from the power supply through various components to the battery pack of the electric vehicle (EV). In particular, the primary and secondary coils must be optimally designed to ensure that power is transferred between the coils to maximise the charging/discharging process while limiting components and engineering cost.

The traditional design approach which mainly involves the production of many prototypes through an iterative process has been discovered to incur high costs with difficulty in the prediction of the design cycle time. Subsequently, most of the final designs of such traditional design approaches are not optimally designed and eventually lead to a further process of optimization. As a result, modelling was used in the design of the components.

In order to reduce the high cost of prototype production and unpredictable design cycles, system-level engineering and simulation-based design are proposed in this research. The design approach offers the advantage of designing an optimal model of an engineering system while reducing the development costs and a number of prototypes constructed in order to validate a design. The overall algorithm design is shown in Figure 4.1.

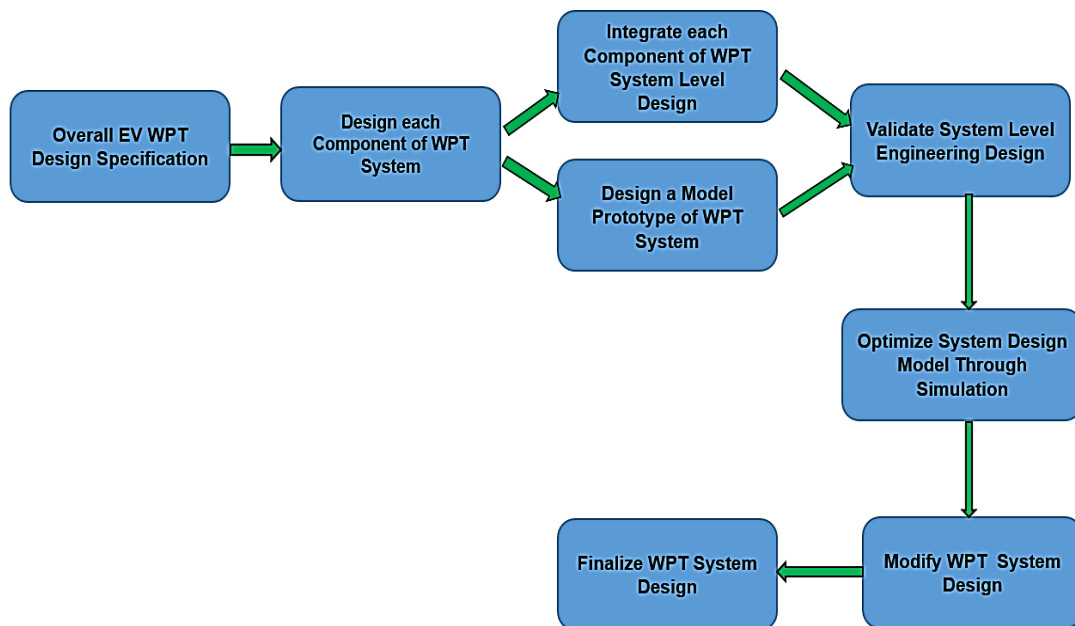


Figure 4.1: Overview of Optimized System-level Engineering and Simulation-based Design.

For the purpose of this research, only the aspect of the electromagnetic subcomponent of the WPT system was the design approach applied.

The approach includes the specification of the general structure of the WPT infrastructure from the transmitter coil to the receiver coil underneath the chassis of the EV. This aspect was already

considered in section 2.14.3 of this report. Each component and sub-component of the system was selected and designed based on the findings from the literature review and modelling outcomes. This aspect was extensively discussed in section 3.5 of this report. The findings from the literature review and modelling outcomes consist of common sizes of resonant coils, type of material used, the geometric shape of material for a specific model and the mathematical constants used in the finite modelling of particular engineering material.

The modelling design and simulation analysis were done using a numerical method known as finite element modelling (FEM) using Ansys Maxwell 3-D software. The simulation and analysis procedures of the software are highlighted in section 4.3.

Each of the specified components was integrated together to form a model, which can be validated using data obtained from experimental results or published research works. The typical component integration and validation using the Ansys Maxwell 3-D FEM software was implemented in section 4.4. Each component was modelled based published material properties from both research works and manufacturers' specifications. The validated system-level design together with the accompanying initial and boundary conditions is used to design and simulate the proposed ferrite-core WPT coil systems chosen in this research for optimization.

The initial optimization through computer modelling and simulations in order to create a robust and more efficient model was implemented in CHAPTER 5. Since there is no limit to the number of iterative process required to create an optimal model, series of coil design modifications was implemented in CHAPTER 6 in order to achieve a final high-power, higher efficient flux-pipe models for static and dynamic charging operations. An experimental prototype can then be developed based on the final optimized modelling specifications used in the simulation. This was not implemented in this research.

4.3 Finite Element Modelling and Analysis

Finite element modelling (FEM) is among the numerous numerical methods employed in the solution of field problems in engineering. Other numerical methods are Boundary Element Modelling (BEM), Finite Difference Modelling (FDM), Finite Volume Modelling (FVM) and Meshless Method (MM)[175], [176]. Though many engineering phenomena can be represented by "governing equations" and "boundary conditions," sometimes, it is quite difficult to generate a set of algebraic equations for an entire domain. Thus, in order to reduce an engineering problem into a set of algebraic equations, finite element modelling is employed[176]. This is accomplished by dividing the entire domain into a finite number of small and several elements. Consequently, a piecewise polynomial interpolation of the field quantity is implemented over an element and adjacent elements sharing the Degree of Freedom (DOF) at the nodes are connected in order to obtain each elements' algebraic equations. The resulting equations are now solved in order to obtain the unknown variable at the nodes[176].

FEM as a numerical method is employed because it can easily handle very complex geometry involving an infinite degree of freedom cutting across a wide range of engineering problems like dynamics, solid mechanics, fluids, heat problems, electrostatic problems, and electromagnetic field problems. In addition, FEM can be used to analyze and solve engineering problems containing indeterminate structures and complex loading of point loads, element loads and time or frequency-dependent loading[176].

Popular commercial software packages employing the FEM numerical methods are Abaqus, Adina, Ansys, and COSMOL. The commercial software implements the typical finite element analysis (FEA) procedure in three stages namely; the preprocessing, processing, and post-processing stages. The preprocessing stage is the stage where the finite element model is built. This involves the selection of the type of analysis, element type, and material properties.

The preprocessing stage is the stage where the nodes are made; elements are built by assigning the necessary connectivity of the nodes. Then the boundary conditions and loads are applied and the boundary value problems are solved. In this research, an Ansys software package known as Ansys Maxwell 3D Electromagnetic suite was used to solve the boundary value problem of the proposed MRC model coils.

In Ansys Maxwell, electromagnetic field problems are solved by solving the necessary “Maxwell’s equations in a finite region of space with appropriate boundary conditions and - when necessary- with user-specified initial conditions in order to obtain a solution with guaranteed uniqueness”[177]. The software is specially adapted to solve electric field, magnetostatic fields, eddy current fields, or transient fields’ problem. A mesher is employed to automatically mesh the solid model by assembling all the small elements also known as the tetrahedral in the 3D model[177]. The overall process chart is shown in Figure 4.2.

The initial mesh generation was obtained by constructing together the elements known as a tetrahedron (four-sided pyramid). A second-order quadratic polynomial (basis function) is then used to approximate the desired electromagnetic field in each of the elements.

After the tetrahedra are defined, the resulting finite elements are then placed in a large, sparse equation matrix given by:

$$[S][H] = [J] \quad 4.1$$

Where S is the area of the excitation terminals in m², H is the magnetic field intensity and J is the current density. The resulting matrix is then solved using standard matrix solution techniques like the Sparse Gaussian Elimination implemented in Maxwell 3D using a direct solver and the Incomplete Choleski Conjugate Gradient Method implemented in Maxwell 3D using an ICCG Iterative solver.

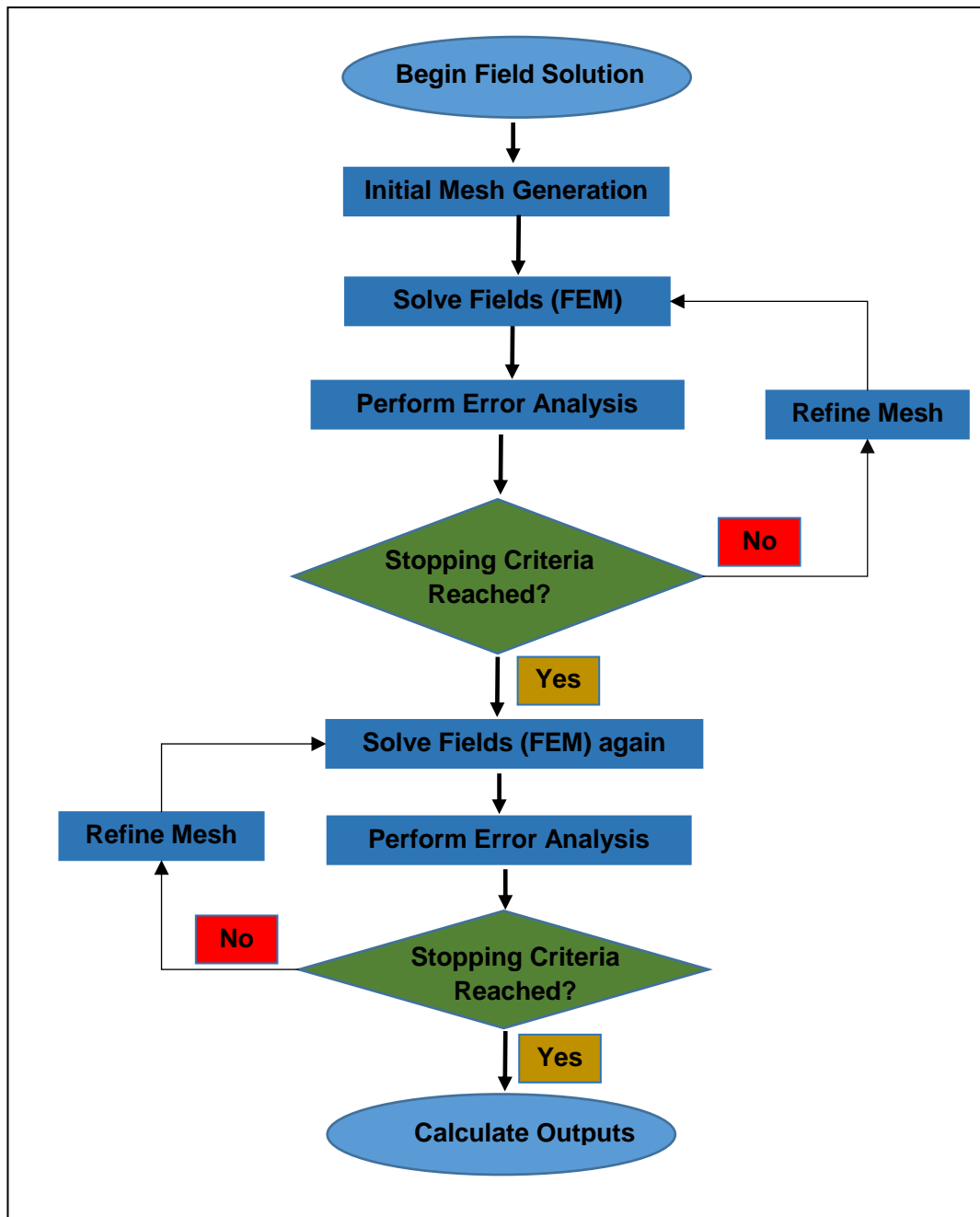


Figure 4.2: Flowchart Algorithm for Finite Element Modeling and Analysis in Ansys Maxwell 3D

There are forms of the fundamental defining equation for each solver that provides an error value for any of the fields solved. For example, in the simulation of magnetostatic problems, “the defining equation is the no-monopoles equation given by;

$$\nabla \cdot \vec{B} = 0 \quad 4.2$$

However, for practical purpose, when the field solution was returned to equation 4.2, an error term is obtained given by:

$$\nabla \cdot \vec{B} = Error \quad 4.3$$

Subsequently, the error produced by the error terms is then computed for the entire volume, which is then compared with the calculated total energy, and a percentage number for the error energy is obtained by:

$$\% Error = \frac{Energy Error}{Total Energy} \times 100\% \quad 4.4$$

The percentage error number for the energy together with total energy is returned for each adaptive pass, which is then used to measure the convergence of the solution, which determines the stopping criteria.

If the acceptable prescribed percentage is not met, mesh refinement is undertaken until a percentage value equal to or less than the acceptable prescribed percentage is attained. For the proposed model design, the prescribed percentage for all simulations is set at 5%. Despite the numerous advantages of the FEM, it has some limitations which include the presence of inherent errors during computation, the ability to only obtain approximate solutions and ease of mistakes by the users[176]. In order to reduce errors arising from the limitations, a second criteria test is implemented to guarantee the true convergence of the solution and the acceptable prescribed percentage value truly met and confirmed.

The finite element analysis (FEA) of proposed MRC coil models will be in three different part- Magnetostatic analysis, Eddy current analysis and Circuit analysis.

4.3.1 FEM Magnetostatic Analysis

The magnetostatic analysis is one of the important analysis performed in Ansys Maxwell. The analysis is performed after the selection of the Magnetostatic solution type in the Ansys Maxwell graphical user interface. The magnetic analysis can be applied on permanent magnets, motors, solenoids, inductors and stray field calculations[177].

The magnetostatic analysis is usually used to compute static (DC) magnetic fields under steady-state conditions for objects in a stationary position. The magnetic fields sources can be permanent magnets, DC currents in conductors or static magnetic fields represented by external boundary conditions. This research will employ the use of static fields represented by boundary conditions external to the model. The flowchart for the solution process is illustrated in Figure 4.3.

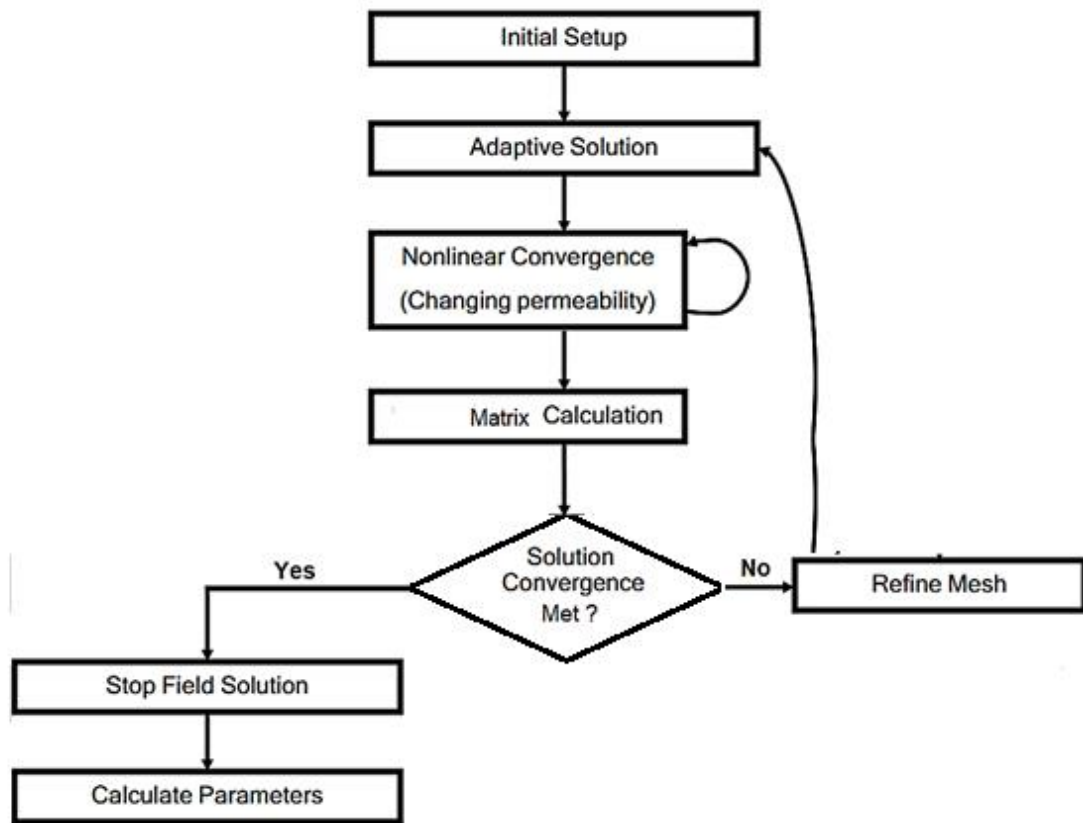


Figure 4.3: Magnetostatic Solution Process for Ansys Modelling Software[177].

Once the problem statement has been defined properly and the solution process initiated, Maxwell 3D will start an automated process that takes over and follow through numerous stages of the solution process as illustrated in Figure 4.3.

In order to arrive at an accurate solution, the solution convergence is evaluated twice or else the mesh is refined and taken back to the adaptive solution process again. When the solution criteria are met, the field solution is stopped and the required parameters are calculated.

The matrix calculation is normally based on the solved magnetic field (H). Consequently, the Magnetic flux (B) and current density (J) are automatically calculated. When the field solution is stopped, derived quantities from the magnetic field solutions like inductances, coupling factor and magnetic flux density are calculated as the required parameters.

In this research, the required parameters to be evaluated during the magnetostatic analysis are the magnetic flux density, self-inductance, mutual inductance and the coupling factor.

4.3.2 FEM Eddy Current Analysis

The eddy current analysis is another the important analysis performed in Ansys Maxwell. The analysis is performed after the selection of the Eddy Current solution type in the Ansys Maxwell graphical user interface. The eddy current analysis can be applied on permanent magnets, motors, solenoids, inductors and stray field calculations[177].

The eddy current analysis is usually used to compute steady-state, time-varying (AC) magnetic fields at a given frequency (which is normally the domain solution). The analysis is normally done in steady-state conditions for objects in a stationary position. The magnetic fields sources can be sinusoidal AC current (peak) in conductors or time-varying magnetic fields represented by external boundary conditions. This research will employ the use of time-varying magnetic fields represented by boundary conditions external to the model. The flowchart for the solution process is illustrated in Figure 4.4.

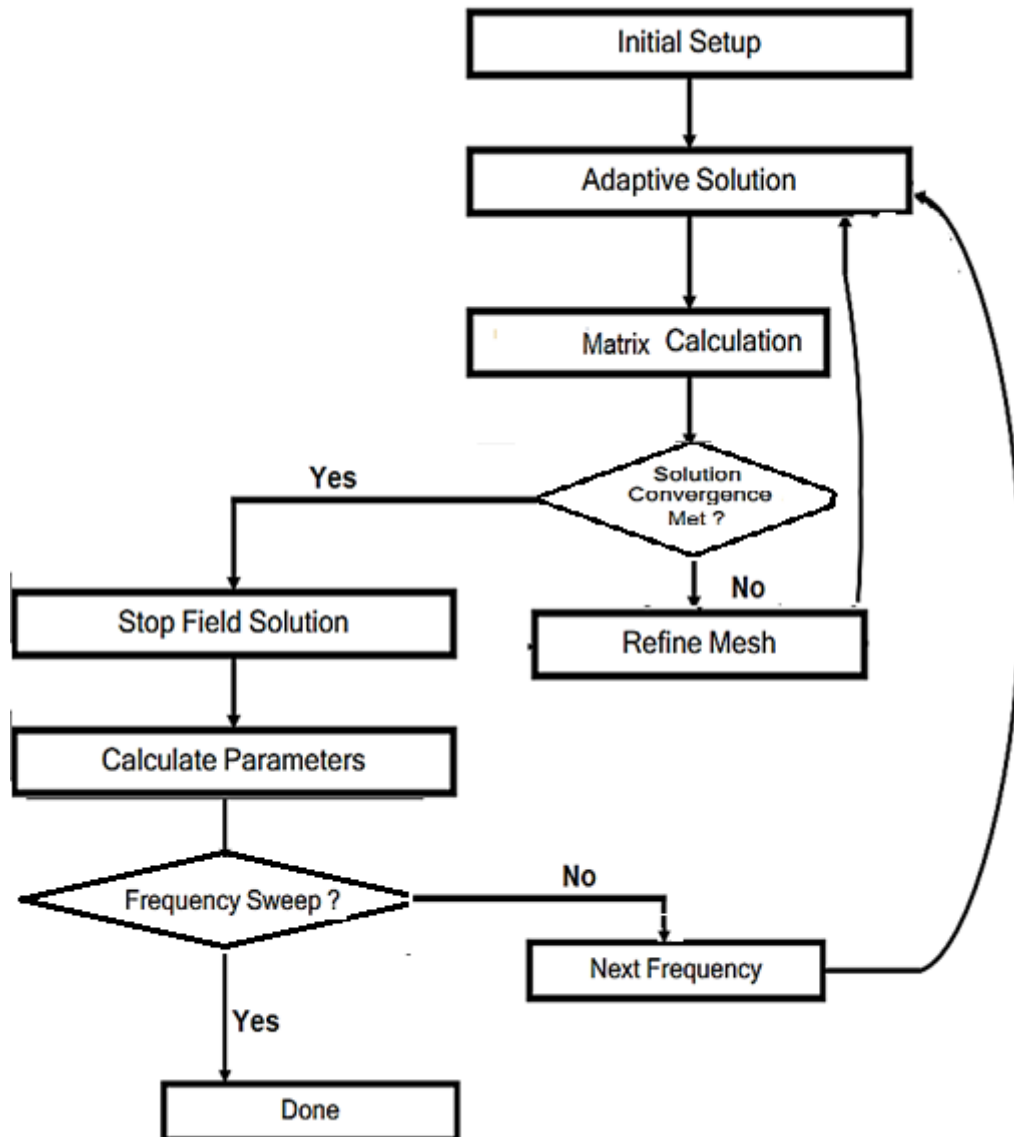


Figure 4.4: Eddy Current Solution Process for Ansys Modelling Software [[177]]

Once the problem statement has been defined properly and the solution process initiated, Maxwell 3D will start an automated process that takes over and follow through numerous stages of the solution process as illustrated in Figure 4.4.

In order to arrive at an accurate solution, the solution convergence is evaluated twice or else the mesh is refined and taken back to the adaptive solution process again. When the solution criteria are met, the field solution is stopped and the required parameters are calculated.

The matrix calculation is normally based on the solved magnetic field (H). Consequently, the Magnetic flux (B) and current density (J) are automatically calculated. When the field solution is stopped, derived quantities from the magnetic field solutions like all the parameters calculated for the magnetostatic analysis with the addition of the eddy current losses, core losses, reactance and impedance are calculated as the required parameters.

The frequency sweep is optional in the solution process when only the eddy current losses, core losses, reactance, and impedance of the model is required at a particular frequency. However, it is mandatory if the model will be used to evaluate the coil-to-coil efficiency, power input, power output, input voltage, voltage output and power factor of the model.

In this research, the required parameters to be evaluated during the eddy current analysis are the ohmic losses, eddy current losses, core losses, coupling factor, self-inductance, reactance, and impedance of the coils.

4.3.3 Mathematical Analysis of Equivalent Circuit Model

The equivalent circuit analysis of the resonant WPT coil models involves the representation of the self-inductance of the primary and secondary coils with the mutual inductance between the coils. The leakage inductance is represented with an equivalent inductance which is the difference between the self-inductance and mutual inductance for the individual transmitter and receiver coils of the system as illustrated in Figure 4.5 and Figure 4.6. From the equivalent circuit representation, a mathematical expression of the input power, output power, efficiency and optimum load resistance is evaluated.

Two compensation topologies will be employed for performance analysis in this section. The analysis will cover the S-S compensation topology[72] and the S-P compensation topology[119] as they are the most common. The S-S compensation topology is suitable for bidirectional wireless power transfer due to the symmetry of the compensation capacitor with respect to the load and supply voltage. On the other hand, the S-P compensation topology can only be employed for unidirectional wireless power transfer due to the difference in the connection of the compensation capacitors. For example, if the transmitter and receiver coils are reversed for an S-P topology, the compensation scheme becomes P-S topology with different performance metrics.

4.3.3.1 Mathematical Analysis of the S-S Compensation Topology

The mathematical analysis can be done by analysing the equivalent circuit representation of the ferrite-core MRC model. The equivalent circuit representation for the series-series topology is shown in Figure 4.5.

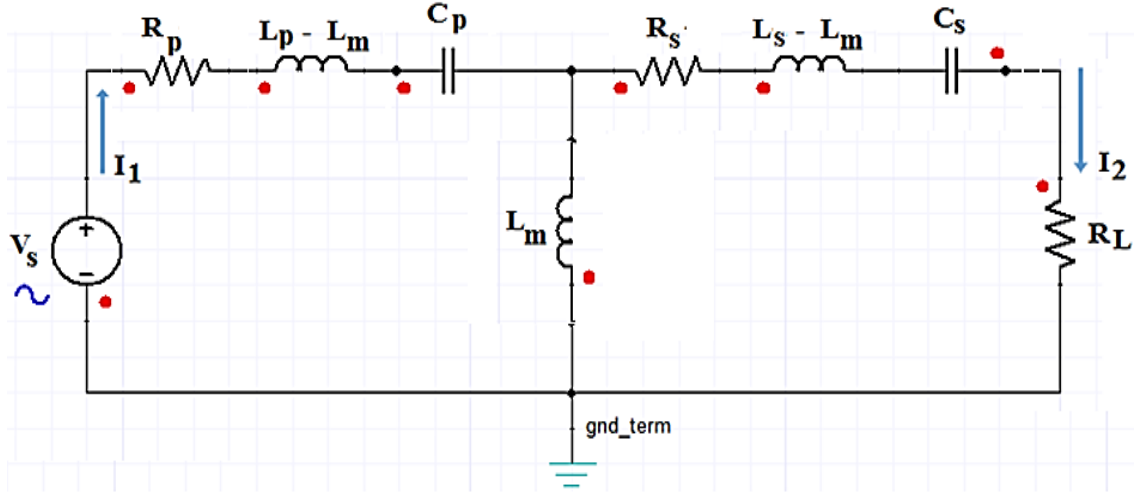


Figure 4.5: Equivalent Circuit for an S-S Compensation Topology

$R_p(\Omega)$, $R_s(\Omega)$ and $R_L(\Omega)$ are the intrinsic resistance of the primary coil and intrinsic resistance of the secondary coil and the load resistance respectively. $L_p(H)$, $L_s(H)$ and $L_m(H)$ are the primary self-inductance, secondary self-inductance and mutual inductance respectively. $V_s(V)$, $C_p(F)$ and $C_s(F)$ are the source voltage, primary compensating capacitance and secondary compensation capacitance respectively.

The primary inductive reactance, secondary inductive reactance and mutual inductive reactance in the circuit are given mathematically as:

$$X_{lp} = \omega L_p, \quad X_{ls} = \omega L_s, \quad X_m = \omega L_m \quad 4.5$$

The parameter ω is the angular resonant frequency of the WPT system model measured in rad/s and mathematically represented as $\omega = 2\pi f$, where f is the resonant frequency measured in Hertz (Hz)

Similarly, the primary capacitive reactance and secondary reactance in the circuit are given mathematically as:

$$X_{cp} = \frac{1}{\omega C_p}, \quad X_{cs} = \frac{1}{\omega C_s} \quad 4.6$$

The total impedance Z_{Total} in the circuit and is given mathematically as:

$$Z_{Total} = R_p + j(X_{lp} - X_{cp}) - jX_m + jX_m // (R_s + R_L + j(X_{ls} - X_{cs}) - jX_m) \quad 4.7$$

Since the circuit will be operating at a resonance frequency F_{res} , the LC components will cancel out their reactance and Z_{Total} is given by:

$$Z_{Total} = R_p - jX_m + jX_m // (R_s + R_L - jX_m) \quad 4.8$$

Equation 4.8 is further simplified as:

$$Z_{Total} = R_p - jX_m + \frac{jX_m(R_s + R_L - jX_m)}{jX_m + (R_s + R_L - jX_m)} \quad 4.9$$

$$Z_{Total} = R_p - jX_m + \frac{jX_m(R_s + R_L)}{(R_s + R_L)} + \frac{X_m^2}{(R_s + R_L)}$$

$$Z_{Total} = R_p + \frac{X_m^2}{(R_s + R_L)}$$

$$Z_{Total} = \frac{R_p(R_s + R_L) + X_m^2}{(R_s + R_L)} \quad 4.10$$

The input current I_1 is given mathematically as:

$$I_1 = \frac{V_s}{Z_{Total}} = \frac{V_s(R_s + R_L)}{R_p(R_s + R_L) + X_m^2} \quad 4.11$$

Similarly, the output current I_2 can be calculated using current divider theorem:

$$I_2 = \frac{X_m}{(X_m + R_s + R_L - X_m)} I_1$$

$$I_2 = \frac{X_m}{(R_s + R_L)} \frac{V_s(R_s + R_L)}{R_p(R_s + R_L) + X_m^2}$$

$$I_2 = \frac{X_m \cdot V_s}{R_p(R_s + R_L) + X_m^2} \quad 4.12$$

The power input is calculated as:

$$P_{in} = V_s I_1 = \frac{V_s^2(R_s + R_L)}{R_p(R_s + R_L) + X_m^2} \quad 4.13$$

Similarly, the power output can be obtained as below:

$$P_{out} = I_2^2 R_L = \frac{V_s^2 \cdot X_m^2 \cdot R_L}{((R_p R_s + R_p R_L) + X_m^2)^2} \quad 4.14$$

The efficiency of the system can be represented by the following equation:

$$\eta = \frac{P_{out}}{P_{in}} = \frac{X_m^2 \cdot R_L}{(R_s + R_L)((R_p R_s + R_p R_L) + X_m^2)} \quad 4.15$$

Similarly, the optimal efficiency for the maximum load resistance can be obtained by:

$$R_L = 1 + \sqrt{\frac{X_m^2}{(R_p + R_s)}} \quad 4.16$$

Substituting the value of R_L into equation 4.15 gives the maximum efficiency as:

$$\eta_{max} = \frac{X_m^2}{\sqrt{(R_p R_s + X_m^2)} \sqrt{(R_p R_s)}} \quad 4.17$$

4.3.3.2 Mathematical Analysis of the S-P Compensation Topology

The mathematical analysis can be done by analysing the equivalent circuit representation of the ferrite-core MRC model in an S-P compensation configuration. The equivalent circuit representation for the series-parallel topology is shown in Figure 4.6.

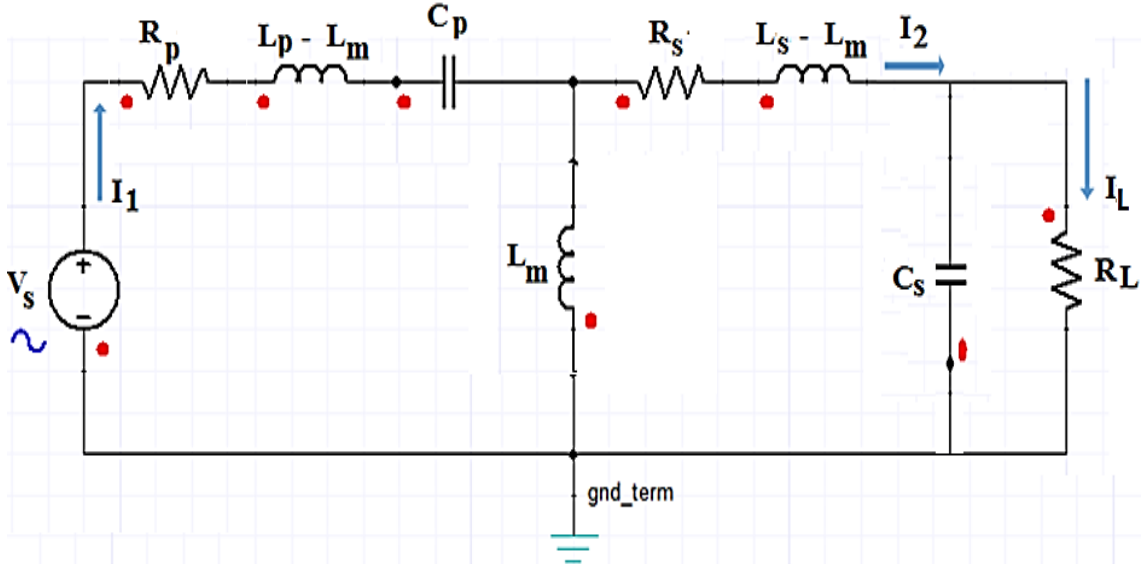


Figure 4.6: Equivalent Circuit for an S-P Compensation Topology

$R_p(\Omega)$, $R_s(\Omega)$ and $R_L(\Omega)$ are the intrinsic resistance of the primary and intrinsic resistance of the secondary coil and the load resistance respectively. $L_p(H)$, $L_s(H)$ and $L_m(H)$ are the primary self-

inductance, secondary self-inductance and mutual inductance respectively. $V_s(V)$, $C_p(F)$ and $C_s(F)$ are the source voltage, primary compensating capacitance and secondary compensation capacitance respectively.

For easy analysis of the circuit, the primary values of each circuit components are converted into the secondary equivalents using the transformer turn ratio mathematically represented by $a = N_1/N_2$ [119]. Since the value of a is 1 since the turn ratio used in this research will be the same for both the primary and secondary coils. Thus, the analysis will be taken from the secondary side.

The primary inductive reactance, secondary inductive reactance and mutual inductive reactance in the circuit are given mathematically as:

$$X_{lp} = \omega L_p, \quad X_{ls} = \omega L_s, \quad X_m = \omega L_m \quad 4.18$$

The parameter ω is the angular resonant frequency of the WPT system model measured in rad/s and mathematically represented as $\omega = 2\pi f$, where f is the resonant frequency measured in Hertz (Hz)

Similarly, the primary capacitive reactance and secondary reactance in the circuit is given mathematically as[119]:

$$X_{cp} = \frac{1}{\omega C_p} = \frac{X_m (X_{ls} - X_m)}{X_m + (X_{ls} - X_m)} + X_{lp} - X_m \quad 4.19$$

$$X_{cp} = \frac{1}{\omega C_p} = \frac{X_{ls}X_m - X_m^2 + X_{ls}X_{lp} - X_{ls}X_m}{X_{ls}} \quad 4.20$$

$$X_{cp} = \frac{1}{\omega C_p} = \frac{X_{ls}X_{lp} - X_m^2}{X_{ls}} + X_m \quad 4.21$$

The parameter ω is the angular resonant frequency of the WPT system model measured in rad/s and mathematically represented as $\omega = 2\pi f$, where f is the resonant frequency measured in Hertz (Hz)

The secondary reactance in the circuit is given mathematically as:

$$X_{cs} = \frac{1}{\omega C_s} = (X_{ls} - X_m) + X_m = X_{ls} \quad 4.22$$

Referring to the primary side, the input voltage V_{in} is given by:

$$V_{in} = \frac{X_m}{X_m + (X_{ls} - X_m)} V_2 = \frac{X_m}{X_{ls}} V_L \quad 4.23$$

Similarly, input current I_{in} is given by:

$$I_{in} = \frac{X_m + (X_{ls} - X_m)}{X_m} I_L = \frac{X_{ls}}{X_m} I_L \quad 4.24$$

Similarly, the power output can be obtained as below:

$$P_{out} = I_2^2 R_L \quad 4.25$$

The power input is the sum of the power output and the losses in the primary and secondary windings given by:

$$P_{in} = I_2^2 I_L + I_1^2 R_p + I_2^2 R_s \quad 4.26$$

The efficiency of the system can be represented by the following equation:

$$\eta = \frac{P_{out}}{P_{in}} = \frac{I_2^2 R_L}{I_2^2 I_L + I_1^2 R_p + I_2^2 R_s} \quad 4.27$$

Thus, the efficiency is approximately given by[119]:

$$\eta = \frac{P_{out}}{P_{in}} = \frac{R_L}{R_L + \frac{R_p X_{ls}}{X_m} + R_2 \left\{ \left(1 + \left(\frac{R_L}{X_{cs}} \right) \right)^2 \right\}} \quad 4.28$$

Similarly, the optimal efficiency for the maximum load resistance can be obtained by:

$$R_L = X_{cs} \cdot \sqrt{\frac{X_{ls}}{X_m} \cdot \frac{R_p}{R_s} + 1} \quad 4.29$$

Substituting the value of R_L into equation 4.28 gives the maximum efficiency as[119]:

$$\eta_{max} = \frac{1}{1 + \frac{2R_s}{X_{cs}} \sqrt{\frac{X_{ls}}{X_m} \cdot \frac{R_p}{R_s} + 1}} \quad 4.30$$

Maximum efficiency can be achieved for the WPT model if these appropriate characteristics are adopted for an output power equal to the rated power[119].

4.3.3.3 Mathematically Analysis of Efficiency Based on Quality Factor (Q)

The quality factor (Q) of a resonant coil gives an indication of the level of its inductive properties[43]. The larger the Q factor, the larger the ability of the coil to produce a large magnetic field.

It has been noted by Covic, G. A et al[13] that the amount of power transferred and efficiency of a coil system can be determined by the coils' quality factor and can be represented by the following equations[13]:

$$P_{out} = jX_m I_1 \cdot I_1 \cdot \frac{L_m^2}{L_s L_p} Q_s \quad 4.31$$

$$P_{out} = V_{in} \cdot I_1 \cdot k^2 \cdot Q_s \quad 4.32$$

Similarly, Takanashi, H. et al [143] developed and proposed an equation relating the maximum efficiency with the quality factor and the coupling coefficient and it is given by:

$$\eta_{max} = \frac{1}{1 + \frac{2}{k\sqrt{Q_p \cdot Q_s}}} \quad 4.33$$

$$\eta_{max} = \frac{1}{1 + \frac{2}{k\sqrt{Q_{ps}}}} \quad 4.34$$

Where Q_{ps} is the product of the primary quality factor Q_p and the secondary factor Q_s . Equation 4.34 is very useful in determining the optimum resonant frequency for a given maximum efficiency.

4.3.4 Circuit Analysis of Reduced-Order Model (ROM) of WPT Coils

The circuit analysis of the FEM model involves the performance analysis of the model in terms of power output, power input, and coil-to-coil-efficiency of the coils. The circuit performance is evaluated at resonance with a particular compensation scheme. The analysis can be evaluated in two ways: the mathematical analysis and the Reduced Order Model (ROM) analysis.

This approach involves the transformation of the evaluated 3-D finite element model into a reduced order model and imported into a circuit simulation environment known as Simplorer®. The transformation is illustrated in Figure 4.7. The 3-D model problem is solved by performing a parametric sweep of resonant frequencies and evaluated parameters like coupling coefficient, self-inductance and reactance of the coil mode are stored within the model itself based on the physical parameter specifications like airgap, coil turns, size of modelling materials, types of materials used and appropriated initial and boundary conditions employed.

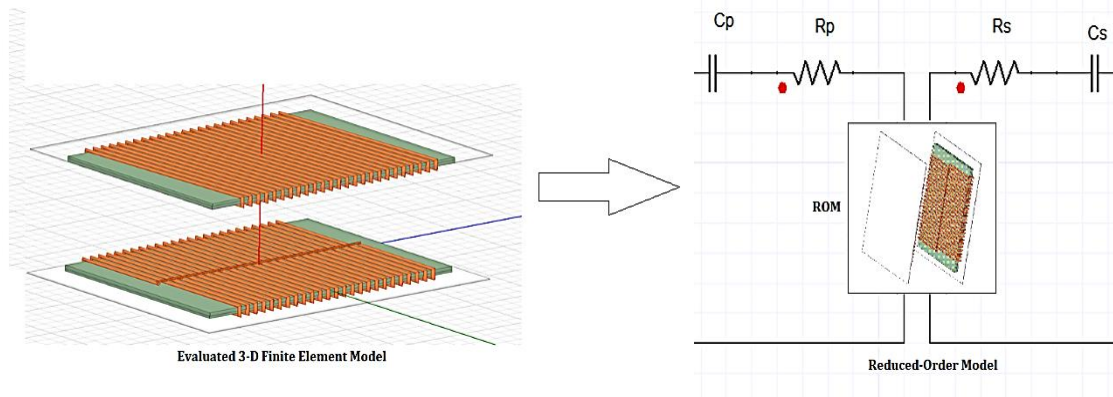


Figure 4.7: Implementation of the Reduced Order Model for Circuit Analysis

The evaluated values of the coupling coefficient, resistance and inductance are normally imported into the circuit environment in a matrix form as illustrated in equation 4.35.

$$L_X = \begin{bmatrix} L_p & L_m \\ L_m & L_s \end{bmatrix}, \quad k_X = \begin{bmatrix} 1 & k_{sp} \\ k_{ps} & 1 \end{bmatrix}, \quad R_X = \begin{bmatrix} R_p & R_m \\ R_m & R_s \end{bmatrix} \quad 4.35$$

L_X , k_X and R_X are the imported matrices of the inductances, coupling coefficient and A.C. resistance of the evaluated WPT coil model. The values of k_{ps} and k_{sp} are the same because of the symmetry of the primary and secondary self-inductance of the coils. R_m is the equivalent mutual resistance between the primary and secondary coils. The values of each individual matrix parameters was used for the calculation of the appropriate values of the primary and secondary compensating capacitance.

Two compensation topologies will be analysed in this section as they are the most common. The analysis will cover the S-S compensation topology[72] and the S-P compensation topology[119]. The two types of analysis are further explained in the next two sections.

4.3.4.1 FEM Analysis of the S-S Compensation Topology

The finite element modelling analysis in Ansys Maxwell 3D for series-series compensation topology can be done by importing the reduced-order model (ROM) of the ferrite-core MRC model into circuit simulation environment known as Ansys Simplorer®. The ROM imported into the circuit environment is the already solved model from the eddy current analysis. The equivalent circuit representation for the series-series topology in the Simplorer® simulation environment is shown in Figure 4.8. The ROM is shown in the square box with the brown and green coloured item. The example is a circular coil model imported into the Simplorer® circuit simulation environment.

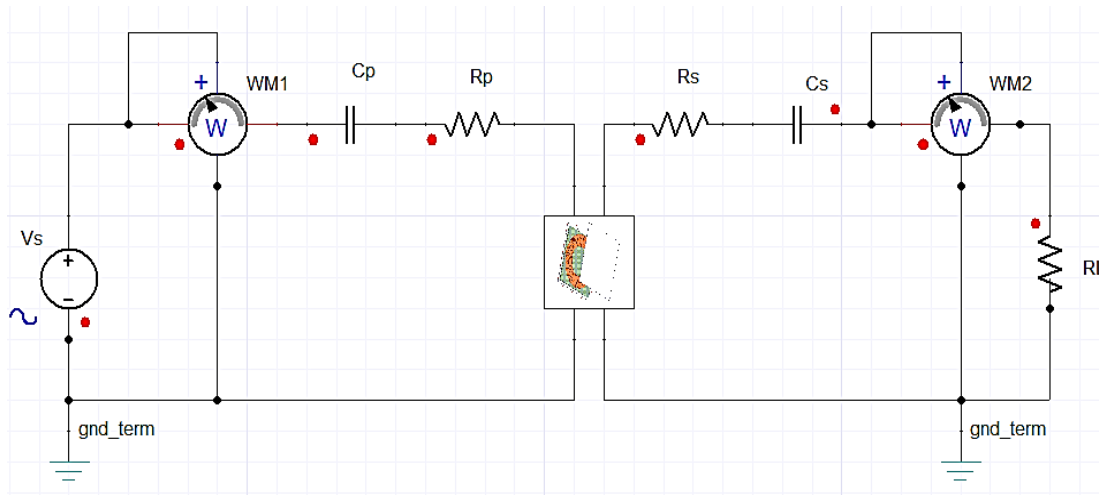


Figure 4.8: Simplorer@ Maxwell ROM Design Implementation for S-S Compensation Topology

The ROM imported into the circuit simulation environment carries along with the evaluated parameters like the self-inductance, mutual inductance, coupling factor and model conditions like airgap and misalignment.

For an accurate generation of result from the circuit simulation, the appropriate parameters like the source voltages V_s , intrinsic resistances and the appropriate capacitance for resonance are specified.

$R_p(\Omega)$, $R_s(\Omega)$, $R_L(\Omega)$ are the intrinsic resistance of the primary coil, intrinsic resistance of the secondary coil and the load resistance respectively. The values of R_p and R_s are normally evaluated during the eddy current analysis and are required to be manually specified before the circuit simulation to avoid runtime errors.

$C_p(F)$ and $C_s(F)$ are the primary compensation capacitance and secondary compensation capacitance respectively. They are mostly evaluated as a function of the self-inductance of the primary coil $L_p(H)$ and self-inductance of the secondary coil $L_s(H)$ respectively.

The primary capacitance and secondary capacitance in the circuit are given mathematically as:

$$C_p = \frac{1}{\omega_o^2(1 - k^2)L_p}, \quad C_s = \frac{1}{\omega_o^2(1 - k^2)L_s} \quad 4.36$$

The parameter ω_o is the angular resonant frequency of the WPT system model measured in rad/s and mathematically represented as $\omega_o = 2\pi f_o$, where f_o is the resonant frequency measured in Hertz (Hz). The parameter with the label WM1 and WM2 are the wattmeter for the primary side and secondary side respectively. They are both used to evaluate at both sides, the voltage input, voltage output, input current, output current, input power and output power of the system. The coil-to-coil efficiency is then calculated based on the input and output power.

4.3.4.2 FEM Analysis of the S-P Compensation Topology

The finite element modelling analysis in Ansys Maxwell 3D for series-parallel compensation topology can be done by importing the reduced-order model (ROM) of the ferrite-core MRC model into circuit simulation environment just as the case with the S-S compensation topology. The ROM imported into the circuit environment is the already-solved model from the eddy current analysis. The equivalent circuit representation for the parallel-series topology in the Simplorer® simulation environment is shown in Figure 4.9. The ROM is shown in the square box with the brown and green coloured item. The example is a circular coil model imported into the Simplorer® circuit simulation environment.

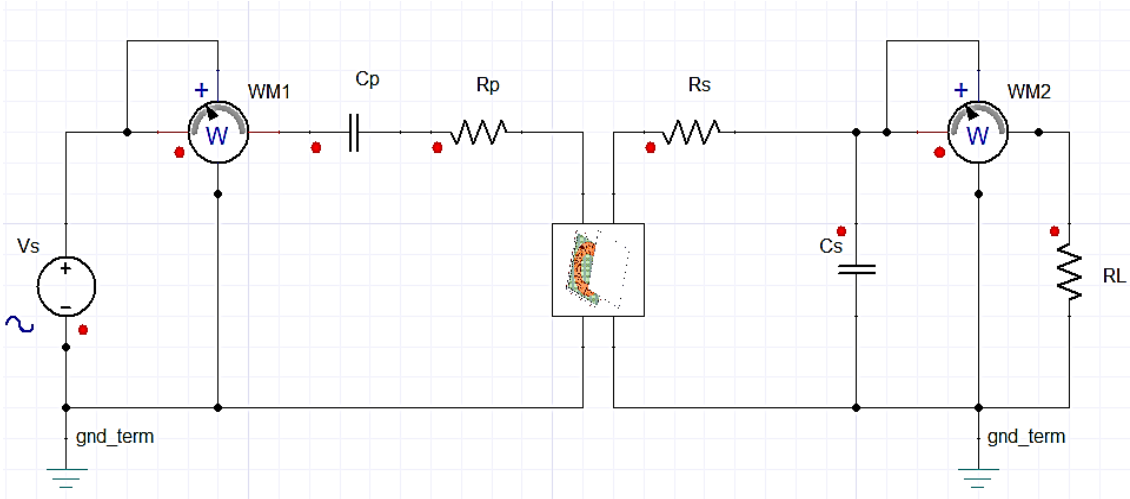


Figure 4.9: Simplorer® Maxwell ROM Design Implementation for S-P Compensation Topology

The ROM imported into the circuit simulation environment carries along with the evaluated parameters like the self-inductance, mutual inductance, coupling factor and model conditions like airgap and misalignment.

For an accurate generation of result from the circuit simulation, the appropriate parameters like the source voltages V_s , intrinsic resistances and the appropriate capacitance for resonance are specified.

$R_p(\Omega)$, $R_s(\Omega)$, $R_L(\Omega)$ are the intrinsic resistance of the primary coil, intrinsic resistance of the secondary coil and the load resistance respectively. The values of R_p and R_s are normally evaluated during the eddy current analysis and are required to be manually specified before the circuit simulation to avoid runtime errors.

$C_p(F)$ and $C_s(F)$ are the primary compensation capacitance and secondary compensation capacitance respectively. They are mostly evaluated as a function of the self-inductance of the primary coil $L_p(H)$ and self-inductance of the secondary coil $L_s(H)$ respectively.

The primary capacitance and secondary capacitance in the circuit are given mathematically as:

$$C_p = \frac{1}{\omega_o^2(1 - k^2)L_p}, \quad C_s = \frac{1}{\omega_o^2 L_s} \quad 4.37$$

The parameter k is the coupling factor between the primary coil and the secondary coil while ω_o is the angular resonant frequency of the WPT system model measured in rad/s and mathematically represented as $\omega_o = 2\pi f_o$, where f_o is the resonant frequency measured in Hertz (Hz). The parameter with the label WM1 and WM2 are the wattmeter for the primary side and secondary side respectively. They are both used to evaluate at both sides, the voltage input, voltage output, input current, output current, input power and output power of the system. The coil-to-coil efficiency is then calculated based on the input and output power.

4.4 Specification of Initial and Boundary Conditions.

In order to accurately design the optimal inductive coil for wireless power transfer for an electric vehicle, there is a need to investigate the model designs of existing works of literature. The essence is to accurately specify the necessary boundary conditions and the distance between adjacent coils turns based on the number of coils turns in order to get result values close to the experimental results. The boundary conditions give the user a level of control on the characteristics of faces, planes or interfaces between objects in a particular system[177].

A test case for such validation is the system approach work of Lempidis et al[11] on Wired and Wireless charging of electric vehicles.

From his work of literature[11] on the coil system with two circular coils, it was noted that the performance of the circular coils can be calculated analytically based on a set of equations. But, the mathematical equations for the behaviour and performance of other coil model systems are quite complex and very difficult to be calculated analytically. An easy approach is to use the Finite Element Modelling (FEM) method which can be numerically simulated and then validated with real inductive coils. The research work proposed by Lempidis et al[11] consists of three coil system designs which were validated by experiments. The three coil system designs are planar coil design, double D coil design and a combination of double D and solenoid coil design.

4.4.1 Planar Coil Design Systems.

The coil model employs the simplest system design with a pair of ring coils in the shape of an octagon. The octagon-shaped ring coils were modelled with a maximum diameter of 58cm separated by an airgap of 200mm. The physical dimensions of the octagon-shaped coil design indicating the number of turns and the cross-sectional diameter of the copper wire used are presented in Table 4.1.

Table 4.1: Physical Parameter Specification for the Planar Coil Designs.

| Table 4.2: Physical Parameter | Measurement Value |
|------------------------------------|-------------------|
| Diameter of Coil (D) | 58cm |
| Cross-section Diameter of Coil (d) | 0.3cm |
| Airgap between Coils (Z) | 20cm |
| Number of Coil turns (N) | 8 |

Based on the physical dimension presented in the proposed research work, the coil system was reproduced and designed in this research work using the ANSYS Electromagnetics software tool. The proposed planar coil design using ANSYS simulation software and the experimental design from the work of literature is shown in Figure 4.10

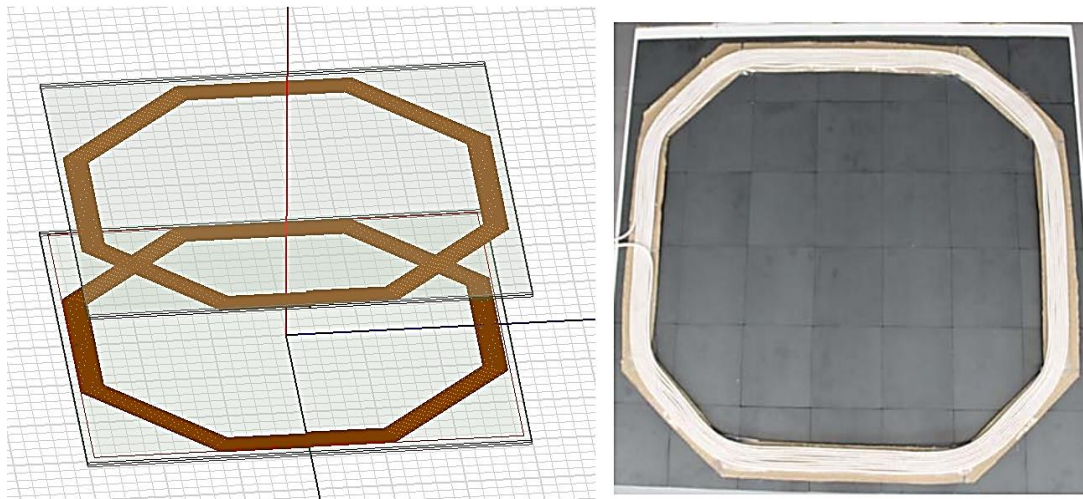


Figure 4.10: Proposed FEM Simulation Design and Design of Planar Resonant Coils Taken from Literature [11]

One of the biggest challenges is the specification of the optimum boundary condition in order to get a value close to the experimental results. In addition, the appropriate specification of the distance between adjacent coil turns is highly essential in order to arrive at an accurate solution.

In the reproduction of the published model design, an optimal value for the change of radius between adjacent coils was gotten as 1.5 times the cross-section diameter of the coils. For the case of model design, it is calculated mathematically as $1.5 \times 0.3\text{cm} = 4.5\text{cm}$.

Based on the specified distance between adjacent coil turns, a parametric sweep of boundary volume was carried out in order to determine the optimum offset value of the boundary condition of the region that gives the minimum error difference with respect to the journal experimental results. The simulation results (Simulation) in this research, journal experimental results (Practical) and result variations (Error Difference) based on the parametric sweep of the boundary region offset specifications from 0 to 50 is shown in Table 4.3

Table 4.3: Comparison of FEM Simulated Result of Planar Resonant Coil Design with Experimental Result Taken from Literature.

| Parameters | | Boundary Region Offset | | | | |
|---------------------------|------------------------------|------------------------|---------|--------|--------|--------|
| | | 10 | 20 | 30 | 40 | 50 |
| Primary Self-inductance | Practical (μH) | 133.27 | 133.27 | 133.27 | 133.27 | 133.27 |
| | Simulation (μH) | 129.11 | 135.02 | 138.25 | 139.23 | 140.67 |
| | Error Difference | -3.2 % | 1.3 % | 3.6 % | 4.3 % | 5.3 % |
| Secondary Self-inductance | Practical (μH) | 131.33 | 131.33 | 131.33 | 131.33 | 131.33 |
| | Simulation (μH) | 129.03 | 135.20 | 138.90 | 139.48 | 140.68 |
| | Error Difference | -1.8 % | 2.9 % | 5.5 % | 5.8 % | 6.6 % |
| Mutual Self-inductance | Practical (μH) | 23.65 | 23.65 | 23.65 | 23.65 | 23.65 |
| | Simulation (μH) | 17.15 | 21.11 | 23.25 | 24.45 | 25.39 |
| | Error Difference | -37.9 % | 12.0 % | -1.7 % | 3.3 % | 6.9 % |
| Coupling Coefficient | Practical | 0.18 | 0.18 | 0.18 | 0.18 | 0.18 |
| | Simulation | 0.133 | 0.156 | 0.168 | 0.175 | 0.180 |
| | Error Difference | -35.4 % | -15.2 % | -7.3 % | -2.6 % | 0.3 % |

From the result obtained in Table 4.3, it is observed that simulated results at the region offset of 40 and 50 gives the closest values of electrical parameters to the journal experimental results.

At a region offset of 40, the maximum error obtained was 5.8% and the minimum error obtained was 2.6%. For the region offset of 50, the maximum error obtained was 6.9 % while the minimum error obtained was 0.3%. The optimum offset region was chosen based on the region offset that gave the minimum value of maximum error. In this first case, the offset region of 40 was chosen because it has a maximum error value of 5.8% which is lower than 6.9% maximum error obtained using an offset value of 50.

4.4.2 Double D Coil Design Systems.

The coil model employs the simple system design using a pair of D-shaped coils for both the transmitter and receiver. The D-shaped ring coils were modelled with a maximum diameter of 58cm separated by an airgap of 200mm. The physical dimensions of the D-shaped coil design indicating the number of turns and the cross-sectional diameter of the copper wire used are presented in Table 4.4.

Table 4.4: Physical Parameter Specification for a Pair of Double-D Coil Designs.

| Physical Parameter | Measurement Value |
|--|-------------------|
| Diameter of Coil (D) | 58cm |
| Cross-section Diameter of Coil (d) | 0.3cm |
| Airgap between pair of Coils (Z) | 20cm |
| Number of Coil turns of each D-shaped coil (N) | 6 |

Based on the physical dimension presented in the proposed research work, the coil system was reproduced and designed in this research work using the ANSYS Electromagnetics software tool. The proposed double-D coil designs using ANSYS modelling software and the experimental design from the work of literature is shown in Figure 4.11[11]

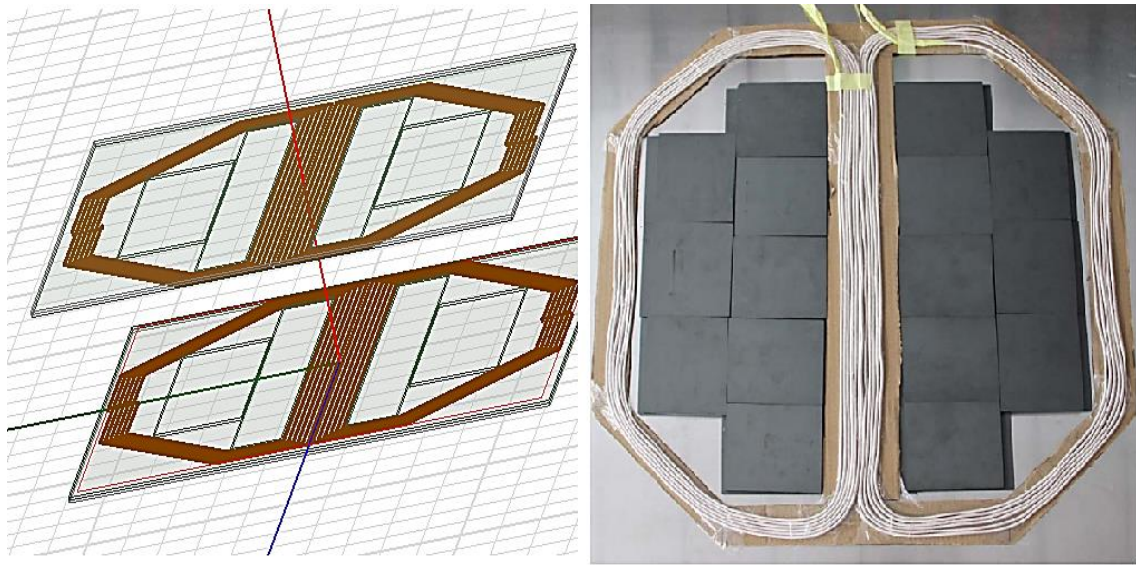


Figure 4.11: Proposed FEM Simulation Design and Physical Design of a Pair of Double-D Resonant Coils Taken from Literature[11]

As applicable to the planar coil design, one of the biggest challenges is the specification of the optimum boundary condition in order to get a value close to the experimental results. In addition, the appropriate specification of the distance between adjacent coil turns is highly essential in order to arrive at an accurate solution.

In the reproduction of the published model design, an optimal value for the change of radius between adjacent coils was gotten as 2 times the cross-section diameter of the coils. For the case of model design, it is calculated mathematically as: $(2 \times 0.3\text{cm}) = 0.60\text{cm}$.

Based on the specified distance between adjacent coil turns, a parametric sweep of boundary volume was carried out in order to determine the optimum offset value of the boundary condition of the region that gives the minimum error difference with respect to the journal experimental results. The simulation results (Simulation) in this research, journal experimental results (Practical) and result variations (Error Difference) based on the parametric sweep of the boundary region offset specifications from 0 to 50 are shown in Table 4.5.

Table 4.5: Comparison of FEM Simulated Result with Experimental Result for Double-D Resonant Coil Design Taken from Literature.

| Parameters | | Boundary Region Offset | | | | |
|----------------------------------|------------------------------|------------------------|--------|--------|--------|--------|
| | | 10 | 20 | 30 | 40 | 50 |
| Primary Self-inductance | Practical (μH) | 131.19 | 131.19 | 131.19 | 131.19 | 131.19 |
| | Simulation (μH) | 131.19 | 131.95 | 131.72 | 132.05 | 131.75 |
| | Error Difference | -1.9 % | -1.3 % | -1.5 % | -1.2 % | -1.5 % |
| Secondary Self-inductance | Practical (μH) | 130.44 | 130.44 | 130.44 | 130.44 | 130.44 |
| | Simulation (μH) | 131.56 | 131.83 | 131.75 | 132.07 | 131.78 |
| | Error Difference | 0.9 % | 1.1 % | 1.0 % | 1.2 % | 1.0 % |
| Mutual Self-inductance | Practical (μH) | 37.40 | 37.40 | 37.40 | 37.40 | 37.40 |
| | Simulation (μH) | 40.58 | 40.02 | 39.81 | 39.72 | 39.66 |
| | Error Difference | 8.0 % | 6.7 % | 6.2 % | 6.0 % | 5.8 % |
| Coupling Coefficient | Practical | 0.28 | 0.28 | 0.28 | 0.28 | 0.28 |
| | Simulation | 0.26 | 0.27 | 0.28 | 0.28 | 0.29 |
| | Error Difference | -7.3 % | -3.1 % | -0.4 % | 0.9 % | 2.2 % |

From the result obtained in Table 4.5, it is observed that simulated results at the region offset of 40 and 50 gives the closest values of circuit parameters to the journal experimental results.

At a region offset of 40, the maximum error obtained was 6.0% and the minimum error obtained was 0.9%. For the region offset of 50, the maximum error obtained was 5.8 % while the minimum error obtained was 1.0%. The optimum offset region in this scenario was chosen still chosen to be 40. The value was chosen based on the consistent error values that noted with offset region of 40.

4.4.3 Double D and Solenoid Coils Combination Design.

The coil model employs the simple system design using a pair of D-shaped coils for the transmitter, while a flux-pipe model design was used for the receiver. The D-shaped ring coils were modelled with a maximum diameter of 58cm separated by an airgap of 200mm. Similarly, the flux-pipe model design was modelled with a maximum length of 21cm at an airgap of 20mm. The physical dimensions of the D-shaped coil design and flux-pipe model design indicating the number of turns and the cross-sectional diameter of the copper wire used are presented in Table 4.6.

Table 4.6: Physical Parameter Specification for Double-D Coil and Solenoid Coil Designs.

| Physical Parameter | Measurement Value |
|---|-------------------|
| Diameter of Double-D Coil (D) | 58cm |
| Cross-section Diameter of Coil (d) | 0.3cm |
| Airgap between Coils (Z) | 20cm |
| Number of Coil turns for Double-D Coil(N) | 6 |
| Length of Solenoid Coil | 21cm |
| Number of Coil turns for Solenoid Coil | 18 |

Based on the physical dimension presented in the proposed research work, the coil system was reproduced and designed in this research work using the ANSYS Electromagnetics software tool. The proposed double-D coil designs using ANSYS modelling software and the experimental design from the work of literature is shown in Figure 4.11[11].

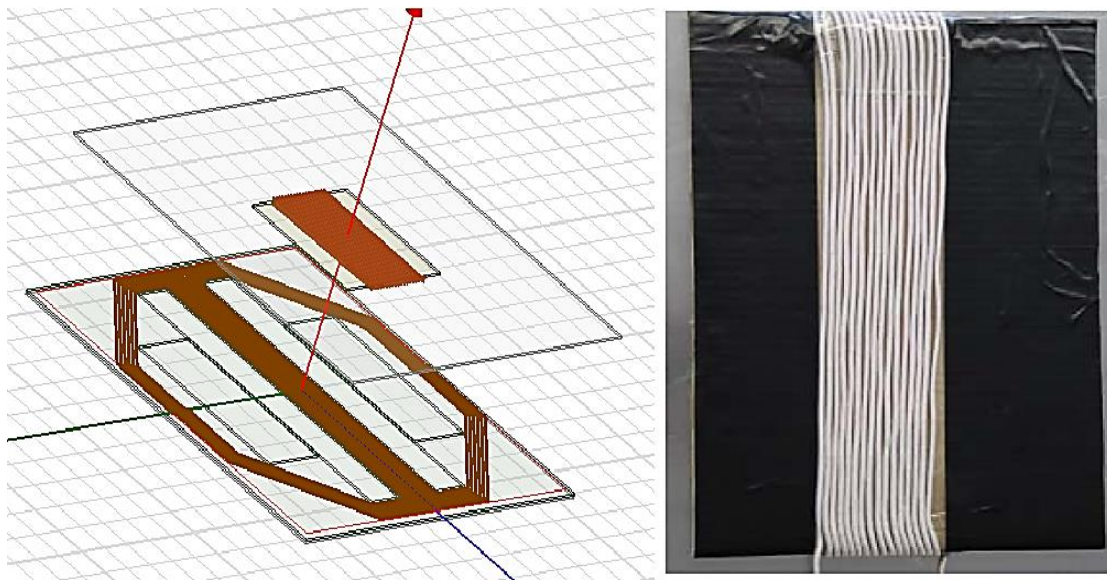


Figure 4.12: FEM Simulation Design and Physical Design of a Pair of Double-D and Solenoid Resonant Coils Taken from Literature[11]

As applicable to the planar coil and Double-D designs, one of the biggest challenges is the specification of the optimum boundary condition in order to get a value close to the experimental results. In addition, the appropriate specification of the distance between adjacent coil turns is highly essential in order to arrive at an accurate solution.

In the reproduction of the published model design for the flux-pipe design, an optimal value for the change of radius between adjacent coils was gotten as 2 times the cross-section diameter of the copper wire. For the case of model design, it is calculated mathematically as: $(2 \times 0.3\text{cm}) = 0.60\text{cm}$.

Based on the specified distance between adjacent coil turns, a parametric sweep of boundary volume was carried out in order to determine the optimum offset value of the boundary condition of the region that gives the minimum error difference with respect to the journal experimental results. The simulation results (Simul.) in this research, journal experimental results (Pract.) and result variations (% Error) based on the parametric sweep of the boundary region offset (R_off) specifications from 0 to 50 are shown in Table 4.7.

Table 4.7: Comparison of FEM Simulated Result with Experimental Result for Double-D and Solenoid Resonant Coil Design Taken from Literature.

| Parameters | | Boundary Region Offset | | | | |
|----------------------------------|------------------------------|------------------------|--------|--------|--------|--------|
| | | 10 | 20 | 30 | 40 | 50 |
| Primary Self-inductance | Practical (μH) | 124.49 | 124.49 | 124.49 | 124.49 | 124.49 |
| | Simulation (μH) | 124.85 | 126.18 | 127.37 | 127.20 | 127.55 |
| | Error Difference | 0.3 % | 1.3 % | 2.3 % | 2.1 % | 2.4 % |
| Secondary Self-inductance | Practical (μH) | 126.47 | 126.47 | 126.47 | 126.47 | 126.47 |
| | Simulation (μH) | 103.86 | 117.29 | 124.91 | 128.67 | 131.01 |
| | Error Difference | -21.8 % | -7.8 % | -1.2 % | 1.7 % | 3.5 % |
| Mutual Self-inductance | Practical (μH) | 23.35 | 23.35 | 23.35 | 23.35 | 23.35 |
| | Simulation (μH) | 25.61 | 24.99 | 24.14 | 23.19 | 22.43 |
| | Error Difference | 8.8 % | 6.6 % | 3.3 % | -0.7 % | -4.1 % |
| Coupling Coefficient | Practical | 0.19 | 0.19 | 0.19 | 0.19 | 0.19 |
| | Simulation | 0.22 | 0.21 | 0.19 | 0.18 | 0.17 |
| | Error Difference | 15.5 % | 7.5 % | 0.7 % | -4.9 % | -9.4 % |

From the result obtained in Table 4.7, it is observed that simulated results at the boundary region offset of 30 gives the closest values of electrical parameters to the journal experimental results with a maximum parameter error margin of 3.3% in the simulated results for the mutual inductance between the primary and secondary coil. Likewise, the boundary region offset gives a good value of circuit parameters to the journal experimental results with a maximum parameter error margin of 4.9%. Taking a critical analysis of the trend of results, it is observed that the boundary region off-set of 40 gives a fairly constant and consistent value of circuit parameters with respect to the journal experimental result with not more than 6% error for all the three coil design systems.

As a result, the boundary region off-set 40 was specified for Ansys FEM design and simulation for this research as well as the optimal formula for radius change between adjacent coil turns chosen for each of the model design specifications. The values were chosen for any appropriate design where it is applicable.

4.5 Validation of a Circular MRC Coil-to-Coil Design Model

A circular loop resonant coil for wireless power transfer was designed proposed by Hyeon-Chang .S. et al [111]. They proposed about 10 sets of equations which were applied in the optimal design of the circular coil model. The optimal model design[111] was verified and validated with ADS software simulation for generic application at a resonant frequency of 13.56MHz.

Their proposed research results, the values of $\frac{k}{\Gamma}$ were calculated against the same coil radius of the transmitter and receiver coils at the same time varying the cross-sectional radius of the coil at an airgap of 1.5m.

Using the optimum initial and boundary conditions used for validation of research work of Lempidis [11], the Ansys simulation environment with an offset region of 40 together with Matlab mathematical software was used to validate their simulation results. The results obtained at coils' resonant cross-sectional radius of 1mm, 2mm, 3mm, 4mm and 10mm with a coil radius of 0.5m and my generated results are compared in Table 4.8.

Table 4.8: Comparison of Simulation Results of (k/Γ) for Different Values of Cross-Sectional Radius at 0.5m Coil Radius

| Coil Cross-sectional Radius | 1mm | 2mm | 3mm | 4mm | 10mm |
|---|------|------|-------|-------|-------|
| Values of $\frac{k}{\Gamma}$ (Journal Results[111]) | 5.00 | 8.94 | 11.50 | 13.00 | 21.00 |
| Values of $\frac{k}{\Gamma}$ (Validation Design Model) | 4.90 | 8.40 | 11.00 | 13.40 | 20.80 |

From the results shown in Table 4.8, it is observed that the validation model design formulae agree with the journal results with a minimum error margin of 2% and a maximum error margin of 6%.

A further result validation and comparison was undertaken for various values of $\frac{k}{\Gamma}$ for the various cross-sectional radius of 1mm, 2mm, 3mm, 4mm and 10mm at coil radius of 1m while still maintaining the 1.5m airgap and resonant frequency of 13.56MHz. The results are shown in Table 4.9.

Table 4.9: Comparison of Simulation Results of (k/Γ) for Different Values of Cross-Sectional Radius at 1m Coil Radius

| Coil Cross-sectional Radius | 1mm | 2mm | 3mm | 4mm | 10mm |
|---|-------|-------|-------|-------|-------|
| Values of $\frac{k}{\Gamma}$ (Journal Results[111]) | 13.00 | 16.00 | 18.00 | 18.97 | 21.50 |
| Values of $\frac{k}{\Gamma}$ (Validation Design Model) | 12.80 | 16.30 | 17.80 | 18.90 | 20.77 |

It is observed that the proposed model design formulae agree with the journal results with a minimum error margin of 0.37% and a maximum error margin of 2%.

Finally, optimal coil-to-coil efficiency values were simulated for a known resonant coil cross-sectional radius and circular radius while keeping the airgap at 1.5m and the resonant frequency at 13.56MHz. The results are compared in Table 4.10.

Table 4.10: Comparison of Simulation Results of Efficiency Values for Different Values of Cross-Sectional and Circular Coil Radius.

| Coil Cross-sectional Radius | 2mm | 10mm |
|---|---------|---------|
| Resonant Coils Circular Radius | 0.9630m | 0.6979m |
| Efficiency Values (Coil-to-Coil [111]) | 88.48% | 91.91% |
| Efficiency Values (Validation of Coil-to-Coil Design Model) | 88.43% | 91.89% |

From the results presented in Table 4.10, it is observed that the proposed coil-to-coil design model efficiency values agree with the efficiency values of the journal publications very closely. The minimum and maximum error margin were less than 1%. The overall WPT system efficiency is observed to have a significant difference with the coil-to-coil efficiency at small cross-sectional area due to the presence of the skin effects at high resonant frequencies. This explains the close efficiency values obtained with the coil at a higher cross-sectional area of 10mm.

Thus, the use of the appropriate boundary offset, initial and boundary conditions and the specification of the distance between adjacent coils was justified as it gives a minimum accuracy value of 94%.

4.6 Summary

In this section, the selection of the optimal design algorithm was undertaken. The system-level engineering and simulation-based design were adopted because of the low cost and the ability to create good prototypes within a short period. The method involves specifying the model parameters using practical engineering data and then simulating the design using simulation software. The final optimized model can then be developed into a prototype based on modelling specifications used in the simulation.

A numerical method known as finite element modelling approach was applied in this research using Ansys Maxwell 3D modelling and simulation software. FEM as a numerical method is employed because it can easily handle very complex geometry involving an infinite degree of freedom cutting across a wide range of engineering problems like dynamics, solid mechanics, fluids, heat problems, electrostatic problems, and electromagnetic field problems. In addition, FEM can be used to analyze

and solve engineering problems containing indeterminate structures and complex loading of point loads, element loads, and time or frequency-dependent loading.

The circuit analysis of the FEM design involves the performance analysis of the model in terms of power output, power input, and coil-to-coil-efficiency of the coils. The circuit performance is evaluated at resonance with a particular compensation scheme. The analysis can be evaluated in two ways: the mathematical analysis and the Reduced Order Model analysis (ROM). Some set of equations were presented for evaluation of input power, output power, efficiency and appropriate capacitance for the optimum performance of the model coil designs.

An optimal initial and boundary conditions were selected and were validated by replicating and simulating published model designs. The experimental models of Lempidis[11] and Hyeon-Chang .S. et al [111] were replicated and simulated using a parametric sweep of initial and boundary conditions. From the simulation result presented, the boundary region off-set 40 was specified for Ansys FEM design and simulation for this research. For circular model designs, the appropriate distance between adjacent coils was evaluated as 1.5 times the value of the cross-sectional diameter of the copper wire used. Similarly, for flux-pipe designs, the appropriate distance between adjacent coils was evaluated as twice the value of the cross-sectional diameter of the copper wire used.

From the simulation results obtained, it was noted that my modelling methodology was within an error margin of $\pm 6\%$ of all the experimental models reported in the work of literature and will be used for all my design optimizations and simulations.

CHAPTER 5 Selection and Analysis of Coil Models

5.1 Introduction

The electromagnetic Resonance-based WPT technology is known for its high power transfer efficiency in many electrical and electronic application including the charging of electric vehicles. The technology is known for quick charging and optimal transmission of power through frequency control. The frequency control is essential in order to lower the losses because of low magnetic coupling. The technology can be used for both dynamic and static charging of an electric vehicle. The electromagnetic resonance-based WPT technology normally employs the use of capacitors connected to both the secondary and primary coils to compensate for the flux leakage because of large airgap due to the divergent nature of the electromagnetic flux. The resultant LC circuit employs a phenomenon known as resonance to enable the efficient transfer of power at a particular resonant frequency.

According to Chun Qiu et al [70], there are basically two types of magnetic resonance-based WPT method- the low frequency and high-frequency magnetic resonance-based WPT method. The low-frequency method normally operates under a resonant frequency of 200 kHz while employing the use of a ferrite core to boost the magnetic coupling between the resonant coils. On the other hand, the high-frequency method operates with a frequency higher than 1Mz without the need for the ferrite core.

The proposed optimal WPT designs, modelled in this chapter employed the use of the ferrite core, low-frequency MRC-based method for wireless charging of EVs. Designing an optimal resonant coil with high coupling coefficient involves altering the physical shape of a length of wire around a ferrite core within a confined physical space. Three common model designs were analyzed in this chapter to ascertain their individual performance characteristics with respect to variation in airgap, lateral displacement, longitudinal displacement, power output, coil-to-coil efficiencies, and efficiencies under different types and level of misalignment.

5.2 Selection of Proposed Coil Topology and Design Specification

According to the work of Kurschner .D. et al[128], At constant Q-factor, if the coil diameter (D) is greater than twice the length of the airgap (Z), the PTE of the resonant coils will be greater than 80%. With the coil diameter (D) greater than four times the length of the airgap, a PTE of close to 90% can be achieved. Similarly, with the appropriate consideration for safety regulation, Lempidis [11] proposed that the range of airgap for most electric vehicles should be from 11cm to 20cm.

Adopting the maximum airgap of 20cm, in order to achieve a PTE between 80% and 90%, resonant coils of diameter ranging from 40cm to 80cm will be required. With due consideration for safety requirements and the width of most EVs, an arbitrary diameter corresponding to the 25th percentile of the 40cm-80cm diameter range was used in this research. As a result, the coil design specifications were limited to the maximum length of 50cm. In order not to go beyond the maximum diameter of 50cm, a Litz copper coil length of 15.4m was used for the coil design.

Starting with the modelling of three simple coil designs of circular, rectangular and flux-pipe models, the appropriate coils were designed and created. The physical design parameters of the three design are illustrated in Table 5.1

Table 5.1: Table of Parameter Specifications for Simple Coil Designs

| Parameter | Flux-Pipe Model | Circular Model | Rectangular Model |
|---------------------------|-----------------|------------------------|----------------------|
| Length of Copper Wire | 15.4m | 15.4m | 15.4m |
| Airgap | 200 mm | 200 mm | 200 mm |
| Thickness of Coil Wire | 6 mm | 6 mm | 6 mm |
| Dimension of Coils | Width: 297 mm | Inner Diameter: 286 mm | Inner Length: 286 mm |
| | Length: 312 mm | Outer Diameter: 500 mm | Outer Length: 500 mm |
| Number of Coil Turns (N) | 26 | 12 | 12 |
| Core Thickness | 12 mm | 5 mm | 5 mm |
| Dimension of Ferrite Core | Width: 283 mm | Width: 508 mm | Width: 508 mm |
| | Length: 385 mm | Length: 508 mm | Length: 508 mm |
| Shield Thickness | 1.5 mm | 1.5 mm | 1.5 mm |
| Dimension of Shield | Width: 337 mm | Width: 548 mm | Width: 548 mm |
| | Length: 427 mm | Length: 548 mm | Length: 548 mm |

Based on the parameter specification of each of the resonant coil models, appropriate design for each model was built in the Ansys Electronic Desktop environment and it is illustrated in Figure 5.1.

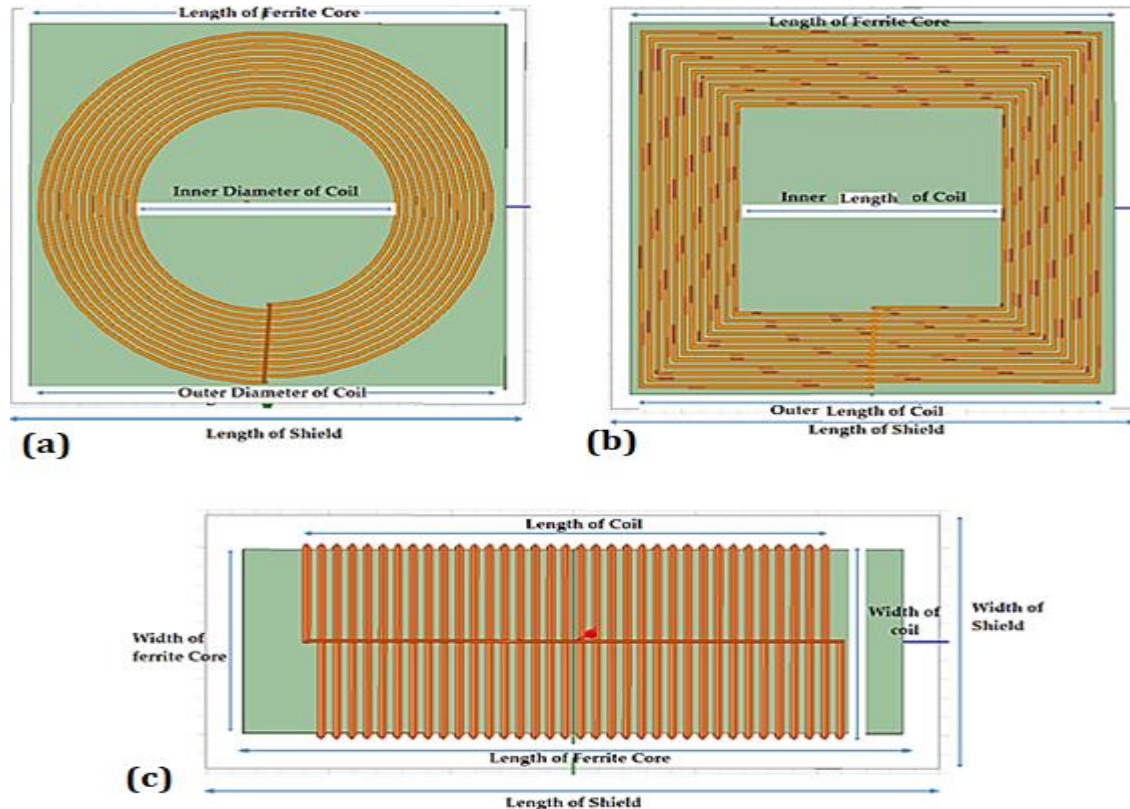


Figure 5.1: The Different Coil Design Topologies. (a) The Circular Resonant Coil Design (b) The Rectangular Resonant Coil. (c) The Flux Pipe Resonant Coil Design

5.3 Magnetostatic Analysis of Resonant Coils

As discussed in chapter 4, the magnetostatic analysis employs a matrix calculation in order to solve the magnetic field. When the field solution is stopped, derived quantities from the magnetic field solutions like inductances, coupling factor and magnetic flux density are calculated as the output parameters.

As discussed in the literature, the ferrite core was incorporated for each of the individual coil design in order to boost and concentrate the magnetic field to give a stronger coupling, higher self-inductance, and higher mutual inductance. In order to validate the importance of a ferrite core in coil designs, an initial magnetostatic analysis was performed on each of the coil designs in the absence of a ferrite core and the results were evaluated. The circuit parameters for circular coils, rectangular coils, and flux-pipe coil model in the absence of ferrite core were evaluated at an excitation current of 50 A and the results are presented in Table 5.2.

Table 5.2: Evaluated Circuit Parameters for Coil Model Designs without Ferrite Cores

| Parameter | Circular Coil Design | Rectangular Coil Design | Flux-Pipe Coil Design |
|----------------------------------|----------------------|-------------------------|-----------------------|
| Excitation Current (A) | 50 | 50 | 50 |
| Airgap (mm) | 200 | 200 | 200 |
| Primary Self-Inductance, L_p | 62.69 μ H | 74.83 μ H | 13.10 μ H |
| Secondary Self-Inductance, L_s | 59.86 μ H | 71.36 μ H | 12.78 μ H |
| Mutual Self-Inductance, L_m | 6.11 μ H | 7.49 μ H | 0.12 μ H |
| Coupling Coefficient, k | 0.100 | 0.103 | 0.009 |

Similarly, the circuit parameters for circular coils, rectangular coils, and flux-pipe coil model in the presence of the ferrite core were calculated and presented in Table 5.3.

Evaluating the results in Table 5.2 and Table 5.3, it is observed that the inductances and coupling strength increases significantly with the presence of ferrite core, when compared with coil designs without ferrite cores. The positive impact of the ferrite core is more noticeable with the flux-pipe coil design.

The circular coil and rectangular coil have similar mutual inductance but differ significantly in the value in their respective coupling coefficient and self-inductances. Similarly, the flux-pipe model has a significantly higher coupling coefficient, mutual inductance and self-inductances than the circular and rectangular coil models. The initial values of simulation results agree with reports from most work of literature.

Table 5.3: Evaluated Circuit Parameters Coil Model Designs with Ferrite Cores

| Parameter | Circular Coil Design | Rectangular Coil Design | Flux-Pipe Coil Design |
|----------------------------------|----------------------|-------------------------|-----------------------|
| Excitation Current (A) | 50 | 50 | 50 |
| Airgap (mm) | 200 | 200 | 200 |
| Primary Self-Inductance, L_p | 124.69 μH | 136.84 μH | 287.09 μH |
| Secondary Self-Inductance, L_s | 124.56 μH | 136.84 μH | 286.98 μH |
| Mutual Self-Inductance, L_m | 23.01 μH | 23.48 μH | 91.22 μH |
| Coupling Coefficient, k | 0.184 | 0.171 | 0.318 |

The increase in the inductances and coupling factor for the flux-pipe coil design is as a result of the increase in wire turns and coil area. The high number of coil-turns create a high amount of magnetic field at a particular excitation current and because the coils are tightly wound on the ferrite core to create a larger cross-sectional area, there is less opposition to the creation of magnetic flux for a fixed amount of amp-turns.

For the next series of simulations, the magnetic flux density distribution and coupling factor for the circular coils, rectangular coils and flux-pipe coils was analysed under the magnetostatic analysis by performing a parametric sweep of excitation currents, misalignment and airgap variations of each coil designs.

5.3.1 Magnetic Flux Density Distribution in Ferrite Cores

The ferrite core magnetostatic simulations are based on the static magnetic field. The simulation is necessary to ensure the WPT system operates in the linear mode and does not go into saturation. This is because a given magnetic material of a specific size can only withstand a certain level of magnetic energy.

The magnetostatic simulations will help in the investigation of the optimal level of power and current the core of each coil design models can withstand before going into saturation. This involves ramping up the excitation current until the ferrite core enters the saturation mode using a parametric sweep. Thus the maximum current can be obtained in the linear mode.

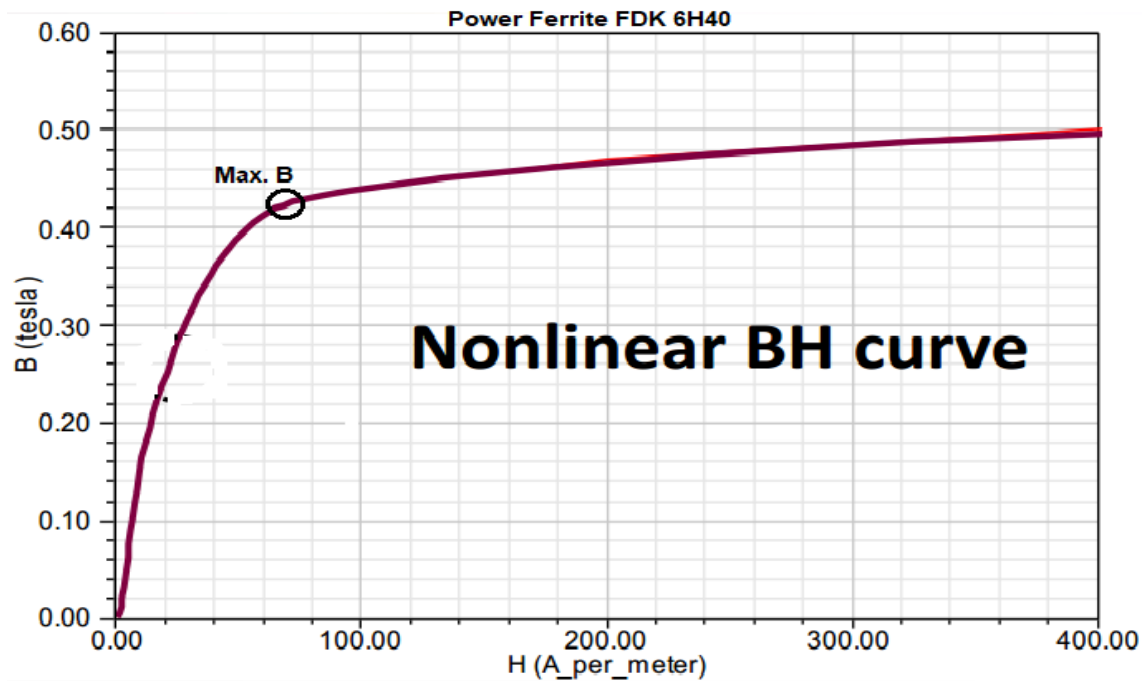


Figure 5.2: The B-H Curve for FDK 6H40 Ferrite Core

The ferrite core material used in the modelling of the three coil designs is the power ferrite FDK 6H40 produced by FDK Incorporation[178]. The standard material characteristics are illustrated in appendix 2A. From the technical data sheet published by the manufacturer, the magnetic saturation of the selected FDK 8H40 is 0.43 T. The B-H curve of the ferrite core is illustrated in Figure 5.2.

The external electric field strength is directly related to the value of the excitation current in the coil windings. For efficient and effective performance of the ferrite core material, the external excitation current must fall within the linear region of the BH curve.

Using the appropriate initial and boundary conditions, finite element analysis was implemented on the three coil designs at an excitation current of 50 A. The magnetic flux distribution in the ferrite core material for the circular, rectangular and flux-pipe model coils is illustrated in Figure 5.3.

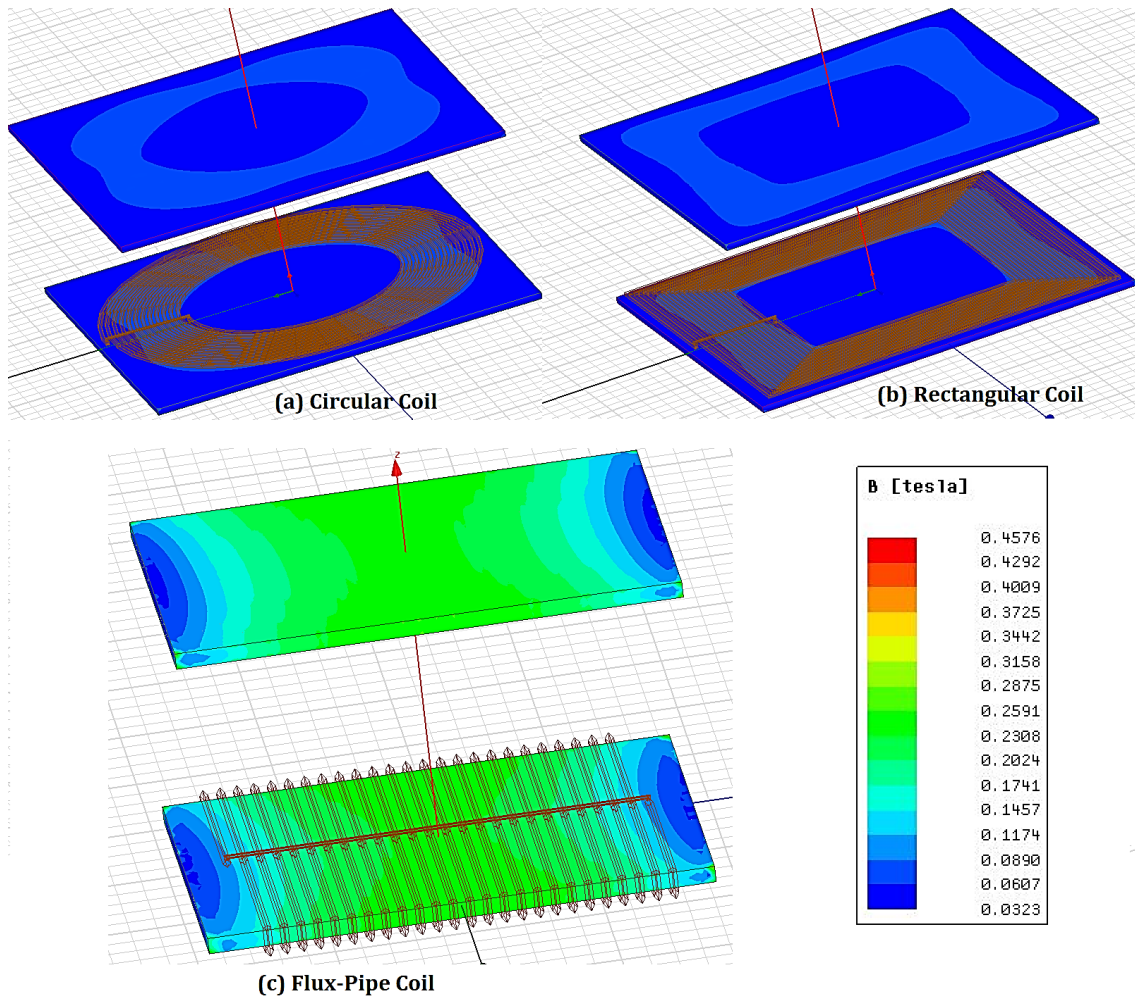


Figure 5.3: Magnetic Flux Distribution in Coil Designs at Excitation Current of 50 A.

The simulation result presented in Figure 5.3 was implemented at an airgap of 200 mm. From the magnetic flux distribution shown, it is noted that at the excitation current of 50 A, all the three coil designs have a magnetic flux distribution of less than 0.35 T, which falls below the saturation limit of 0.43 T. For each of the resonant coil models the maximum values of the flux density distribution is concentrated around the middle of the coil windings. This is an indication that the electric field strength is maximum at those regions.

In order to ascertain the maximum current each of the three models can withstand before going into saturation, the three model designs were subjected to a parametric sweep of excitation currents from 0 A to 100A at different airgaps of 150 mm and 200 mm. The performance result of the coil designs at 150 mm and 200 mm are shown in Figure 5.4.

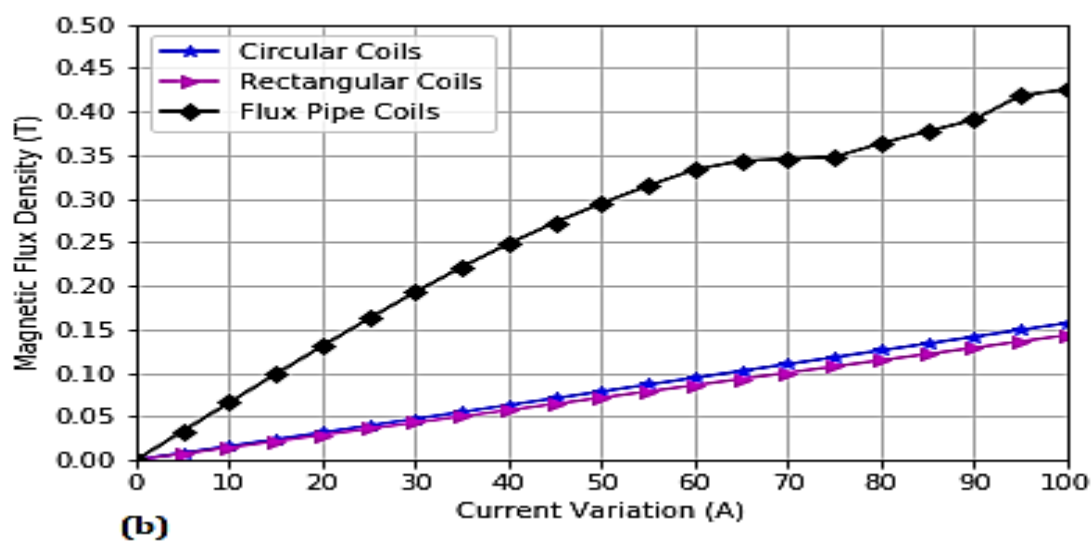
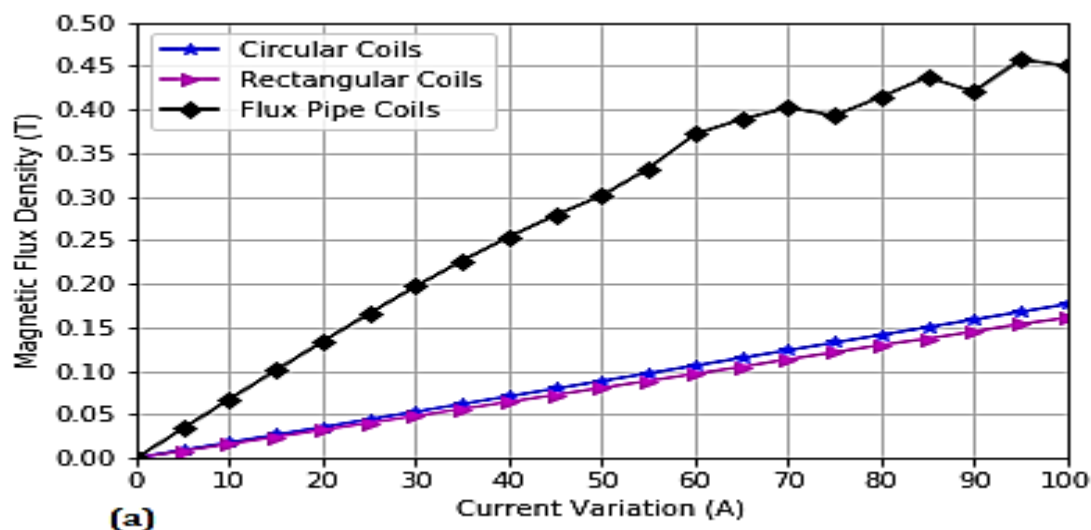


Figure 5.4: Magnetic Flux Distribution in Ferrite Cores with Variation in Excitation Current. (a) Flux Distribution at 150mm Airgap. (b) Flux Distribution at 200mm Airgap

It is noted that for all the model coil designs, an increase in the airgap leads to a decrease in the magnetic flux distribution for a given excitation current. For example, at 50 A, the magnetic flux distribution in the core of the flux pipe coil was 0.32 T and 0.29 T at 150 mm and 200 mm airgap respectively. Similarly, the circular and rectangular model showed similar performance of 0.09 T and 0.07 T at the same excitation current of 50 A at airgaps of 150 mm and 200 mm respectively.

It was also noted that the cores of the circular and rectangular coils can withstand an excitation current of up to 100 A without getting saturated while the flux pipe core can only withstand an excitation current of 85 A at 150 mm airgap and an excitation current of 100 A at 200 mm airgap. The low-performance output of the flux-pipe core is because of more ampere-turns on the core when compared with the core of the circular and rectangular coils.

It is also noted for the flux pipe coil model that, as the magnetic flux density distribution begins to show unpredictable values, as it gets closer to the saturation point of 0.43 T. For most practical design, it is advisable to operate the coil model designs at most 10 % lower than the saturation limit.

In summary, the circular and rectangular coil models can withstand higher current excitations than the flux-pipe coil model.

5.4 Parametric Analysis of the Resonant Coil Designs

Before the optimization of these existing simple designs, there was, need to perform a parametric sweep analysis of each coil design based on the variation of the airgap, lateral misalignment, and longitudinal misalignment. The 3- dimensional positional parameters of the secondary coils were varied along the x, y and z coordinate systems.

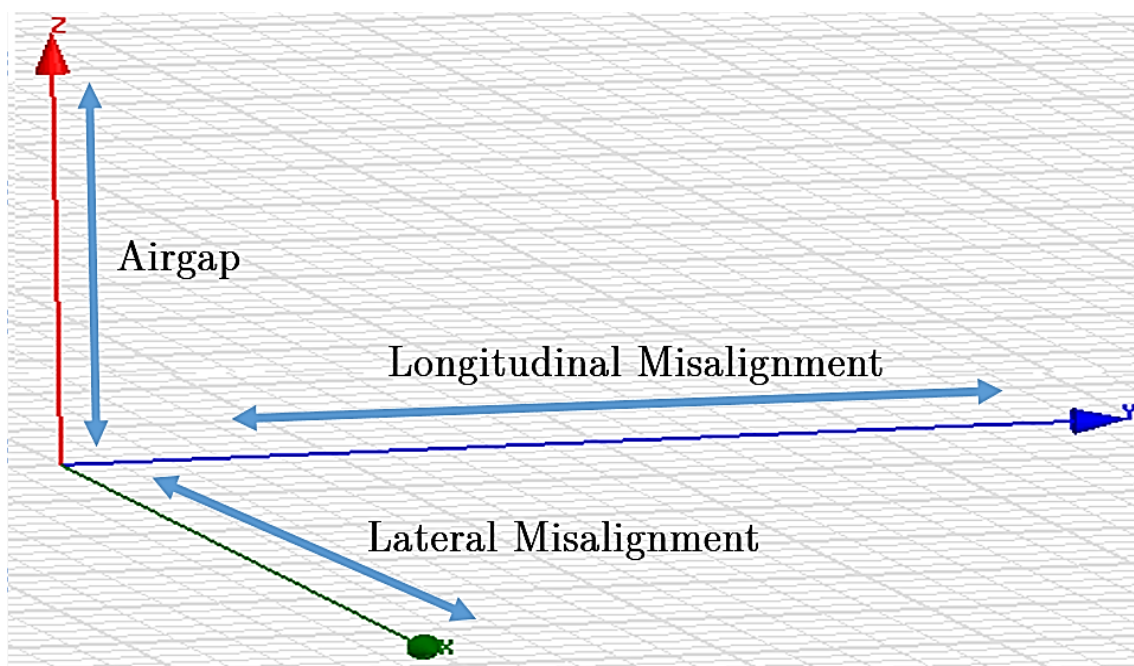


Figure 5.5: 3-Dimensional Positional Arrangement for Airgap, Lateral Misalignment, and Longitudinal Misalignment.

The parametric sweep along the x-axis corresponds to the lateral misalignment (green line), the parametric sweep along the y-axis corresponds to the longitudinal misalignment (the blue line), while the airgap variation is done through a parametric sweep along the z-axis (red line). This is illustrated diagrammatically in Figure 5.5.

5.4.1 Performance Analysis of Lateral Misalignment of Resonant Coils

This parametric analysis is performed by varying the position of the secondary coil along the x-axis and the value of the coupling coefficient measured based on each unit displacement of the coil along that axis. The three resonant coil design was subjected to a lateral displacement of between 0 to 300mm (30cm) with a step increase of 10mm. The variation in the coupling coefficient for each unit increase in lateral displacement along the x-axis is shown in Figure 5.6.

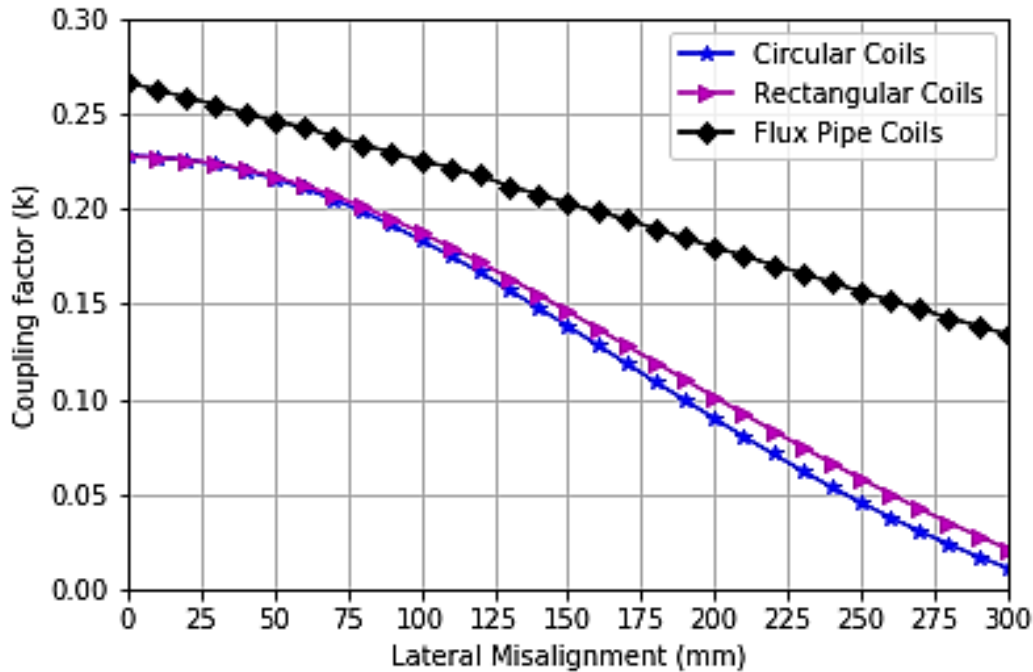


Figure 5.6: Lateral Misalignment Parametric Analysis of Resonant Coils

From the result shown in Figure 5.6, it is noted that the circular and rectangular coil designs offer similar performance characteristics with respect to each unit lateral displacement of the secondary coils. They have the lowest coupling coefficient of 0.02 and 0.01 at 300 mm lateral displacement while showing a strong coupling coefficient of close to 0.23 at no lateral misalignment. The result is expected due to the similarity in shape with almost the same inner and outer diameter. On the other hand, the flux-pipe model coil offers the best performance having a high coupling coefficient of 0.15 at 30cm displacement. This is more than 7 times the value of the coupling coefficient for the rectangular and circular coils. In addition, a coupling coefficient of 0.33 at no displacement is a significant improvement when compared with the other two coils.

The performance characteristics are expected due to the strength of the magnetic field based on the physical configuration of each coil designs. The magnetic field strength at a range of specific lateral misalignments is illustrated in Figure 5.7.

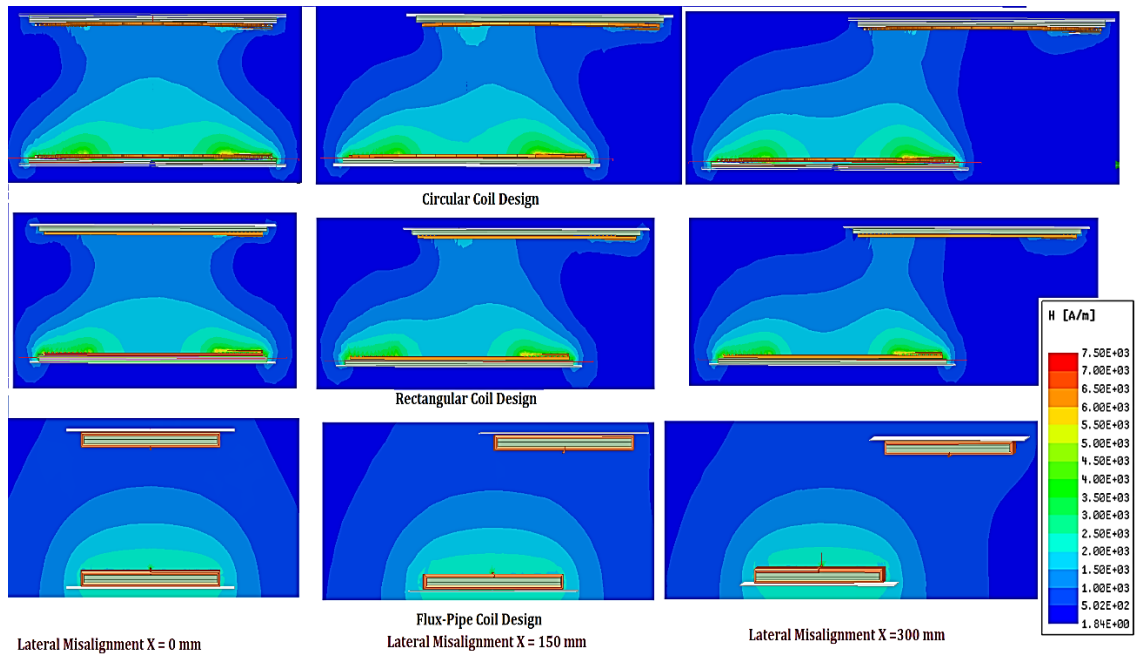


Figure 5.7: Magnetic Field Distribution around Coil Designs at Different Lateral Misalignment

The flux-pipe coil design is shown to have a stronger magnetic field strength when compared with the circular and rectangular coil designs. The higher coupling noticed with the flux-pipe coil is because of stronger magnetic fields at the edges and fringe of the ferrite core, which easily couples with the secondary coil. The interesting phenomenon is illustrated in Figure 5.7. Thus, the fringe magnetic fields are responsible for the higher coupling strength with increase in misalignment when compared with the circular and rectangular coils. As a result, a greater amount of magnetic flux reaches the secondary coils, thus, responsible for the stronger magnetic coupling.

5.4.2 Performance Analysis of Longitudinal Misalignment of Resonant Coils

This parametric analysis is performed by varying the position of the secondary coil along the y-axis and the value of the coupling coefficient is evaluated based on each unit displacement of the coil along that axis. The three resonant coil designs were subjected to longitudinal displacement of between 0 to 300mm. The variation of the coupling coefficient for each unit increase in longitudinal displacement along the y-axis is shown in Figure 5.8.

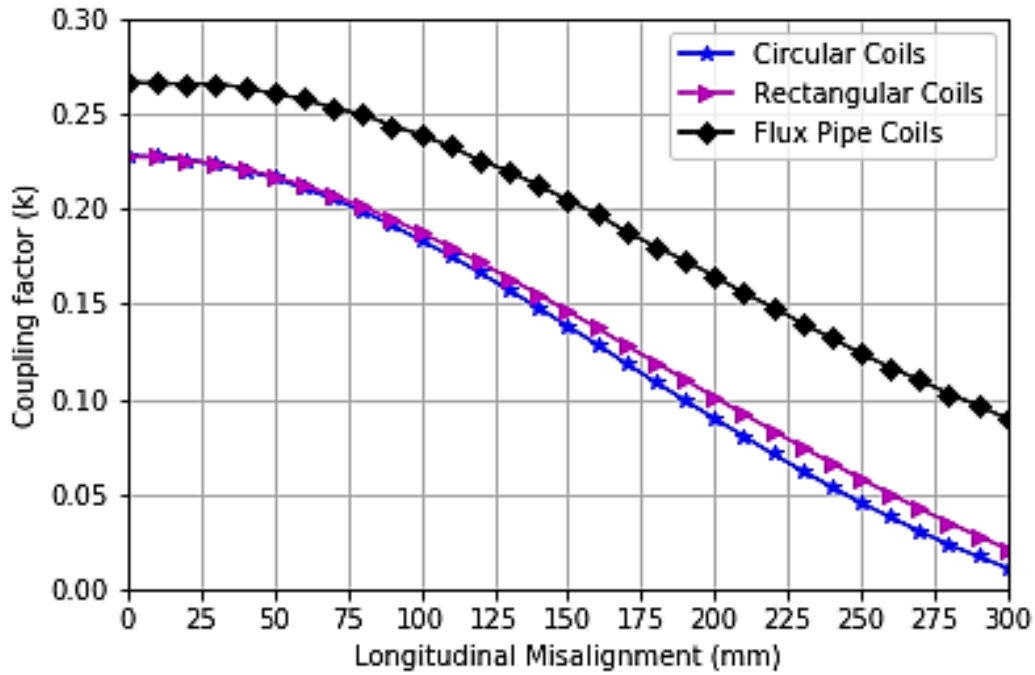


Figure 5.8: Longitudinal Misalignment Parametric Analysis of Resonant Coils

From the result shown in Figure 5.8, it is noted that the circular and rectangular coil designs offer similar performance characteristics with respect to each unit displacement of the secondary coils, having the lowest coupling coefficient of 0.020 and 0.025 at 300 mm lateral displacement while showing a coupling coefficient of close to 0.23 at no longitudinal misalignment. The result is expected due to the similarity in shape with almost the same inner and outer diameter as well as the symmetry of the coils on both the x-axis and the y-axis.

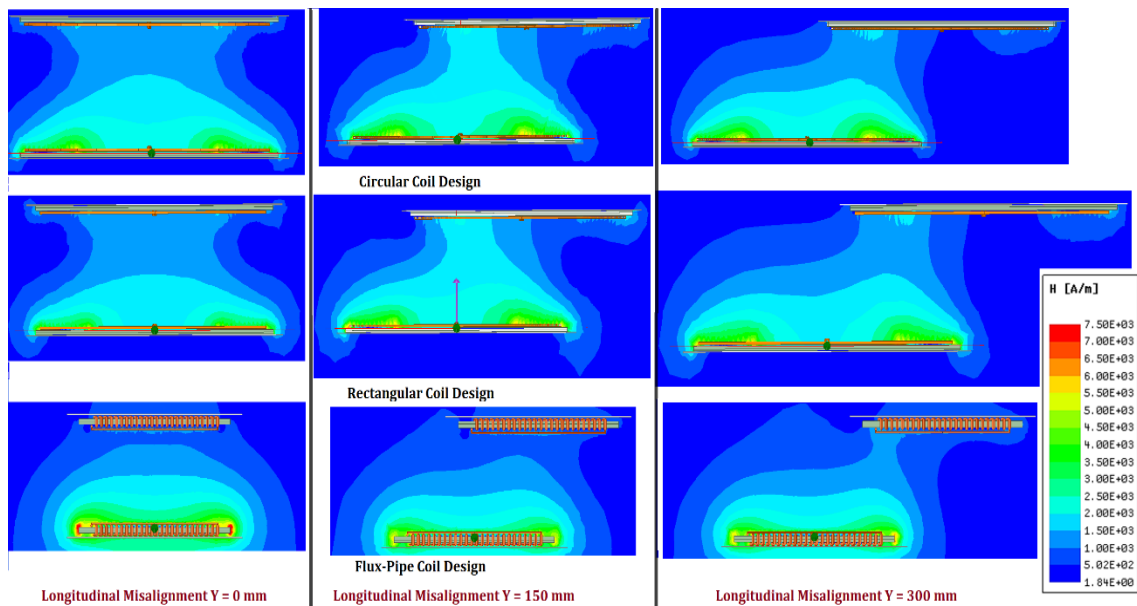


Figure 5.9: Magnetic Field Distribution around Coil Designs at Different Longitudinal Misalignment

On the other hand, the flux pipe coil offers the best performance having a high coupling coefficient of 0.13 at 300 mm displacement. This is more than 7 times the value of the coupling coefficient for the rectangular and circular coils. In addition, a coupling coefficient of 0.33 at no displacement is significant compared with the other two coils. The higher coupling noticed with the flux-pipe coil is because of stronger magnetic fields at the edges and fringe of the ferrite core, which easily couples with the secondary coil. The interesting phenomenon is illustrated in Figure 5.9. Thus, the fringe magnetic fields are responsible for the higher coupling strength with increase in misalignment when compared with the circular and rectangular coils.

Comparing the results in Figure 5.9 with Figure 5.7, it is noted that though the flux-pipe design has the same zero misalignments, the coupling strength at 300 mm lateral misalignment is higher than the coupling strength at 300 longitudinal misalignments. This is because the magnetic field distribution at the edges and fringe of the copper turns is higher than that obtained at the edges and fringes of the ferrite core. The higher magnetic field distribution is because of coil turns which translates to higher ampere-turns.

5.4.3 Performance Analysis of Resonant Coils with Variation in Airgap

This parametric analysis is performed by varying the position of the secondary coil along the z-axis and the value of the coupling coefficient is measured based on each unit displacement of the coil along that axis.

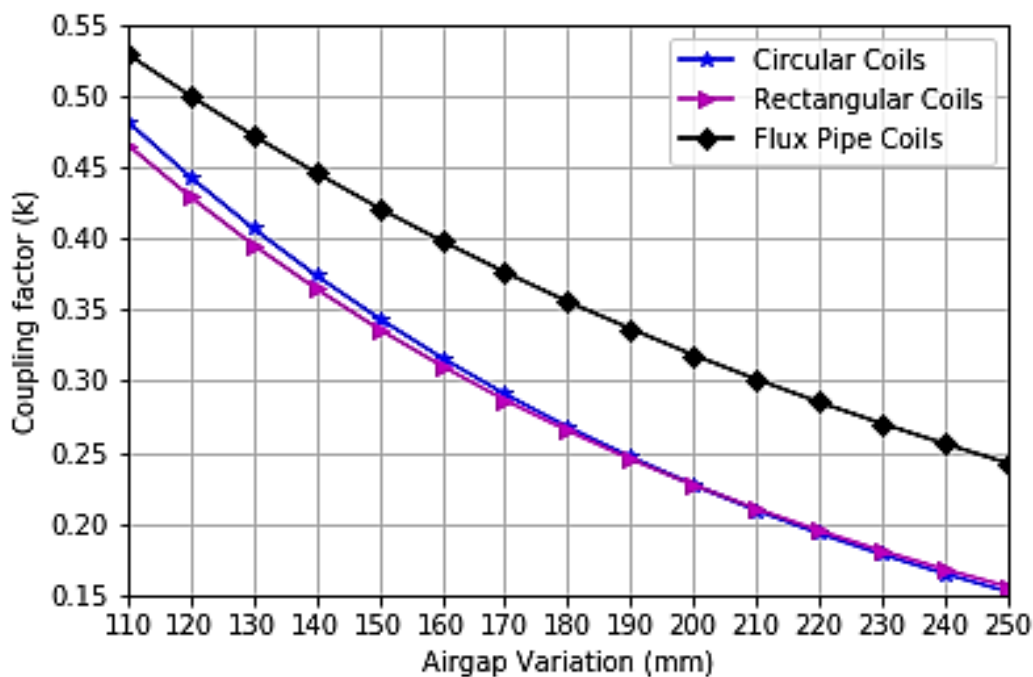


Figure 5.10: Airgap Variation Parametric Analysis of Resonant Coils

The three resonant coil design was subjected to longitudinal displacement of between 110mm to 250mm. The variation of the coupling coefficient for each unit increase in airgap variation along the z-axis is shown in Figure 5.10.

From the result shown in Figure 5.10, it is noted that the circular and rectangular coil designs offer similar performance characteristics with respect to each unit vertical displacement of the secondary coils. The circular and rectangular also showed the lowest coupling coefficient of 0.15 at 250 mm airgap while showing a strong coupling coefficient of close to 0.46 and 0.47 at airgap of 110 mm respectively. The result was expected due to the similarity in shape with almost the same inner and outer diameter. On the other hand, the flux-pipe coil offers a slightly better performance having a high coupling coefficient of 0.24 at 250 mm airgap. This is almost 60% increase in the value of the coupling coefficient of the rectangular and circular coils. In addition, a coupling coefficient of 0.53 at 11cm airgap is a significant improvement in relation to the rectangular coil design and the circular coil at that airgap.

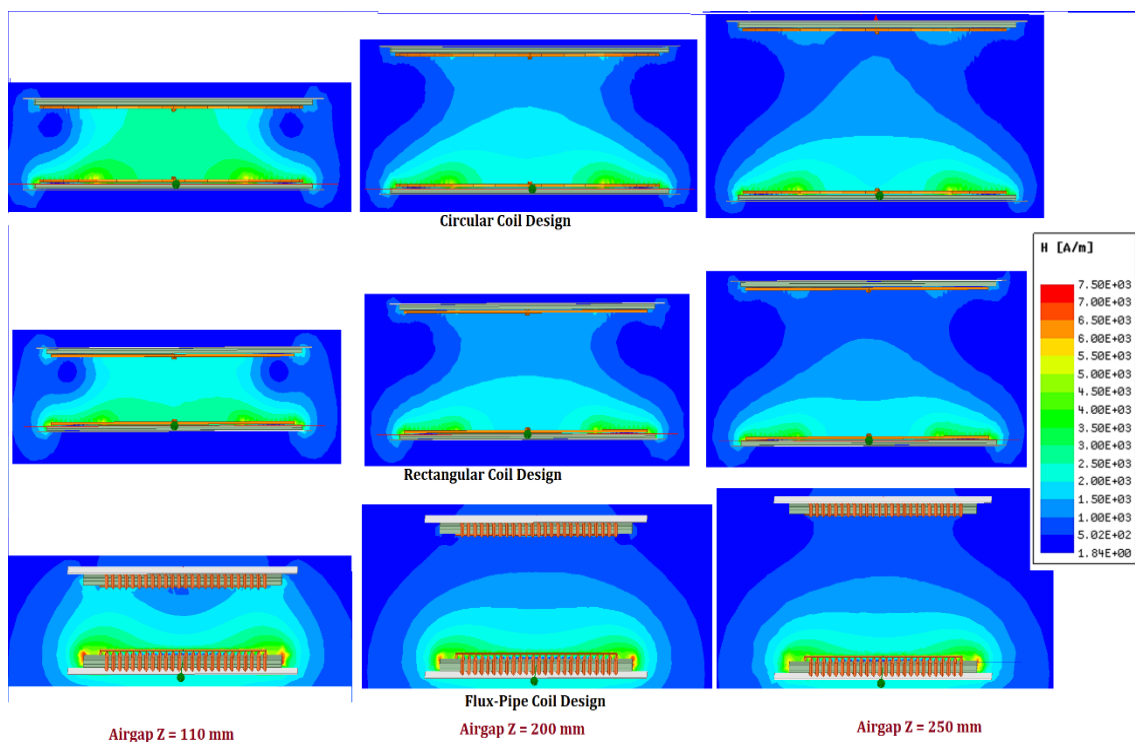


Figure 5.11: Magnetic Field Distribution around Coil Designs at Different Airgaps

The increase in the coupling strength with a decrease in the airgap is because of the capacity of the secondary coil of each coil designs to capture more leakage magnetic field with closer proximity to the primary coil. Magnetic fields do not travel in a straight line but in a curved manner and do radiate as they travel further from the source. Thus, the closer the receiver coil to the transmitter coil, the higher the number of useful magnetic flux lines that are coupled with the secondary coil.

From the three parametric analysis of the three coils, it was noted that the flux-pipe coil model offers the overall best performance for all the cases analyzed. As a result, it will be appropriate to investigate a further improvement of flux-pipe model coils in terms of its coupling coefficient while using the same length of copper wire for the coils as well as maintaining the same surface area and thickness of the aluminium shield and the ferrite core.

5.5 Further Analysis of Conventional Flux-Pipe Topology

The flux-pipe resonant coil design is modelled by winding a piece of copper wire around a ferrite bar in order to provide the shape shown in Figure 5.1(c). For a constant length of copper wire, there are many ways of generating the length and width dimension of the coil. The initial starting point is to model the core such that the length and the breadth are almost equal, and the flux-pipe model was denoted as the reference model (Ref Model). Then the width and length are modified in order to generate different shape geometries of different length and breadth. A typical shape and dimension parameters of a flux-pipe resonant coil is illustrated in Figure 5.12.

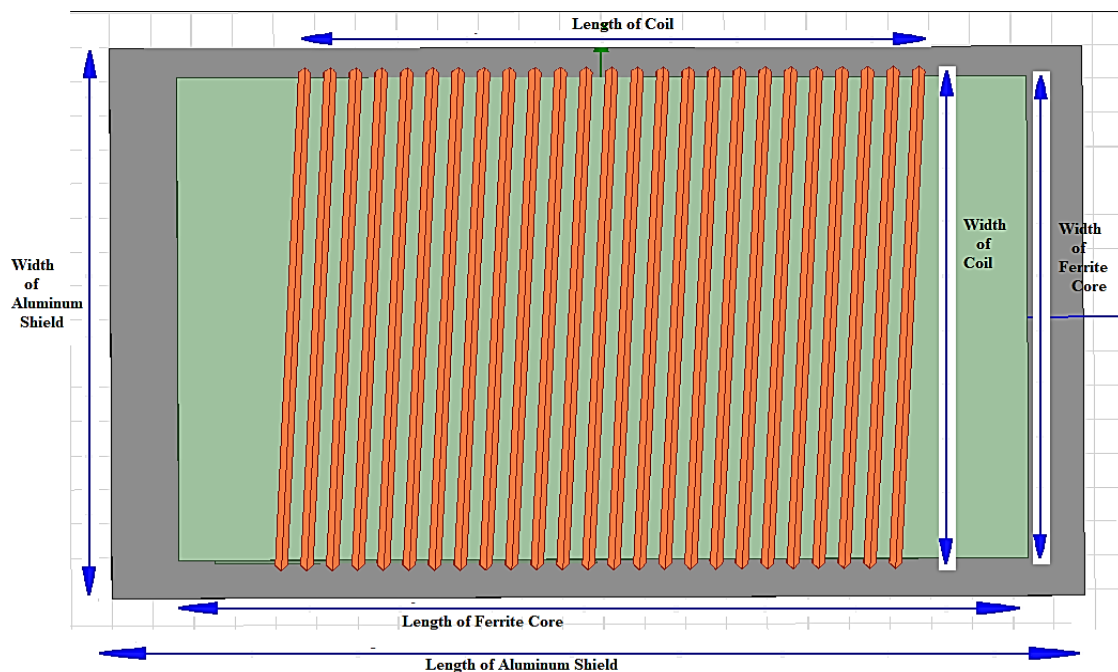


Figure 5.12: Dimension Parameters Specification of the Flux-Pipe Resonant Coil Model

For the sake of fair comparisons and analysis, the various materials used for the modelling of different flux-pipe geometries will have the same length and thickness of copper wire, the same area (by changing the length and width in Figure 5.12) and thickness of ferrite bar and the same thickness and area of the shielding sheet. For the model design, a copper wire of length 15.4m with a cross-sectional diameter of 6mm was used. For the ferrite core, the thickness of the core was 12mm with an area of 0.109m². Likewise, an aluminium shield of 1.5mm thickness with an area of 0.142 m² was used.

In the creation of the different geometric dimensions and sizes from the basic shape shown in Figure 5.12, a parameter known as Coil dimension factor (K_{df}) was applied to create 5 different dimensional models by varying the coil length (DL_y) and coil width (DL_x). The coil dimension factor (K_{df}) is given mathematically as

$$K_{df} = 2 \frac{DL_y}{DL_x} \quad 5.1$$

The numerical value of 2 is the constant evaluated as the optimum distance between adjacent coil turns. The various dimension of the models showing the number of coil turns, values of the coil dimension factor and other parameters are illustrated in Table 5.4.

Table 5.4: Model Designs of Flux-Pipe Topology with Variation in Length and Width

| Parameter | Model 1 | Model 2 | Model Ref | Model 3 | Model 4 |
|------------------------------------|---------|---------|-----------|---------|---------|
| Coil Dimension Factor (K_{df}) | 0.34 | 0.64 | 1.05 | 1.46 | 1.94 |
| Width of Coils (DL_y) | 552mm | 386mm | 297mm | 257mm | 227mm |
| Length of Coils (DL_x) | 168mm | 240mm | 312mm | 360mm | 408mm |
| Number of Coil Turns (N) | 14 | 20 | 26 | 30 | 34 |
| Width of Ferrite Core | 538mm | 372mm | 283mm | 243mm | 213mm |
| Length of Ferrite Core | 203mm | 293mm | 385mm | 448mm | 511mm |
| Width of Aluminum Shield | 592mm | 426mm | 337mm | 297mm | 267mm |
| Length of Aluminum Shield | 239mm | 332mm | 425mm | 477mm | 530mm |

Since the surface areas of the coil, ferrite core and aluminium shield are each maintained at their own set constant value across the five models, an increase in the width of any of the components requires a corresponding decrease in the length for the same component. The resulting finite element model designs and physical representation in Ansys simulation environment are presented in Figure 5.13.

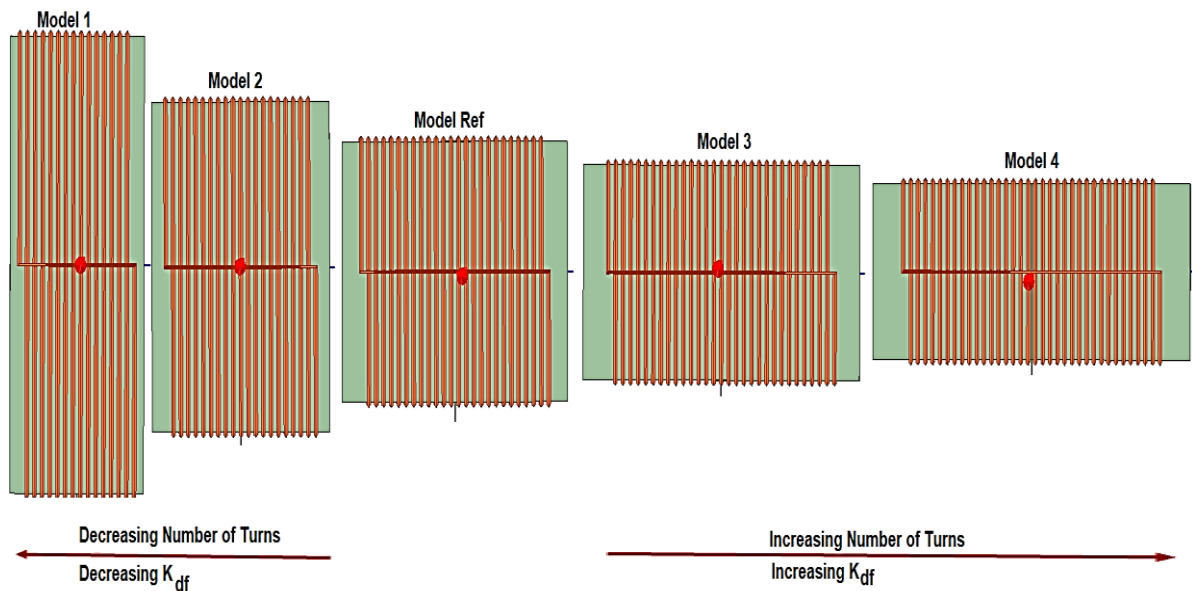


Figure 5.13: Physical Design Variations of Proposed Flux-Pipe Resonant Coil

The ferrite core used in the modelling of the flux-pipe resonant coil topology was employed to improve the coil permeability to the magnetic flux and increase the self-inductance and mutual inductance of the coils. But there is a limit to the magnitude of the flux that can be produced for a particular type of core material and a further increase in excitation current will not produce a further increase in magnetic flux intensity. In effect, the ferrite core of the coil becomes magnetically saturated.

As discussed in chapter 4, the magnetostatic analysis employs a matrix calculation in order to solve the magnetic field. When the field solution is stopped, derived quantities from the magnetic field solutions like inductances, coupling factor and magnetic flux density are calculated as the output parameters. With respect to the Model 1, Model 2, Model Ref, Model 3, and Model 4 flux-pipe coil model, the coil circuit parameters were calculated and illustrated in Table Table 5.5.

Table 5.5: Evaluated Circuit Parameters for Flux-Pipe Resonant Coil Models

| Parameter | Model 1 | Model 2 | Model Ref | Model 3 | Model 4 |
|--|---------|---------|-----------|---------|---------|
| Coil Dimension Factor (K_{df}) | 0.34 | 0.64 | 1.05 | 1.46 | 1.94 |
| Excitation Current (A) | 50 | 50 | 50 | 50 | 50 |
| Airgap (mm) | 200 | 200 | 200 | 200 | 200 |
| Primary Self-Inductance, L_p (μH) | 132.20 | 205.87 | 289.06 | 356.24 | 458.45 |
| Secondary Self-Inductance, L_s (μH) | 132.26 | 206.02 | 289.42 | 356.15 | 457.00 |
| Mutual Inductance, L_m (μH) | 16.97 | 40.11 | 77.00 | 120.07 | 186.14 |
| Coupling Coefficient, k | 0.128 | 0.195 | 0.266 | 0.337 | 0.406 |

The value of the coil dimension factor has a very strong relationship with the value of self-inductance, mutual inductance and the coupling coefficient. As the values of the coil dimension factor increases, the coupling factor, mutual inductance, and the self-inductance of each of the flux-pipe model increases. It is also pertinent to note that the coil dimension factor is also strongly related to the

number of coil turns. Thus, in order to design a flux-pipe resonant with a high value of coupling coefficient and self-inductance, the coil dimension factor must be selected to be greater than 1.

For the next series of simulations, the magnetic flux density distribution and coupling factor for the circular coils, rectangular coils and flux-pipe coils was analysed under the magnetostatic analysis by performing a parametric sweep of excitation currents, misalignment and airgap variations of each coil designs

5.6 Magnetic Flux Distribution for Flux-Pipe Resonant Coil Designs

Using the appropriate initial and boundary conditions, finite element analysis was performed on the five flux-pipe model designs at an excitation current of 50 A. The magnetic flux distribution in the ferrite core material for model 1, model 2, model Ref, model 3 and model 4 is illustrated in Figure 5.14.

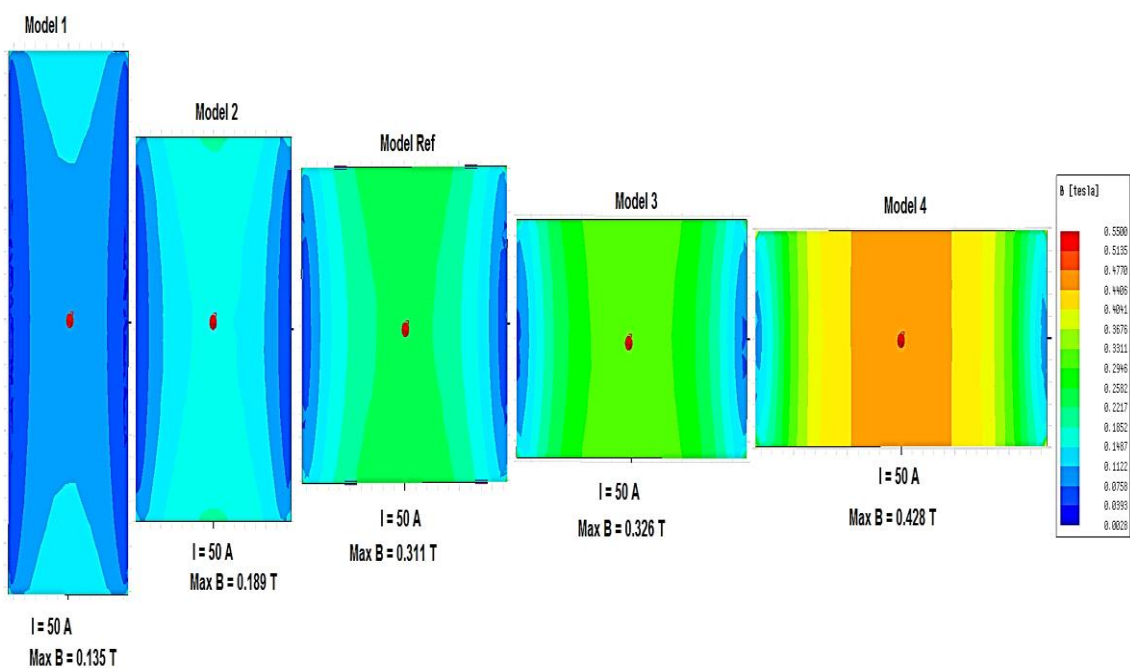


Figure 5.14: Magnetic Flux Distribution in Ferrite Cores for Flux-Pipe Resonant Coils

The simulation result presented in Figure 5.14 implemented at an airgap of 200 mm. From the magnetic flux distribution shown, it is noted that at the excitation current of 50 A, the magnetic flux density increases with an increase in the number of turns. It is noted that ferrite core of model 1, model 2, Ref model, model 3 and model 4 has a maximum flux density of 0.14 T, 0.18 T, 0.30 T, 0.33 T and 0.43 T respectively. For each of the flux-pipe resonant coil models, the maximum values of the flux-density distribution are concentrated around the middle of the coil windings. This is an indication that the electric field strength is maximum at those regions

A magnetostatic analysis was carried out on the five model designs to determine the magnitude of excitation current that will lead to magnetic saturation for each individual ferrite core of the flux-pipe models. This is achieved by subjecting the various models to a parametric sweep of steady-state

current while measuring the value of the magnetic flux density for each step increase in steady-state current. As a result, the five model designs were subjected to a parametric sweep of excitation currents from 0 A to 100A at different airgaps of 150 mm and 200 mm. The performance results of the flux-pipe model designs at 150 mm and 200 mm are shown in Figure 5.15.

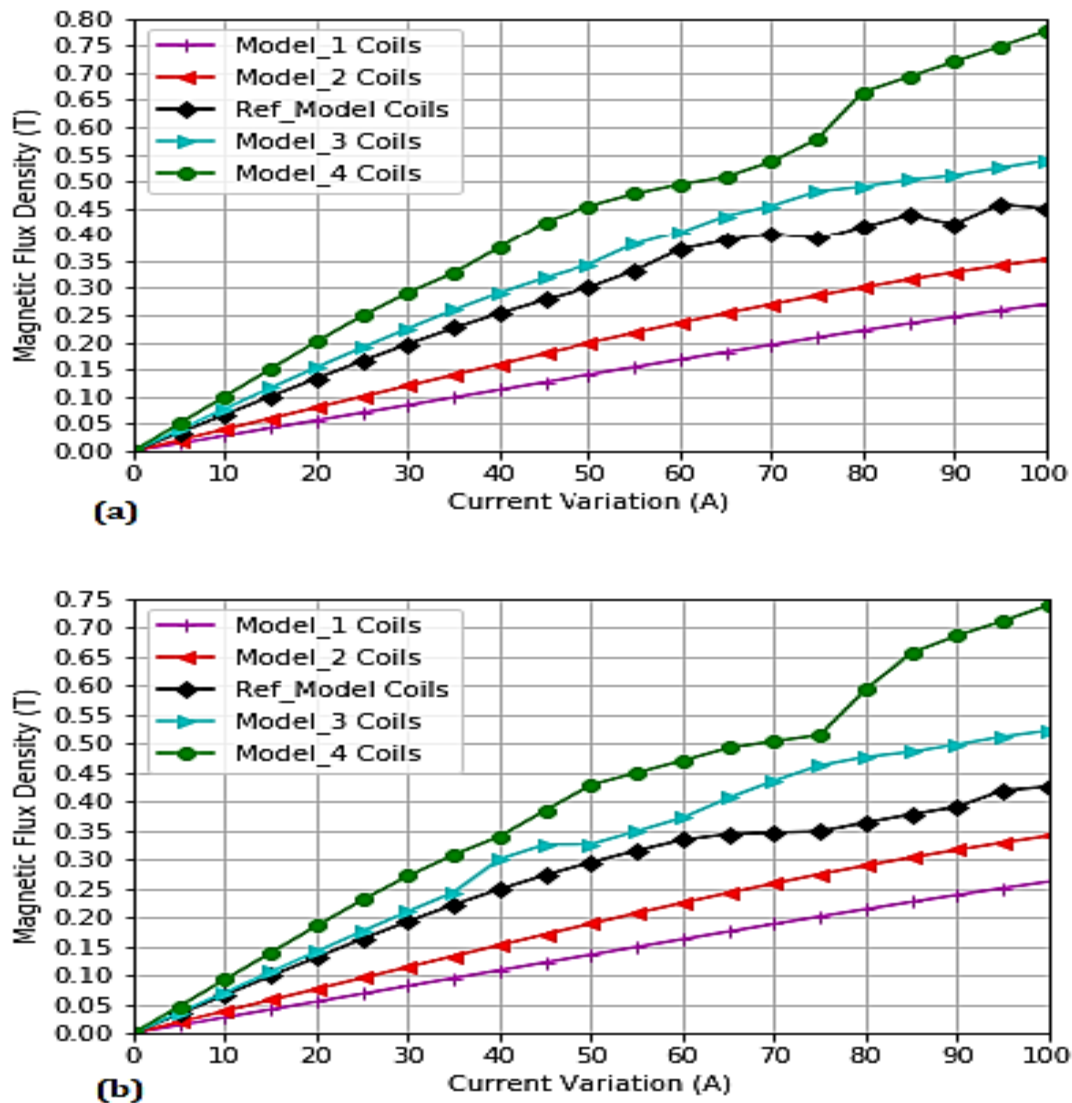


Figure 5.15: Variation of Magnetic Flux Density with Current Excitation. (a) Variations at Airgap of 150mm. (b) Variations at Airgap of 200mm

From the result shown in Figure 5.15 in conjunction with Table 5.4, it can be surmised that an increase in the number of turns causes a corresponding increase in the value of ampere-turns thereby reducing the amount of the current required to drive the ferrite core to magnetic saturation. Also, it is noted that the coil model with a smaller number of coil turn require a higher magnitude of current to drive the core into magnetic saturation while the coil model with the highest number of coil turns requires the lowest magnitude of current to drive its core into saturation. For example, Model 1 with 14 number of turns can withstand an excitation current at 100 A at both airgap settings of 150mm and 200mm without attaining the saturation limit of the core. This is in contrast with Model 4 with 34 number of

turns which can only withstand a maximum current of 45 A at 150mm airgap and 50 A at 200mm airgap.

5.7 Parametric Analysis of Flux-Pipe Resonant Coil Designs

Initial finite element analysis of the five models to ascertain their coupling strength performance under lateral, longitudinal misalignment as well as airgap variation was performed. The secondary coil 3-dimensional positional measurement parameters are varied along the x, y and z coordinate systems.

The parametric sweep along the x-axis corresponds to the lateral misalignment (green line), the parametric sweep along the y-axis corresponds to the longitudinal misalignment (the blue line), while the airgap variation is done through a parametric sweep along the z-axis (red line). This is illustrated diagrammatically in Figure 5.5.

5.7.1 Lateral Misalignment Performance of Flux-Pipe Resonant Coils

This parametric analysis for the lateral misalignment was performed by varying the position of the secondary coil along the x-axis and the value of the coupling coefficient was evaluated based on each unit displacement of the coil along that axis.

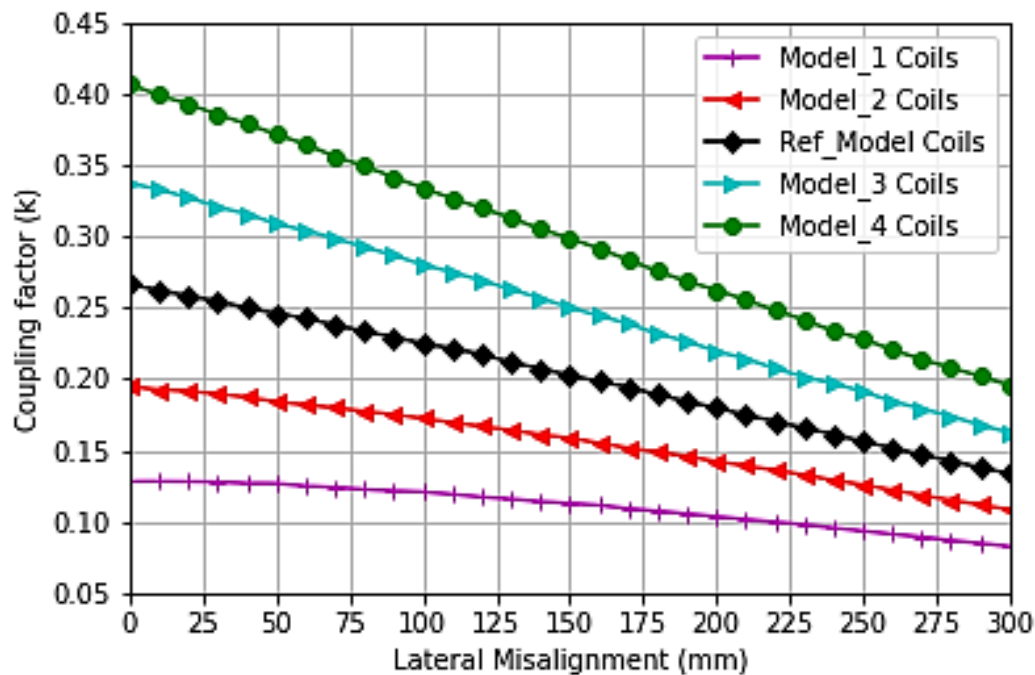


Figure 5.16: Lateral Misalignment Parametric Analysis of Flux-Pipe Resonant Coils.

The five model resonant coil designs were subjected to a lateral displacement of between 0 to 300mm (30cm) with a step increase of 10mm (1cm). The variation of the coupling coefficient for each unit increase in lateral displacement along the X-axis is shown in Figure 5.16.

From the result shown in Figure 5.16, it is noted that an increase in the number of turns improves the misalignment performance at any particular value of lateral misalignment. For example, Model 1 with 14 number of coils has the least coupling coefficient of 0.10 at the lateral misalignment of 300 mm. Similarly, Model 4 with 34 number of turns has the highest coupling coefficient of 0.23 at lateral misalignment of 300 mm. The same trend was also noted at zero misalignments. Model 1 with 14 number of coils has the least coupling coefficient of 0.16 at zero lateral misalignments while Model 4 with 34 number of turns has the highest coupling coefficient of 0.47 at zero lateral misalignments.

Thus, it can be concluded that a flux-pipe WPT model with more number of turns has a better lateral misalignment performance when compared with the similar model configuration with a lesser number of turns.

5.7.2 Longitudinal Misalignment Performance of Flux-Pipe Resonant Coils

The analysis for the longitudinal misalignment was performed by varying the position of the secondary coil along the y-axis and the value of the coupling coefficient was evaluated based on each unit displacement of the coil along that axis. The three resonant coil design was subjected to a longitudinal displacement of between 0 to 300mm. The variation of the coupling coefficient for each unit increase in longitudinal displacement along the y-axis is shown in Figure 5.17.

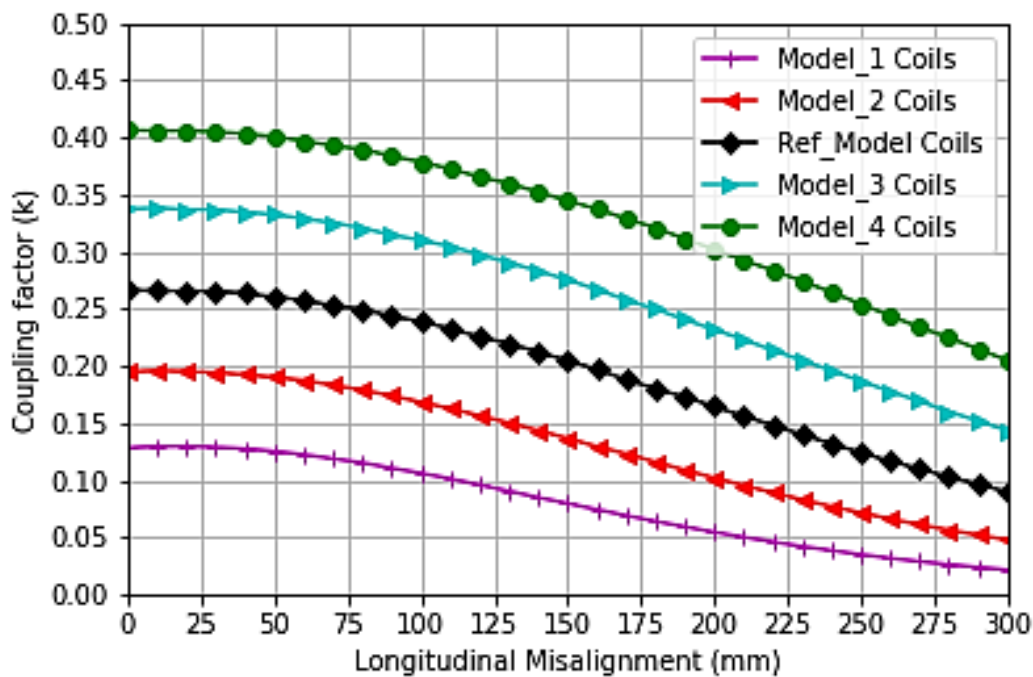


Figure 5.17: Longitudinal Misalignment Parametric Analysis of Flux-Pipe Resonant Coils

From the result shown in Figure 5.17, it is noted that an increase in the number of turns improves the longitudinal misalignment performance at any particular value of longitudinal misalignment. For example, Model 1 with 14 number of coils has the least coupling coefficient of 0.05 at lateral

misalignment of 300 mm. Similarly, Model 4 with 34 number of turns has the highest coupling coefficient of 0.26 at lateral misalignment of 300 mm.

The same trend was also noted at zero misalignments. Model 1 with 14 number of coils has the least coupling coefficient of 0.16 at zero lateral misalignments while Model 4 with 34 number of turns has the highest coupling coefficient of 0.47 at zero lateral misalignments. Thus, it can be concluded that a flux-pipe WPT model with more number of turns has a better longitudinal misalignment performance when compared with the similar model configuration with less number of turns.

Comparing the results obtained for the longitudinal misalignment analysis with the results obtained for the lateral misalignment analysis, it can be concluded that flux-pipe resonant coil with K_{df} less than 1 has a better magnetic coupling for each unit displacement when subjected to lateral misalignment than when subjected to longitudinal misalignment. Similarly, a flux-pipe resonant coil with K_{df} greater than 1 has a better magnetic coupling for each unit displacement when subjected to longitudinal misalignment than when subjected to lateral misalignment.

5.7.3 Performance of Flux-Pipe Resonant Coils under Airgap Variation

The performance analysis for airgap variation was undertaken by varying the position of the secondary coil along the Z-axis and the value of the coupling coefficient measured based on each unit displacement of the coil along that axis. The five flux-pipe resonant coil designs were subjected to vertical displacement of between 110mm to 250mm.

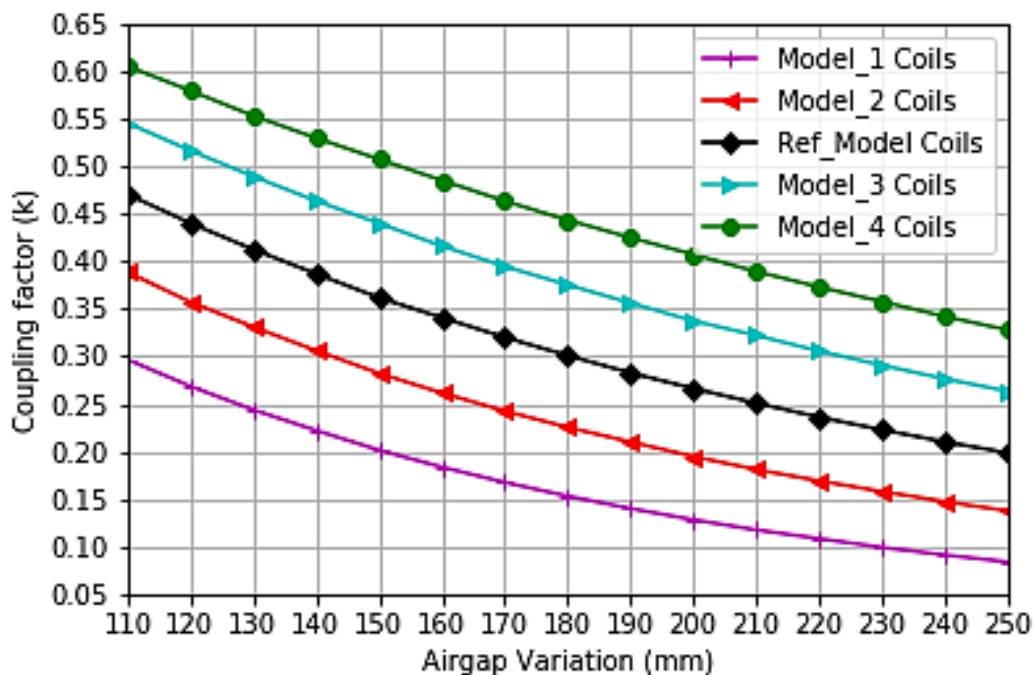


Figure 5.18: Airgap Variation Parametric Analysis of Flux-Pipe Resonant Coils

The variation of the coupling coefficient for each unit increase in airgap along the Z-axis is shown in Figure 5.18. From the result shown in Figure 5.18, it is noted that an increase in the number of turns improves coupling performance at any particular value of airgap. For example, Model 1 with 14 number of coils has the least coupling coefficient of 0.10 at airgap of 250 mm. Similarly, Model 4 with 34 number of turns has the highest coupling coefficient of 0.40 at airgap of 250 mm.

The same trend was also noted at zero misalignments. Model 1 with 14 number of turns has the least coupling coefficient of 0.35 at airgap of 110 mm while Model 4 with 34 number of turns has the highest coupling coefficient of 0.67 at airgap of 110 mm. It is important to note that a strong coupling factor of 0.5 was obtained at an airgap of 120 mm for Model Ref, 150 mm for Model 3 and 190mm for Model 4.

Thus, it can be concluded that a flux-pipe WPT model with more number of turns has a better performance at larger airgap when compared with the similar model configuration with less number of turns.

Model 4 has the highest magnetic coupling under all the parametric analyses. Thus, Model 4 with 34 number of turns gives the optimal design and will be used for eddy current and circuit analyses with the circular and rectangular model designs.

5.8 Eddy Current Analysis of Resonant Coils

As discussed in chapter 4, the eddy current analysis is performed to identify and ascertain the level of losses in the coil system. There are basically three types of losses present in a resonant coil system: the ohmic losses, eddy current losses and core losses. The ohmic losses are losses as a result of the resistance in the coil windings, eddy current losses are losses that occur at the shield plates as a result of magnetic flux leakages while core losses are losses in the ferrite core as a result of the magnetization and demagnetization of the core due to the high-frequency alternating current.

The first analysis performed was to ascertain the level of losses in each coil designs as a result of operating the WPT system for a level 2 power ratings of 8 kW as defined by SAE J1772 regulations. The initial evaluation of the losses for each of the coil design is undertaken by injecting an excitation current of 32 A in the coil windings at a resonant frequency of 85 kHz. The resonant frequency of 85 kHz was chosen because it is the operating frequency proposed by SAE J2954 task force for interoperability of different WPT charging systems. The results of the analyses are presented in Table 5.6.

Table 5.6: Coil Parameters and Loss Evaluation of Resonant Coil for 8 kW Power Application

| Parameter | Circular Coil | Rectangular Coil | Flux-Pipe Coil |
|----------------------------------|----------------------|----------------------|----------------------|
| Airgap | 200 mm | 200 mm | 200 mm |
| Primary Self-Inductance, L_p | 124.69 μH | 136.84 μH | 357.88 μH |
| Secondary Self-Inductance, L_s | 124.56 μH | 136.84 μH | 357.02 μH |
| Coupling Coefficient, k | 0.184 | 0.171 | 0.385 |
| Ohmic Losses | 42 W | 62 W | 179 W |
| Core Losses | 8 W | 8 W | 493 W |
| Eddy Current Losses | 11 W | 20 W | 105 W |
| Total Power Losses | 61 W | 90 W | 777 W |

For such medium power application, it is noted that the flux-pipe coil model has a significant power loss of more than 10 times of the power losses in the circular model under the same circuit operation. The circular coil has a higher coupling coefficient and lower losses when compared with the rectangular coil. Despite the high power losses in the flux-pipe coil, it is observed that the self-inductance and coupling coefficient is more than twice the values obtained in either of the circular and rectangular coils.

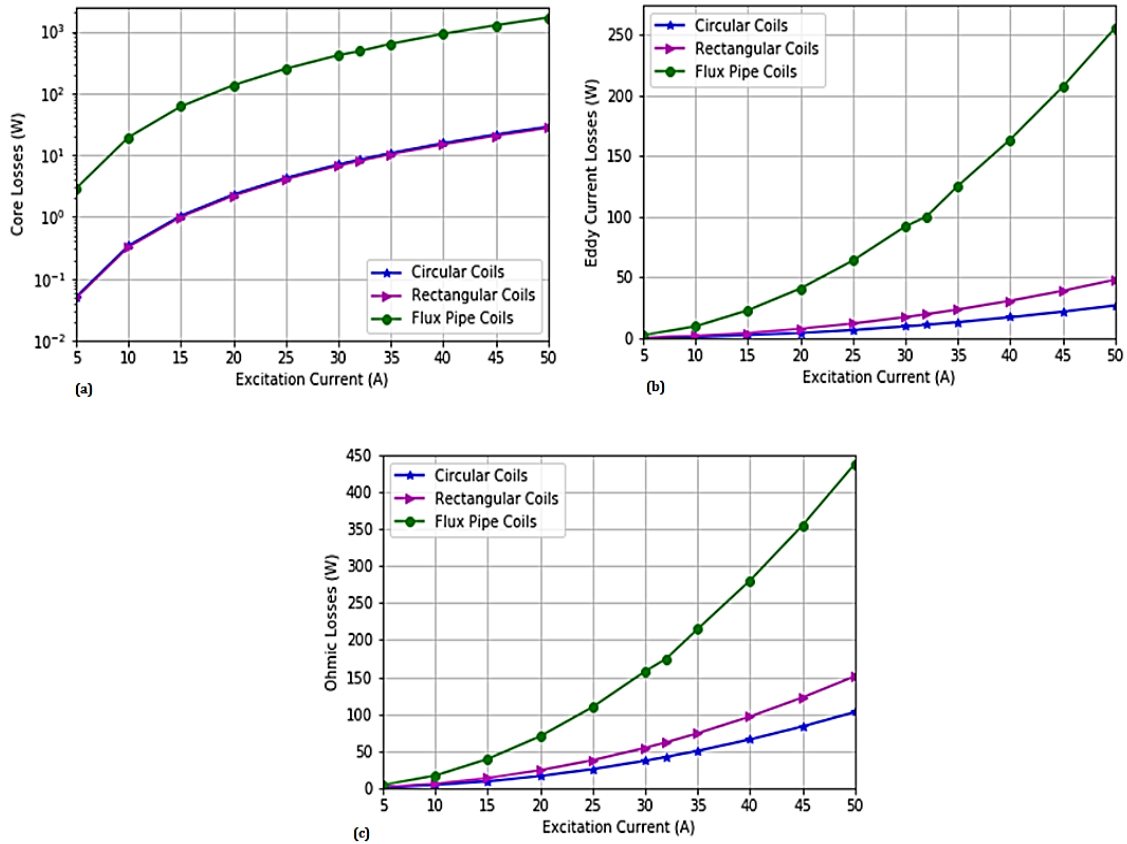


Figure 5.19: Losses in Coil Models due to Variation in Excitation Current. (a) Core Losses. (b) Eddy Current Losses (c) Ohmic Losses

The second analysis was then performed to ascertain the level of losses in each coil designs as a result of an increase in excitation currents. This was achieved by injecting a parametric sweep of excitation currents into the coil windings at high operating frequency (like 85 kHz) and the losses for each value of excitation current was evaluated. The results of the analyses are presented in Figure 5.19.

From the results presented in Figure 5.19, it is noted that there is a gradual increase in the three types of losses with an increase in current for all the models analysed. The circular and rectangular coils have similar performance due to their similarity in shape having relatively the same amount of losses with losses in the rectangular coils slightly higher. Model 4 of the flux-pipe model has the highest amount of losses for the three losses analysed at each value of current. This expected because of the high number of ampere-turns in the flux-pipe model as a result of the higher number of turn ratios and the presence of double flux on each side of the core. The presence of high losses in the system significantly impacts on the efficiency and power output. For most practical applications, the current is reduced which leads to low power output.

Similarly, a frequency response of the various coil models was performed by varying the frequency at a fixed excitation current (typically 32 A for an 8 kW WPT system). The losses encountered over the range of frequencies from 5 kHz to 100 kHz are illustrated in Figure 5.20.

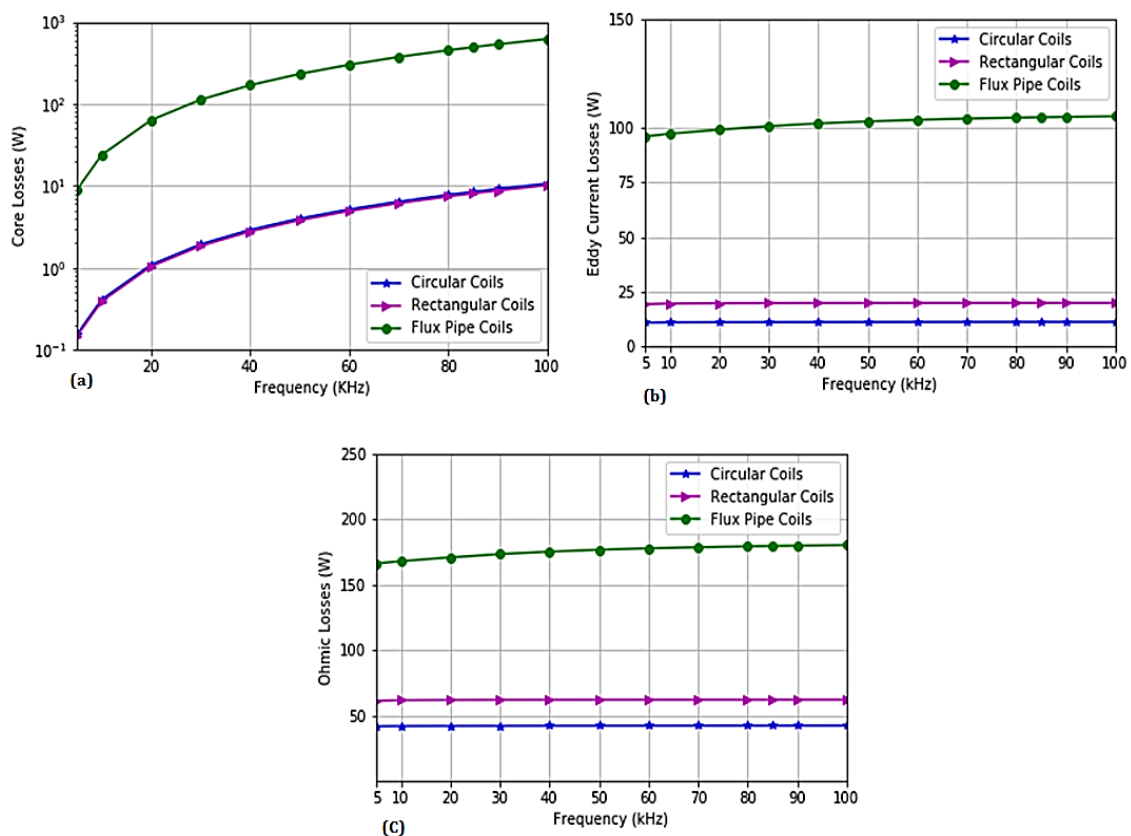


Figure 5.20: Losses in Coil Models due to Variation in Frequency. (a) Core Losses. (b) Eddy Current Losses (c) Ohmic Losses

From the results presented in Figure 5.20, the ohmic losses and eddy current losses are relatively constant over a range of frequency above the threshold frequency (around 10kHz).

But, there is a significant increase in core losses with an increase in frequency for all the three models. The higher the rate of magnetization/demagnetization of the ferrite core, the higher the core losses. As a result, most practical designs are operated at low frequencies to limit the amount of eddy current losses in the system.

5.9 Circuit Analysis of Resonant Coils

In the circuit analysis, the performance of the coil designs in terms of coil-to-coil efficiency and power output is evaluated. The parameters required for accurate analysis are obtained from the eddy current analysis solution. The required parameters for the three model coils at an adaptive frequency of 85 kHz are presented in Table 5.7.

Table 5.7: Circuit Parameters of Resonant Coils from Eddy Current Solution

| Parameter | Circular Coil Design | Rectangular Coil Design | Flux-Pipe Coil Design |
|---------------------------------------|----------------------|-------------------------|-----------------------|
| Airgap | 200 mm | 200 mm | 200 mm |
| Adaptive Frequency | 85 kHz | 85 kHz | 85 kHz |
| Primary Self-Inductance, L_p | 124.69 μH | 136.84 μH | 357.88 μH |
| Secondary Self-Inductance, L_s | 124.56 μH | 136.84 μH | 357.02 μH |
| Mutual Self-Inductance, L_m | 23.01 μH | 23.48 μH | 137.44 μH |
| Coupling Coefficient, k | 0.184 | 0.171 | 0.385 |
| Primary Intrinsic Resistance R_p | 20.57 m Ω | 30.17 m Ω | 84.39 m Ω |
| Secondary Intrinsic Resistance, R_s | 20.52 m Ω | 30.27 m Ω | 85.95 m Ω |

The values of the intrinsic resistance for each coil model is proportional to the ohmic losses presented in Table 5.6. The flux-pipe model has the largest value of intrinsic resistance, which corresponds, with having the largest amount of ohmic losses.

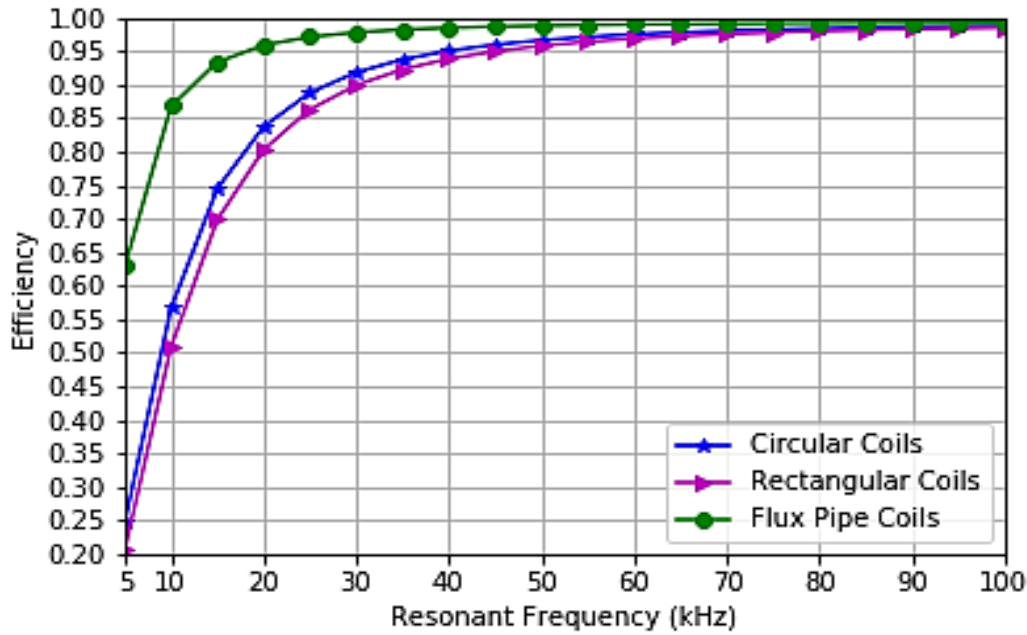


Figure 5.21: Relationship between Maximum efficiency and the Parameter $k\sqrt{Q_{ps}}$ over a range of Frequencies.

Based on the parameters obtained in Table 5.7, the relationship between maximum efficiency η_{max} and the parameter $k\sqrt{Q_{ps}}$ over a range of frequencies from 5 kHz to 100 kHz was evaluated using equation 4.34 and the graph presented in Figure 5.21.

Based on the result presented in Figure 5.21, it is noted that increases in resonant frequencies positively impact on the maximum efficiency of the coil. While the rectangular and circular coil showed similar performance characteristics, the flux-pipe model has a better performance over each step increase in frequency. From the result presented in Figure 5.21, an optimum resonant frequency of 40 kHz was adopted for the model 4 flux-pipe model while optimum resonant frequencies of 85 kHz and 100 kHz was adopted for the circular coil and rectangular coil respectively.

For the flux-pipe model, the maximum efficiency achievable at 40 kHz is 99.22%. Similarly, the circular coil can achieve maximum efficiency of 99.31% at the optimum efficiency of 85 kHz while the rectangular coil can achieve maximum efficiency of 99.28%.

For most practical designs, the optimum efficiency and power transferred are dependent on the value of the load resistance. This is because maximum power can be transferred at a particular load, but not at the maximum efficiency for that load. In order to obtain the optimum efficiency for a particular load resistance, a parametric sweep of load resistance is performed and the values of the efficiency and power output evaluated. The result of this analysis for S-S compensation topology and S-P compensation topology is presented in the next two sections.

5.9.1 Impact of Load Resistance for S-S Compensation Topology.

In order to determine the impact of load resistance on the power transfer efficiency and the power output, a parametric sweep of load resistance at the selected resonant frequencies for each model coils was undertaken and the power transfer efficiency and power output was evaluated and calculated. For this research, the range of load resistance analysed was from 10Ω to 300Ω . The results are presented in Figure 5.22.

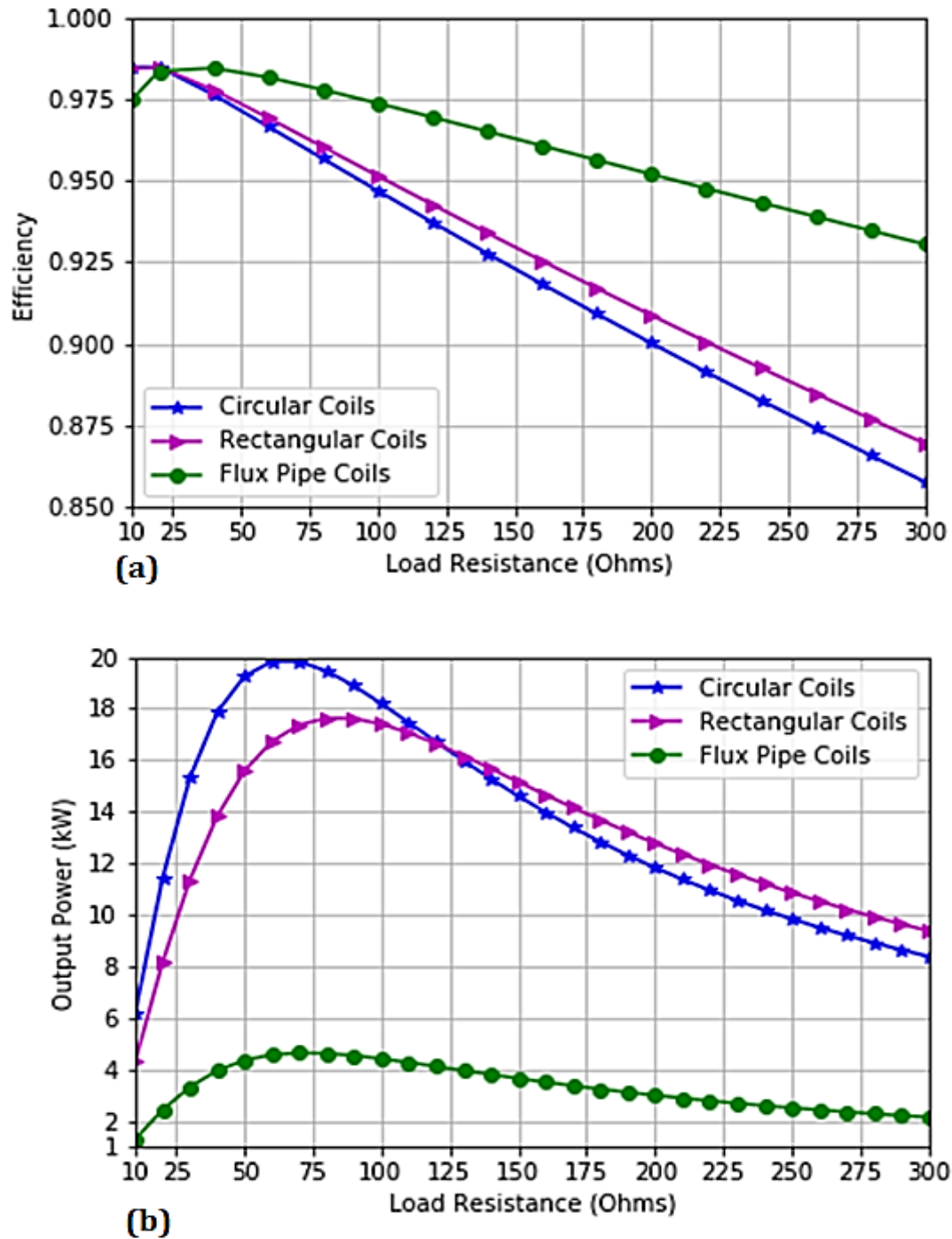


Figure 5.22: Effect of Load Resistance on the Performance of Resonant Coils for S-S Compensation Topology. (a) Effect on Efficiency. (b) Effect on Power Output.

The optimum values of efficiency and power output for each model coil designs do not correspond to a particular value load resistance. For example, the circular coil model achieved a maximum efficiency of 98.48% at a load resistance of 20Ω with an output power of 11.40 kW while maximum power of 19.82kW was transferred at a load resistance of 60Ω at an efficiency of 96.65%. A similar trend was observed for the rectangular coil design and model 4 flux-pipe design. But generally, after the optimum values of the efficiencies and output power was attained for each model coil designs, a further increase in the load resistance leads to a corresponding decrease in both the power output and efficiency.

For practical design implementation, there is always a trade-off between power output and efficiencies depending on the critical requirements for the system operations. Generally, for a wireless power transfer system, the power transfer efficiency is the most important parameter. Thus, for the proposed coil designs, a load resistance of 20Ω was selected as the optimum load resistance. The overall system performance for a load resistance of 20Ω is listed and summarized in Table 5.8.

Table 5.8: Summary of Performance Characteristics of Resonant Coil Models.

| Parameters | S-S Configuration | | |
|-------------------------|-------------------|------------------|---------|
| | Circular Coil | Rectangular Coil | Model 4 |
| Resonant Frequency | 85 kHz | 100 kHz | 40 kHz |
| $k\sqrt{Q_{ps}}$ | 288 | 278 | 252 |
| Input Voltage | 300 V | 300 V | 300 V |
| Output Voltage | 478 V | 403 V | 397 V |
| Load Resistance | 20 Ω | 20 Ω | 20 Ω |
| Input Current | 39.27 A | 27.69 A | 13.75 A |
| Output Current | 23.88 A | 20.17 A | 9.93 A |
| Input Power | 11.58 kW | 8.26kW | 4.00 kW |
| Output Power | 11.40 kW | 8.13 kW | 3.94 kW |
| Total Power Losses | 180 W | 130 W | 60 W |
| Coil-to-Coil Efficiency | 98.85% | 98.47% | 98.44 % |

From the summary of results presented in Table 5.8, it is noted that there is a strong relationship between the term $k\sqrt{Q_{ps}}$, the coil-to-coil efficiency and the power output of resonant coils. The circular coil with the highest value of $k\sqrt{Q_{ps}}$ has the highest efficiency and power output. Similarly, the model 4 flux-pipe coils with the lowest value of $k\sqrt{Q_{ps}}$ has the lowest efficiency and power output.

In order to establish the performance of each coil models based on the SAE J2954 standard under a series-series compensation topology, each coil performance was evaluated at a resonant frequency of 85 kHz with a load resistance of 20 Ω. The result of the simulation is presented in Table 5.9.

Table 5.9: Performance Characteristics of Resonant Coil Models Based on SAE J2954 standard for the S-S Compensation Topology.

| Parameters | S-S Configuration | | |
|-------------------------|-------------------|------------------|-------------|
| | Circular Coil | Rectangular Coil | Model 4 |
| Resonant Frequency | 85 kHz | 85 kHz | 85 kHz |
| $k\sqrt{Q_{ps}}$ | 288 | 237 | 527 |
| Input Voltage | 300 V | 300 V | 300 V |
| Output Voltage | 478 V | 463 V | 201 V |
| Load Resistance | 20 Ω | 20 Ω | 20 Ω |
| Input Current | 39.27 A | 37.57 A | 3.62 A |
| Output Current | 23.88 A | 23.15 A | 5.38 A |
| Input Power | 11.58 kW | 10.95 kW | 1.09 kW |
| Output Power | 11.40 kW | 10.72 kW | 1.08 kW |
| Total Power Losses | 180 W | 230 W | 10 W |
| Coil-to-Coil Efficiency | 98.85 % | 97.86 % | 99.14 % |

From the result presented in Table 5.9, it is observed that the rectangular and circular coil are capable of high bidirectional WPT of over 10 kW at efficiencies above 97 %. These results agree with the submission of many researchers presented in the course of the literature review. In contrast, at 85 kHz, the power output of the flux-pipe model dropped below 1 kW and the efficiency increase by less than 0.5 % despite doubling the value of $k\sqrt{Q_{ps}}$. The poor performance is because of the relatively constant value of maximum efficiency above a particular threshold frequency. For the flux-pipe model, the threshold frequency was 50 kHz as illustrated in Figure 5.21.

5.9.2 Impact of Load Resistance in S-P Compensation Topology.

In order to determine the impact of load resistance on the power transfer efficiency and the power output, a parametric sweep of load resistance at the selected resonant frequencies for each model coils was undertaken and the power transfer efficiency and power output was evaluated and calculated. For the S-P compensation circuit design, the range of load resistance analysed was from 10 Ω to 300 Ω just like the case of the S-S compensation topology. The results are presented in Figure 5.23.

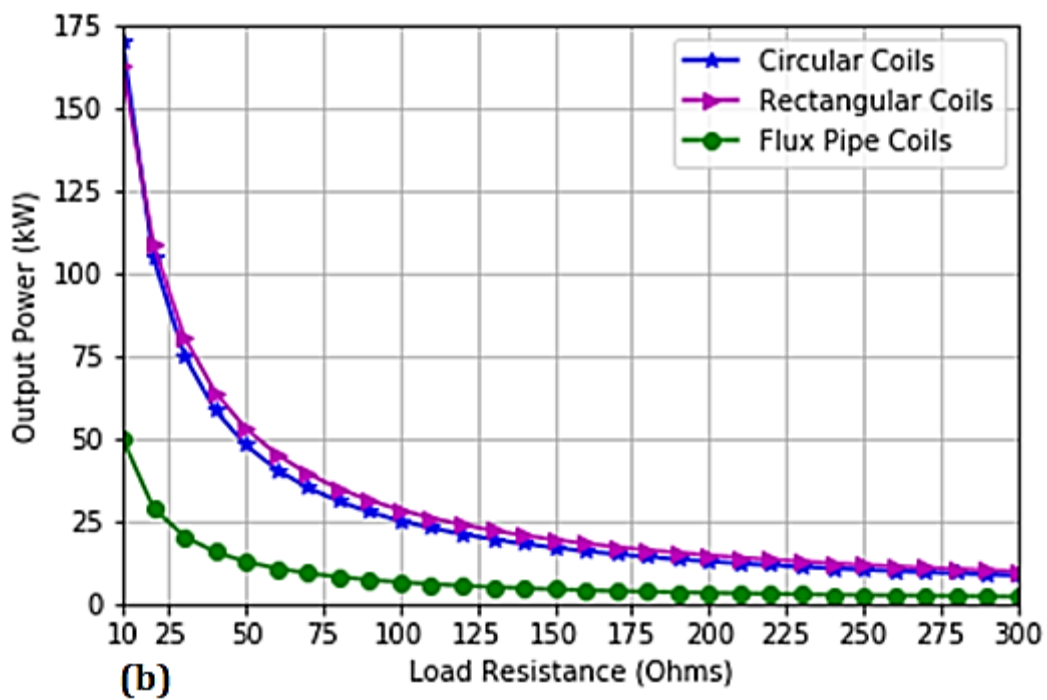
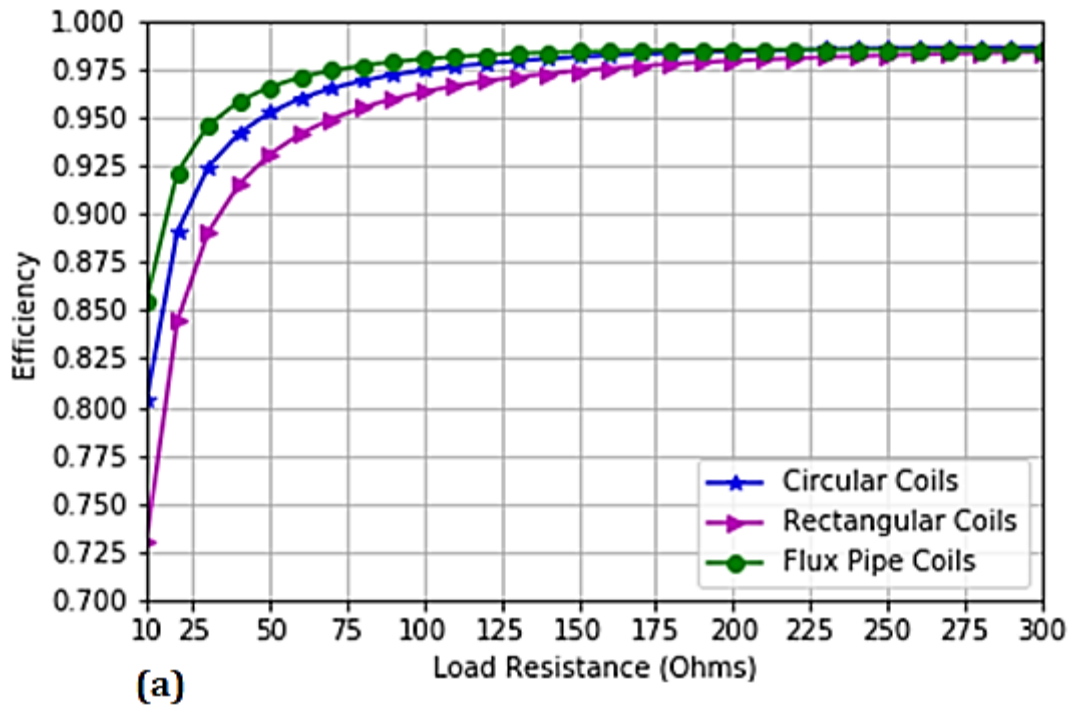


Figure 5.23: Effect of Load Resistance on the Performance of Resonant Coils for S-P Compensation Topology (a) Effect on Efficiency. (b) Effect on Power Output.

For the S-P compensation topology, there is an inverse relationship between the power transferred and the power transfer efficiency. For all the coil model designs, there was an increase in the power transfer efficiency as the value of the load resistance. This is in contrast to the performance obtained in relation to the power output. It is noted that an increase in load resistance leads to a corresponding decrease in power output.

Due to this inverse relationship, the selection of the appropriate load resistance is dependent on the type of application. If the system design is aimed at high power transferred, increasing the load resistance is the most viable option. Also, if the system requirement is aimed at high power transfer efficiency, using a small load resistance would be the most appropriate design.

For practical design implementation, there is always a trade-off between power output and efficiencies depending on the critical requirements for the system operations. Generally, for a wireless power transfer system, the power transfer efficiency is the most important parameter. Thus, for the proposed coil designs employing the S-P compensation topology, a load resistance of 200Ω was selected as the optimum load resistance. The overall system performance for a load resistance of 200Ω is listed and summarized in Table 5.10.

Table 5.10: Performance Characteristics of Resonant Coil Models for the S-P Compensation Configuration

| Parameters | S-P Configuration | | |
|-------------------------|-------------------|------------------|--------------|
| | Circular Coil | Rectangular Coil | Model 4 |
| Resonant Frequency | 85 kHz | 100 kHz | 40 kHz |
| $k\sqrt{Q_{ps}}$ | 288 | 278 | 252 |
| Input Voltage | 300 V | 300 V | 300 V |
| Output Voltage | 1604 V | 1718 V | 819 V |
| Load Resistance | 200 Ω | 200 Ω | 200 Ω |
| Input Current | 43.59 A | 50.18 A | 11.38 A |
| Output Current | 8.02 A | 8.60A | 4.10A |
| Input Power | 13.08 kW | 15.05 kW | 3.41 kW |
| Output Power | 12.88 kW | 14.77 kW | 3.36 kW |
| Total Power Losses | 200 W | 280 W | 50 W |
| Coil-to-Coil Efficiency | 98.40 % | 98.17 % | 98.47 % |

From the results presented in Table 5.10, it is noted that the circular and rectangular coil model have similar characteristics due to the similarity in their shapes with the circular coil having a slightly higher performance is efficiency while the rectangular coil has a higher performance in the amount of power output. The model 4 coil has similar efficiency value with the circular coil but at a lower power output due to the limitations already discussed in details in the literature- the double flux problem.

It is important to note that the S-P compensation comes with high output voltages for all the three model analysed. This is because of the high voltage build-up in the secondary compensating capacitor C_p as shown in Figure 4.9. Since the load resistance R_L is connected in parallel with the compensation capacitor, both have the same voltage across them. As a result, the load resistance R_L needs to be large in order to limit the amount of current flowing in the load to a practical level.

From the summary of results presented in Table 5.10, it is also noted that there is a strong relationship between the term $k\sqrt{Q_{ps}}$, the coil-to-coil efficiency and the power output of resonant coils. The circular coil with the highest value of $k\sqrt{Q_{ps}}$ has the best performance. Similarly, the model 4 with the lowest value of $k\sqrt{Q_{ps}}$ has the lowest circuit performance.

Similarly, in order to establish the performance of each coil models based on the SAE J2954 standard under a series-parallel compensation topology, each coil performance was evaluated at a resonant frequency of 85 kHz with a load resistance of 200 Ω . The result of the simulation is presented in Table 5.11.

Table 5.11: Performance Characteristics of Resonant Coil Models Based on SAE J2954 standard for S-P Compensation Configuration

| Parameters | S-P Configuration | | |
|-------------------------|-------------------|------------------|--------------|
| | Circular Coil | Rectangular Coil | Model 4 |
| Resonant Frequency | 85 kHz | 85 kHz | 85 kHz |
| $k\sqrt{Q_{ps}}$ | 288 | 237 | 527 |
| Input Voltage | 300 V | 300 V | 300 V |
| Output Voltage | 1604 V | 1692 V | 819 V |
| Load Resistance | 200 Ω | 200 Ω | 200 Ω |
| Input Current | 43.59 A | 50.23 A | 11.31 A |
| Output Current | 8.02 A | 8.60A | 4.10A |
| Input Power | 13.08 kW | 15.07 kW | 3.39 kW |
| Output Power | 12.88 kW | 14.78 kW | 3.36 kW |
| Total Power Losses | 200 W | 290 W | 30 W |
| Coil-to-Coil Efficiency | 98.40 % | 98.08 % | 98.96 % |

From the result presented in Table 5.11, it is observed that the rectangular and circular coil are capable of transmitting high power of over 12 kW at efficiencies above 98 %. These results agree with the submission of many researchers presented in the course of the literature review. Similarly, at 85 kHz, the power output of the flux-pipe model remains relatively constant at above 3 kW and the efficiency increase by more than 0.4 % despite doubling the value of $k\sqrt{Q_{ps}}$. The good performance of the flux-pipe coil model is as a result of the good performance characteristics of the S-P compensation topology. The rectangular and circular coil design can be used for unidirectional high power application above 11 kW. In contrast, the flux-pipe resonant coil model is well suited for low power application. But the model can be improved for high power application for both the unidirectional and bidirectional WPT operations.

5.9.3 Impact of Misalignment on the Efficiency of Coil Designs.

From the previous two sections, the optimum values of resonant frequencies and load resistance for each coil model designs were presented for coil designs at airgap of 200mm with no misalignment. For most practical applications, there are possibilities of misalignment in the course of operation of the wireless coil designs. In order to ascertain the impact of coil misalignment on the efficiencies of each of the coil designs, each of the secondary coil of the coil models was subjected to a level of lateral and longitudinal misalignments at a fixed airgap of 200 mm and the efficiency of the coil system was evaluated.

The efficiency performance for the S-S compensation topology for each of the coil model is presented in Figure 5.24. At 150 mm lateral and longitudinal misalignment, the circular and rectangular coil designs efficiencies dropped significantly, but the model 4 flux-pipe design still maintains high efficiency. Similarly, at 300 mm lateral and longitudinal misalignment, the coil-to-coil efficiencies of the circular and rectangular coil systems are almost zero. This is in contrast with the efficiency values of the model 4 flux-pipe coil which maintains coil-to-coil efficiency of above 85%.

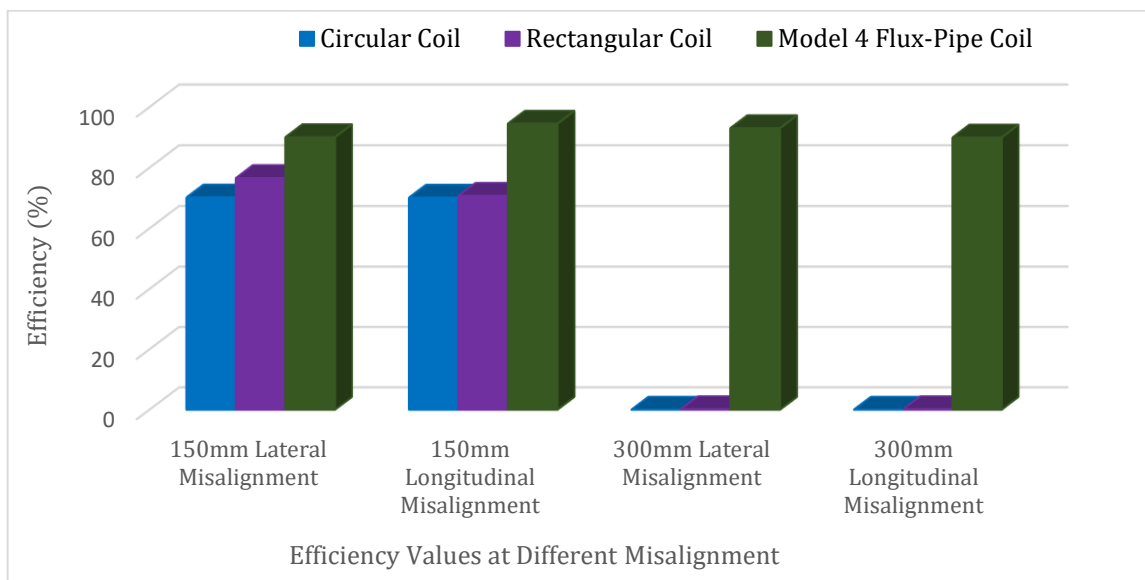


Figure 5.24: Misalignment Performance of Resonant Coil Designs for S-S Compensation Topology

Similarly, the efficiency performance for the S-P compensation topology for each of the coil model is presented in Figure 5.25.

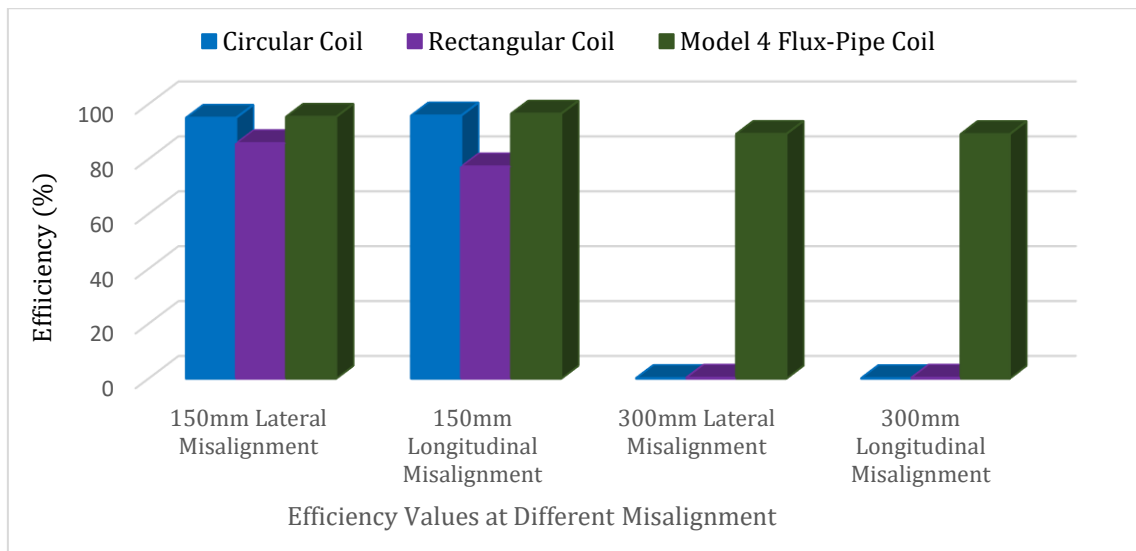


Figure 5.25: Misalignment Performance of Resonant Coil Designs for S-P Compensation Topology.

At 150 mm lateral and longitudinal misalignment, the circular and the flux-pipe model coil designs' displayed similar performance characteristics, but the rectangular coil design efficiency dropped slightly. Similarly, at 300 mm lateral and longitudinal misalignment, the coil-to-coil efficiencies of the circular and rectangular coil systems were almost zero as obtained in the S-S compensation topology. This is in contrast with the efficiency values of the flux-pipe coil which maintains coil-to-coil efficiency of above 80%.

The results obtained and presented in this chapter from all the performance analyses of the three coil designs further confirms all the reports presented in the literature reviews. The performance analysis results obtained for coupling coefficient, misalignment, power output and efficiencies of the circular, rectangular and flux-pipe models all agree with reported work of literature.

5.10 Summary

In this chapter, three common coil designs were modelled and analysed to ascertain their individual performances. The coil designs are circular, rectangular and flux-pipe model resonant coils. Using a coil dimension factor of 1 for the flux-pipe model, the three coil models were subjected to magnetostatic analysis, eddy current and circuit analysis.

In the magnetostatic analysis, the three models were subjected to a parametric analysis to ascertain their current saturation limits and magnetic coupling under various misalignments. From the results presented, the circular coil, rectangular coil model Ref flux pipe models can withstand up to an excitation current of 100 A without their respective ferrite cores going into saturation. Similarly, for each of the resonant coil models, the maximum values of the flux-density distribution are concentrated around the middle of the coil windings. This is an indication that the electric field strength is maximum at those regions.

Similarly, from the results presented for the misalignment performance and variation of the airgap, it was observed that the flux pipe model displayed the best performance for all the misalignment tests performed. It was further noted that enhanced performance can be obtained with the flux-pipe by remodelling the coil design for a greater number of turns based on the increase in the coil dimension factor. The consequence of the increase in the coil-turns causes a corresponding decrease in the path of the magnetic field flux resulting in less opposition to the creation of that flux for any fixed amount of amp-turns.

The enhanced version of the flux-pipe coil design, together with the circular coil and rectangular coil models were subjected to eddy current analysis to ascertain the level of losses present in the coil model systems for various values of current and frequencies. Three types of losses were identified for each of the coil models- the ohmic losses, eddy current losses and core losses. It was noted that the three categories of losses increase with an increase in excitation current; with a flux-pipe model having the highest amount of losses. Similarly, it was noted that for low-frequency range typically from 10kHz to 100kHz, the ohmic and eddy current losses was relatively constant while the core losses increase with an increase in frequency. The flux-pipe model was noted to have the highest amount of losses over the range of frequencies analysed.

From the overall loss results presented for the eddy current analyses, it is noted that core losses increase logarithmically with an increase in frequency and exponentially with an increase in excitation current. It is also noted that the ohmic losses in the system increase logarithmically with an increase in the current while the eddy current losses increase exponentially with an increase in frequency.

The circuit analysis was carried out to ascertain the coil-to-coil efficiencies and power output for each of the coil models under different compensation schemes. From the results obtained and presented, it was observed that the power output and coil-to-coil efficiency of resonant coil models is strongly related to the individual value of $k\sqrt{Q_{ps}}$ of the coils. The higher the value of $k\sqrt{Q_{ps}}$, the higher the values of efficiency and power transferred. It was noted that the circular coil with the highest value of $k\sqrt{Q_{ps}}$ showed the best performance while the flux-pipe model with the least value of $k\sqrt{Q_{ps}}$ has the least performance for both the S-S and S-P compensation scheme adopted. The major factor responsible for the low value of $k\sqrt{Q_{ps}}$ in the flux-pipe model are the high values of the intrinsic resistances of the coils due to a high number of coil turns.

Performance evaluation of the resonant coil designs for application based on the on SAE J2954 standard was undertaken for both series-series and series-parallel compensation topology. It was observed that the rectangular and circular coil designs are capable of bidirectional power transfer of above 8 kW at load resistance of 20 Ω at coil-to-coil efficiency of above 98% while the flux-pipe model is incapable of bidirectional power transfer of up to 1 kW despite doubling the value of $k\sqrt{Q_{ps}}$ at the same load resistance of 20 Ω . In contrast, the flux-pipe is capable of transferring more than 3 kW of

power under the S-P compensation topology at more than 98 % efficiency with a load resistance of 20 Ω . The circular and rectangular coil models were observed to have the capability of transferring more than 11 kW of power at more than 98 % efficiency in using S-P compensation scheme for the same load resistance. Thus, rectangular and circular coil models are capable of wireless power transfer above 8 kW for both the S-S and S-P compensation scheme while the flux-pipe model is capable of wireless power transfer of more than 3 kW using the S-P compensation topology.

Finally, the three model coil designs were subjected to lateral and longitudinal misalignment condition by displacing the secondary coils for each model by 150 mm and 300 mm respectively along the x-axis and y-axis. The evaluated efficiencies obtained at this level of misalignment was presented. It was noted that the rectangular coil and circular coil models were able to achieve an efficiency of 70% and above for a longitudinal and lateral misalignment of 150 mm while their efficiencies dropped to almost zero for the misalignment of 300 mm for both the S-S and S-P compensation scheme. Alternatively, the flux-pipe model design displayed the best performance with a minimum of 80% efficiency for all the misalignment analysis for both the S-S and S-P compensation schemes.

The next chapter will focus on optimal modelling of the flux-pipe model for higher values of $k\sqrt{Q_{ps}}$ and a significant increase in power output and efficiency for static and dynamic bidirectional wireless power transfer.

CHAPTER 6 Design Optimization of Flux-Pipe Model

6.1 Introduction

In this section, further improvement of the flux-pipe resonant coil was undertaken. With the results presented in chapter 5, it was noted that the Model 4 of the flux-pipe resonant coil has higher significant ohmic losses, eddy current losses and core losses when compared with the circular coil and rectangular coil topology. The presence of these losses was majorly responsible for the relatively low power output in the flux-pipe model in relation to the other two models.

The optimization of Model 4 flux-pipe resonant coil is achieved by selecting an appropriate shielding material based on published mathematical equations for eddy current losses. Similarly, appropriate equations for the ohmic losses and core losses was presented. From the mathematical analysis of these loss equations, the physical dimension and shape of Model 4 was modified to minimize these losses and improves the power output.

Two optimized flux-pipe models were created with one model adapted for static charging operations while the second model was designed for dynamic charging operations. Performance analysis of the two models in addition to a hybrid version of the two was carried out to ascertain the level of trade-off and improvements with respect to the traditional flux-pipe resonant coil.

6.2 Performance Limitation of Traditional Flux Pipe Design

A typical flux-pipe resonant coil is designed by tightly wrapping a coil of wire around a ferrite core.

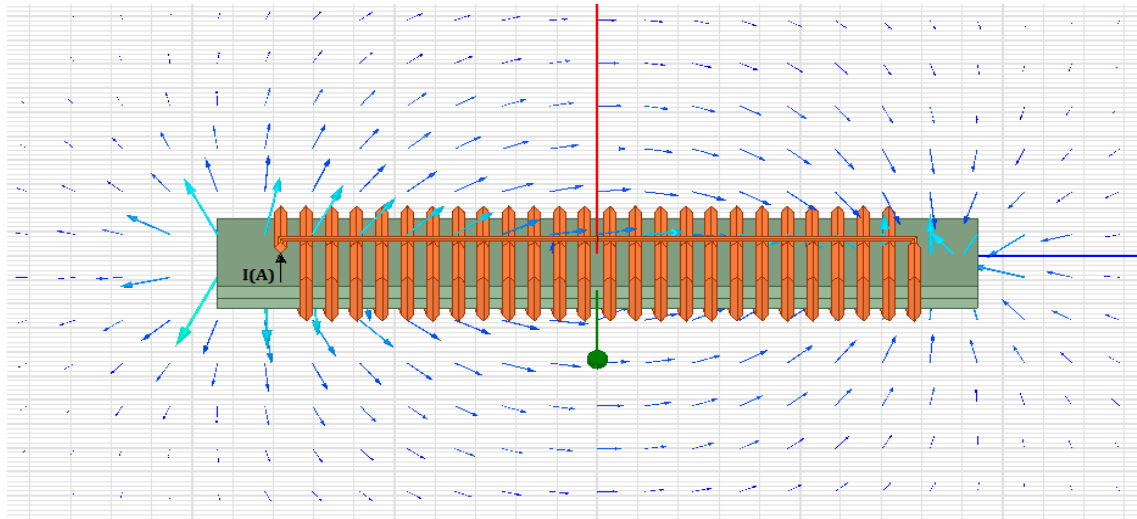


Figure 6.1: Magnetic Field around a Flux-pipe Resonant Coil

Whenever an electric current runs through the wire, a strong magnetic field is created, whose direction is dependent on the direction of the current governed by the right-hand grip rule. A typical illustration of the magnetic field around a flux-pipe resonant coil is illustrated in Figure 6.1. When the input current is an alternating current, a rotating magnetic field is generated around the conductor. If a second flux-

pipe coil (secondary coil) is placed above the first flux-pipe coil, an emf is induced based on Faraday’s law of electromagnetic induction. Because of the low permeability of air, only a partial coupling of the magnetic field occurs with the secondary coil. A significant portion of the magnetic field is leaked to air. The ratio of the coupled magnetic field to the total magnetic field can be described by the coupling factor “k” of the system. For the flux-pipe resonant coil design, there is the presence of an almost equal amount of magnetic flux at the upper and lower sides of the coil. The scenario is illustrated in Figure 6.2.

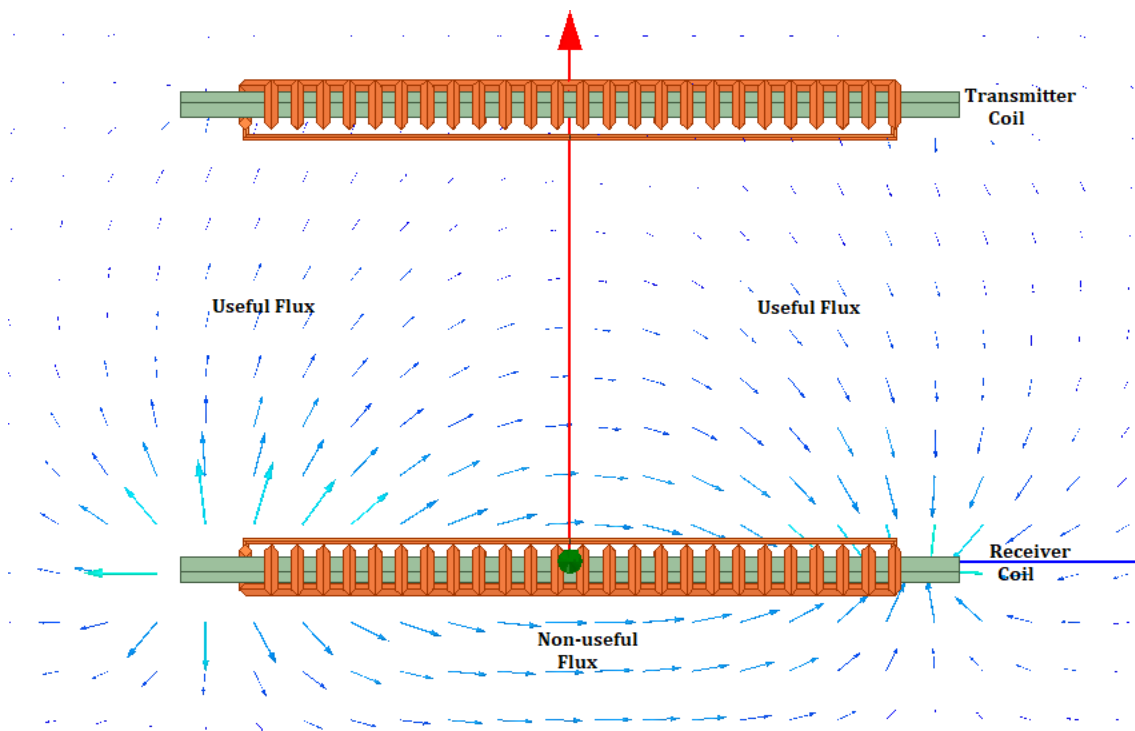


Figure 6.2: Magnetic Flux Distribution around an Unshielded Flux-Pipe Resonant Coil

As discussed in the literature, the major setback responsible for the low adoption of the Flux-pipe resonant coil topology for use in WPT application is the presence of a significant amount of “non-useful” flux with respect to the amount of useful flux in the system.

The “non-useful” flux is responsible for the majority of the eddy current losses on the aluminium shield plates. The importance of using the shielding plate has been discussed extensively in section 2.14.3. The essence of using a shield plate is to either absorb or reflect the non-useful flux and it is illustrated in Figure 6.3. For this particular case of aluminium which is a conductive material, shielding of the electromagnetic field is achieved by reflection of the non-useful flux.

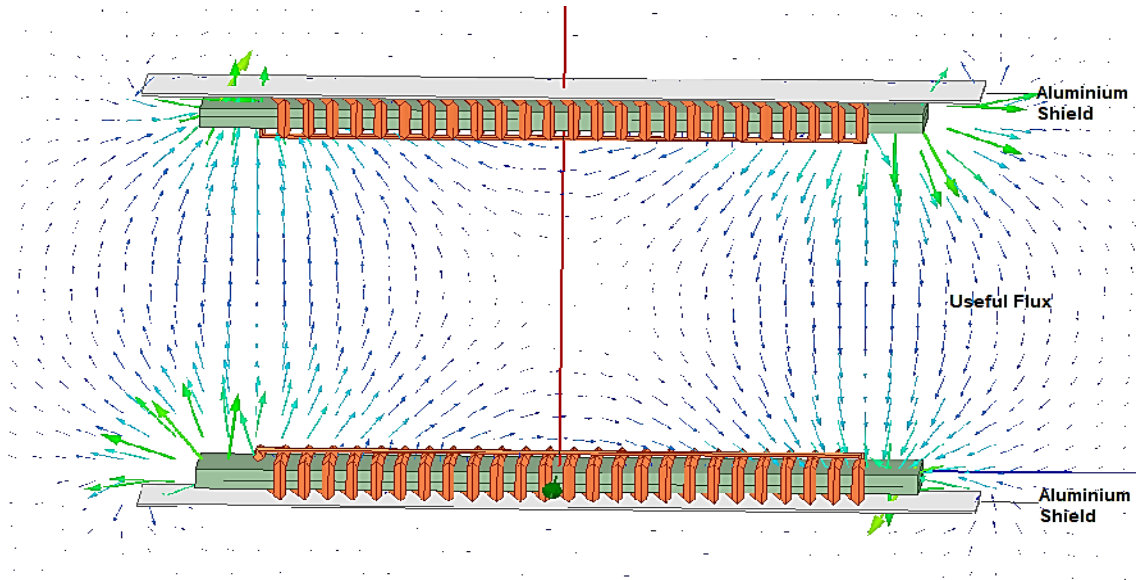


Figure 6.3: Magnetic Flux Distribution around Shielded Flux-Pipe Resonant Coils

Likewise, there is the presence of two additional losses present in the WPT system; the ohmic losses of the copper coil and the core loss in the ferrite core used in boosting the magnetic flux of the flux-pipe coil.

6.3 Governing Equations for Losses in Flux-Pipe Resonant Coil System

The ohmic losses in the coil winding are given mathematically by[19][179];

$$P_{ohmic} = I^2 R_{ac} \quad 6.1$$

Where I (A) is the current in the coil windings and R_{ac} is the A.C resistance of the coil windings consisting of D.C resistance and resistance due to the skin and proximity effect[19]. Optimal design to significantly reduce the ohmic losses in the copper windings will involve the reduction of either the current or the total A.C resistance of the coil or both.

Similarly, the power loss in the ferrite core can be expressed mathematically as[131]:

$$P_{core} = C_m f^\alpha B_{max}^\beta \quad 6.2$$

Where C_m , α and β are constants which are dependent on the grade and properties of the ferrite core used. For the FDK 6H40 ferrite core used for this research, the values of the constants are $C_m = 2.0312$, $\alpha = 1.418$, and $\beta = 2.755$ [131]. f is the resonant frequency (Hz) and B_{max} (T) is the maximum magnetic flux density in the core. Optimal design with low amount core losses will require a significant reduction of the amount of magnetic flux density as well as the resonant frequency at high current.

According to P. P. Parthasaradhy and S. V Ranganayakulu [180], the power loss per unit mass of a thin sheet due to eddy current under certain conditions of uniform material and magnetic field with no skin and proximity effect is given by;

$$P_{eddy} = \frac{\pi^2 \cdot B_{max}^2 \cdot d^2 \cdot f^2}{6 \cdot \rho \cdot D} \quad 6.3$$

Where P_{eddy} is the eddy current power loss per unit mass (W/kg), d is the thickness of the shielding sheet (m), ρ is the resistivity of the material (Ωm) and D is the density of the material (kg/m^3). From the equation given above, it can be observed that using a material with higher resistivity and density reduces the amount of eddy current per unit mass in the shielding plate for a fixed value of B_{max} . Also, it is observed that an increase in the magnetic flux, sheet thickness and resonant frequency increases the eddy current losses. Similarly, the thickness d of the shielding sheet is kept as small as possible in order to further reduce the eddy current power losses.

In order to maintain a very high power transfer efficiency (PTE) of the coil, another important factor known as the quality factor must be increased, it is given mathematically as[16]:

$$Q = \frac{2\pi fL}{R} \quad 6.4$$

Where f is the resonant frequency of the resonator circuit, R is the coil intrinsic resistance and L is the self-inductance of the resonant coil. This indicates the ratio of inductive properties of the coil to its resistive properties. A greater value of Q indicates more inductances and less electrical resistance of the coils i.e. less electrical power losses in the coils. The quality factor can be increased by increasing the resonant frequency but it leads to higher losses in the power electronic components while increasing the self-inductance of the coil will likely increase the intrinsic resistance of the coil, thus, there should be a trade-off to ensure that the intrinsic resistance of the coil is as low as possible.

For a typical flux-pipe resonant coil, there are three areas of optimization- the coil winding, the ferrite core geometry and the selection of appropriate shield material based on equation 6.3 in order to achieve strong coupled, low loss, higher power and higher PTE of resonant coils.

6.4 Optimal Selection of Shielding Material

In the traditional flux-pipe model topology as well as other resonant coil topologies, Aluminium metal sheet is usually used for the shielding of electromagnetic flux[11], [131], [134]. On this aspect, there is a need to proffer another alternative to Aluminium as a shield based on equation 6.4. There are two types of shielding materials commonly used for WPT systems: conductive shield materials and magnetic shield materials. The use of these different materials comes with different forms of losses.

Three common conductive metal used for shielding of electromagnetic fields are copper, and aluminium Using equation 6.3, the eddy current losses per unit mass P_{eddy} was calculated for the two conductive metals as a function of B_{max} and frequency. The results are presented in Table 6.1.

Table 6.1: Eddy Current Loss per unit mass for Different types of Conductive Shields

| Parameters | Aluminium | Copper |
|---|-----------|--------|
| Thickness of Shield d (m) | 0.0015 | 0.0015 |
| Density of Material D | 2700 | 8900 |
| Resistivity of Material ρ (Ω) | 2.82E-08 | 1.68E- |
| P_{eddy} (W/kg) | 19.70 | 10.03 |

From the results presented in Table 6.1, it is noted that the eddy current losses in copper are less than twice the losses in aluminium. In addition, copper not reactive to concrete or lime-bearing cement. Since the governing equation 6.3 do not cover the eddy current losses that occurs in magnetic shields, an eddy current finite element analysis of common conductive and magnetic shields was undertaken using the flux-pipe Model Ref design for a typical 8 kW system with an excitation current of 32 A. The impact of the different types of conductive and magnetic shielding materials on self-inductance, coupling coefficient, ohmic losses, eddy current losses and core losses are illustrated in Table 6.2.

Table 6.2: Performance Characteristics of Flux-Pipe Resonant Coils with Different Shield Materials

| | Conductive Shields | | Magnetic Shields | |
|----------------------------------|--------------------|----------------|------------------|------------------|
| | Aluminium | Copper | Mumetal | Electrical Steel |
| Primary Self-Inductance, L_p | 215.00 μ H | 214.99 μ H | 532.66 μ H | 712.04 μ H |
| Secondary Self-Inductance, L_s | 212.23 μ H | 212.23 μ H | 527.33 μ H | 699.46 μ H |
| Coupling Coefficient, k | 0.255 | 0.255 | 0.096 | 0.064 |
| Ohmic Losses | 131W | 98 W | 1169 W | 483 W |
| Core Losses | 40W | 40 W | 195 W | 575 W |
| Eddy Current Losses | 62 W | 41 W | 1083 W | 294 W |
| Total Power Losses | 233 W | 179 W | 2, 447 W | 1,352 W |

The use of magnetic shields (Mumetal and electrical steel) has a significant impact on the self-inductance, coupling coefficient and power losses in a ferrite-cored WPT system. The use of such type of shielding material causes a significant drop in the magnetic coupling coefficient of between coils despite a massive increase in the self-inductance of each coil. This is because the magnetic shields offer a significantly lower reluctance path for both the useful and non-useful magnetic fluxes which limits the amount of fluxes leaves the primary coil and couples with the secondary coil. As a result of excessive fluxes in the magnetic shield, there is an excess amount of power losses in the system which is proportional to the permeability of the magnetic material. Because of the higher permeability

capability of Mumetal in relation to electrical steel, Mumetal has a higher amount of power losses than that in electrical steel.

For conductive shields, the values of the self-inductance, coupling coefficient and core losses are the same irrespective of the material used. But the type of shielding material used has an impact on the eddy current losses and ohmic losses. The reduction in the eddy current losses in the copper shield is due to the higher density and resistivity when compared with aluminium which agrees to an extent with results presented in Table 6.1. Similarly, the use of copper material shield leads to over 23% reduction in total power losses when compared with the losses obtained for aluminium. Due to the lower loss output, copper was chosen as the optimum shield component for this research.

The losses commonly encountered in WPT systems employing either conductive or magnetic materials as shields for flux-pipe resonant coils are listed in Figure 6.4

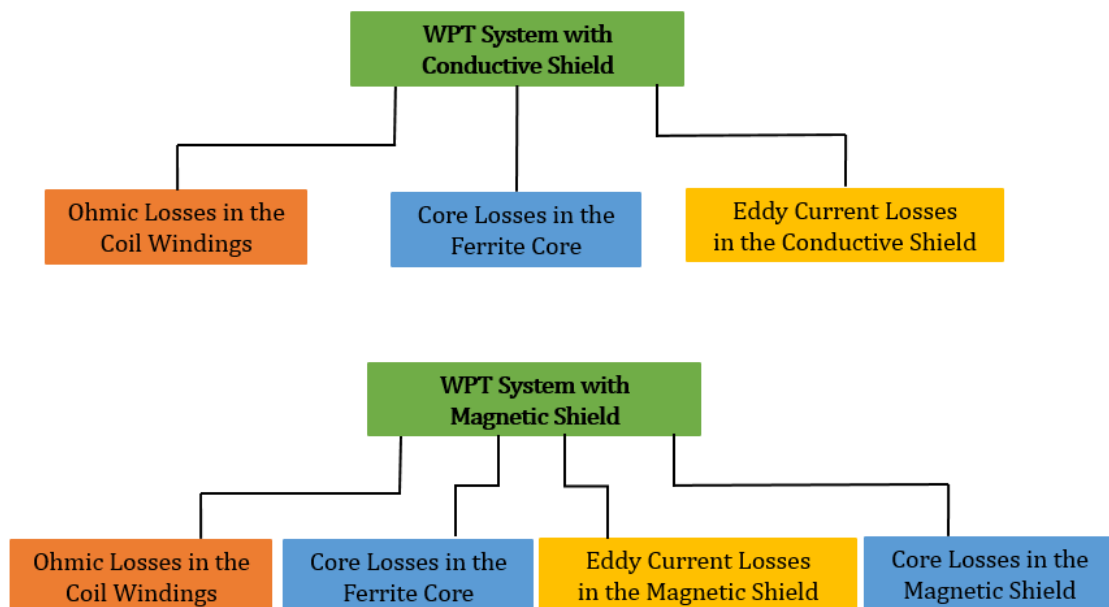


Figure 6.4: Common Losses encountered in WPT Systems with Conductive and Magnetic Shield.

From the information shown in Figure 6.4, it is noted that there is the presence of core losses in the magnetic shield in addition to the eddy current losses. From the results presented in section 5.8 coupled with equation 6.2, it is noted that core losses increase logarithmically with an increase in frequency and exponentially with an increase in excitation current. As a result, the use of a magnetic shield for WPT systems for application with electric vehicles will result in high losses and poor performance. An affordable alternative is the use of conductive shields for WPT system applications.

6.5 Optimization of Coil Windings

For most designs of flux-pipe resonant coil topology, the traditional approach is to wound single copper wire around a magnetic ferrite core as illustrated in Figure 5.1(c). An optimal design alternative is to divide the single copper wire used for windings into two to create two copper winding coils on

the same ferrite core. The two windings are electrically parallel to each other but mutually coupled magnetically in order to aid the maximum flux linkage between the two primary coils and the two secondary coils. The circuit, as well as the finite element modelling, is illustrated in Figure 6.5.

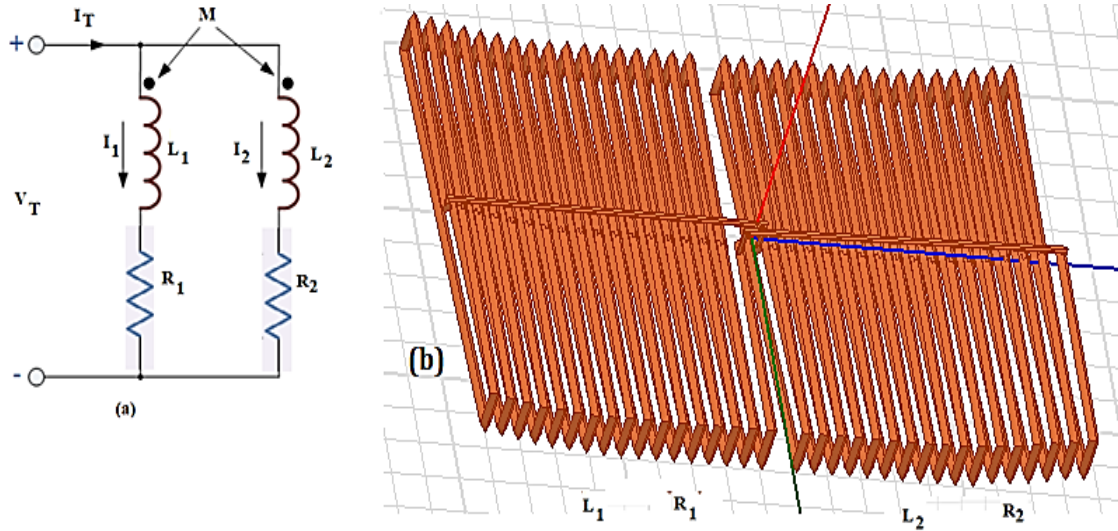


Figure 6.5: Optimal Coil Winding Implementation using Parallel Aiding Configuration. (a) Circuit Representation (b) Finite Element Modeling in Ansys Maxwell 3D

As seen from Figure 6.5, Model_4 design with 34 turns was split-up to create two windings of 17 turns each which are electrical parallel to each other but mutually coupled magnetically. The total current in the initial windings is split between the two coil windings while maintaining the same voltage across them. The total Inductance (L_T) of the two parallel aiding resonant coils is given mathematically as[181]:

$$L_T = \frac{L_1 L_2 - M^2}{L_1 + L_2 - 2M} \quad 6.5$$

Since the two windings have similar sizes and configuration, i.e. $L_1 \approx L_2$, thus equation 6.5 is reduced to the form:

$$L_T = \frac{L_1 + M}{2} \quad 6.6$$

Likewise, the total resistance of the two parallel resonant coils is given by:

$$R_T = R_1 // R_2 = \frac{R_1 R_2}{R_1 + R_2} \quad 6.7$$

Since the two windings have similar sizes and configuration, $R_1 \approx R_2 \approx (R_{model\ 4}/2)$ and equation 6.7 is reduced to the form:

$$R_T = \frac{R_1^2}{2R_1} = \frac{R_1}{2} = \frac{R_{model\ 4}}{4} \quad 6.8$$

As a result of the splitting of the coil windings into two, the total ohmic losses in the two split windings is given by:

$$P_{ohmic} = I_1^2 \cdot R_1 + I_2^2 \cdot R_2 = 2(I_1^2 \cdot R_1) \quad 6.9$$

Thus, the total ohmic losses is approximated as:

$$P_{ohmic} = \frac{(I_T^2 \cdot R_1)}{2} = \frac{(I_T^2 \cdot R_{model\ 4})}{4} \quad 6.10$$

From the expression in equations 6.10, it is observed that the total ohmic losses of the traditional model_4 can be reduced by a factor of 4.

The consequence of the optimal design is that the total self-inductance of the coil is reduced by a factor of less than 4 but greater than 3. This is due to the presence of the mutual inductance M. The overall gain will be the increase in the quality factor of the coil.

In addition to the reduction in ohmic losses, the reduction in the total current by a factor of 2 will leads to a significant reduction in the eddy current and core losses because of the strong relationship between excitation current flowing in the coil windings and the maximum magnetic flux density in the core.

6.6 Geometric Modification of Ferrite Core

In the traditional flux-pipe design topology with a uniform ferrite core, the amount of useful and “non-useful” flux is theoretical the same as shown in Figure 6.2. While the useful flux is mutually coupled with secondary coil and responsible for efficient power transfer, the “non-useful” flux is responsible for the majority of the eddy current losses in the conductive aluminium sheet used for shielding humans and the chassis of the car from the electromagnetic field.

Theoretically speaking, half of the core thickness is responsible for the propagation of the useful flux to the secondary coil and the other half for the propagation of “non-useful” magnetic flux to the aluminium shield. An optimal approach in the reduction of the non-useful flux is the modification of the ferrite core geometry in such a way that tilts the greater volume of the ferrite core to support the useful flux production. This is achieved by slightly bending the ferrite core into a C-shape similar to the horseshoe magnet as well extending the ferrite bar protruding at the edges of the copper winding by significant amount (50 mm was chosen), thus, more than 60% of the ferrite core volume is tilted to support the creation and propagation of the useful magnetic flux at an angle of 30°. The proposed design is illustrated in Figure 6.6.

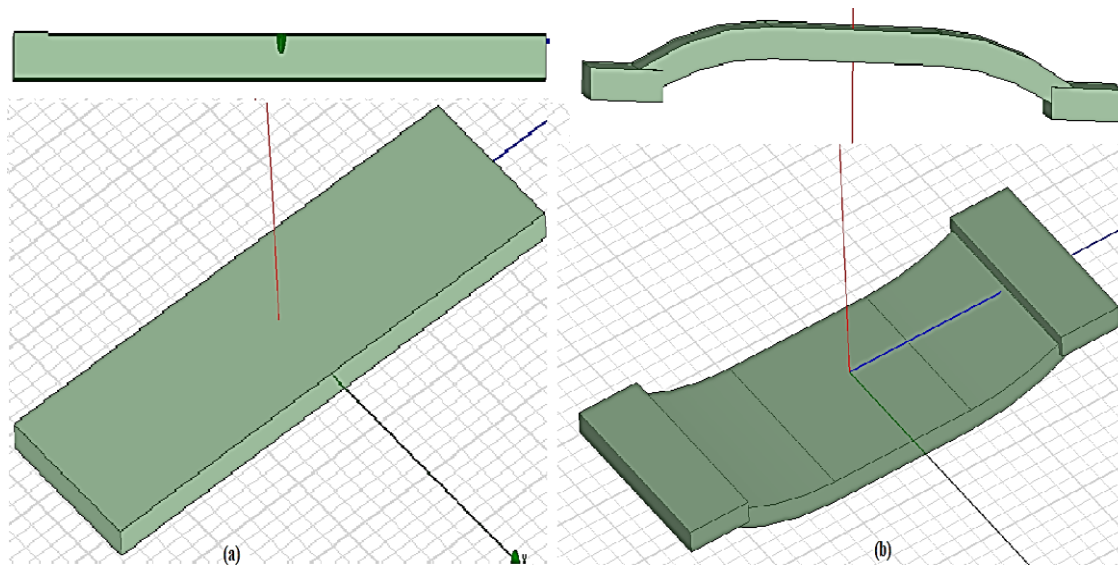


Figure 6.6: Modification of Ferrite Core Geometry for Optimal Performance. (a) The Model_4 Design Topology. (b) The Ungapped-core Model 4 Design Topology

The magnetic flux distribution around the ferrite core is similar to that of the curved trapezoidal magnetic flux concentrator design from the work of K. Zhu and P. W. T. Pong [182]. In the research work of K. Zhu and P. W. T. Pong [182], the sensitivity of a magnetic sensor is improved through creating structures composing of several curved bar-shaped magnetic flux concentrator sandwiches. The proposed optimal design model ensures due to the curved nature of the ferrite core geometry, only a few fluxes are emitted around the curved areas of the ferrite core which are wasted as eddy current losses in the shields. The implication of such a scenario is that more magnetic fluxes are concentrated on the protruded edges of the ferrite cores; which significantly reduces the amount of magnetic flux incident on the shield sheets, thus, reducing the amount of eddy current losses in the shield plate.

6.7 Optimal Selection of Supporting Material

In addition to the use of copper as a shielding material, plexiglass with a thickness of 3mm is placed in between the copper windings and the copper shield to act as support as well as ensure a firm structure for the whole resonant coil topology.

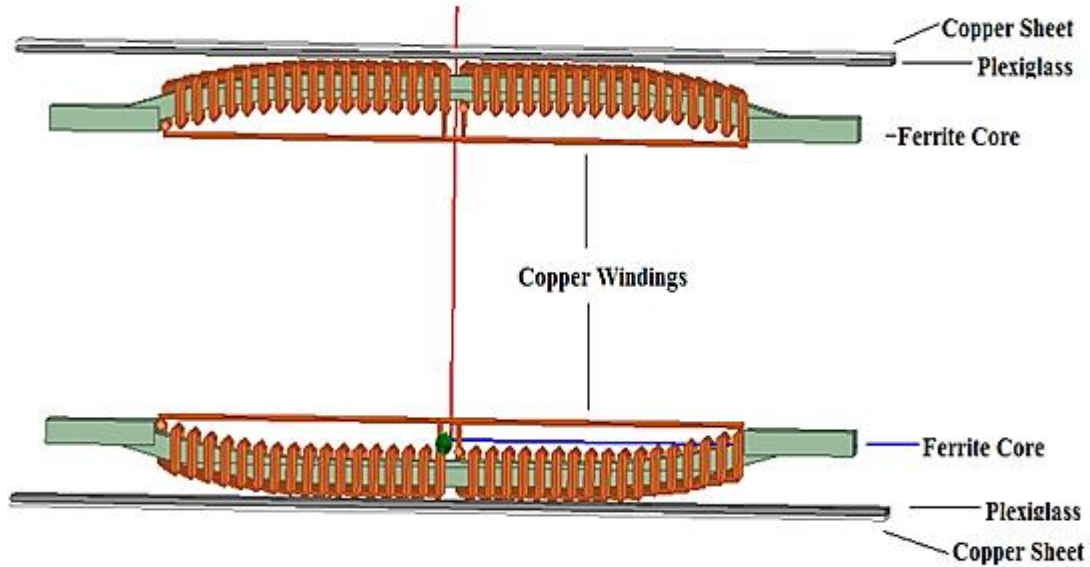


Figure 6.7: The Finite Element 3-D Model of the Ungapped-core Model 4 Flux-Pipe Resonant Coil Topology

The choice of using plexiglass is based on its lightweight as well as its thermal tolerance. The model created as a result of the above-mentioned optimization will be known as ungapped-core model 4. This is because it will be best suited for static charging operations. The overall finite element model of the ungapped model 4 resonant coil design is presented in Figure 6.7.

6.8 Modification of Optimal Flux-Pipe Design for Dynamic Operations

One of the limitations of the ungapped-core Model 4 design is the current capacity of the design. Because of the current limitation, the system can only be well suited for static charging of a single electric vehicle. For dynamic charging operations, the WPT system should be able to charge two or more vehicles at a time. As a result, the WPT system must have a higher power transfer capability in order to charge two or more electric vehicles at a time.

For a given ferrite core, the saturation limit is fixed by the manufacturer and for optimum performance, the WPT system must operate below the saturation limit of the ferrite core. From the simulation results presented in section 5.6, it was noted that there is a strong relationship between the maximum magnetic flux density and the excitation current of the coil. It was concluded that the higher the excitations current, the higher the magnetic flux density.

In order to increase the current-carrying capacity of a ferrite core for a specific magnetic flux density, an air gap is introduced in the ferrite core. The introduction of the air gap in the ferrite core sheers the hysteresis loop of the B/H curve of the core as illustrated in Figure 6.8(b)[183]. The effect of introducing an air gap in the ferrite core is shown in the area enclosed by the green shape in Figure 6.8(b).

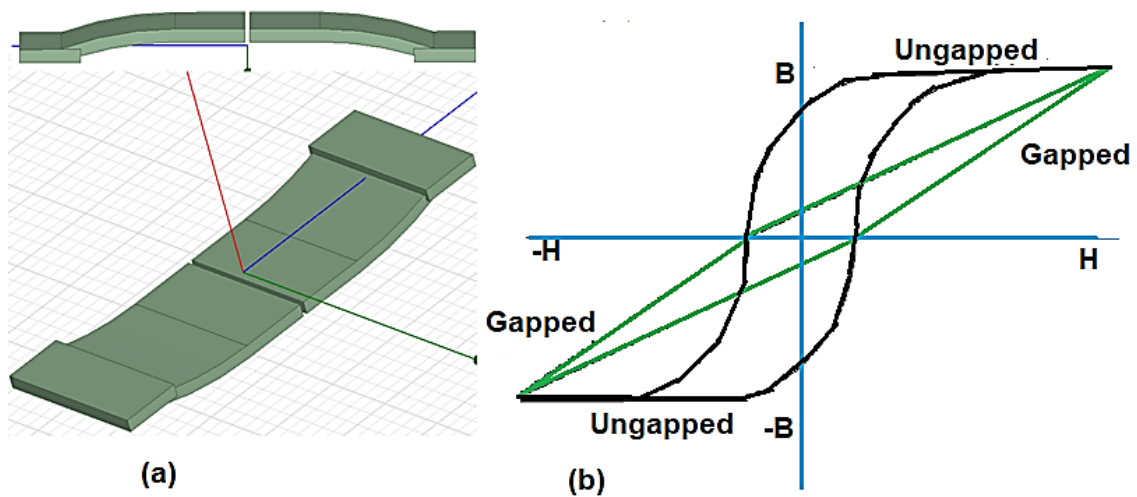


Figure 6.8: Modification of the Ferrite Core for Dynamic Charging. (a) Optimized Model_4 with air gap in the Core. (b) Hysteresis Curve for Gapped and Ungapped Ferrite Core.

The presence of the air gap in the ferrite core does not change the saturation limit, increases the reluctance of the ferrite core and increases the amount of excitation current required to saturate the core. The more the air gap in the core, the lower the permeability of the core and the higher the excitation current required in order to saturate the ferrite core.

In addition, as noted in the results presented in section 5.6, the maximum magnetic flux density is concentrated around the centre of the ferrite core. An introduction of an air gap at the centre of the core will aid a redistribution of the maximum flux density distribution to the centres of the split ferrite cores.

The 3-D finite element model of the ferrite core after the introduction of the air gap is illustrated in Figure 6.8(a). The modified model design will be known as gapped model 4 and the complete model design is shown in Figure 6.9.

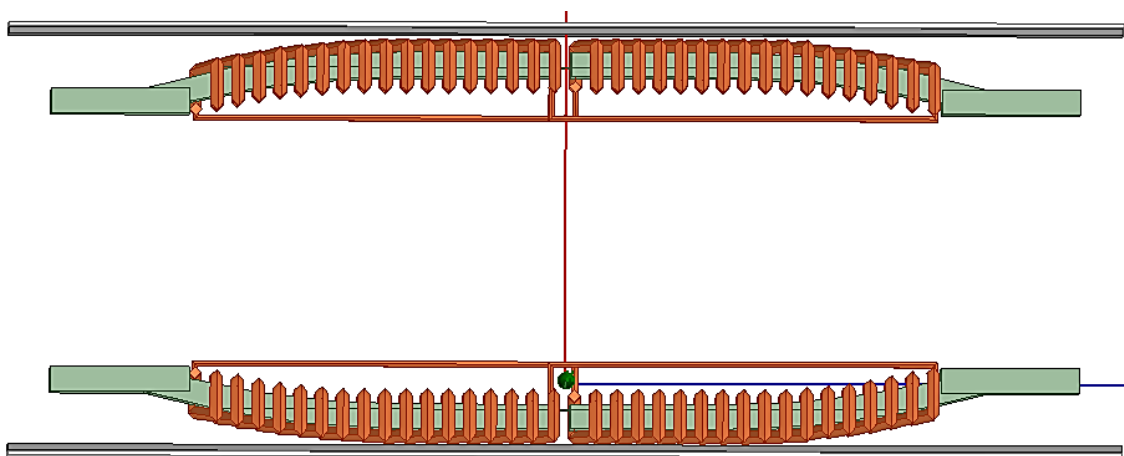


Figure 6.9: The Finite Element 3-D Model of the Gapped-core Model 4 Flux-Pipe Resonant Coil Topology

Due to the small dimensions of gapped model 4, the model will be best suited for a segmented transmitter coil-array system for efficient dynamic charging of electric vehicles. The concept and operation of the segmented transmitter coil array have been discussed extensively in section 2.12.2.

A parametric analysis of air gap from 1 mm to 10 mm at a particular excitation current was implemented on the gapped-core model 4 and it was observed that increase in the airgap causes a decrease in the self-inductance, mutual inductance, magnetic flux density, and coupling coefficient in the model design. In order to strike a balance between the excitation current and coupling factor, an air gap of 5 mm was chosen for the gapped-core model 4.

6.9 Validation of Coil Winding Specification

In order to corroborate the optimal choice of dividing the original coil windings of the traditional flux-pipe into two windings instead of three or more split-coil windings, the 34-turns coil windings were remodelled to create individual three and four different copper windings.

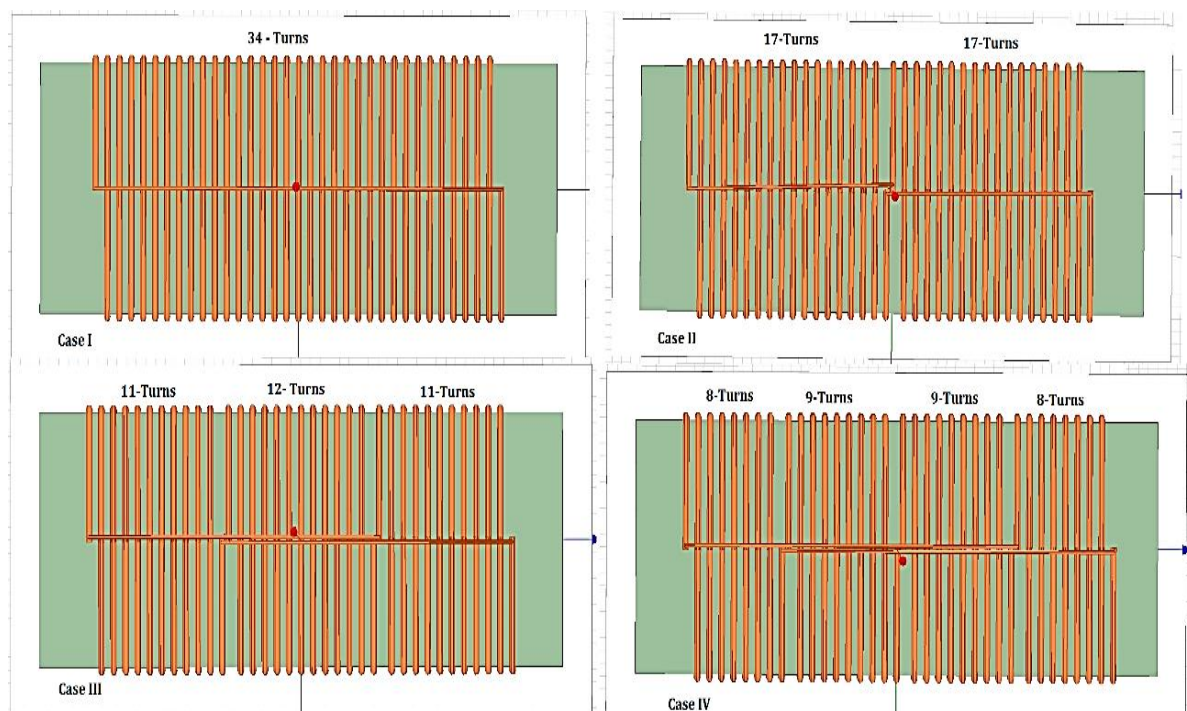


Figure 6.10: Finite Element Modelling of Split of Coil Windings

The three copper windings comprise of two windings with 11 turns each and a winding with 12 turns. The four copper windings comprise of two windings with 8 turns each and another two windings with nine turns each. The different coil windings modelling were implemented and illustrated in Figure 6.10. Similarly, an initial eddy current and circuit analysis were performed on each of the varieties of the coil windings and the results are presented in Table 6.3.

Table 6.3: Coil Parameters and Loss Evaluation of Resonant Coil for 8 kW Power Application

| Parameter | Case I | Case II | Case III | Case IV |
|---------------------------------------|----------------------|---------------------|---------------------|---------------------|
| Number of Split Windings | - | 2 | 3 | 4 |
| Airgap | 200 mm | 200 mm | 200 mm | 200 mm |
| Primary Self-Inductance, L_p | 345.00 μH | 84.83 μH | 31.67 μH | 16.30 μH |
| Secondary Self-Inductance, L_s | 344.54 μH | 84.56 μH | 31.54 μH | 16.21 μH |
| Coupling Coefficient, k | 0.382 | 0.381 | 0.328 | 0.304 |
| Primary Intrinsic Resistance R_p | 131.53 m Ω | 32.73 m Ω | 16.02 m Ω | 8.52 m Ω |
| Secondary Intrinsic Resistance, R_s | 134.49 m Ω | 33.11 m Ω | 16.15 m Ω | 8.67 m Ω |
| $k\sqrt{Q_{ps}}$ | 527 | 523 | 344 | 306 |
| Adaptive Frequency | 85 kHz | 85 kHz | 85 kHz | 85 kHz |
| Excitation current | 32 A | 32 A | 32 A | 32 A |
| Total Power Losses | 962.15 W | 186.38 W | 68.42 | 33.92 W |
| Load Resistance | 20 Ω | 20 Ω | 20 Ω | 20 Ω |
| Coil-to-coil efficiency | 98.54 % | 99.21 % | 97.59 % | 69.78 % |

From the results presented in Table 6.3, it is noted that the power losses, intrinsic resistance, self-inductance, and coupling inductance reduce with an increase in the number of split windings. Despite a substantial reduction in power losses with each incremental increase in the number of split windings, case III and case IV exhibits a significant reduction in coil-to-coil efficiency when compared with case II. With respect to essential parameters like coupling coefficient, $k\sqrt{Q_{ps}}$ and coil-to-coil efficiency, the choice of case II is vindicated. Comparing the models in case I and case II, it is noted that case II has a reduction in the total power losses by a factor of more than five. In addition, the intrinsic resistance of case II is one-fourth of the intrinsic resistance of case I, which agrees with equation 6.8. Thus, the simulation results agree with the theoretical analysis and the choice of case II is justified.

6.10 Magnetostatic Analysis of Optimal Flux-Pipe Resonant Coils

As discussed in section 4.3.1, the magnetostatic analysis employs a matrix calculation in order to solve the magnetic field. When the field solution is stopped, derived quantities from the magnetic field solutions like inductances, coupling factor and magnetic flux density are calculated as the required parameters. The circuit parameters for circular coils, rectangular coils, and flux-pipe coil model, were calculated and illustrated in Table 6.4.

The creation of the Ungapped-core model 4 from model 4 leads to a reduction in the self-inductance, and mutual inductances by more than 70%. This is a potential trade-off for the creation of the optimized ungapped-core Model 4. Similarly, there is a reduction in the coupling coefficient by less than 21% because of the modification to create ungapped-core model 4 from the traditional model 4. Due to the disproportional decrease in the self-inductance and coupling factor, there is expectedly an increase in performance in the Ungapped-core Model 4.

Table 6.4: Evaluated Circuit Parameters of Flux-Pipe Resonant Coil Models

| Parameter | Model 4 | Ungapped-core Model 4 | Gapped-core Model 4 | Gapped/Ungapped Model 4 |
|--|---------|-----------------------|---------------------|-------------------------|
| Excitation Current (A) | 50 | 50 | 50 | 50 |
| Airgap (mm) | 200 | 200 | 200 | 200 |
| Primary Self-Inductance, L_p (μH) | 357.88 | 127.69 | 89.99 | 81.44 |
| Secondary Self-Inductance, L_s (μH) | 357.02 | 127.86 | 90.08 | 105.20 |
| Mutual Inductance, L_m (μH) | 137.44 | 47.06 | 24.61 | 26.42 |
| Coupling Coefficient, k | 0.385 | 0.368 | 0.273 | 0.317 |

Comparing the ungapped-core model 4 and gapped-core model 4, there is a significant decrease in the self-inductance and mutual inductance in gapped-core model 4 by more than 29%. The reduction is expected due to the presence of an air gap in the core of the gapped-core model 4. The presence of the air gap in the core reduces the permeability of the core and increases the reluctance of the ferrite core. It is noted also that there is a reduction in the coupling coefficient by less than 26% because of introducing an air gap in the ferrite core. Due to the disproportionate decrease in the self-inductance and coupling factor, there is expectedly an increase in performance in the gapped-core model 4

For the next series of simulations, the magnetic flux density distribution and coupling factor for the circular coils, rectangular coils and flux-pipe coils was analysed under the magnetostatic analysis by performing a parametric sweep of excitation currents, misalignment and airgap variations of each coil designs.

6.10.1 Magnetic Flux Density Distribution in Ferrite Cores

The ferrite core magnetostatic simulations are based on the static magnetic field. The simulation is necessary to ensure the WPT operates in the linear mode and it does not go into saturation. This is because a given magnetic material of a specific size can only withstand a certain level of magnetic energy.

The magnetostatic simulations will help in the investigation of the optimal level of power and current the core of coil design model can withstand before going into saturation. This involves ramping up the current till magnetic field enters the saturation mode using a parametric sweep. Thus the maximum current can be obtained in the linear mode.

The ferrite core material used in the modelling of the three coil designs is the power ferrite FDK 6H40 produced by FDK Incorporation[178]. The standard material characteristics are illustrated in Appendix C. From the technical data sheet published by the manufacturer, the magnetic saturation of the selected FDK 8H40 is 0.43 T. The B-H curve of the ferrite core is illustrated in Figure 6.11.

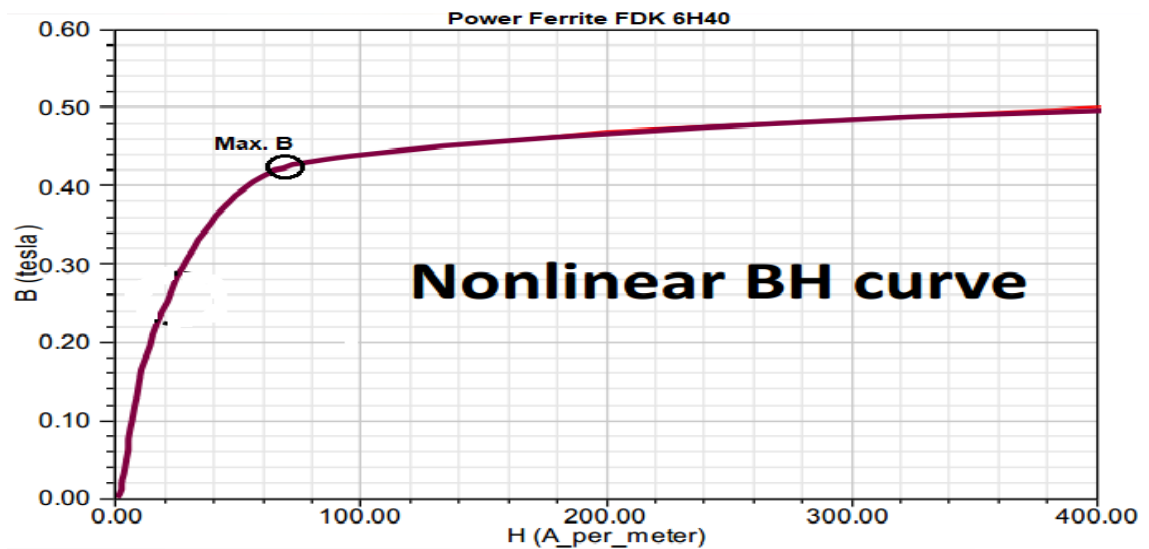


Figure 6.11: The B-H Curve for FDK 6H40 Ferrite Core

Using the appropriate initial and boundary conditions, finite element analysis was implemented on the three coil designs at an excitation current of 50 A. The magnetic flux distribution in the ferrite core material for the model_4, ungapped-core Model 4 and gapped-core model 4 are illustrated in Figure 6.12.

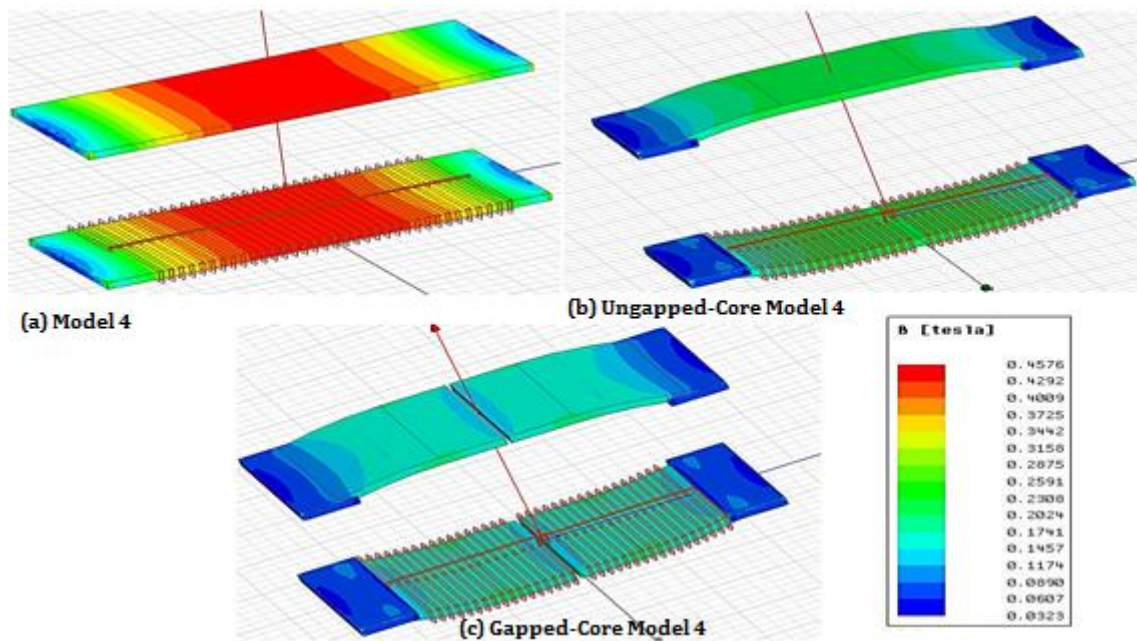


Figure 6.12: Magnetic Flux Distribution in Flux-Pipe Resonant Coils Designs at Excitation Current of 50 A

The simulation result presented in Figure 6.12 was implemented at an airgap of 200 mm at an excitation current of 50 A. From the magnetic flux distribution shown, it is noted that the ungapped-core Model 4 and gapped-core model 4 flux-pipe coil designs have a magnetic flux distribution of less than 0.25 T. This value is significantly lower than the saturation limit of 0.43 T. In contrast, the

ungapped-core Model 4 and gapped-core model 4 has a magnetic flux density of 0.236 T and 0.170 T respectively.

Similarly, the maximum magnetic flux distribution is concentrated at the middle of the ferrite core for the Model 4 and ungapped-core Model 4 but not the case for the gapped-core model 4. Due to the introduction of the air gap, the maximum flux distribution in the core shifts to the centres of the two split cores. It is also noted that the magnetic flux distribution is minimum at the edge of the ferrite core for the three flux-pipe models. This is an indication that the magnetic field intensity is least at the edges of the cores.

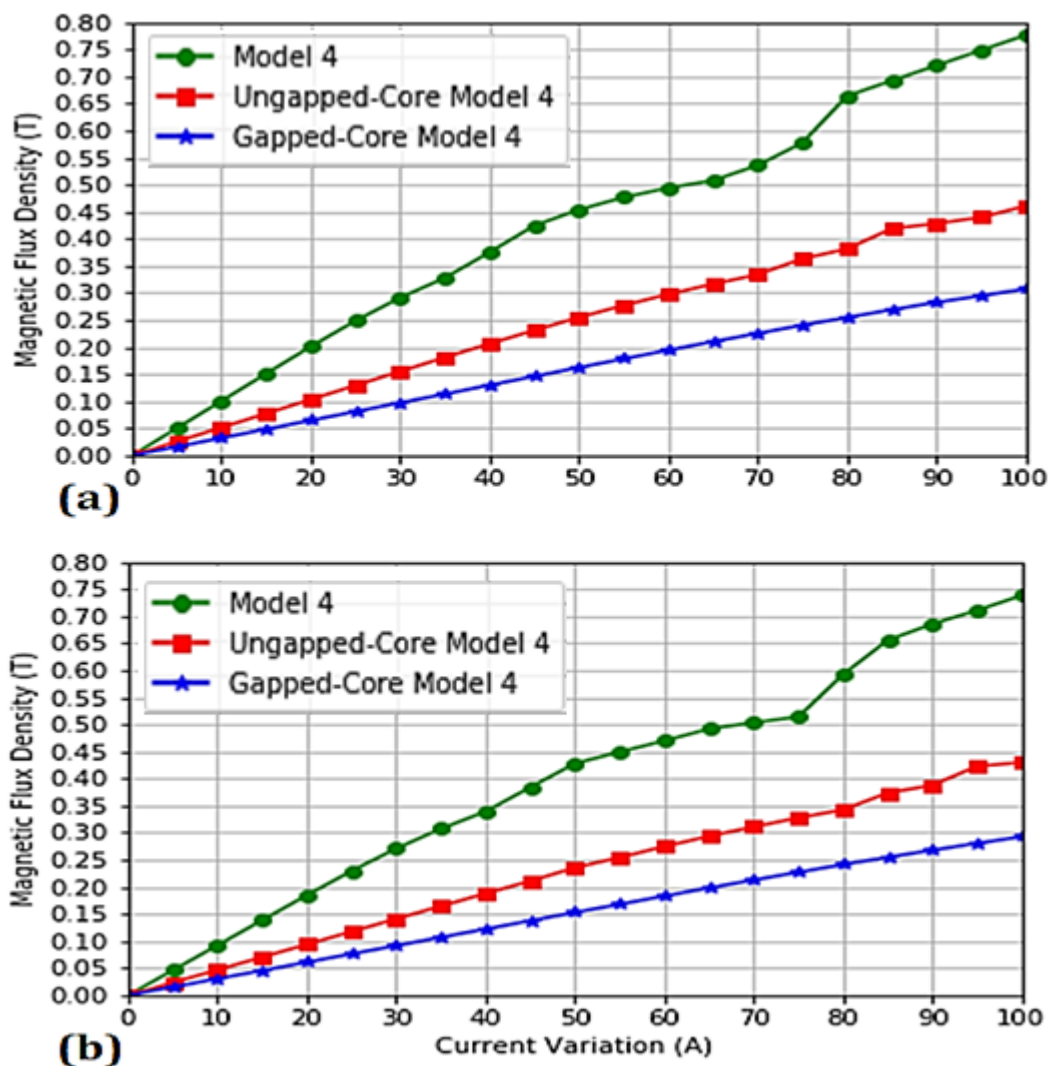


Figure 6.13: Magnetic Flux Distribution in Ferrite Cores with Variation in Excitation Current for Flux-Pipe Models (a) Flux Distribution at 150mm Airgap. (b) Flux Distribution at 200mm Airgap

In order to ascertain the maximum excitation current each of the three model designs can withstand before going into saturation, the model_4, ungapped-core Model 4 and gapped-core model 4 designs were subjected to a parametric sweep of excitation currents from 0 A to 100A at different airgaps of 150 mm and 200 mm. The performance result of the coil designs at 150 mm and 200 mm are shown in Figure 6.13.

From the results obtained in Figure 6.13, it is noted that the ungapped-core Model 4 and gapped-core model 4 coil designs can withstand an excitation current of up to 90 A without being saturated. In contrast, the flux pipe core can only withstand an excitation current of 45 A at 150 mm airgap and excitation current of 50 A at 200 mm airgap. The improved performance output of the ungapped-core Model 4 and gapped-core model 4 cores was because of splitting the excitation current by half; as a result, the maximum magnetic flux density in each core was significantly reduced.

Similarly, the gapped-core model 4 design exhibited the least magnetic flux density at any particular value of the excitation current at the airgap of 150 mm and 200 mm respectively. The reduction in the maximum flux density for the gapped-core model 4 is because of the presence of an air gap in its ferrite core as discussed in section 6.8. As a result. The maximum flux density obtained in ungapped-core Model 4 is theoretically divided into two and shifted to the centres of the split ferrite cores. Thus, the maximum flux density is significantly reduced.

In summary, the optimal ungapped-core Model 4 and gapped-core model 4 can withstand higher current excitations than the traditional model_4 flux-pipe coil, thus, the optimization methodology employed for the design of the two models was justified.

6.11 Parametric Analysis of the Resonant Coil Designs

Before the optimization of these existing simple designs, there is the need to perform a parametric sweep analysis of each coil design based on the variation of the airgap, lateral misalignment, and longitudinal misalignment. The secondary coil 3-dimensional positional measurement parameters are varied along the x, y and z coordinate systems.

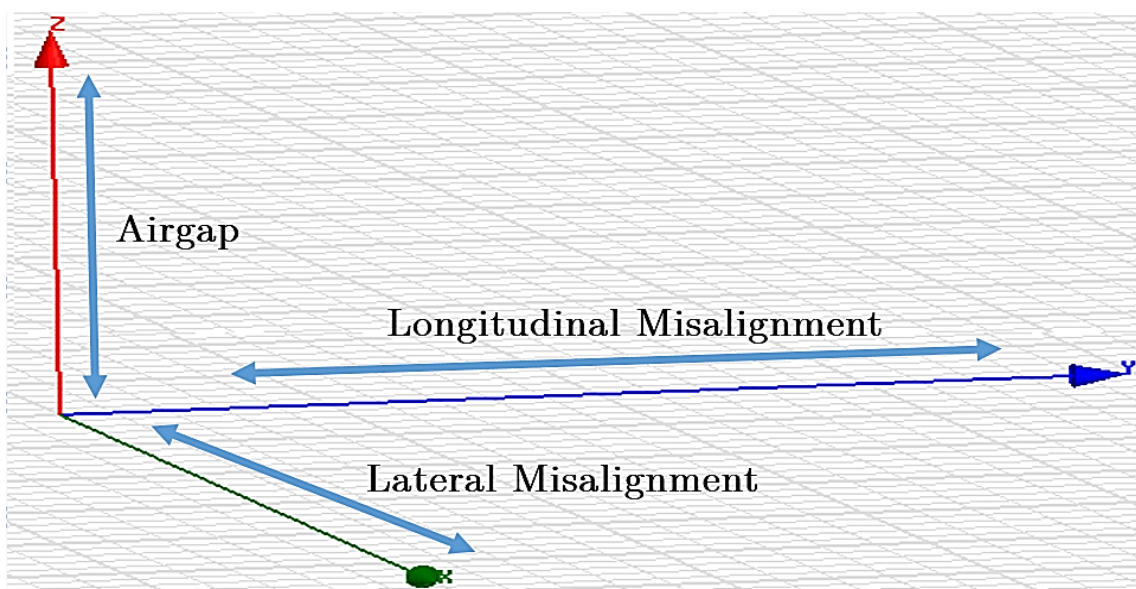


Figure 6.14: 3-Dimensional Positional Arrangement for Airgap, Lateral Misalignment, and Longitudinal Misalignment.

The parametric sweep along the x-axis corresponds to the lateral misalignment (green line), the parametric sweep along the y-axis corresponds to the longitudinal misalignment (the blue line), while the airgap variation is done through a parametric sweep along the z-axis (red line). This is shown diagrammatically in Figure 6.14.

6.11.1 The Parametric Misalignment Performance of Resonant Coils

This lateral parametric analysis was performed by varying the position of the secondary coil along the x-axis and the value of the coupling coefficient is measured based on each unit displacement of the coil along that axis. The variation of the coupling coefficient for each unit increase in lateral displacement along the x-axis for the model_4, ungapped-core model 4 and gapped-core model 4 is shown in Figure 6.15.

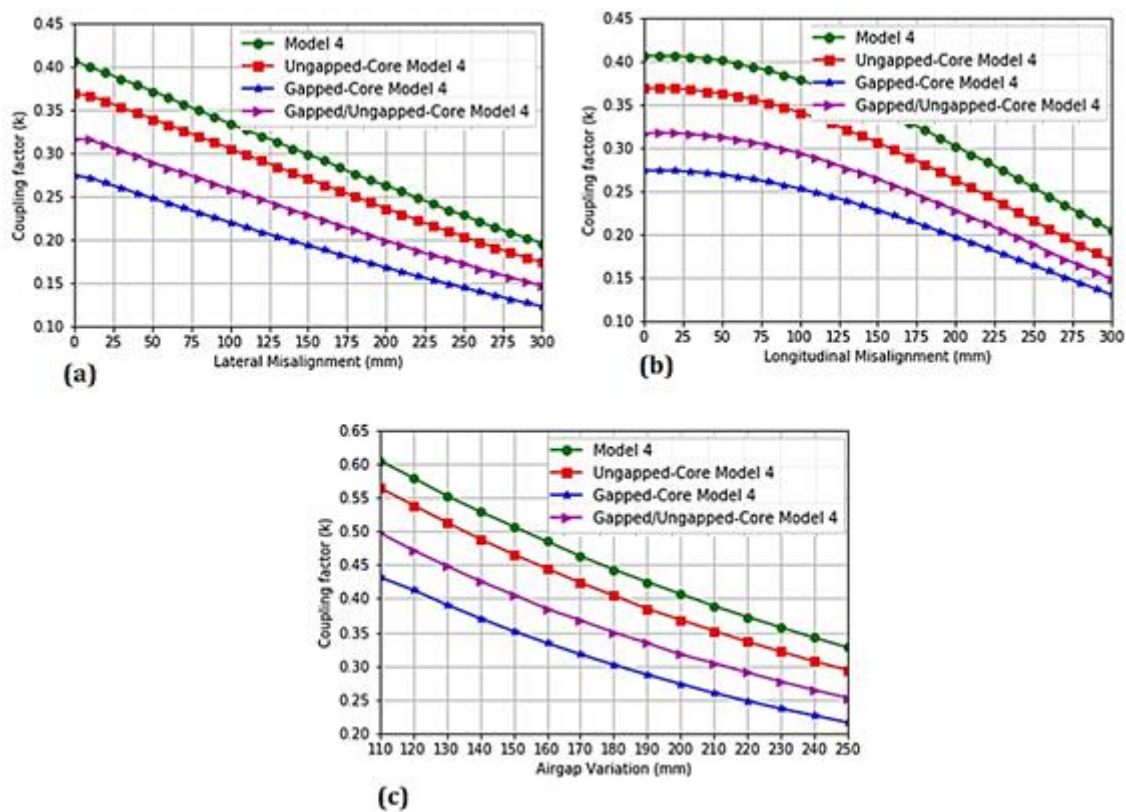


Figure 6.15: Misalignment Parametric Analysis of Flux-Pipe Resonant Coils. (a) Lateral Misalignment (b) Longitudinal Misalignment (c) Airgap Variations

Similarly, the longitudinal parametric analysis was performed by varying the position of the secondary coil along the y-axis and the value of the coupling coefficient is measured based on each unit displacement of the coil along that axis. The variation of the coupling coefficient for each unit increase in longitudinal displacement along the x-axis for the model_4, ungapped-core Model 4 and gapped-core model 4 is shown in Figure 6.15.

Finally, the airgap parametric analysis was performed by varying the position of the secondary coil along the z-axis and the value of the coupling coefficient is measured based on each unit displacement

of the coil along that axis. The variation of the coupling coefficient for each unit increase in airgap along the Z-axis for the model_4, ungapped-core Model 4 and gapped-core model 4 is shown in Figure 6.15.

From the result shown in Figure 6.15, it was noted that the ungapped-core Model 4 and gapped-core model 4 designs displayed lower performance characteristics with respect to each unit displacement of the secondary coils for all the misalignments in relation to the traditional model 4.

The result for the ungapped-core Model 4 and gapped-core model 4 was anticipated due to the slight dip in the core horizontal dimension increasing the overall airgap lightly, thus, reducing the magnetic coupling. Similarly, the gapped-core model 4 has a lower performance characteristic in relation to the static model due to the presence of an air gap in its ferrite core. The gap in the ferrite core increases the reluctance of the core used in boosting the magnetic flux, thus, decreasing the magnetic coupling between the primary and secondary coils.

6.12 Eddy Current Analysis of Resonant Coils

As discussed in section 4.3.2, the eddy current analysis is performed to identify and ascertain the level of losses in the coil system. There are basically three types of losses present in a resonant coil system: the ohmic losses, eddy current losses and core losses. The ohmic losses are losses as a result of the resistance in the coil windings, eddy current losses are losses that occur at the shield plates as a result of magnetic flux leakages while core losses are losses in the ferrite core as a result of the magnetization and demagnetization of the core due to the high-frequency alternating current.

The first analysis performed for each of the four coil models was to establish the level of losses in each coil designs as a result of operating the WPT systems for a level 2 power ratings of 8 kW as defined by SAE J1772 regulations. The initial evaluation of the losses for each of the coil design is undertaken by injecting an excitation current of 32 A in the coil windings at a resonant frequency of 85 kHz. The resonant frequency of 85 kHz was chosen because it is the operating frequency proposed by SAE J2954 task force for interoperability of different WPT charging systems. The results of the analyses are presented in Table 6.5.

Table 6.5: Coil Parameters and Loss Evaluation of Flux-pipe Coils for 8 kW Power Application

| Parameter | Model 4 | Ungapped-core Model 4 | Gapped-core Model 4 | Gapped/Ungapped Model 4 |
|----------------------------------|----------------|-----------------------|---------------------|-------------------------|
| Airgap | 200 mm | 200 mm | 200 mm | 200 mm |
| Primary Self-Inductance, L_p | 357.88 μ H | 127.69 μ H | 89.99 μ H | 81.44 μ H |
| Secondary Self-Inductance, L_s | 357.02 μ H | 127.86 μ H | 90.08 μ H | 105.20 μ H |
| Coupling Coefficient, k | 0.385 | 0.368 | 0.273 | 0.317 |
| Ohmic Losses | 179 W | 24 W | 19 W | 21 W |
| Core Losses | 493 W | 98 W | 32 W | 57 W |
| Eddy Current Losses | 105 W | 10 W | 7 W | 8 W |
| Total Power Losses | 777 W | 132 W | 58 W | 86 W |

For such medium power application, it is noted that there was a significant reduction of more than 400 % in the total losses for the ungapped-core model 4 coil when compared with the traditional model 4. The gapped-core Model 4 and gapped/ungapped model 4 has more than 100 % and 50 % reduction in the total power losses when compared with the losses in the ungapped-core model 4. The total losses in gapped-core Model 4 and gapped/ungapped model 4 is less than the total losses obtained with the rectangular coil. From the initial result shown in Table 6.5, the optimization methodology for the flux-pipe coil was justified.

The second analysis performed was to ascertain the level of losses on each coil as a result of an increase in excitation currents at a fixed frequency. This was achieved by injecting a parametric sweep of excitation current into the coil windings at high frequency (85 kHz in this case) and the losses for each value of excitation current was evaluated. The results of the analyses are presented in Figure 6.16.

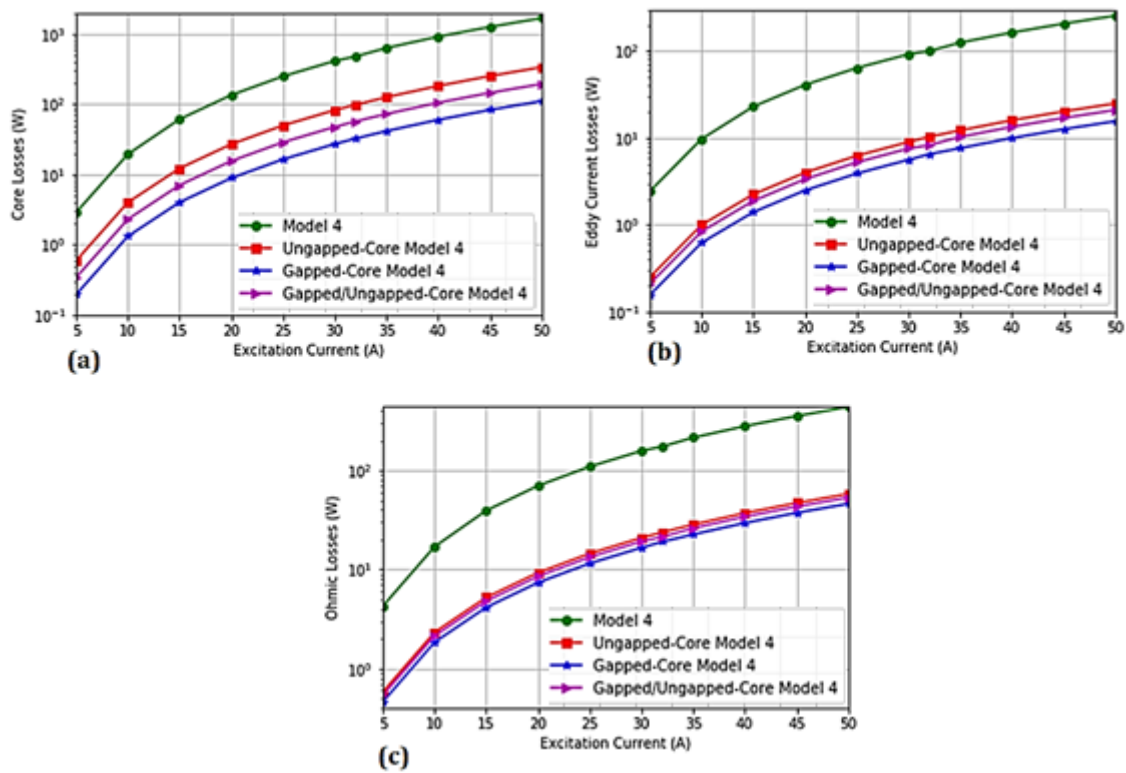


Figure 6.16: Losses in Coil Models due to Variation in Excitation Current. (a) Core Losses. (b) Eddy Current Losses (c) Ohmic Losses

From the results presented in Figure 6.16, it is noted that there is a gradual increase in the three types of losses with an increase in current for all the flux pipe models analysed. The ungapped-core model 4, hybrid model 4, and gapped-core Model 4 designs have similar performance characteristics for the ohmic and eddy current loss analyses due to their similarity in winding designs. The difference in performance for core losses between the ungapped-core model 4 and gapped-core model 4 is as a result of the presence of an air gap in the core of the gapped-core model 4. The presence of an air gap in the ferrite core reduces the maximum flux density, thereby reducing the core losses in the core.

It is also noted that the significant reduction in the losses of the model 4 and gapped-core model 4 was a direct consequence of the optimal design approach adopted.

Similarly, a frequency response of the various coil models was performed by varying the frequency at a fixed excitation current (typically 32 A). The losses encountered over a range of frequencies from 5 kHz to 100 kHz are illustrated in Figure 6.17.

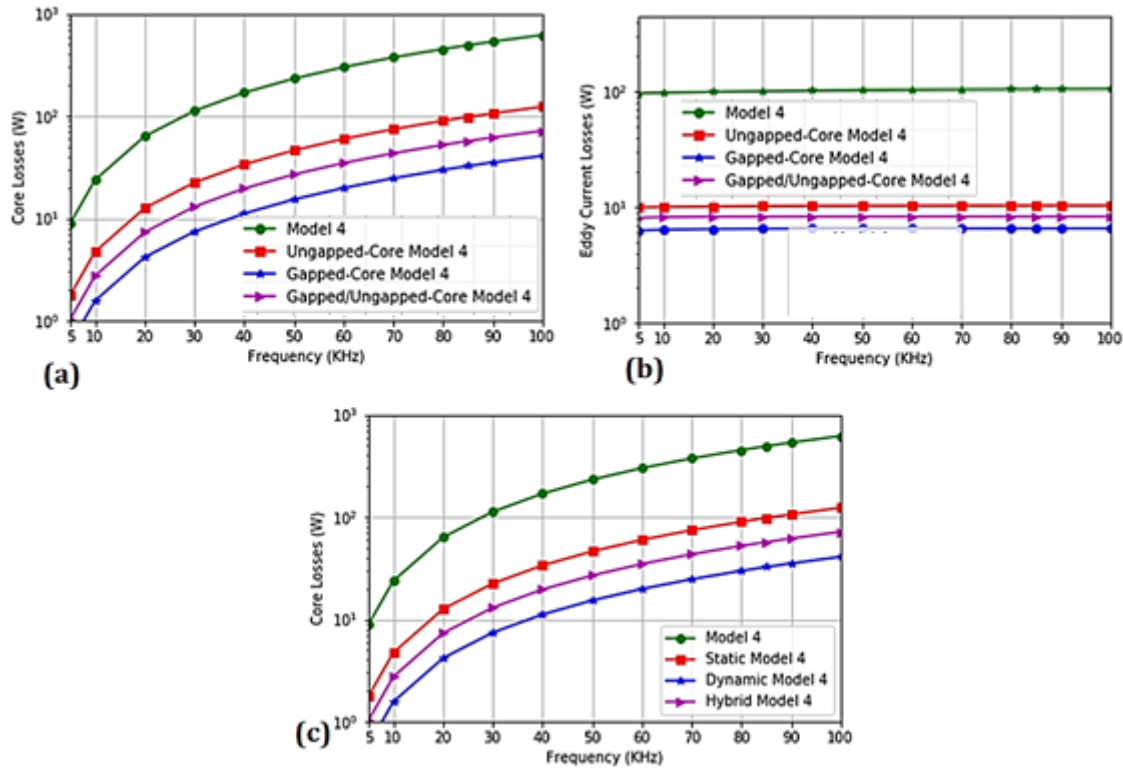


Figure 6.17: Losses in Flux-Pipe Coil Models due to Variation in Frequency (a) Core Losses (b) Eddy Current Losses (c) Ohmic Losses

From the results presented in Figure 6.17, the ohmic losses and eddy current losses are relatively constant over a range of frequency above the threshold frequency (around 10kHz). But, there is a significant increase in core losses with an increase in frequency for all the three models.

The higher the rate of magnetization/demagnetization of the ferrite core, the higher the core losses. As a result, most practical designs are operated at low frequencies to limit the amount of eddy current losses in the system.

6.13 Circuit Analysis and Performance

In the circuit analysis, the performance of the coil designs in terms of coil-to-coil efficiency and power output were evaluated. The parameters required for accurate analysis are obtained from the eddy current analysis solution. The required parameters for the three model coils at an adaptive frequency of 85 kHz are presented in Table 6.6.

Table 6.6: Circuit Parameters of Resonant Coils from Eddy Current Solution

| Parameter | Model 4 | Ungapped-core Model 4 | Gapped-core Model 4 | Gapped/Ungapped Model 4 |
|------------------------------------|------------------|-----------------------|---------------------|-------------------------|
| Airgap | 200 mm | 200 mm | 200 mm | 200 mm |
| Adaptive Frequency | 85 kHz | 85 kHz | 85 kHz | 85 kHz |
| Primary Self-Inductance, L_p | 357.88 μ H | 127.69 | 89.99 | 81.44 |
| Secondary Self-Inductance, L_s | 357.02 μ H | 127.86 | 90.08 | 105.20 |
| Mutual Self-Inductance, L_m | 137.44 μ H | 47.06 | 24.61 | 26.42 |
| Coupling Coefficient, k | 0.385 | 0.368 | 0.273 | 0.317 |
| Primary Intrinsic Resistance R_p | 84.39 m Ω | 23.42 m Ω | 21.86 m Ω | 26.42 m Ω |
| Secondary Intrinsic Resistance, | 85.95 m Ω | 22.98 m Ω | 21.61 m Ω | 25.18 m Ω |

The presence of high intrinsic resistance in the model 4 resonant coil is largely responsible for the high amount of ohmic losses. This is in addition to the high value of the excitation current. Due to the coil windings modification, there was more than 78% reduction in the value of the intrinsic resistance in the gapped-core Model 4 and ungapped-core model 4 which is more than 70 % reduction in the self-inductance with respect to the traditional model 4. The ratio of the intrinsic resistance of the model 4 and ungapped-core model 4 for the primary and secondary coils are 3.60 and 3.74 respectively. These values of intrinsic resistance are close to the theoretical value of 4 illustrated in equation 6.8. The intrinsic resistance of the gapped-core Model 4 and hybrid model 4 follows the same pattern and are quite close to the theoretical value of 4. Similarly, the ratio of the self-inductance values of the model 4 and ungapped-core model 4 gives a value close to the expected value as shown in equation 6.6. This implies that there is an overall performance improvement in the Ungapped-core model 4 and Gapped-core Model 4 designs and the accuracy of the model performance conform to the governing mathematical equations.

Based on the parameters obtained in Table 6.6, the relationship between maximum efficiency η_{max} and the parameter $k\sqrt{Q_{ps}}$ over a range of frequencies was evaluated using equation 4.34 and the graph presented in Figure 6.18.

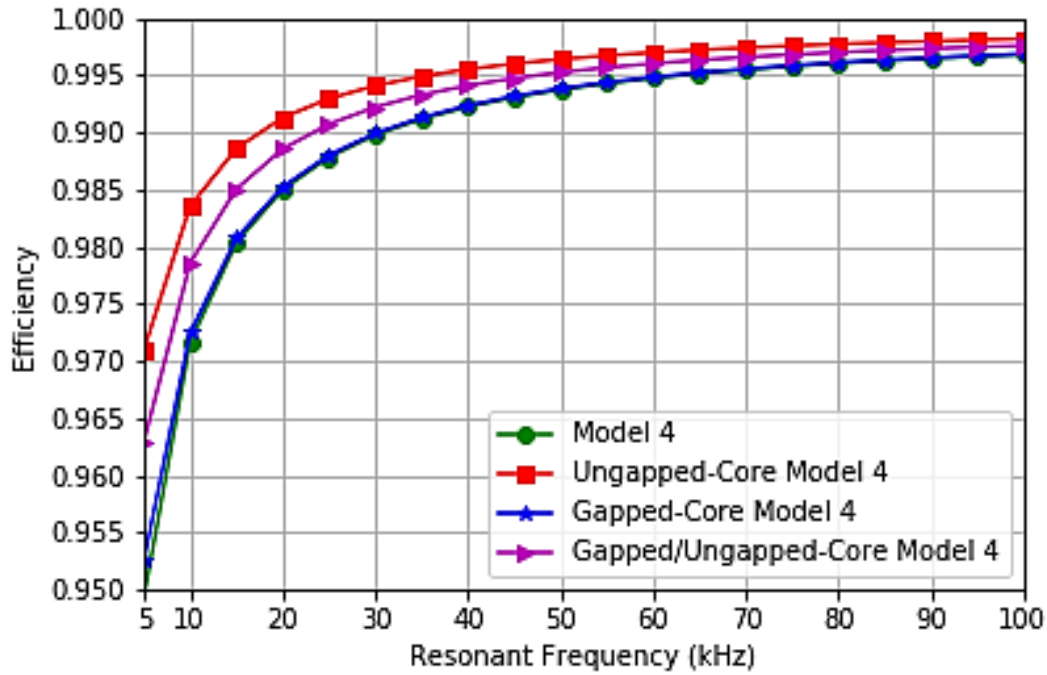


Figure 6.18: Relationship between Maximum efficiency and the Parameter $k\sqrt{Q_{ps}}$ over a range of Frequencies.

Based on the result presented in Figure 6.18, it is noted that increases in resonant frequencies positively impact on the maximum efficiency of the coil. While the rectangular and circular coil showed similar performance characteristics, the flux-pipe model has a better performance over each step increase in frequency. From the result presented in Figure 6.18, an optimum resonant frequency of 50 kHz was adopted for the ungapped-core model 4 design while an optimum resonant frequency of 60 kHz was adopted for the gapped-core model 4 design. For the ungapped-core model 4, the maximum efficiency achievable at 50 kHz is 99.63% and the gapped-core model 4 can achieve maximum efficiency of 99.48 at the optimum efficiency of 60 kHz

For most practical designs, the optimum efficiency and power transferred are dependent on the value of the load resistance. The reason being that maximum power can be transferred but not at the maximum efficiency. In order to obtain the optimum efficiency for a particular load resistance, a parametric sweep of load resistance is performed and the values of the efficiency and power output evaluated. The result of these analyses for S-S compensation topology and S-P compensation topology is presented in the next two sections.

6.13.1 Performance Characteristics of Optimal Flux-Pipe Resonant Coil in an S-S Compensation Topology.

For practical design implementation, there is always a trade-off between power output and efficiencies depending on the critical requirements for the system application. Generally, for a wireless power transfer system, the power transfer efficiency is the most important parameter. Thus, for the proposed

coil designs, a load resistance of 20Ω was selected as the optimum load resistance. The overall system performance for a load resistance of 20Ω is listed and summarized in Table 6.7.

Table 6.7: Summary of Performance Characteristics of Resonant Coil Models for S-S Configuration

| Parameters | S-S Configuration | | | |
|-------------------------|-------------------|-----------------------|---------------------|-------------------------|
| | Model 4 | Ungapped-core Model 4 | Gapped-core Model 4 | Gapped/Ungapped Model 4 |
| Resonant Frequency | 40 kHz | 50 kHz | 60 kHz | 55 kHz |
| $k\sqrt{Q_{ps}}$ | 252 | 550 | 384 | 393 |
| Input Voltage | 300 V | 300 V | 300 V | 300 V |
| Output Voltage | 397 V | 470 V | 626 V | 555 V |
| Load Resistance | 20Ω | 20Ω | 20Ω | 20Ω |
| Input Current | 13.75 A | 37.22 A | 75.67 A | 55.83 A |
| Output Current | 9.93 A | 23.48 A | 31.30 A | 27.80 A |
| Input Power | 4.00 kW | 11.15 kW | 19.89 kW | 15.66 kW |
| Output Power | 3.94 kW | 11.02 kW | 19.60 kW | 15.46 kW |
| Total Power Losses | 60 W | 130 W | 290 W | 200 W |
| Coil-to-Coil Efficiency | 98.44 % | 98.89 % | 98.55 % | 98.73 % |

From the summary of results presented in Table 6.7, it is noted that there is a strong relationship between the term $k\sqrt{Q_{ps}}$, the coil-to-coil efficiency and the power output of resonant coils. The ungapped-core model 4 with the highest value of $k\sqrt{Q_{ps}}$ has the highest efficiency and power output. Similarly, the model 4 with the lowest value of $k\sqrt{Q_{ps}}$ has the lowest efficiency and power output.

In order to establish the performance of each of the flux-pipe coil models; based on the SAE J2954 standard under a series-series compensation topology, each coil performance was evaluated at a resonant frequency of 85 kHz with a load resistance of 20Ω . The result of the simulation is presented in Table 6.8.

All the three versions of the optimum flux-pipe models were able to achieve a coil-to-coil efficiency of above 99% at the operating frequency of 85 kHz with the same load of 20Ω .

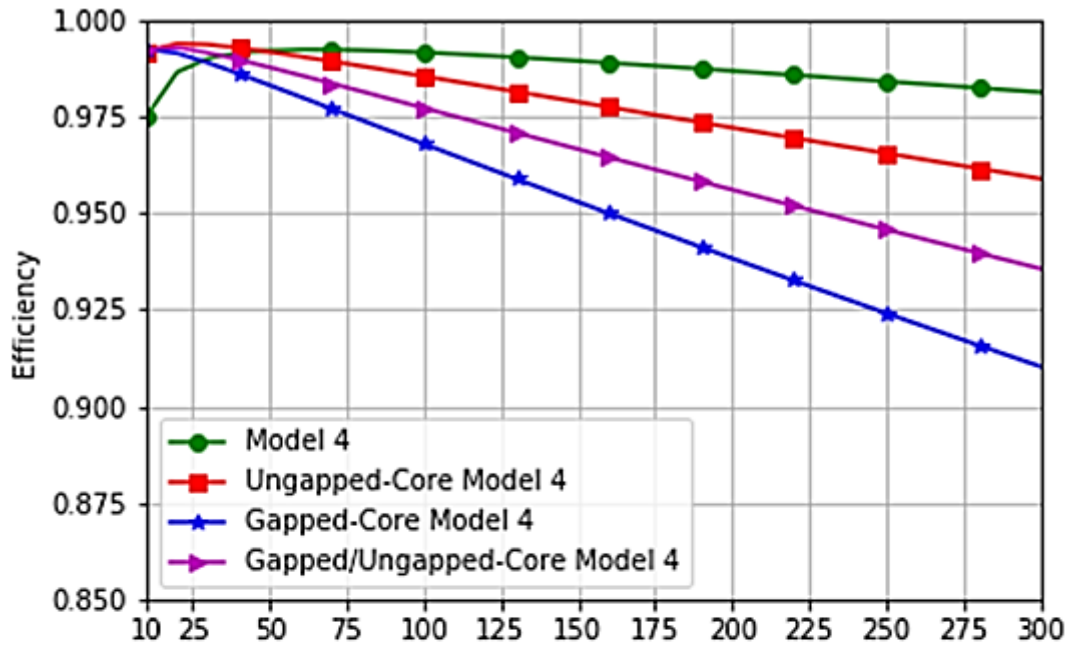
Table 6.8: Performance Characteristics of Flux-pipe Coil Models Based on SAE J2954 standard for the S-S Compensation Topology.

| Parameters | S-S Configuration | | | |
|-------------------------|-------------------|-----------------------|---------------------|-------------------------|
| | Model 4 | Ungapped-core Model 4 | Gapped-core Model 4 | Gapped/Ungapped Model 4 |
| Resonant Frequency | 85 kHz | 85 kHz | 85 kHz | 85 kHz |
| $k\sqrt{Q_{ps}}$ | 527 | 924 | 539 | 602 |
| Input Voltage | 300 V | 300 V | 300 V | 300 V |
| Output Voltage | 201 V | 330 V | 487 V | 394 V |
| Load Resistance | 20 Ω | 20 Ω | 20 Ω | 20 Ω |
| Input Current | 3.62 A | 14.00 A | 41.83 A | 26.14 A |
| Output Current | 5.38 A | 14.4 A | 24.35 A | 19.68 |
| Input Power | 1.09 kW | 4.78 kW | 11.97 kW | 7.80 kW |
| Output Power | 1.08 kW | 4.75 kW | 11.86 kW | 7.74 kW |
| Total Power Losses | 10 W | 30 W | 110 W | 60 W |
| Coil-to-Coil Efficiency | 99.14 % | 99.37 % | 99.12 % | 99.27 % |

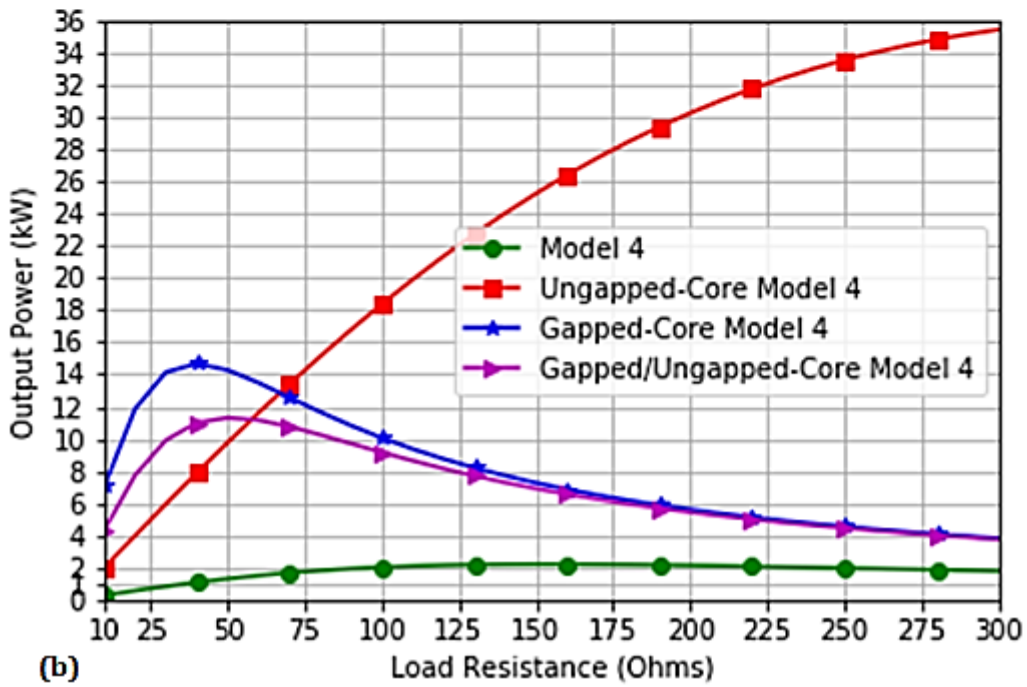
The ungapped-core model 4 was able to achieve the highest efficiency but it comes by trading off the power output which is just a little above 4.5 kW. The ungapped-core model 4 is well suited for bidirectional wireless power transfer for low power applications. In contrast, the gapped-core Model 4 and gapped/ungapped model 4 are well suited for high and medium power transfer applications. The presence of these excellent performance characteristics of the gapped-core Model 4 makes it highly suitable for dynamic charging of electric vehicles.

In the course of charging/discharging cycle of an EV battery, the load resistance varies based on the state of charge (SoC) of the battery. In order to evaluate the performance characteristics of each of the four coil models at the SAEJ2954 specified operating frequency of 85 kHz, a parametric sweep of different load resistance of between 10 Ω to 300 Ω was undertaken and the evaluated value of coil-to-coil efficiency and power output are illustrated in Figure 6.19.

From the results presented in Figure 6.19, it is noted that the traditional flux-pipe model (model 4) maintains the relatively the highest coil-to-coil efficiency over a large range of load resistances but performed poorly in terms of power output over the same range of load resistances.



(a)



(b)

Figure 6.19: Effect of Load Resistance on the Performance of Resonant Coils for S-S Compensation Topology. (a) Effect on Efficiency. (b) Effect on Power Output.

While the dynamic and hybrid models displayed similar power output performance when compared with the circular and rectangular coils, the static model displayed an unconventional relationship between power output and load resistance.

For the dynamic and hybrid model designs, the maximum power output do not correspond to the maximum efficiency while static model displayed a positive relationship between the coil-to-coil

efficiency and power output over the range of load resistance. This improved performance was achieved while maintaining higher coil-to-coil efficiency when compared with the dynamic and hybrid model. For practical applications, low load resistance is recommended because of current limit, which may drive the core into saturation. A critical look at the performance trend shown in Figure 6.19(a), it is observed increasing the number of gapped cores in a flux-pipe WPTs decreases the coil-to-coil efficiency over a range of load resistances.

6.13.2 Performance Characteristics of Optimal Flux-Pipe Resonant Coil in an S-P Compensation Topology.

For the S-P compensation topology, there is an inverse relationship between the power transferred and the power transfer efficiency over the same range of load resistances presented for the S-S topology. This is illustrated in Figure 6.21Figure 6.20.

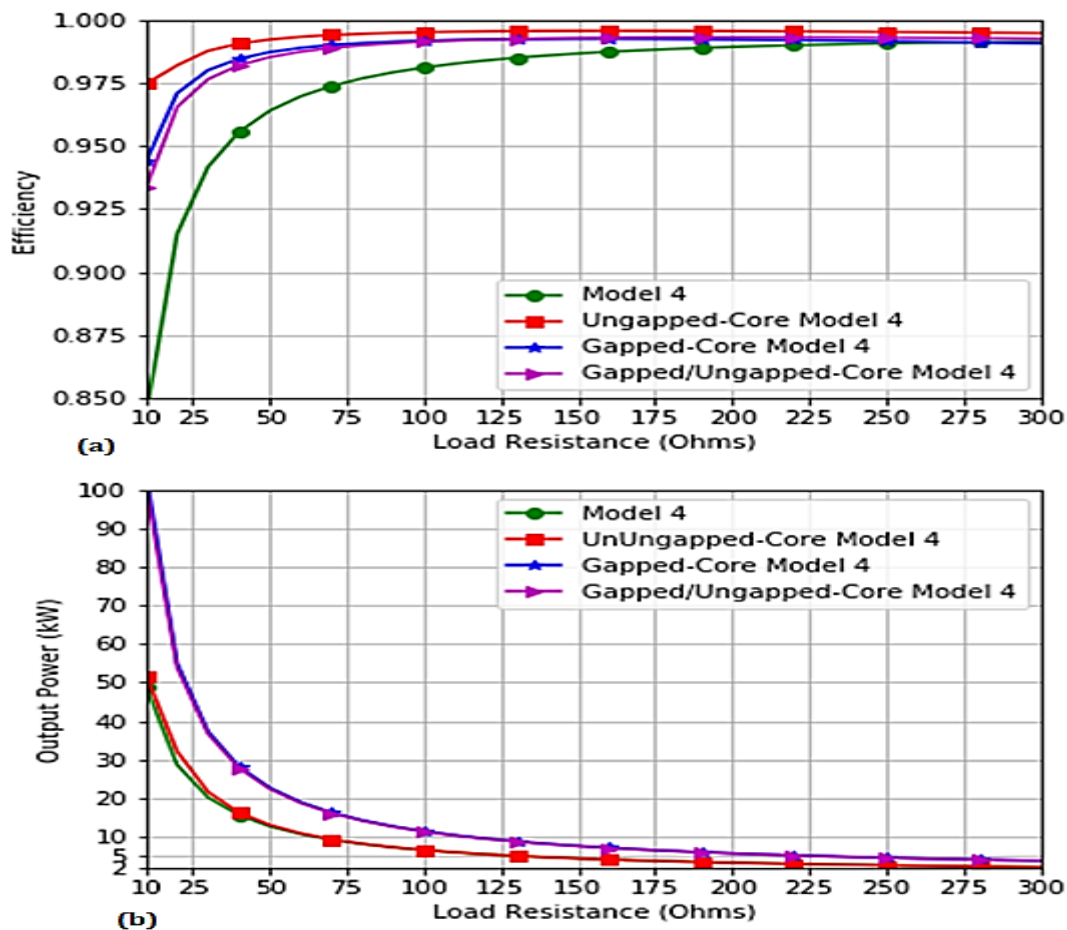


Figure 6.20: Effect of Load Resistance on the Performance of Resonant Coils for S-P Compensation Topology (a) Effect on Efficiency. (b) Effect on Power Output

For each of the individual coil model designs, there was an increase in the power transfer efficiency as the value of the load resistance increases. This is in contrast to the performance obtained for the power output with respect to the increase in load resistances. At low load resistances, there is significantly high power output obtained with the gapped/ungapped model 4 and gapped model 4 producing over

100 kW of output power at load resistance of 10 Ω ; but decreases sharply with an increase in load resistance with all the individual coil designs producing less than 10 kW of output power at load resistance greater than 125 Ω .

For practical design implementation, there is always a trade-off between power output and efficiencies depending on the critical requirements for the system application. Generally, for a wireless power transfer system, the power transfer efficiency is the most important parameter. Thus, for the developed coil designs employing the S-P compensation topology, the load resistance of 50 Ω was selected as the optimum load resistance for the ungapped-core model 4 and gapped-core Model 4. The overall system performance for a load resistance of 50 Ω is listed and summarized in Table 6.9.

Table 6.9: Summary of Performance Characteristics of Resonant Coil Models for S-P Configuration

| Parameters | S-P Configuration | | | |
|-------------------------|-------------------|-----------------------|---------------------|-------------------------|
| | Model 4 | Ungapped-core Model 4 | Gapped-Core Model 4 | Gapped/Ungapped Model 4 |
| Resonant Frequency | 40 kHz | 50 kHz | 60 kHz | 55 kHz |
| $k\sqrt{Q_{ps}}$ | 252 | 550 | 384 | 393 |
| Input Voltage | 300 V | 300 V | 300 V | 300 V |
| Output Voltage | 819 V | 811 V | 1068 V | 1060 V |
| Load Resistance | 200 Ω | 50 Ω | 50 Ω | 50 Ω |
| Input Current | 11.38 A | 44.26 A | 77.06 A | 76.13 A |
| Output Current | 4.10A | 16.22 A | 21.36 A | 21.21 A |
| Input Power | 3.41 kW | 13.28 kW | 23.12 kW | 22.84 kW |
| Output Power | 3.36 kW | 13.16 kW | 22.80 kW | 22.50 kW |
| Total Power Losses | 50 W | 120 W | 320 W | 340 W |
| Coil-to-Coil Efficiency | 98.47 % | 99.12 % | 98.64 % | 98.49 % |

From the results presented in Table 6.9, it is noted that the ungapped-core model 4 and gapped-core Model 4 model have higher performance than the traditional model in terms of power output and efficiency. There is also a strong correlation between the term $k\sqrt{Q_{ps}}$ and the efficiency of the WPT system. The ungapped-core model 4 has the highest value of $k\sqrt{Q_{ps}}$ and coil-to-coil efficiency. In relation to the input current, output current, power input and power output; the ungapped-core model 4 was able to achieve improved performance over the traditional model 4 by a factor of almost 4 in addition to having higher coil-to-coil efficiency.

Similarly, the gapped-core model 4 was able to achieve higher performance by a factor of almost 7 in relation to the input current, output current, input power and output power with respect to the performance of the traditional model 4. The improved performance was attained in addition to having higher coil-to-coil efficiency.

It is important to note that the S-P compensation comes with high output voltages for the three flux-pipe designs. This is because of the high voltage build-up in the secondary compensating capacitor C_p as shown in Figure 4.9. Since the load resistance R_L is connected in parallel with the compensating capacitor, both have the same voltage across them. As a result, the load resistance R_L needs to be large in order to limit the amount of current flowing in the load to a practical level.

From the summary of results presented in Table 6.9, it is also noted that there is a strong relationship between the term $k\sqrt{Q_{ps}}$, the coil-to-coil efficiency and the power output of resonant coils. The circular coil with the highest value of $k\sqrt{Q_{ps}}$ has the best performance. Similarly, the model 4 with the lowest value of $k\sqrt{Q_{ps}}$ has the lowest circuit performance.

In order to establish the performance of each flux-pipe coil models based on the SAE J2954 standard under a series-parallel compensation topology, each coil performance was evaluated at a resonant frequency of 85 kHz with a load resistance of 200 Ω for the model 4 and 50 Ω for the optimized flux-pipe models. The result of the simulation is presented in Table 6.10.

Table 6.10: Performance Characteristics of Flux-pipe Coil Models Based on SAE J2954 standard for the S-P Compensation Topology.

| Parameters | S-P Configuration | | | |
|-------------------------|-------------------|-----------------------|---------------------|-------------------------|
| | Model 4 | Ungapped-core Model 4 | Gapped-core Model 4 | Gapped/Ungapped Model 4 |
| Resonant Frequency | 85 kHz | 85 kHz | 85 kHz | 85 kHz |
| $k\sqrt{Q_{ps}}$ | 527 | 924 | 539 | 602 |
| Input Voltage | 300 V | 300 V | 300 V | 300 V |
| Output Voltage | 819 V | 811 V | 1067 V | 1060 V |
| Load Resistance | 200 Ω | 50 Ω | 50 Ω | 50 Ω |
| Input Current | 11.38 A | 44.19 A | 76.93 A | 75.99 A |
| Output Current | 4.10A | 16.22 A | 21.34 A | 21.19 A |
| Input Power | 3.41 kW | 13.26 kW | 23.08 kW | 22.80 kW |
| Output Power | 3.36 kW | 13.15 kW | 22.78 kW | 22.46 kW |
| Total Power Losses | 50 W | 110 W | 300 W | 340 W |
| Coil-to-Coil Efficiency | 98.47 % | 99.21 % | 98.71 % | 98.51 % |

From the results presented in Table 6.10, all the three optimized flux-pipe models are capable of high power transfer at coil-to-coil efficiency of above 98.50 %. The ungapped-core model 4 can be used for unidirectional wireless power transfer requiring high power ratings. Similarly, the gapped-core model 4 and gapped/ungapped model 4 are capable of charging two or more cars during the dynamic mode of operations. Thus, the proposed optimum coil designs are capable of system operations and interoperability with other WPT systems using the SAE J2954 standard.

6.13.3 Impact of Misalignment on the Efficiency of Coil Designs.

From the previous sections, the optimum values of resonant frequencies and load resistance for each coil model designs were presented for coil designs at airgap of 200mm and with no misalignment. For most practical applications, there are possibilities of misalignment in the course of operation of the wireless coil designs. In order to ascertain the impact of coil misalignment on the efficiencies of each of the coil designs, each of the secondary coil of the coil models was subjected to a level of lateral and longitudinal misalignment at a fixed airgap of 200 mm. The efficiencies of the coil system under these misalignments were evaluated.

The efficiency performance for the S-S compensation topology for each of the four flux-pipe resonant coil models is presented in Figure 6.21. For all the various misalignment scenarios analysed for the S-S compensation topology, the traditional model 4 has the least performance in terms of efficiency. The result was expected because of the low value of $k\sqrt{Q_{ps}}$ for the traditional Model 4. Similarly, the ungapped-core model 4 with the highest value of $k\sqrt{Q_{ps}}$ has the highest value of efficiency for all the misalignment scenarios.

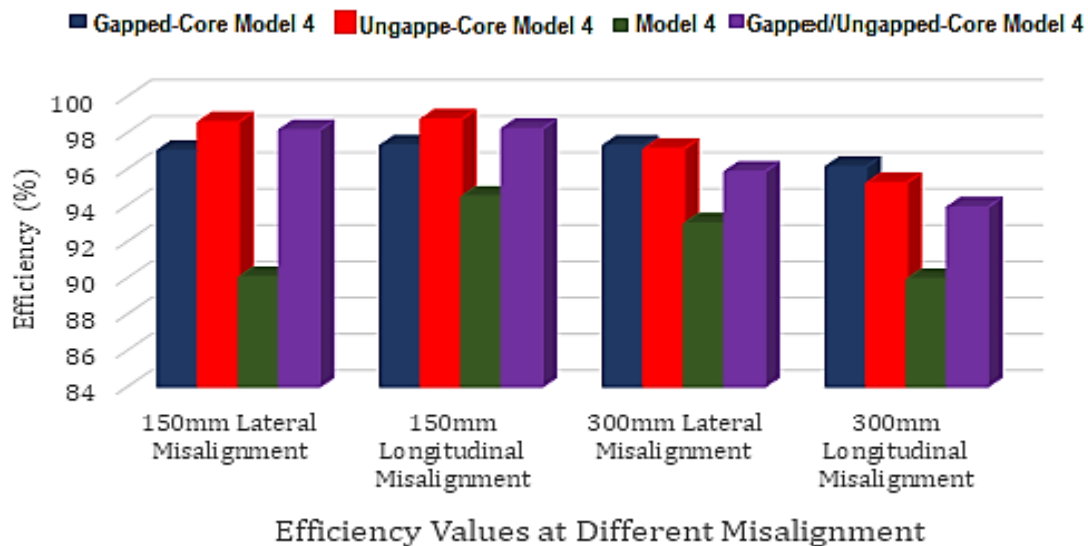


Figure 6.21: Misalignment Performance of Flux-Pipe Resonant Coil Designs for S-S Compensation Topology

The low value of $k\sqrt{Q_{ps}}$ for the model 4 design was because of higher intrinsic resistance of the coils, which lower the value of the quality factor. As a consequence, the higher value of k for the model 4 was insufficient to boost the numerical value of $k\sqrt{Q_{ps}}$. In contrast, the ungapped-core model 4 and gapped-core Model 4 designs exhibited a higher performance as a result of the significant reduction of the intrinsic resistances of the coil models because of the parallel combination of the inductances, thus, increasing the value of the quality factor. The significant boost in the quality factor for both coil designs caused a significant increase in the numerical value of $k\sqrt{Q_{ps}}$ despite having lower k value in relation to the high value of k in the traditional model 4.

The lower value of $k\sqrt{Q_{ps}}$ for the gapped-core model 4 in relation to the numerical value obtained for the ungapped-core model 4 was because of the air gap in the core of the gapped-core Model 4 design. The air gap in the core reduces the self-inductance of the primary and secondary coils and mutual inductance between the primary and secondary coils. The air gap in the core also causes an increase in the reluctance of the ferrite core. Since the value of the primary and secondary intrinsic resistance of gapped-core Model 4 is the same with that of the ungapped-core model 4, the reduction in the self-inductances of the gapped-core Model 4 leads to a reduction in the value Q_{ps} .

Similarly, the efficiency performance for the S-P compensation topology for each of the coil model is presented in Figure 6.22.

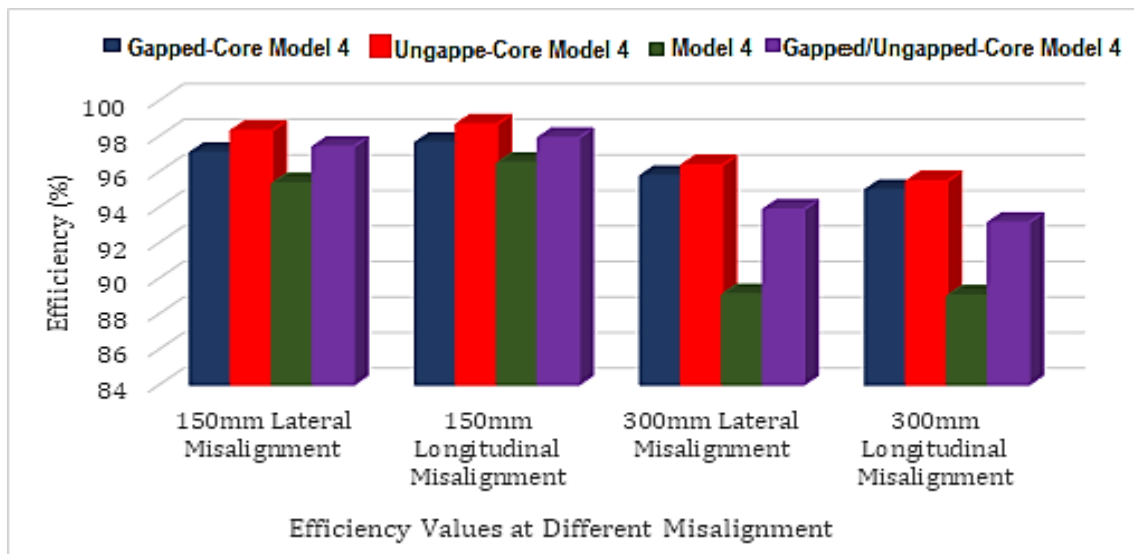


Figure 6.22: Misalignment Performance of Resonant Coil Designs for S-P Compensation Topology.

In the case of the S-P compensation scheme, the three flux-pipe model designs displayed minimum efficiency performance of 94% for a lateral and longitudinal misalignment of 150 mm while at lateral and longitudinal misalignment of 300 mm, the efficiency performance of model 4 dropped significantly below 90%. The ungapped-core model 4 and gapped-core model 4 at 300 mm misalignment were able to maintain coil-to-coil efficiency above 90%.

The performance of the individual flux-pipe models follows a similar trend noted in the case of the S-S compensation scheme; the higher value of $k\sqrt{Q_{ps}}$ causes an increase in the coil-to-coil efficiency.

From the results presented for the effective performance of all the flux-pipe models under the S-S and S-P compensation scheme, it is noted that a higher value of $k\sqrt{Q_{ps}}$ leads to a corresponding increase in coil-to-coil efficiency at a lower load resistance. For flux-pipes with similar values of intrinsic resistance, a reduction in the self-inductance of the coils as a result of air the gap in the ferrite core increases the power transferability of the coil designs.

6.14 Electromagnetic Field Radiation Analysis

In order to ascertain the design performance in relation to the regulation limit, field analysis of the magnetic flux density at the maximum current and for both transmitter and receiver under the S-P and S-S compensation scheme was implemented. The magnetic flux distribution around the ungapped-core model 4 and gapped-core model 4 is illustrated in Figure 6.23.

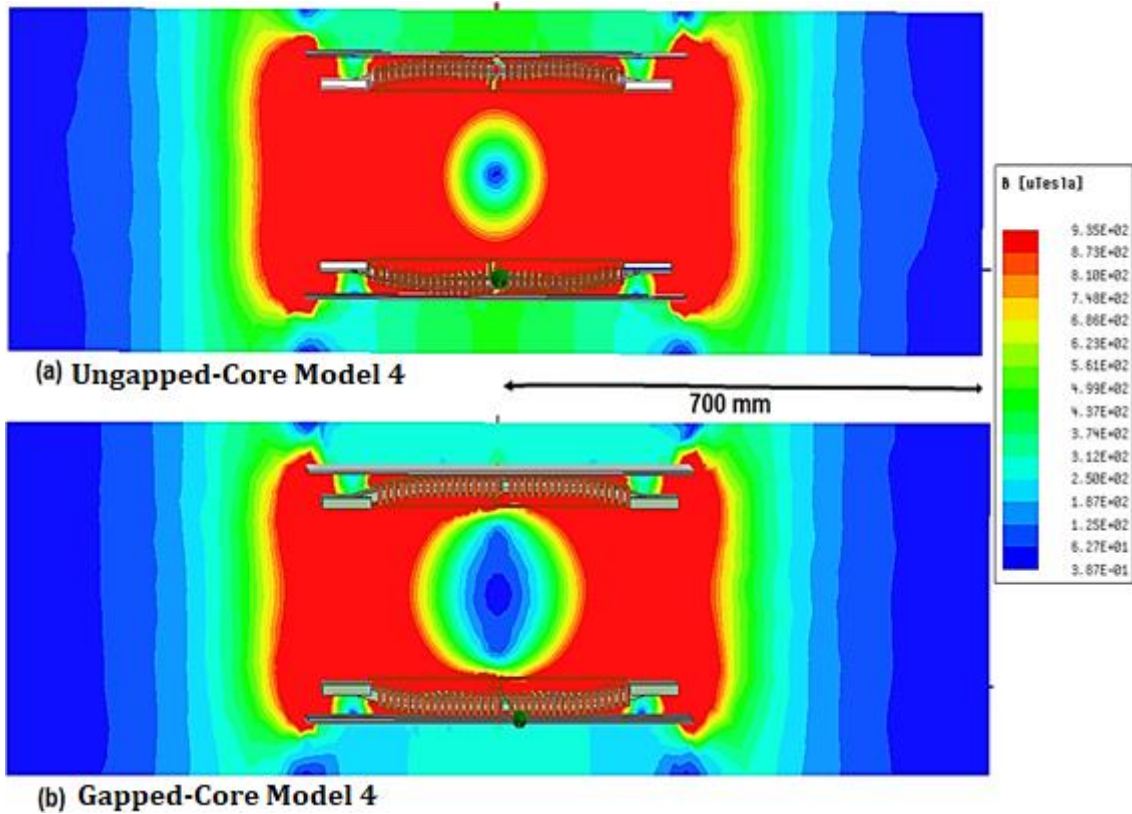


Figure 6.23: Magnetic Field Radiation of Proposed Optimal Flux-Pipe Models. (a) Ungapped-core Model 4. (b) Gapped-core Model 4.

The electromagnetic field radiation is maximum around the coil windings because of the level of power transfer at those regions. The electromagnetic field radiation at the edges is due to the presence of leakage magnetic field in between the coils. Similarly, the intensity of the magnetic field decreases as the distance increases from the centre of the model coils. The magnetic field intensity is at the farthest distance from the centre of the flux-pipe models along either of the positive or negative Y-axis.

From guidelines proposed by ICNIRPP, the human body must not be exposed to the magnetic field beyond $27.3 \mu\text{T}$. Similarly, the average exposure at the head, chest and groin must not exceed $6.25 \mu\text{T}$. A cursory look at Figure 6.23, the strength of the magnetic field at 700 mm from the centre of both the ungapped-core model 4 and Gapped-core Model 4 is around $0.387 \mu\text{T}$, which is far less than the average limit of $6.25 \mu\text{T}$. This is an indication that at the rated power output specified for the two models, the models' operation is in line with safety regulations. Thus, the proposed optimal model's optimization technique is justified and practically feasible.

6.15 Summary

In this chapter, an optimal design of the traditional flux-pipe resonant coil for high power output and efficiency was undertaken. Based on some sets of governing equations, the windings of the coil was split into two parts in order to reduce the excitation current by half. Similarly, the ferrite core was modelled into a C-shape in order to reduce the amount of eddy current losses. A copper shield was selected as optimum shielding material because of its lower eddy current power loss per unit mass when compared with aluminium.

Based on these design modifications, an optimized model known as ungapped-core model 4 that is suited for static charging of electric vehicles was created. With the introduction of the air gap in the ferrite core of the ungapped-core model 4, an optimized model for dynamic charging was created. The gapped-core model 4 is well suited for high power operations.

Two types of shielding materials commonly used for WPT systems were identified. They are conductive shield materials and magnetic shield materials. The use of these type of materials comes with different types of losses. The losses commonly encountered in WPT systems using either of these shielding materials are ohmic losses, core losses and eddy current losses. Using a conductive shield, there are majorly three types of losses present in the system: ohmic losses in the coil windings, core losses in the ferrite core and eddy current in the conductive shield. Similarly, using a magnetic shield for a WPT system, an additional loss known as core losses in the magnetic shield is present in addition to all the losses present in the system using a conductive shield. Due to the presence of this additional loss in the magnetic shield, the use of the magnetic shield is not a viable option for use with WPT systems applicable to electric vehicles.

An affordable and appropriate alternative is the use of conductive shields for WPT system applications. Three common conductive metal used for shielding of electromagnetic fields are copper, aluminium and zinc. The mathematical equation for Eddy current losses per unit mass for the conductive shield was applied to the two conductive materials. The eddy current losses in copper are less than the losses obtained in aluminium; in addition, copper is not reactive to concrete or lime-bearing cement. As a result of these advantages, copper was chosen as the optimum shield component for this research.

Magnetostatic analysis of the optimized flux-pipe models was subjected to a parametric analysis to ascertain their current saturation limits and magnetic coupling under various misalignments. From the results presented, the ungapped-core model 4 and Gapped-core model 4 can withstand an excitation current of up to 90 A without their respective ferrite cores going into saturation. Similarly, from the results presented for the misalignment performance, there was a decrease in the performance of the two optimized models due to the slight dip in the ferrite core, thus increasing the overall airgap distances between the coils. There was also a decrease in the magnetic coupling for the Gapped-core model 4 for all the misalignment cases in relation to the performance of the ungapped-core model 4.

The decrease in performance was due to the introduction of an air gap in the core which reduces the self-inductance, mutual inductance and the permeability of the ferrite core.

The two optimized flux-pipe coil designs in addition to a hybrid version were subjected to eddy current analysis to ascertain the amount of losses present in the coil model systems for various values of current and frequencies. It was noted that the three optimized models showed a significant decrease in the ohmic, eddy current and core losses in relation to the traditional flux-pipe model. Similarly, the gapped-core model 4 has the least amount of losses as a result of the air gap in its core which justifies its suitability for high power dynamic charging operations.

In the circuit analysis of the two optimized flux-pipe models, the two models were able to transfer more electrical power with higher efficiencies than the traditional flux-pipe model. The higher performance of the two models was maintained under both the S-P and S-S compensation scheme. The higher performance was attainable because the two models have a greater value of $k\sqrt{Q_{ps}}$ due to the significant reduction in the total intrinsic resistances of the coils.

From the simulation results presented, the model designed for static charging operations can transfer up to 13.28kW of power across the airgap at a coil-to-coil efficiency of 99.12% while the model design for dynamic charging of electric vehicles can transfer up to 22.80 kW of power across the airgap at a coil-to-coil efficiency of 98.64% without exceeding the average limit specified for the exposure of human body to electromagnetic fields.

The three optimized flux-pipe coils were operated at a resonant frequency of 85 kHz which is the SAE J2954 standard for both the bidirectional and unidirectional power transfer operations. It was noted established that the Gapped-core Model 4 and hybrid model 4 are capable of bidirectional wireless power transfer at high power ratings of above 11 kW while the ungapped-core model 4 is capable of bidirectional wireless power transfer at power ratings lower than 5 kW.

Finally, the three optimal flux-pipe model designs were subjected to lateral and longitudinal misalignment condition by displacing the secondary coils for each model by 150 mm and 300 mm respectively along the x-axis and y-axis. The evaluated efficiencies obtained at this level of misalignment was presented. It was noted that the ungapped-core model 4, hybrid model 4 and the Gapped-core Model 4 were able to achieve higher efficiencies than the traditional flux-pipe models for all the cases of misalignments. The ungapped-core model 4 has the overall best performance in terms of efficiency. This was because the ungapped-core model 4 has the highest numerical value of $k\sqrt{Q_{ps}}$.

CHAPTER 7 Conclusion and Recommendations

In this chapter, the major observations from the presented simulation results are highlighted. Similarly, the limitations encountered in the course of this research are listed and discussed. Finally, the future works based on the presented results and recommendations for researchers who might want to further optimize the optimal flux-pipe models presented in this research.

7.1 Conclusion from Research

In this research, a system-level engineering and simulation-based modelling methodology were employed for the optimal design, analyses, optimizations, and evaluations of the flux-pipe resonant coil for high-power and efficient bidirectional wireless power transfer applicable to electric vehicles.

Based on the results presented in this research, the following observations were noted.

- The magnetic coupling factor, power output and efficiencies of wireless power transfer model topologies are largely dependent on the media of transmission and the operating frequencies.
- The ferrite core MRC-based wireless power systems are one of the most suitable WPT topologies for the charging of electric vehicles because of the low cost, high efficiency and high power output.
- In the modelling and simulation of ferrite core MRC-based wireless power systems, proper specifications of initial and boundary conditions is highly essential for the accurate solution of model designs using the finite element modelling approach.
- The maximum efficiency attainable by any wireless power transfer system is dependent on the numerical values of $k\sqrt{Q_p \cdot Q_s}$. The higher the value of $k\sqrt{Q_p \cdot Q_s}$ the higher the maximum attainable efficiency for a particular resonant frequency.
- The optimum resonant frequency for any model ferrite-cored resonant is inversely proportional to the level of magnetic coupling between the primary and secondary coils. The higher the value of the magnetic coupling between the coils, the lower the value of the optimum resonant frequency for effective and efficient wireless power transfer.
- The ferrite core MRC-based wireless power models using circular or rectangular coil designs have some specific advantages and disadvantages. The coil designs are capable of having high power outputs and efficiencies at low power losses under little or no misalignment conditions. Their efficiencies drop significantly with increase in horizontal misalignments.

- The ferrite core MRC-based wireless power systems using the traditional flux-pipe topology has some specific benefits and drawbacks. The benefits include high coupling coefficient, high misalignment tolerance and high efficiencies under misalignment conditions. The major drawbacks are the low values of power output due to the generation of an equal amount of useful and non-useful fluxes and the presence of high power losses
- The self-inductance, mutual inductance and magnetic coupling performance of flux-pipe resonant coils can be enhanced with more number of turns than increasing the length of the coil turns.
- An affordable and appropriate shielding alternative for WPT system is the use of conductive shields. Three common conductive metal used for shielding of electromagnetic fields are copper, aluminium and zinc. The mathematical equation for Eddy current losses per unit mass for the conductive shield was applied to the three conductive materials. It was noted that zinc has the least eddy current losses per unit mass but it is not commonly used due to chemical properties. Zinc is very sensitive to sulphurous components in the air and alkaline material. Similarly, the eddy current losses in copper are less than twice the losses in aluminium; in addition, copper is not reactive to concrete or lime-bearing cement
- From the overall loss results presented for the eddy current analyses, it is noted that core losses increase logarithmically with an increase in frequency and exponentially with an increase in excitation current. It is also noted that the ohmic losses in the system increase logarithmically with an increase in the current while the eddy current losses increase exponentially with increase in frequency.
- The flux-pipe model can be optimized for high power outputs and low losses by three major modifications. The modifications include 1) Splitting the coil windings into two and connecting them in parallel in order to reduce the intrinsic resistance of the coils and increases the quality factor of the coils. 2) Use of copper sheet as the appropriate shielding material instead of copper due to its lower eddy current losses per unit mass. 3) Introduction of the air gap in the ferrite core in order to increase the amount of excitation current required to drive the core into saturation.

7.2 Research Limitations

The finite element modelling simulation approach requires computer facilities with a high amount of memory (greater than 16GB of RAM) and a high number of computer cores (greater than 8 cores). The simulations can last a number of days or weeks depending on the complexity and required mesh of the model problem that will create accurate solutions. The alternative solution is the use of clusters for

finite analysis but most high-performance computing facilities operate using the queue system. In addition, there might be an incompatibility in the operating systems used in the modelling and analysis of model designs.

Another limitation is the difficulty in accessing design parameters for the accurate replication of published experimental models for the validation of initial and boundary conditions needed for accurate modelling. Due to the absence of some key physical and circuit parameters of many published research works, model validation undertaken in this research was only possible with two published research works. As a result, simulation validations was undertaken by comparing simulation results with theoretical analyses and validated mathematical equations.

Due to the nature and shape of the ferrite core of the optimized flux-pipe models, it was difficult to order for ferrite core material for experimental validation. This is primarily as a result of the proposed C-shape ferrite core proposed in this research which is not among the standard shapes commercially produced by most industrial manufacturers.

Accurate procurement of the ferrite core will involve a specifications of the angle and length of the arc of the core. An alternative approach is to purchase the standard rectangular cores, cut them into smaller bar-shapes which can be moulded into a C-shape by joining each ferrite core bars using an adhesive. But the solution will introduced series of tiny air gaps in the final shape designs which will create significant experimental errors.

7.3 Future Work

A comprehensive design and analysis of the magnetic aspects of flux-pipe resonant coils was conducted in this research. The work focused on the magnetostatic, eddy current and a.c. analysis of model coil designs. But there are some aspects of the overall wireless power system that have not been studied and would require further investigation.

To begin with, future work should cover the analysis of the coil design performance with respect to the effects of frequency. This can be evaluated by performing extensive transient simulation analyses. Also, future work should cover a thermal evaluation of the coil designs as a result of local loss distribution. Since the flux-pipe model design proposed in this research is optimized for higher power transfer, higher power comes with power loss increase which would be expected to increase temperatures. The thermal changes would then affect the electrical properties of components and this should be investigated.

With respect to the overall wireless power systems infrastructure, the coil performance characteristics when power electronic controls (consisting of inverters, rectifiers and converters) are incorporated should be investigated.

Going forward with the evaluated system design specifications, future work will cover the analysis and evaluation of system design performance when subjected to static and dynamic operating conditions. The dynamic operating conditions will consider the level of power transfer with combinations of multiple pick-ups.

Investigations into the impact of wireless power operations on power quality and stability should be undertaken. With the possibility of harmonics present in the course of system operations, implementation of efficient algorithms for the reduction or elimination of the harmonics should be investigated.

In the literature review, extensive research and analysis was done in the area of smart grids and the prospect of vehicle-to-grid technology. The potential operations and benefits that were highlighted would require a gradual implementation in the future.

References

- [1] V. Monteiro, H. Gonçalves, and J. L. Afonso, "Impact of electric vehicles on power quality in a Smart Grid context," *Proceeding Int. Conf. Electr. Power Qual. Util. EPQU*, pp. 660–665, 2011, doi: 10.1109/EPQU.2011.6128861.
- [2] A. Poullikkas, "Sustainable options for electric vehicle technologies," *Renew. Sustain. Energy Rev.*, vol. 41, pp. 1277–1287, 2015, doi: 10.1016/j.rser.2014.09.016.
- [3] C. Liu, K. T. Chau, D. Wu, and S. Gao, "Opportunities and Challenges of Vehicle-to-Home, Vehicle-to-Vehicle, and Vehicle-to-Grid Technologies," *Proc. IEEE*, vol. 101, no. 11, pp. 2409–2427, 2013, doi: 10.1109/JPROC.2013.2271951.
- [4] M. A. Hannan, F. A. Azidin, and A. Mohamed, "Hybrid electric vehicles and their challenges: A review," *Renew. Sustain. Energy Rev.*, vol. 29, pp. 135–150, 2014, doi: 10.1016/j.rser.2013.08.097.
- [5] M. F. M. Sabri, K. A. Danapalasingam, and M. F. Rahmat, "A review on hybrid electric vehicles architecture and energy management strategies," *Renew. Sustain. Energy Rev.*, vol. 53, pp. 1433–1442, 2016, doi: 10.1016/j.rser.2015.09.036.
- [6] J. García-Villalobos, I. Zamora, J. I. San Martín, F. J. Asensio, and V. Aperribay, "Plug-in electric vehicles in electric distribution networks: A review of smart charging approaches," *Renew. Sustain. Energy Rev.*, vol. 38, pp. 717–731, 2014, doi: 10.1016/j.rser.2014.07.040.
- [7] S. Price and R. Summers, "A technology roadmap for rehabilitation engineering," *Int. Energy Agency, Tech. Rep.*, no. June, pp. 3471–3473, 2005, doi: 10.1109/iembs.2004.1403974.
- [8] C. E. Warrender *et al.*, "Analysis of a consumer survey on plug-in hybrid electric vehicles," *Transp. Res. Part A Policy Pract.*, vol. 64, pp. 14–31, 2014, doi: 10.1016/j.tra.2014.02.019.
- [9] IEA, "Global EV Outlook 2019," 2019.
- [10] M. Ho Kwon *et al.*, "Development of Electric Vehicle Simulator for Performance Analysis," *Univers. J. Mech. Eng.*, vol. 2, no. 7, pp. 231–239, 2017, doi: 10.13189/ujme.2014.020704.
- [11] G. Lempidis, Y. Zhang, M. Jung, R. Marklein, S. Sotiriou, and Y. Ma, "Wired and wire less charging of electric vehicles," in *2014 4th International Electric Drives Production Conference (EDPC)*, 2014, pp. 1–7, doi: 10.1109/EDPC.2014.6984421.
- [12] M. Brazil, I. Mareels, J. de Hoog, D. A. Thomas, and T. Alpcan, "Optimal Charging of Electric Vehicles Taking Distribution Network Constraints Into Account," *IEEE Trans. Power Syst.*, vol. 30, no. 1, pp. 365–375, 2014, doi: 10.1109/tpwrs.2014.2318293.
- [13] G. A. Covic and J. T. Boys, "Modern trends in inductive power transfer for transportation applications," *IEEE J. Emerg. Sel. Top. Power Electron.*, vol. 1, no. 1, pp. 28–41, 2013, doi: 10.1109/JESTPE.2013.2264473.
- [14] M. Ehsani, "Plug-in Hybrid Electric Vehicles," *Transp. Technol. Sustain.*, pp. 1–3, 2013.
- [15] B. Lane, "Electric vehicle market statistics," 2019.
- [16] X. Mou and H. Sun, "Wireless power transfer: Survey and roadmap," in *IEEE Vehicular Technology Conference*, 2015, vol. 2015, pp. 1–5, doi: 10.1109/VTCSpring.2015.7146165.
- [17] M. Bojarski, K. K. Kutty, D. Czarkowski, and F. De Leon, "Multiphase resonant inverters for bidirectional wireless power transfer," in *2014 IEEE International Electric Vehicle Conference, IEVC 2014*, 2015, pp. 1–7, doi: 10.1109/IEVC.2014.7056191.
- [18] R. de, R. Esteves, and D. Freitas, "FPGA Based Powertrain Control for Electric Vehicles," *Electr. Veh.*

- *Model. Simulations*, 2012, doi: 10.5772/18491.

- [19] S. Sotiriou, "Analysis of Operation and System Losses of an Inductive Power Transfer System for Wireless Charging of Electric Vehicles," Delft University of Technology, 2014.
- [20] D. Voglitsis, "Theoretical Analysis and Experimental Investigation of a Bidirectional Inductive Power Transfer System Applicable for Electric Vehicle Charging," 2014.
- [21] M. Amin and J. Stringer, "The electric power grid: Today and tomorrow," *MRS Bull.*, vol. 33, no. 4, pp. 399–407, 2008, doi: 10.1557/mrs2008.80.
- [22] Z. Darabi and M. Ferdowsi, "Impact of Plug-In Hybrid Electric Vehicles on Electricity Demand Profile," *Power Syst.*, vol. 53, no. 4, pp. 319–349, 2012, doi: 10.1007/978-3-642-21578-0_11.
- [23] X. Fang, S. Misra, G. Xue, and D. Yang, "Smart grid - The new and improved power grid: A survey," *IEEE Commun. Surv. Tutorials*, vol. 14, no. 4, pp. 944–980, 2012, doi: 10.1109/SURV.2011.101911.00087.
- [24] J. Bhatt, V. Shah, and O. Jani, "An instrumentation engineer's review on smart grid: Critical applications and parameters," *Renew. Sustain. Energy Rev.*, vol. 40, pp. 1217–1239, 2014, doi: 10.1016/j.rser.2014.07.187.
- [25] C. Liu, K. T. Chau, D. Wu, and S. Gao, "This paper investigates and proposes methodologies, approaches, and foresights for the emerging technologies of V2H, V2V, and V2G," vol. 101, no. 11, pp. 2409–2427, 2013, doi: 10.1109/JPROC.2013.2271951.
- [26] C. H. Ou, H. Liang, and W. Zhuang, "Investigating Wireless Charging and Mobility of Electric Vehicles on Electricity Market," *IEEE Trans. Ind. Electron.*, vol. 62, no. 5, pp. 3123–3133, 2015, doi: 10.1109/TIE.2014.2376913.
- [27] H. Farhangi, "The path of the smart grid," *IEEE Power Energy Mag.*, vol. 8, no. 1, pp. 18–28, 2010, doi: 10.1109/MPE.2009.934876.
- [28] J. Y. Yong, V. K. Ramachandaramurthy, K. M. Tan, and N. Mithulananthan, "A review on the state-of-the-art technologies of electric vehicle, its impacts and prospects," *Renew. Sustain. Energy Rev.*, vol. 49, pp. 365–385, 2015, doi: 10.1016/j.rser.2015.04.130.
- [29] W. Su, H. Eichi, W. Zeng, and M. Y. Chow, "A survey on the electrification of transportation in a smart grid environment," *IEEE Trans. Ind. Informatics*, vol. 8, no. 1, pp. 1–10, 2012, doi: 10.1109/TII.2011.2172454.
- [30] E. Ancillotti, R. Bruno, and M. Conti, "The role of communication systems in smart grids: Architectures, technical solutions and research challenges," *Comput. Commun.*, vol. 36, no. 17–18, pp. 1665–1697, 2013, doi: 10.1016/j.comcom.2013.09.004.
- [31] M. Yilmaz and P. T. Krein, "Review of the impact of vehicle-to-grid technologies on distribution systems and utility interfaces," *IEEE Transactions on Power Electronics*, vol. 28, no. 12, pp. 5673–5689, 2013, doi: 10.1109/TPEL.2012.2227500.
- [32] K. W. Hu, P. H. Yi, and C. M. Liaw, "An EV SRM Drive Powered by Battery/Supercapacitor with G2V and V2H/V2G Capabilities," *IEEE Trans. Ind. Electron.*, vol. 62, no. 8, pp. 4714–4727, 2015, doi: 10.1109/TIE.2015.2396873.
- [33] T. N. Guzin, K. Ince, and F. Karaosmanoglu, "Design and power management of a grid-connected Dc charging station for electric vehicles using solar and wind power," *2015 3rd Int. Istanbul Smart Grid Congr. Fair, ICSG 2015*, pp. 1–4, 2015, doi: 10.1109/SGCF.2015.7354921.
- [34] S. Sandrine and P. JOHN, "Greening the Accounts," *Power Syst.*, vol. 19, no. 11, pp. 2–4, 2012, doi: 10.13140/RG.2.1.2679.2164.

- [35] F. Mwasilu, J. J. Justo, E. K. Kim, T. D. Do, and J. W. Jung, "Electric vehicles and smart grid interaction: A review on vehicle to grid and renewable energy sources integration," *Renew. Sustain. Energy Rev.*, vol. 34, pp. 501–516, 2014, doi: 10.1016/j.rser.2014.03.031.
- [36] T. E. Stamati and P. Bauer, "On-road charging of electric vehicles," *2013 IEEE Transp. Electrification Conf. Expo Components, Syst. Power Electron. - From Technol. to Bus. Public Policy, ITEC 2013*, 2013, doi: 10.1109/ITEC.2013.6573511.
- [37] K. Kuhlmann, S. Wolf, C. Pieper, G. Xu, and J. Ahmad, "The Future of Battery Production for Electric Vehicles," 2018.
- [38] K. Rajashekara, "Present status and future trends in electric vehicle propulsion technologies," *IEEE J. Emerg. Sel. Top. Power Electron.*, vol. 1, no. 1, pp. 3–10, 2013, doi: 10.1109/JESTPE.2013.2259614.
- [39] T. Stamati and P. Bauer, "Green energy for on-road charging of electric vehicles," *2012 15th Int. Symp. Mechatronika*, 2012.
- [40] D.M. Vilathgamuwa and J.P.K. Sampath, "Plug In Electric Vehicles in Smart Grids," *Power Syst.*, vol. 19, no. 11, pp. 2–4, 2013, doi: 10.13140/RG.2.1.2679.2164.
- [41] X. Lu, P. Wang, D. Niyato, D. I. Kim, and Z. Han, "Wireless Charging Technologies: Fundamentals, Standards, and Network Applications," *IEEE Commun. Surv. Tutorials*, vol. 18, no. 2, pp. 1413–1452, 2016, doi: 10.1109/COMST.2015.2499783.
- [42] C. Liu, K. T. Chau, D. Wu, and S. Gao, "Opportunities and Challenges of Vehicle-to-Home, Vehicle-to-Vehicle, and Vehicle-to-Grid Technologies," *Proc. IEEE*, vol. 101, no. 11, pp. 2409–2427, 2013, doi: 10.1109/JPROC.2013.2271951.
- [43] K. A. Kalwar, M. Aamir, and S. Mekhilef, "Inductively coupled power transfer (ICPT) for electric vehicle charging - A review," *Renew. Sustain. Energy Rev.*, vol. 47, pp. 462–475, 2015, doi: 10.1016/j.rser.2015.03.040.
- [44] WEILAI LI B.A.Sc, "HIGH EFFICIENCY WIRELESS POWER TRANSMISSION AT LOW FREQUENCY USING PERMANENT MAGNET COUPLING," *University of British Columbia*, 2009. [Online]. Available: <https://open.library.ubc.ca/cIRcle/collections/ubctheses/24/items/1.0067661>.
- [45] C. Qiu, K. T. Chau, C. Liu, and C. C. Chan, "EVS27 International Battery, Hybrid and Fuel Cell Electric Vehicle Symposium Overview of Wireless Power Transfer for Electric Vehicle Charging," pp. 1–9, 2013.
- [46] L. Gheorghe, H. Vasile, R. Marcel, and A. Mihai, "Control of Hybrid Electrical Vehicles," *Electr. Veh. - Model. Simulations*, pp. 41–66, 2011.
- [47] International Energy Agency, "Technology Roadmap," *Encycl. Prod. Manuf. Manag.*, no. June, pp. 781–782, 2006, doi: 10.1007/1-4020-0612-8_961.
- [48] S. Chen, Y. Ji, and L. Tong, "Large scale charging of electric vehicles," *IEEE Power Energy Soc. Gen. Meet.*, pp. 1–9, 2012, doi: 10.1109/PESGM.2012.6345497.
- [49] M. Neath, U. K. Madawala, and D. Thrimawithana, "PhD: Bidirectional Inductive Power Transfer System: Analysis and Control," *Dep. Electr. Comput. Eng.*, vol. PhD, p. 172, 2014.
- [50] J. Donadee, M. Ilić, and O. Karabasoglu, "Optimal autonomous charging of electric vehicles with stochastic driver behavior," *2014 IEEE Veh. Power Propuls. Conf. VPPC 2014*, 2015, doi: 10.1109/VPPC.2014.7007115.
- [51] IEA, "Technology Roadmap- Electric and plug-in hybrid electric vehicles," *International Energy Agency*, 2009. [Online]. Available: http://www.iea.org/papers/2009/EV_PHEV_Roadmap.pdf. [Accessed: 28-Jan-2016].

- [52] H. Li, H. Liu, A. Ji, F. Li, and Y. Jia, "Design of a hybrid solar-wind powered charging station for electric vehicles," *ICMREE 2013 - Proc. 2013 Int. Conf. Mater. Renew. Energy Environ.*, vol. 3, pp. 977–981, 2013, doi: 10.1109/ICMREE.2013.6893835.
- [53] W. Kempton and S. E. Letendre, "Electric vehicles as a new power source for electric utilities," *Transp. Res. Part D Transp. Environ.*, vol. 2, no. 3, pp. 157–175, 1997, doi: 10.1016/S1361-9209(97)00001-1.
- [54] IEA, "Global EV Outlook 2018," *Global EV Outlook 2018*, 2018. [Online]. Available: http://centrodeinnovacion.uc.cl/assets/uploads/2018/12/global_ev_outlook_2018.pdf. [Accessed: 11-Apr-2019].
- [55] R. L. Herrera, A. G. Otero, E. E. Martínez, P. H. Ramírez, and G. M. Antuña, "Estudio molecular del gen MLL en 30 pacientes con leucemias agudas," *Rev. Cuba. Hematol. Inmunol. y Hemoter.*, vol. 16, no. 1, pp. 38–44, 2000.
- [56] B. Sri Kaloko, mr. Soebagio, and M. Hery Purnomo, "Design and Development of Small Electric Vehicle using MATLAB/Simulink," *Int. J. Comput. Appl.*, vol. 24, no. 6, pp. 19–23, 2011, doi: 10.5120/2960-3940.
- [57] M. K. Uddin, G. Ramasamy, S. Mekhilef, K. Ramar, and Y. C. Lau, "A review on high frequency resonant inverter technologies for wireless power transfer using magnetic resonance coupling," *2014 IEEE Conf. Energy Conversion, CENCON 2014*, pp. 412–417, 2014, doi: 10.1109/CENCON.2014.6967539.
- [58] B. Berman, "a Quick Guide To Cryogens," 2016. [Online]. Available: <https://www.plugincars.com/plugin-hybrid-cars>.
- [59] CNET, "Hybrid Vs Nano.Pdf," 2009. [Online]. Available: <https://www.cnet.com/roadshow/news/hybrid-vs-electric-car-buyers-guide-mild-series-plugin-battery-hydrogen-fuel-cell/>. [Accessed: 11-Feb-2019].
- [60] UCS, "Electric Vehicle Batteries: Materials, Cost, Lifespan," 2018.
- [61] M. Fuller, "Wireless charging in California: Range, recharge, and vehicle electrification," *Transp. Res. Part C Emerg. Technol.*, vol. 67, pp. 343–356, 2016, doi: 10.1016/j.trc.2016.02.013.
- [62] S. Lukic and Z. Pantic, "Cutting the Cord: Static and Dynamic Inductive Wireless Charging of Electric Vehicles," *IEEE Electrifi. Mag.*, vol. 1, no. 1, pp. 57–64, 2013, doi: 10.1109/mele.2013.2273228.
- [63] J. M. Miller, "Wireless Plug-in Electric Vehicle (PEV) Charging," 2012. [Online]. Available: https://www.energy.gov/sites/prod/files/2014/03/f10/vss061_miller_2012_o.pdf. [Accessed: 11-Apr-2019].
- [64] S. Habib, M. Kamran, and U. Rashid, "Impact analysis of vehicle-to-grid technology and charging strategies of electric vehicles on distribution networks - A review," *Journal of Power Sources*, vol. 277, pp. 205–214, 2015, doi: 10.1016/j.jpowsour.2014.12.020.
- [65] M. Yilmaz, V. T. Buyukdegirmenci, and P. T. Krein, "General design requirements and analysis of roadbed inductive power transfer system for dynamic electric vehicle charging," *2012 IEEE Transp. Electrifi. Conf. Expo, ITEC 2012*, 2012, doi: 10.1109/ITEC.2012.6243497.
- [66] Z. Pantic and S. Lukic, "Computationally-efficient, generalized expressions for the proximity-effect in multi-layer, multi-turn tubular coils for wireless power transfer systems," *IEEE Trans. Magn.*, vol. 49, no. 11, pp. 5404–5416, 2013, doi: 10.1109/TMAG.2013.2264486.
- [67] G. E. Leyh and M. D. Kennan, "Efficient wireless transmission of power using resonators with coupled electric fields," *40th North Am. Power Symp. NAPS2008*, pp. 1–4, 2008, doi: 10.1109/NAPS.2008.5307364.
- [68] A. B. Munir, N. Kumar, M. E. Karim, A. W. Reza, and S. Das Barman, "Wireless powering by magnetic

- resonant coupling: Recent trends in wireless power transfer system and its applications," *Renew. Sustain. Energy Rev.*, vol. 51, pp. 1525–1552, 2015, doi: 10.1016/j.rser.2015.07.031.
- [69] C. M. Chun T. Rim, "Wireless Power Transfer for EV and Mobile Devices," *Wiley*, 2011. [Online]. Available: <https://onlinelibrary.wiley.com/doi/book/10.1002/9781119329084>. [Accessed: 11-Apr-2019].
- [70] Z. Huang, S. C. Wong, and C. K. Tse, "Design methodology of a series-series inductive power transfer system for electric vehicle battery charger application," *2014 IEEE Energy Convers. Congr. Expo. ECCE 2014*, vol. 61, no. 1, pp. 1778–1782, 2014, doi: 10.1109/ECCE.2014.6953633.
- [71] M. Budhia, J. T. Boys, G. A. Covic, and C. Y. Huang, "Development of a single-sided flux magnetic coupler for electric vehicle IPT charging systems," *IEEE Trans. Ind. Electron.*, vol. 60, no. 1, pp. 318–328, 2013, doi: 10.1109/TIE.2011.2179274.
- [72] K. A. Kalwar, M. Aamir, and S. Mekhilef, "Inductively coupled power transfer (ICPT) for electric vehicle charging - A review," *Renew. Sustain. Energy Rev.*, vol. 47, pp. 462–475, 2015, doi: 10.1016/j.rser.2015.03.040.
- [73] C. Panchal, S. Stegen, and J. Lu, "Review of static and dynamic wireless electric vehicle charging system," *Engineering Science and Technology, an International Journal*, vol. 21, no. 5, pp. 922–937, 2018, doi: 10.1016/j.jestch.2018.06.015.
- [74] K. T. Chau, D. Zhang, J. Z. Jiang, C. Liu, and Y. Zhang, "Design of a Magnetic-Geared Outer-Rotor Permanent-Magnet Brushless Motor for Electric Vehicles," *IEEE Trans. Magn.*, vol. 43, no. 6, pp. 2504–2506, 2007, doi: 10.1109/TMAG.2007.893714.
- [75] R. Thakur and A. NATALE, "High efficiency wireless power transmission at low frequency using permanent magnet coupling," *Cardiol. Clin.*, vol. 27, no. 1, pp. xv–xv, 2009.
- [76] S.-N. Suzuki, M. Ishihara, and Y. Kobayashi, "The Improvement of the Noninvasive Power-Supply System," *IEEE Trans. Magn.*, vol. 47, no. 10, pp. 2811–2814, 2011.
- [77] M. Kline, I. Izyumin, B. Boser, and S. Sanders, "Capacitive power transfer for contactless charging," *Conf. Proc. - IEEE Appl. Power Electron. Conf. Expo. - APEC*, pp. 1398–1404, 2011, doi: 10.1109/APEC.2011.5744775.
- [78] M. P. Theodoridis, "Effective capacitive power transfer," *IEEE Trans. Power Electron.*, vol. 27, no. 12, pp. 4906–4913, 2012, doi: 10.1109/TPEL.2012.2192502.
- [79] A. M. Sodagar and P. Amiri, "Capacitive coupling for power and data telemetry to implantable biomedical microsystems," *2009 4th Int. IEEE/EMBS Conf. Neural Eng. NER '09*, pp. 411–414, 2009, doi: 10.1109/NER.2009.5109320.
- [80] C. Liu and A. P. Hu, "Steady state analysis of a capacitively coupled contactless power transfer system," *2009 IEEE Energy Convers. Congr. Expo. ECCE 2009*, pp. 3233–3238, 2009, doi: 10.1109/ECCE.2009.5316216.
- [81] I. J. Yoon and H. Ling, "Investigation of near-field wireless power transfer in the presence of lossy dielectric materials," *IEEE Trans. Antennas Propag.*, vol. 61, no. 1, pp. 482–488, 2013, doi: 10.1109/TAP.2012.2215296.
- [82] B. H. Waters, B. J. Mahoney, G. Lee, and J. R. Smith, "Optimal coil size ratios for wireless power transfer applications," in *Proceedings - IEEE International Symposium on Circuits and Systems*, 2014, pp. 2045–2048, doi: 10.1109/ISCAS.2014.6865567.
- [83] R. Matias, B. Cunha, and R. Martins, "Modeling inductive coupling for wireless power transfer to integrated circuits," *2013 IEEE Wirel. Power Transf. WPT 2013*, vol. 2, no. 1, pp. 198–201, 2013, doi: 10.1109/WPT.2013.6556917.

- [84] S. H. Lee and R. D. Lorenz, "A design methodology for multi-kW, large airgap, MHz frequency, wireless power transfer systems," *IEEE Energy Convers. Congr. Expo. Energy Convers. Innov. a Clean Energy Futur. ECCE 2011, Proc.*, pp. 3503–3510, 2011, doi: 10.1109/ECCE.2011.6064242.
- [85] S. H. Lee and R. D. Lorenz, "Development and validation of model for 95%-efficiency 220-W wireless power transfer over a 30-cm air gap," *IEEE Trans. Ind. Appl.*, vol. 47, no. 6, pp. 2495–2504, 2011, doi: 10.1109/TIA.2011.2168555.
- [86] C. Sen Wang, G. A. Covic, and O. H. Stielau, "Power Transfer Capability and Bifurcation Phenomena of Loosely Coupled Inductive Power Transfer Systems," *IEEE Trans. Ind. Electron.*, vol. 51, no. 1, pp. 148–157, 2004, doi: 10.1109/TIE.2003.822038.
- [87] H. Takanashi, Y. Sato, Y. Kaneko, S. Abe, and T. Yasuda, "A large air gap 3 kW wireless power transfer system for electric vehicles," *2012 IEEE Energy Convers. Congr. Expo. ECCE 2012*, pp. 269–274, 2012, doi: 10.1109/ECCE.2012.6342813.
- [88] B. Peschiera and S. S. Williamson, "Review and comparison of inductive charging power electronic converter topologies for electric and plug-in hybrid electric vehicles," *2013 IEEE Transp. Electrification Conf. Expo Components, Syst. Power Electron. - From Technol. to Bus. Public Policy, ITEC 2013*, pp. 1–6, 2013, doi: 10.1109/ITEC.2013.6573474.
- [89] S. M. Lukic, M. Saunders, Z. Pantic, S. Hung, and J. Taiber, "Use of inductive power transfer for electric vehicles," *IEEE PES Gen. Meet. PES 2010*, pp. 1–6, 2010, doi: 10.1109/PES.2010.5589673.
- [90] J. Francfort, "Electric vehicle charging levels and requirements overview," *Cities*, no. December, 2010.
- [91] B. Kim, "Analysis and Design of Wireless Power Transfer System with an Intermediate Coil for High Efficiency," *IEEE Veh. Technol. Conf.*, pp. 1034–1040, 2013.
- [92] P. Ning, J. M. Miller, O. C. Onar, C. P. White, and L. D. Marlino, "A compact wireless charging system development," *Conf. Proc. - IEEE Appl. Power Electron. Conf. Expo. - APEC*, pp. 3045–3050, 2013, doi: 10.1109/APEC.2013.6520733.
- [93] T. D. Nguyen, S. Li, W. Li, and C. C. Mi, "Feasibility study on bipolar pads for efficient wireless power chargers," *Conf. Proc. - IEEE Appl. Power Electron. Conf. Expo. - APEC*, pp. 1676–1682, 2014, doi: 10.1109/APEC.2014.6803531.
- [94] T. J. Gretk and A. Kurs, "Power Transfer Through Strongly Coupled Resonances by Andr6 Kurs Submitted to the Department of Physics in partial fulfillment of the requirements for the degree of at the Thesis Supervisor Accepted by Power Transfer Through Strongly Coupled Resonances by," *Physics (College. Park. Md)*, 2007.
- [95] K. Fotopoulou and B. W. Flynn, "Wireless power transfer in loosely coupled links: Coil misalignment model," *IEEE Trans. Magn.*, vol. 47, no. 2 PART 2, pp. 416–430, 2011, doi: 10.1109/TMAG.2010.2093534.
- [96] Altfuels, "One Last Day With an EV1." [Online]. Available: <http://www.altfuels.org/events/testdriv/farewell.shtml>. [Accessed: 11-Apr-2019].
- [97] L. Xie, Y. Shi, Y. T. Hou, and A. Lou, "Wireless power transfer and applications to sensor networks," *IEEE Wirel. Commun.*, vol. 20, no. 4, pp. 140–145, 2013, doi: 10.1109/MWC.2013.6590061.
- [98] S. Hasanzadeh and S. Vaez-Zadeh, "Efficiency analysis of contactless electrical power transmission systems," *Energy Convers. Manag.*, vol. 65, pp. 487–496, 2013, doi: 10.1016/j.enconman.2012.07.007.
- [99] M. Budhia, G. Covic, and J. Boys, "A new IPT magnetic coupler for electric vehicle charging systems," *IECON Proc. (Industrial Electron. Conf.)*, pp. 2487–2492, 2010, doi: 10.1109/IECON.2010.5675350.

- [100] Z. Tang, M. Christini, T. Koga, and ANSYS, "Wireless Power Transfer using Maxwell and Simplorer," *2012 Automot. Simul. World Congr.*, pp. 1–38, 2012.
- [101] M. Budhia, G. A. Covic, and J. T. Boys, "Design and optimisation of magnetic structures for lumped inductive power transfer systems," *2009 IEEE Energy Convers. Congr. Expo. ECCE 2009*, pp. 2081–2088, 2009, doi: 10.1109/ECCE.2009.5316197.
- [102] O. Jonah and S. V. Georgakopoulos, "Wireless power transfer in concrete via strongly coupled magnetic resonance," *IEEE Trans. Antennas Propag.*, vol. 61, no. 3, pp. 1378–1384, 2013, doi: 10.1109/TAP.2012.2227924.
- [103] D. Huang, Y. Urzhumov, D. R. Smith, K. Hoo Teo, and J. Zhang, "Magnetic superlens-enhanced inductive coupling for wireless power transfer," *J. Appl. Phys.*, vol. 111, no. 6, 2012, doi: 10.1063/1.3692757.
- [104] S. Drid, "Minimization of the Copper Losses in Electrical Vehicle Using Doubly Fed Induction Motor Vector Controlled," 2003.
- [105] M. Budhia, G. A. Covic, J. T. Boys, and C. Y. Huang, "Development and evaluation of single sided flux couplers for contactless electric vehicle charging," *IEEE Energy Convers. Congr. Expo. Energy Convers. Innov. a Clean Energy Futur. ECCE 2011, Proc.*, no. Dd, pp. 614–621, 2011, doi: 10.1109/ECCE.2011.6063826.
- [106] A. K. Sah, "Design of Wireless Power Transfer System via Magnetic Resonant Coupling at 13.56MHz," *Proc. IOE Grad. Conf. 2013*, no. 1, pp. 202–210, 2013.
- [107] J. Zhang, X. Yuan, and C. Wang, "A study of three-coil magnetically coupled resonators for wireless power transfer," *2015 IEEE Int. Wirel. Symp. IWS 2015*, pp. 1–4, 2015, doi: 10.1109/IEEE-IWS.2015.7164536.
- [108] S. C. Moon, B. C. Kim, S. Y. Cho, and G. W. Moon, "Analysis and design of wireless power transfer system with an intermediate coil for high efficiency," *2013 IEEE ECCE Asia Downunder - 5th IEEE Annu. Int. Energy Convers. Congr. Exhib. IEEE ECCE Asia 2013*, pp. 1034–1040, 2013, doi: 10.1109/ECCE-Asia.2013.6579235.
- [109] M. Kesler, "Highly Resonant Wireless Power Transfer," *WiTricity Corp*, pp. 1–13, 2013.
- [110] B. Kim, "Llkp Lik •," pp. 1034–1040, 2013.
- [111] H.-C. Son, J.-W. Kim, Y.-J. Park, and K.-H. Kim, "Efficiency analysis and optimal design of a circular loop resonant coil for wireless power transfer," *2010 Asia-Pacific Microw. Conf.*, no. L, pp. 849–852, 2010.
- [112] O. Jonah and S. V. Georgakopoulos, "Wireless power transfer in concrete via strongly coupled magnetic resonance," *IEEE Trans. Antennas Propag.*, vol. 61, no. 3, pp. 1378–1384, 2013, doi: 10.1109/TAP.2012.2227924.
- [113] Y. Zhang, F. He, F. Liu, K. Chen, Z. Zhao, and L. Yuan, "Comparison of two bidirectional wireless power transfer control methods," in *2016 Asia-Pacific International Symposium on Electromagnetic Compatibility, APEMC 2016*, 2016, pp. 68–70, doi: 10.1109/APEMC.2016.7522832.
- [114] V. Prasanth and P. Bauer, "Study of misalignment for on Road Charging," *2013 IEEE Transp. Electrification Conf. Expo Components, Syst. Power Electron. - From Technol. to Bus. Public Policy, ITEC 2013*, no. 1, pp. 1–8, 2013, doi: 10.1109/ITEC.2013.6573478.
- [115] G. Meunier, J.-P. Ferrieux, R. Périot, G. Kwimang, J. Roudet, and J.-R. Sibué, "A Global Study of a Contactless Energy Transfer System: Analytical Design, Virtual Prototyping, and Experimental Validation," *IEEE Trans. Power Electron.*, vol. 28, no. 10, pp. 4690–4699, 2012, doi: 10.1109/tpel.2012.2235858.

- [116] N. Shinohara, "Wireless power transmission progress for electric vehicle in Japan," *IEEE Radio Wirel. Symp. RWS*, pp. 109–111, 2013, doi: 10.1109/RWS.2013.6486657.
- [117] R. Mecke and C. Rathge, "High frequency resonant inverter for contactless energy transmission over large air gap," *PESC Rec. - IEEE Annu. Power Electron. Spec. Conf.*, vol. 3, pp. 1737–1743, 2004, doi: 10.1109/PESC.2004.1355378.
- [118] M. Chigira, Y. Nagatsuka, Y. Kaneko, S. Abe, T. Yasuda, and A. Suzuki, "Small-size light-weight transformer with new core structure for contactless electric vehicle power transfer system," *IEEE Energy Convers. Congr. Expo. Energy Convers. Innov. a Clean Energy Futur. ECCE 2011, Proc.*, pp. 260–266, 2011, doi: 10.1109/ECCE.2011.6063778.
- [119] Y. Nagatsuka, N. Ehara, Y. Kaneko, S. Abe, and T. Yasuda, "Compact contactless power transfer system for electric vehicles," *2010 Int. Power Electron. Conf. - ECCE Asia -, IPEC 2010*, pp. 807–813, 2010, doi: 10.1109/IPEC.2010.5543313.
- [120] M. Budhia, G. A. Covic, J. T. Boys, and C. Y. Huang, "Development and evaluation of single sided flux couplers for contactless electric vehicle charging," *IEEE Energy Convers. Congr. Expo. Energy Convers. Innov. a Clean Energy Futur. ECCE 2011, Proc.*, no. Dd, pp. 614–621, 2011, doi: 10.1109/ECCE.2011.6063826.
- [121] S. Li and C. C. Mi, "Wireless power transfer for electric vehicle applications," *IEEE J. Emerg. Sel. Top. Power Electron.*, vol. 3, no. 1, pp. 4–17, 2015, doi: 10.1109/JESTPE.2014.2319453.
- [122] T. D. Nguyen, S. Li, W. Li, and C. C. Mi, "Feasibility study on bipolar pads for efficient wireless power chargers," *Conf. Proc. - IEEE Appl. Power Electron. Conf. Expo. - APEC*, pp. 1676–1682, 2014, doi: 10.1109/APEC.2014.6803531.
- [123] J. Berke, "Germany paid people to use electricity over the holidays because its grid is so clean," *Independent*, 2018. [Online]. Available: <https://www.independent.co.uk/environment/germany-power-grid-pays-customers-christmas-sustainability-renewable-energy-a8141431.html>. [Accessed: 19-Jan-2019].
- [124] S. Samanta and A. K. Rathore, "A new inductive wireless power transfer topology using current-fed half bridge CLC transmitter LC receiver configuration," *ECCE 2016 - IEEE Energy Convers. Congr. Expo. Proc.*, no. C, pp. 2–9, 2016, doi: 10.1109/ECCE.2016.7854716.
- [125] J. Y. Lee and B. M. Han, "A bidirectional wireless power transfer EV charger using self-resonant PWM," *IEEE Trans. Power Electron.*, vol. 30, no. 4, pp. 1784–1787, 2015, doi: 10.1109/TPEL.2014.2346255.
- [126] N. A. Keeling, J. T. Boys, and G. A. Covic, "Unity power factor inductive power transfer pickup for high power applications," *IECON Proc. (Industrial Electron. Conf.)*, pp. 1039–1044, 2008, doi: 10.1109/IECON.2008.4758097.
- [127] H. H. Wu, A. Gilchrist, K. D. Sealy, and D. Bronson, "A high efficiency 5 kW inductive charger for EVs using dual side control," *IEEE Trans. Ind. Informatics*, vol. 8, no. 3, pp. 585–595, 2012, doi: 10.1109/TII.2012.2192283.
- [128] D. Kürschner, C. Rathge, and U. Jumar, "Design methodology for high efficient inductive power transfer systems with high coil positioning flexibility," *IEEE Trans. Ind. Electron.*, vol. 60, no. 1, pp. 372–381, 2013, doi: 10.1109/TIE.2011.2181134.
- [129] A. P. Sample, D. A. Meyer, and J. R. Smith, "Analysis, experimental results, and range adaptation of magnetically coupled resonators for wireless power transfer," *IEEE Trans. Ind. Electron.*, vol. 58, no. 2, pp. 544–554, 2011, doi: 10.1109/TIE.2010.2046002.
- [130] Z. Dang and J. A. A. Qahouq, "Modeling and investigation of magnetic resonance coupled wireless power transfer system with lateral misalignment," *Conf. Proc. - IEEE Appl. Power Electron. Conf. Expo. - APEC*, pp. 1317–1322, 2014, doi: 10.1109/APEC.2014.6803477.

- [131] M. Mohammad, S. Kwak, and S. Choi, "Core design for better misalignment tolerance and higher range of wireless charging for HEV," *Conf. Proc. - IEEE Appl. Power Electron. Conf. Expo. - APEC*, vol. 2016-May, no. 2, pp. 1748–1755, 2016, doi: 10.1109/APEC.2016.7468104.
- [132] T. Ishizaki, D. Fukada, and I. Awai, "A novel concept for 2-dimensional free-access wireless power transfer system using asymmetric coupling resonators with different sizes," *2011 IEEE MTT-S Int. Microw. Work. Ser. Innov. Wirel. Power Transm. Technol. Syst. Appl. IMWS-IWPT 2011 - Proc.*, pp. 243–246, 2011, doi: 10.1109/IMWS.2011.5877121.
- [133] T. Mizuno, T. Ueda, S. Yachi, R. Ohtomo, and Y. Goto, "Efficiency Dependence on Wire Type for Wireless Power Transfer of Magnetic Resonant Coupling," *15th Int. Conf. Electrical Mach. Syst.*, pp. 1–4, 2012.
- [134] E. G. Kilinc, C. Dehollain, and F. Maloberti, "Design and optimization of inductive power transmission for implantable sensor system," *2010 11th Int. Work. Symb. Numer. Methods, Model. Appl. to Circuit Des. SM2ACD 2010*, no. 1, pp. 10–14, 2010, doi: 10.1109/SM2ACD.2010.5672335.
- [135] D. Kerschner, C. Rathge, and A. Hoppe, "Design of inductive power transmission systems considering tolerances and power loss," *IECON Proc. (Industrial Electron. Conf.)*, pp. 378–383, 2009, doi: 10.1109/IECON.2009.5414952.
- [136] "How Does Temperature Affect Magnetism," *HSI Sensing*, 2017. [Online]. Available: <https://www.hsisensing.com/temperature-affect-magnetism/>. [Accessed: 23-Feb-2019].
- [137] J. L. Villa, J. Sallán, J. F. Sanz Osorio, and A. Llombart, "High-misalignment tolerant compensation topology for ICPT systems," *IEEE Trans. Ind. Electron.*, vol. 59, no. 2, pp. 945–951, 2012, doi: 10.1109/TIE.2011.2161055.
- [138] W. Li, H. Zhao, S. Li, J. Deng, T. Kan, and C. C. Mi, "Integrated LCC Compensation Topology for Wireless Charger in Electric and Plug-in Electric Vehicles," *IEEE Trans. Ind. Electron.*, vol. 62, no. 7, pp. 4215–4225, 2015, doi: 10.1109/TIE.2014.2384003.
- [139] A. P. Hu and J. T. boys, "PhD: Selected Resonant Converters For IPT Power Supplies," *Dep. Electr. Electron. Eng.*, no. May, pp. 1–213, 2001.
- [140] Z. Pantic, S. Bai, and S. M. Lukic, "ZCS LCC-compensated resonant inverter for inductive-power-transfer application," *IEEE Trans. Ind. Electron.*, vol. 58, no. 8, pp. 3500–3510, 2011, doi: 10.1109/TIE.2010.2081954.
- [141] G. Covic and J. Boys, "Inductive power transfer (IPT) powering our future," *Power Electron. Res. Group, Univ. Auckland, New Zealand, Tech. Rep.*, 2010.
- [142] H. H. Wu, A. Gilchrist, K. D. Sealy, and D. Bronson, "A high efficiency 5 kW inductive charger for EVs using dual side control," *IEEE Trans. Ind. Informatics*, vol. 8, no. 3, pp. 585–595, 2012, doi: 10.1109/TII.2012.2192283.
- [143] H. Takanashi, Y. Sato, Y. Kaneko, S. Abe, and T. Yasuda, "A large air gap 3 kW wireless power transfer system for electric vehicles," *2012 IEEE Energy Convers. Congr. Expo. ECCE 2012*, pp. 269–274, 2012, doi: 10.1109/ECCE.2012.6342813.
- [144] S. Ahn, C. Hwang, and H. H. Park, "Optimized shield design for reduction of EMF from wireless power transfer systems," *IEICE Electron. Express*, vol. 11, no. 2, pp. 1–9, 2014, doi: 10.1587/elex.10.20130930.
- [145] K. W. Klontz, A. Esser, P. J. Wolfs, and D. M. Divan, "Converter selection for electric vehicle charger systems with a high-frequency high-power link," *Power Electron. Spec. Conf. 1993. PESC '93 Rec. 24th Annu. IEEE*, pp. 855–861, 2002, doi: 10.1109/pesc.1993.472021.
- [146] B. Yang, "Chapter 4 LLC Resonant Converter," *Flux*, 2001. [Online]. Available: <https://pdfs.semanticscholar.org/6d8a/4889938d83b6b4f870ccfbffaf438a5aaac.pdf>. [Accessed: 2025-10-10]

11-Apr-2019].

- [147] O. H. Stielau and G. A. Covic, "Design of loosely coupled inductive power transfer systems," *PowerCon 2000 - 2000 Int. Conf. Power Syst. Technol. Proc.*, vol. 1, pp. 85–90, 2000, doi: 10.1109/ICPST.2000.900036.
- [148] N. A. Keeling, G. A. Covic, and J. T. Boys, "A unity-power-factor IPT pickup for high-power applications," *IEEE Trans. Ind. Electron.*, vol. 57, no. 2, pp. 744–751, 2010, doi: 10.1109/TIE.2009.2027255.
- [149] C. Sen Wang, O. H. Stielau, and G. A. Covic, "Design considerations for a contactless electric vehicle battery charger," *IEEE Trans. Ind. Electron.*, vol. 52, no. 5, pp. 1308–1314, 2005, doi: 10.1109/TIE.2005.855672.
- [150] K. Throngnumchai, T. Kai, and Y. Minagawa, "A study on receiver circuit topology of a cordless battery charger for electric vehicles," *IEEE Energy Convers. Congr. Expo. Energy Convers. Innov. a Clean Energy Futur. ECCE 2011, Proc.*, pp. 843–850, 2011, doi: 10.1109/ECCE.2011.6063858.
- [151] C. Y. Huang, J. T. Boys, and G. A. Covic, "LCL pickup circulating current controller for inductive power transfer systems," *IEEE Trans. Power Electron.*, vol. 28, no. 4, pp. 2081–2093, 2013, doi: 10.1109/TPEL.2012.2199132.
- [152] Z. Salam, M. Amjad, M. Facta, and S. Mekhilef, "Analysis and implementation of transformerless LCL resonant power supply for ozone generation," *IEEE Trans. Power Electron.*, vol. 28, no. 2, pp. 650–660, 2013, doi: 10.1109/TPEL.2012.2202130.
- [153] A. J. Moradewicz and M. P. Kazmierkowski, "Contactless energy transfer system with FPGA-controlled resonant converter," *IEEE Trans. Ind. Electron.*, vol. 57, no. 9, pp. 3181–3190, 2010, doi: 10.1109/TIE.2010.2051395.
- [154] J. Sallán, J. L. Villa, A. Llombart, and J. F. Sanz, "Optimal design of ICPT systems applied to electric vehicle battery charge," *IEEE Trans. Ind. Electron.*, vol. 56, no. 6, pp. 2140–2149, 2009, doi: 10.1109/TIE.2009.2015359.
- [155] Y. Matsuo, S. Washimiya, F. Nakao, K. Takehara, K. Harada, and H. Sakamoto, "Large air-gap coupler for inductive charger [for electric vehicles]," *IEEE Trans. Magn.*, vol. 35, no. 5, pp. 3526–3528, 2002, doi: 10.1109/20.800578.
- [156] P. Richardson, D. Flynn, and A. Keane, "Optimal charging of electric vehicles in low-voltage distribution systems," *IEEE Trans. Power Syst.*, vol. 27, no. 1, pp. 268–279, 2012, doi: 10.1109/TPWRS.2011.2158247.
- [157] M. Soma, D. C. Galbraith, and R. L. White, "Soma et al_Radio-Frequency Coils in Implantable Devices Misalignment Analysis and Design Procedure_IEEE Biomed Eng vol34 (1987).pdf," *IEEE Trans. Biomed. Eng.*, vol. 34, no. 4, pp. 276–282, 1987.
- [158] M. Chigira, Y. Nagatsuka, Y. Kaneko, S. Abe, T. Yasuda, and A. Suzuki, "Small-size light-weight transformer with new core structure for contactless electric vehicle power transfer system," *IEEE Energy Convers. Congr. Expo. Energy Convers. Innov. a Clean Energy Futur. ECCE 2011, Proc.*, pp. 260–266, 2011, doi: 10.1109/ECCE.2011.6063778.
- [159] K. N. Mude and M. T. Outeiro, "Coil misalignment analysis under different radius of coil and wire for Wireless Power Transfer System," *Proc. IECON 2017 - 43rd Annu. Conf. IEEE Ind. Electron. Soc.*, vol. 2017-Janua, pp. 5319–5323, 2017, doi: 10.1109/IECON.2017.8216921.
- [160] T. Chi, Y. Ho, B. Gomersall, L. Ran, C. E. Transfer, and C. P. Supply, "Contactless Charging for Electric Vehicles with a Large Air Gap Keywords Model lling Electric cal Equivalent Circui t Paramete ers," *Power*, vol. 44, no. 0, pp. 1–10, 2011.
- [161] X. Wei, Z. Wang, and H. Dai, "A critical review of wireless power transfer via strongly coupled

magnetic resonances," *Energies*, vol. 7, no. 7. pp. 4316–4341, 2014, doi: 10.3390/en7074316.


- [162] J. F. Sanz, J. L. Villa, J. Sallán, J. M. Perié, and L. G. Duarte, "UNPLUGGED project: Development of a 50 kW inductive electric vehicle battery charge system," *2013 World Electr. Veh. Symp. Exhib. EVS 2014*, pp. 1–7, 2014, doi: 10.1109/EVS.2013.6914934.
- [163] Y. Hori, "Novel EV society based on motor/ capacitor/ wireless - Application of electric motor, supercapacitors, and wireless power transfer to enhance operation of future vehicles," *2012 IEEE MTT-S Int. Microw. Work. Ser. Innov. Wirel. Power Transm. Technol. Syst. Appl. IMWS-IWPT 2012 - Proc.*, pp. 3–8, 2012, doi: 10.1109/IMWS.2012.6215827.
- [164] Y. Li *et al.*, "Wireless energy transfer system based on high Q flexible planar-Litz MEMS coils," *8th Annu. IEEE Int. Conf. Nano/Micro Eng. Mol. Syst. IEEE NEMS 2013*, vol. 1, no. L, pp. 837–840, 2013, doi: 10.1109/NEMS.2013.6559855.
- [165] T. Mizuno, S. Yachi, A. Kamiya, and D. Yamamoto, "Improvement in efficiency of wireless power transfer of magnetic resonant coupling using magnetoplated wire," *IEEE Trans. Magn.*, vol. 47, no. 10, pp. 4445–4448, 2011, doi: 10.1109/TMAG.2011.2158525.
- [166] J. Kim, J. Kim, C. Song, and H. Kim, "Wireless power transfer technology using magnetic field resonance," *Asia-Pacific Microw. Conf. Proceedings, APMC*, vol. 2, pp. 459–461, 2013, doi: 10.1109/APMC.2013.6694830.
- [167] S. Hasanzadeh, S. Vaez-Zadeh, and A. H. Isfahani, "Optimization of a contactless power transfer system for electric vehicles," *IEEE Trans. Veh. Technol.*, vol. 61, no. 8, pp. 3566–3573, 2012, doi: 10.1109/TVT.2012.2209464.
- [168] D. Ongayo and M. Hanif, "Comparison of circular and rectangular coil transformer parameters for wireless Power Transfer based on Finite Element Analysis," *2015 IEEE 13th Brazilian Power Electron. Conf. 1st South. Power Electron. Conf. COBEP/SPEC 2016*, no. March 2016, 2015, doi: 10.1109/COBEP.2015.7420222.
- [169] M. Al-Saadi, S. Valtchev, L. Romba, J. Gonçalves, and A. Crăciunescu, "Comparison of Spiral and Square Coil Configurations in Wireless Power Transfer System for Contactless Battery Charging," *2019 Electr. Veh. Int. Conf. EV 2019*, 2019, doi: 10.1109/EV.2019.8892897.
- [170] D. Barth, B. Klaus, and T. Leibfried, "Litz wire design for wireless power transfer in electric vehicles," in *WPTC 2017 - Wireless Power Transfer Conference*, 2017, doi: 10.1109/WPT.2017.7953819.
- [171] OSCO, "What is Litz Wire? Benefits of Litz Wire." [Online]. Available: <http://www.osco.uk.com/userfiles/download/Cable/OSCO Litz Wire Brochure.pdf>. [Accessed: 25-Feb-2019].
- [172] B. Olukotun, J. S. Partridge, and R. W. G. Bucknall, "Optimal Finite Element Modelling and 3-D Parametric Analysis of Strong Coupled Resonant Coils for Bidirectional Wireless Power Transfer," *Proc. - 2018 53rd Int. Univ. Power Eng. Conf. UPEC 2018*, pp. 1–6, 2018, doi: 10.1109/UPEC.2018.8541867.
- [173] K. Throngnumchai, A. Hanamura, Y. Naruse, and K. Takeda, "Design and evaluation of a wireless power transfer system with road embedded transmitter coils for dynamic charging of electric vehicles," *World Electr. Veh. J.*, vol. 6, no. 4, pp. 848–857, 2013, doi: 10.1109/EVS.2013.6914937.
- [174] J. Welbler, "Emctd_1293_Weibler," 1993. [Online]. Available: http://mri-q.com/uploads/3/4/5/7/34572113/lindgren_metals_used_for_rf_shielding.pdf. [Accessed: 25-Feb-2019].
- [175] P. M. Anselone, "Theoretical Numerical Analysis (Peter Linz)," *SIAM Rev.*, vol. 22, no. 3, pp. 376–377, 2005, doi: 10.1137/1022072.
- [176] D. M. Frangopol and D. Saydam, "Structural performance indicators for bridges," *Bridg. Eng. Handb.*

Fundam. Second Ed., vol. 810, pp. 185–206, 2014, doi: 10.1201/b15616.

- [177] ANSYS Inc., “Maxwell 2D / Maxwell 3D.” [Online]. Available: http://ansoft-maxwell.narod.ru/en/CompleteMaxwell2D_V15.pdf. [Accessed: 25-Nov-2018].
- [178] FDK, “Material Characteristics 6H series Material Characteristics 6H series.” [Online]. Available: <http://www.fdk.com/cyber-e/pdf/FP-FPE001.pdf>. [Accessed: 30-Sep-2018].
- [179] K. Jaber, B. Ben Saleh, A. Fakhfakh, and R. Neji, “Modeling and simulation of electrical vehicle in VHDL-AMS,” *2009 16th IEEE Int. Conf. Electron. Circuits Syst. ICECS 2009*, pp. 908–911, 2009, doi: 10.1109/ICECS.2009.5410828.
- [180] P. P. Parthasaradhy and S. V Ranganayakulu, “Hysteresis and eddy current losses of magnetic material by Epstein frame method-novel approach,” *Int. Conf. Innov. Electr. Electron. Eng.*, pp. 85–93, 2014.
- [181] Aspencore, “Inductors in Parallel and Parallel Inductor Circuits,” *Electronics-tutorials*. [Online]. Available: <https://www.electronics-tutorials.ws/inductor/parallel-inductors.html>. [Accessed: 08-Apr-2019].
- [182] K. Zhu and P. W. T. Pong, “Curved trapezoidal magnetic flux concentrator design for improving sensitivity of magnetic sensor in multi-conductor current measurement,” *2016 5th Int. Symp. Next-Generation Electron. ISNE 2016*, vol. 2, pp. 1–2, 2016, doi: 10.1109/ISNE.2016.7543342.
- [183] G. G. Orenchak, “Specify saturation properties of ferrite cores to prevent field failure,” *TSC Ferrite International*. [Online]. Available: <http://www.tscinternational.com/tech13.pdf>. [Accessed: 08-Mar-2019].

Appendices

Appendix A1: Electrical Conductivities of Metals

|  TIBTECH | Electrical conductivity (10.E6 Siemens/m) | Electrical resistivity (10.E-8 Ohm.m) | Thermal Conductivity (W/m.k) | Thermal expansion coef. 10E-6(k-1) from 0 to 100°C | Density (g/cm3) | Melting point or degradation (°C) |
|--|--|--|---------------------------------|---|--------------------|--------------------------------------|
| Silver | 62,1 | 1,6 | 420 | 19,1 | 10,5 | 961 |
| copper | 58,5 | 1,7 | 401 | 17 | 8,9 | 1083 |
| Gold | 44,2 | 2,3 | 317 | 14,1 | 19,4 | 1064 |
| Aluminium | 36,9 | 2,7 | 237 | 23,5 | 2,7 | 660 |
| Molybden | 18,7 | 5,34 | 138 | 4,8 | 10,2 | 2623 |
| Zinc | 16,6 | 6,0 | 116 | 31 | 7,1 | 419 |
| Lithium | 10,8 | 9,3 | 84,7 | 56 | 0,54 | 181 |
| Tungsten | 8,9 | 11,2 | 174 | 4,5 | 19,3 | 3422 |
| Brass | 15,9 | 6,3 | 150 | 20 | 8,5 | 900 |
| Carbon (ex PAN) | 5,9 | 16,9 | 129 | 0,2 | 1,8 | 2500 |
| Nickel | 14,3 | 7,0 | 91 | 13,3 | 8,8 | 1455 |
| Iron | 10,1 | 9,9 | 80 | 12,1 | 7,9 | 1528 |
| Palladium | 9,5 | 10,5 | 72 | 11 | 12 | 1555 |
| Platinum | 9,3 | 10,8 | 107 | 9 | 21,4 | 1772 |
| Tin | 8,7 | 11,5 | 67 | 23,5 | 7,3 | 232 |
| Bronze 67Cu33Sn | 7,4 | 13,5 | 85 | 17 | 8,8 | 1040 |
| Carbon steel | 5,9 | 16,9 | 90 | 12 | 7,7 | 1400 |
| Lead | 4,7 | 21,3 | 35 | 29 | 11,3 | 327 |
| Titanium | 2,4 | 41,7 | 21 | 8,9 | 4,5 | 1668 |
| St.Steel316L EN1.4404 | 1,32 | 76,0 | 15 | 16,5 | 7,9 | 1535 |
| St.Steel 304 EN1.4301 | 1,37 | 73,0 | 16,3 | 16,5 | 7,9 | 1450 |
| Mercury | 1,1 | 90,9 | 8 | 61 | 13,5 | -39 |
| Fe. Cr. Alloy | 0,74 | 134 | 16 | 11,1 | 7,2 | +1440 |
| st.Steel 310 EN1.4841 | 1,28 | 78 | 14,2 | 17 | 7,75 | 2650 |

Appendix A2: Permeability and Relative Permeability of Metals

| Medium | Susceptibility χ_m (volumetric SI) | Permeability μ [H/m] | Relative permeability μ/μ_0 | Magnetic field | Frequency (max) |
|--|---|---|--------------------------------------|----------------|--|
| Metglas 2714A (annealed) | | 1.26×10^0 | 1 000 000 ^[7] | at 0.5 T | 100 kHz |
| Iron (99.95% pure Fe annealed in H) | | 2.5×10^{-1} | 200 000 ^[8] | | |
| NANOPERM® | | 1.0×10^{-1} | 80 000 ^[9] | at 0.5 T | 10 kHz |
| Mu-metal | | 2.5×10^{-2} | 20 000 ^[10] | at 0.002 T | |
| Mu-metal | | 6.3×10^{-2} | 50 000 ^[11] | | |
| Cobalt-Iron (high permeability strip material) | | 2.3×10^{-2} | 18 000 ^[12] | | |
| Permalloy | 8000 | 1.0×10^{-2} | 8000 ^[10] | at 0.002 T | |
| Iron (99.8% pure) | | 6.3×10^{-3} | 5000 ^[8] | | |
| Electrical steel | | 5.0×10^{-3} | 4000 ^[10] | at 0.002 T | |
| Ferritic stainless steel (annealed) | | $1.26 \times 10^{-3} - 2.26 \times 10^{-3}$ | 1000–1800 ^[13] | | |
| Martensitic stainless steel (annealed) | | $9.42 \times 10^{-4} - 1.19 \times 10^{-3}$ | 750–950 ^[13] | | |
| Ferrite (manganese zinc) | | $>8.0 \times 10^{-4}$ | 640 (or more) | | 100 kHz ~ 1 MHz |
| Ferrite (nickel zinc) | | $2.0 \times 10^{-5} - 8.0 \times 10^{-4}$ | 16–640 | | 100 kHz ~ 1 MHz ^[citation needed] |
| Carbon Steel | | 1.26×10^{-4} | 100 ^[10] | at 0.002 T | |
| Nickel | | $1.26 \times 10^{-4} - 7.54 \times 10^{-4}$ | 100 ^[10] – 600 | at 0.002 T | |
| Martensitic stainless steel (hardened) | | $5.0 \times 10^{-5} - 1.2 \times 10^{-4}$ | 40–95 ^[13] | | |
| Austenitic stainless steel | | $1.260 \times 10^{-6} - 8.8 \times 10^{-6}$ | 1.003–7 ^{[13][14] [note 1]} | | |
| Neodymium magnet | | 1.32×10^{-6} | 1.05 ^[15] | | |
| Platinum | | $1.256 970 \times 10^{-6}$ | 1.000 265 | | |
| Aluminum | 2.22×10^{-5} ^[16] | $1.256 665 \times 10^{-6}$ | 1.000 022 | | |
| Wood | | $1.256 637 60 \times 10^{-6}$ | 1.000 000 43 ^[16] | | |
| Air | | $1.256 637 53 \times 10^{-6}$ | 1.000 000 37 ^[17] | | |
| Concrete (dry) | | | 1 ^[18] | | |
| Vacuum | 0 | $4\pi \times 10^{-7}$ (μ_0) | 1, exactly ^[19] | | |
| Hydrogen | -2.2×10^{-9} ^[16] | $1.256 6371 \times 10^{-6}$ | 1.000 0000 | | |
| Teflon | | 1.2567×10^{-6} ^[10] | 1.0000 | | |
| Sapphire | -2.1×10^{-7} | $1.256 6368 \times 10^{-6}$ | 0.999 999 76 | | |
| Copper | -6.4×10^{-6} or -9.2×10^{-6} ^[16] | $1.256 629 \times 10^{-6}$ | 0.999 994 | | |
| Water | -8.0×10^{-6} | $1.256 627 \times 10^{-6}$ | 0.999 992 | | |
| Bismuth | -1.66×10^{-4} | $1.256 43 \times 10^{-6}$ | 0.999 834 | | |
| Superconductors | -1 | 0 | 0 | | |

Appendix B: Typical Automobile Physical Dimensions

BMW Z4



Dimensions: length 4.09 m, width 1.52 m, height 1.30 m
Fuel consumption (combined): 8.8 litres/100 km
Emissions: 214 g/km
Engine: torque 210 N • m, power 120 kW

Ford Focus 5-door 1.8i Zetec



Dimensions: length 4.17 m, width 1.70 m, height 1.43 m
Fuel consumption (combined): 7.7 litres/100 km
Emissions: 183 g/km
Engine: torque 160 N • m, power 85 kW

Range Rover SE 4.4V8



Dimensions: length 4.95 m, width 2.01 m, height 1.86 m
Fuel consumption (combined): 17.4 litres/100 km
Emissions: 389 g/km
Engine: torque 440 N • m, power 210 kW



Rover 75 2.0 CDT

Dimensions: length 4.75 m, width 1.76 m,
height 1.39 m

Fuel consumption (combined): 5.8 litres/100 km

Emissions: 163 g/km

Engine: torque 26 N • m, power 85 kW



Toyota Yaris 1.3 VVT-I

Dimensions: length 3.64 m, width 1.66 m,
height 1.50 m

Fuel consumption (combined): 5.6 litres/100 km

Emissions: 150 g/km

Engine: torque 124 N • m, power 64 kW

Standard material characteristics (Power material)

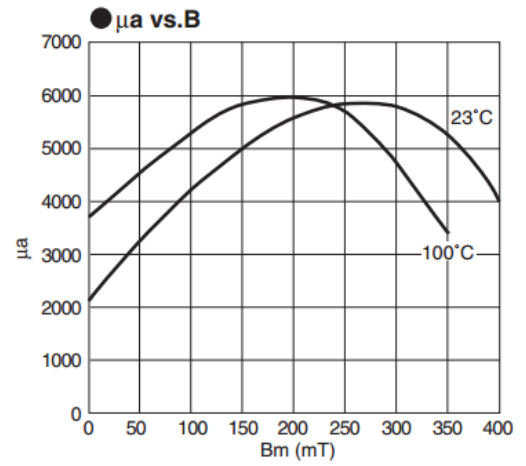
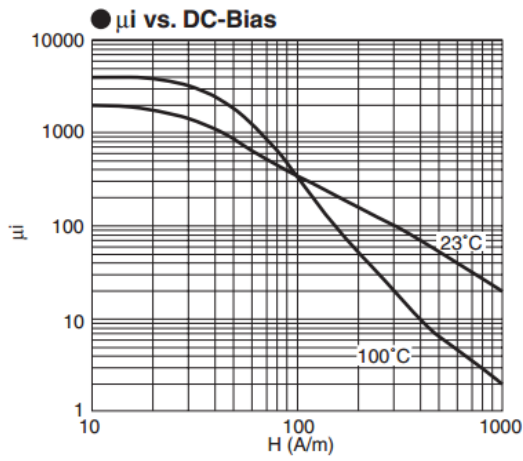
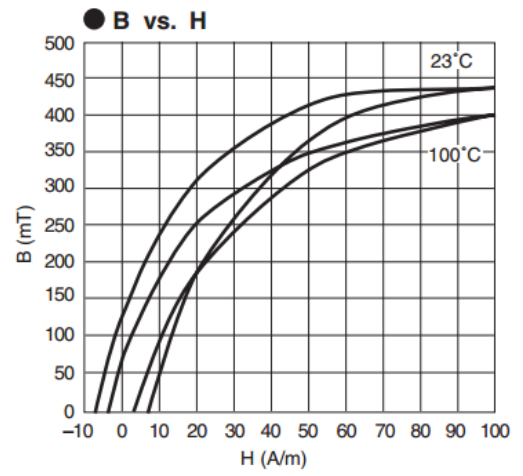
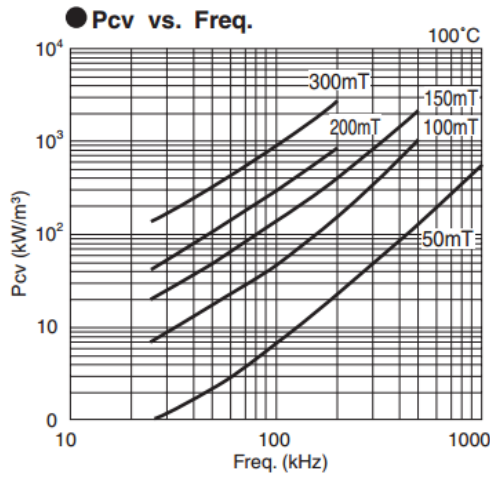
| Property | Symbol | Condition | Unit | 6H10 | 6H20 | 6H40 | 6H41 | 6H42 | 7H10 | 7H20 | |
|----------------------------------|--------------------|-------------|------------------------------|-------------------|------|------|------|------|------|------|-----|
| AC initial permeability | μ_i | 0.1 MHz | — | 2500 | 2300 | 2400 | 2500 | 3400 | 1500 | 1000 | |
| Saturation magnetic flux density | Bs (1000 A/m) | 23 °C | mT | 510 | 510 | 530 | 530 | 530 | 480 | 480 | |
| | | 100 °C | | 390 | 390 | 430 | 430 | 430 | 380 | 380 | |
| Residual magnetic flux density | Br | 23 °C | mT | 110 | 130 | 110 | 110 | 110 | 150 | 130 | |
| Coercivity | Hc | 23 °C | A/m | 13 | 13 | 10 | 10 | 10 | 30 | 25 | |
| Relative loss factor | $\tan\delta/\mu_i$ | 0.1 MHz | $\times 10^{-6}$ | <5 | <5 | <3 | <3 | <3 | <5 | <4 | |
| Core loss | 200 mT | 25 kHz | 23 °C | kW/m ³ | — | — | 90 | 75 | 60 | — | — |
| | | | 40 °C | | — | — | 75 | 60 | 50 | — | — |
| | | | 60 °C | | 65 | 80 | 60 | 50 | 40 | — | — |
| | | | 80 °C | | 55 | 65 | 50 | 40 | 45 | — | — |
| | | | 100 °C | | 80 | 55 | 40 | 45 | 55 | — | — |
| | | 100 kHz | 23 °C | | — | — | 650 | 550 | 450 | — | — |
| | | | 40 °C | | — | — | 550 | 450 | 350 | — | — |
| | | | 60 °C | | 450 | 550 | 450 | 350 | 300 | — | — |
| | | | 80 °C | | 400 | 450 | 350 | 300 | 325 | — | — |
| | | | 100 °C | | 500 | 400 | 300 | 325 | 375 | — | — |
| | 50 mT | 500 kHz | 60 °C | kW/m ³ | — | — | — | — | — | 100 | 50 |
| | | | 80 °C | | — | — | — | — | — | 80 | 40 |
| | | | 100 °C | | — | — | — | — | — | 100 | 50 |
| | | 1 MHz | 60 °C | | — | — | — | — | — | 400 | 200 |
| | | | 80 °C | | — | — | — | — | — | 400 | 200 |
| 100 °C | — | — | — | — | — | — | 500 | 250 | | | |
| Temperature coefficient | $\alpha_{\mu r}$ | 20 °C~80 °C | $\times 10^{-6}$ | 8 | 8 | 8 | 8 | 8 | 8 | 8 | |
| Curie temperature | Tc | — | °C | >200 | >200 | >200 | >200 | >200 | >200 | >200 | |
| Resistivity | ρ | — | $\Omega \cdot m$ | 3 | 3 | 2 | 2 | 2 | 5 | 5 | |
| Apparent density | d | — | $\times 10^3 \text{ kg/m}^3$ | 4.8 | 4.8 | 4.9 | 4.9 | 4.9 | 4.8 | 4.8 | |

Note: 1) The values were obtained with toroidal cores (FR25/15/5).

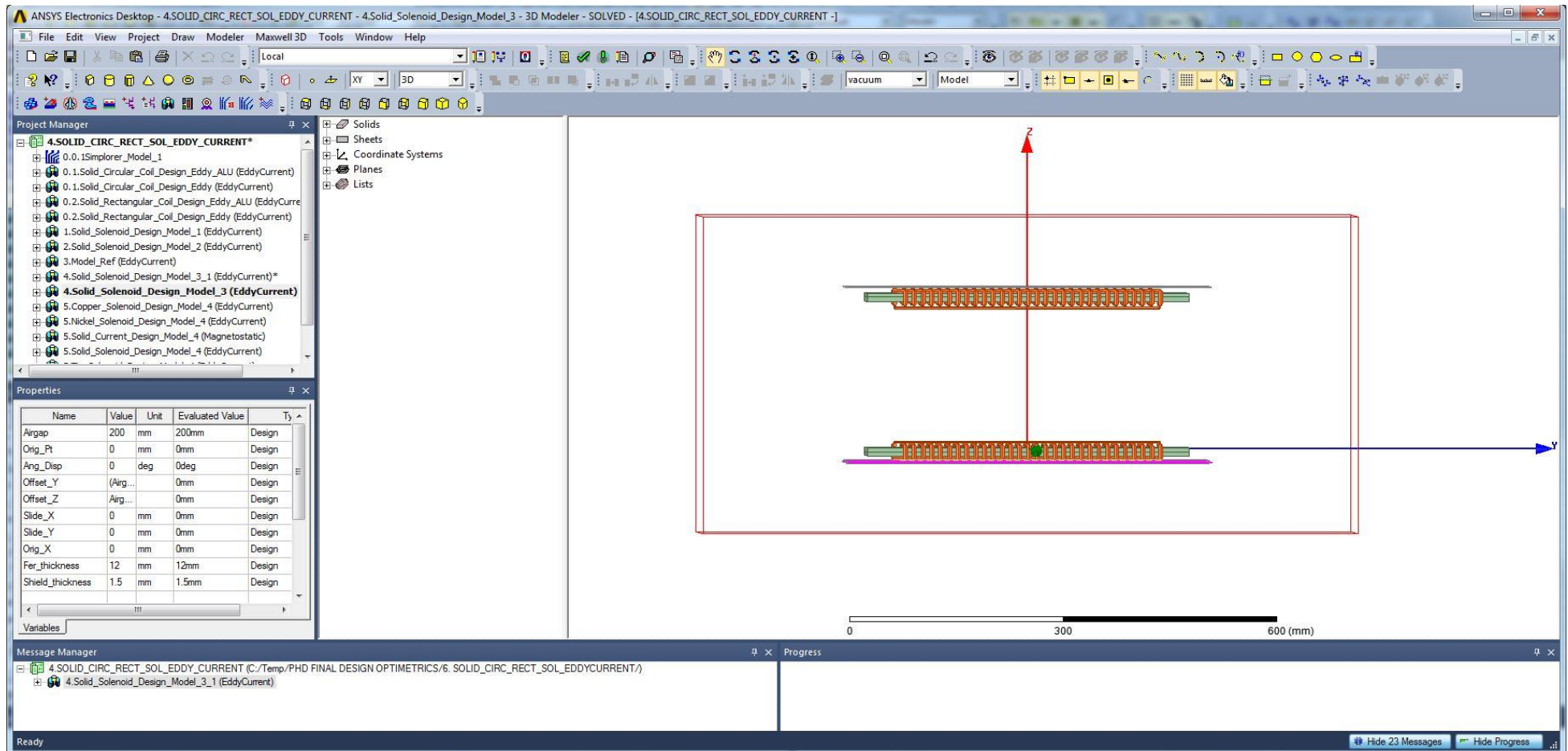
2) The values were obtained at 23±2 °C unless otherwise specified.

3) Initial permeability was measured at 10kHz, 0.8A/m.

6H40



Appendix D1: Ansys Electronics Simulation Environment for the Flux-Pipe 3-D Modelling



Appendix D2: Ansys Electronics Simulation Environment for the Rectangular Coil 3-D Modelling

The screenshot displays the Ansys Electronics Desktop environment for a 3D model of a rectangular coil. The interface is divided into several key sections:

- Project Manager (Left):** Shows a hierarchical tree of the project components, including various design models and analysis setups.
- Properties (Left):** A table listing design parameters and their values.
- 3D Model (Center):** A 3D visualization of the rectangular coil assembly, showing a green core and orange windings, with a coordinate system (X, Y, Z) overlaid.
- Message Manager (Bottom):** Displays a log of simulation progress and a message indicating that the simulation was aborted by the user.

| Name | Value | Unit | Evaluated Value | Ty |
|------------------|----------|------|-----------------|--------|
| Airgap | 200 | mm | 200mm | Design |
| Orig_Pt | 0 | mm | 0mm | Design |
| Ang_Displ | 0 | deg | 0deg | Design |
| Orig_X | 0 | mm | 0mm | Design |
| Offset_Y | (Airg... | mm | 0mm | Design |
| Fer_thickness | 8 | mm | 8mm | Design |
| Offset_Z | Airg... | mm | 0mm | Design |
| Slide_X | 0 | mm | 0mm | Design |
| Slide_Y | 0 | mm | 0mm | Design |
| Shield_thickness | 3 | mm | 3mm | Design |
| coil_width | 6 | mm | 6mm | Design |
| coil_space | 12.7 | mm | 12.7mm | Design |
| Outer_R | 245 | mm | 245mm | Design |
| Inner_R | 137 | mm | 137mm | Design |

Message Manager Log:

- 4.SOLID_CIRC_RECT_SOL_EDDY_CURRENT (C:/Temp/PHD FINAL.DESIGN.OPTIMETRICS/6.SOLID_CIRC_RECT_SOL_EDDYCURRENT/)
- 4.Solid_Solenoid_Design_Model_3_1 (EddyCurrent)
- 5.Copper_Solenoid_Design_Model_4 (EddyCurrent)
- Simulation was aborted by user on server: Local Machine. (3:10:21 PM Mar 06, 2019)

Appendix D3: Ansys Electronics Simulation Environment For the Circular Coil 3-D Modelling

The screenshot displays the Ansys Electronics Desktop environment for a 3D model of a circular coil. The main 3D view shows a rectangular assembly with a central circular coil structure. The coordinate system (X, Y, Z) is visible, with the Z-axis pointing upwards. A scale bar at the bottom of the 3D view indicates dimensions up to 600 mm.

The Project Manager on the left lists the following components:

- 4.SOLID_CIRC_RECT_SOL_EDDY_CURRENT*
 - 0.0.1.Simplorer_Model_1
 - 0.1.Solid_Circular_Coil_Design_Eddy_ALU (EddyCurrent)
 - 0.1.Solid_Circular_Coil_Design_Eddy (EddyCurrent)**
 - 0.2.Solid_Rectangular_Coil_Design_Eddy_ALU (EddyCurrent)
 - 0.2.Solid_Rectangular_Coil_Design_Eddy (EddyCurrent)
 - 1.Solid_Solenoid_Design_Model_1 (EddyCurrent)
 - 2.Solid_Solenoid_Design_Model_2 (EddyCurrent)
 - 3.Model_Ref (EddyCurrent)
 - 4.Solid_Solenoid_Design_Model_3_1 (EddyCurrent)*
 - 3D Components
 - Model
 - Boundaries
 - Excitations
 - Parameters
 - Mesh Operations
 - Analysis
 - Setup1
 - Optimetrics

The Properties table below the Project Manager shows the following parameters:

| Name | Value | Unit | Evaluated Value | T ₁ |
|------------------|----------|------|-----------------|----------------|
| Airgap | 200 | mm | 200mm | Design |
| Orig_Pt | 0 | mm | 0mm | Design |
| Ang_Displ | 0 | deg | 0deg | Design |
| Offset_Y | (Airg... | mm | 0mm | Design |
| Offset_Z | Airg... | mm | 0mm | Design |
| Slide_X | 0 | mm | 0mm | Design |
| Slide_Y | 0 | mm | 0mm | Design |
| Orig_X | 0 | mm | 0mm | Design |
| Fer_thickness | 12 | mm | 12mm | Design |
| Shield_thickness | 1.5 | mm | 1.5mm | Design |
| coil_width | 375 | mm | 375mm | Design |
| Cur_inp | 50 | A | 50A | Design |
| Nturns | 30 | | 30 | Design |
| Gap | 0.3 | mm | 0.3mm | Design |

The Message Manager at the bottom shows the following messages:

- 4 SOLID_CIRC_RECT_SOL_EDDY_CURRENT (C:/Temp/PHD FINAL DESIGN OPTIMETRICS/6. SOLID_CIRC_RECT_SOL_EDDYCURRENT/)
- 4.Solid_Solenoid_Design_Model_3_1 (EddyCurrent)
- 5.Copper_Solenoid_Design_Model_4 (EddyCurrent)
- Simulation was aborted by user on server: Local Machine, (3:10:21 PM Mar 06, 2019)

Appendix D4: Ansys Electronics Simulation Environment for the Simplorer Circuit Simulations for S-S Compensation Scheme

The screenshot displays the Ansys Electronics Desktop interface for a circuit simulation. The main workspace shows a schematic diagram of an S-S compensation scheme. The circuit consists of an AC voltage source labeled E1 connected to a series combination of a capacitor C1 and a resistor R1. This is followed by a transformer component. After the transformer, there is another series combination of a resistor R2 and a capacitor C2. The circuit then branches into two parallel paths: one containing a resistor R3, and the other containing a wattmeter WM2. A second wattmeter WM1 is placed in series with the AC source. The circuit is grounded at two points labeled gnd_term.

The Project Manager on the left side of the window shows a hierarchical tree of simulation components:

- Model_4_HorseShoe_Design_Loss_Analysis*
 - 2_Solid_HorseShoe_Current_Analysis (Magnetostatic)*
 - 2_Solid_HorseShoe_Normal (EddyCurrent)
 - 2_Solid_HorseShoe_X_Parametrics (Magnetostatic)
 - 2_Solid_HorseShoe_Y_Parametrics (Magnetostatic)
 - 2_Solid_HorseShoe_Z_Parametrics (Magnetostatic)
 - 2_Solid_HorseShoe_Parametrics (EddyCurrent)
 - 2_Solid_Solenoid_Design_Model_4_Fer (EddyCurrent)
 - 2_Solid_Solenoid_Design_Model_4_Radiation (EddyCurrent)
 - 0.0.1.Simplorer_Horse_S_P
 - 0.0.1.Simplorer_Horse_S_S
 - Definitions
- Opt_Model_4_HorseShoe_Design_Loss_Analysis*
 - 2_Solid_HorseShoe_Current_Analysis (Magnetostatic)
 - 2_Solid_HorseShoe_Gap_Analysis (EddyCurrent)
 - 2_Solid_HorseShoe_Normal (EddyCurrent)
 - 2_Solid_HorseShoe_X_Parametrics (Magnetostatic)
 - 2_Solid_HorseShoe_Y_Parametrics (Magnetostatic)
 - 2_Solid_HorseShoe_Z_Parametrics (Magnetostatic)

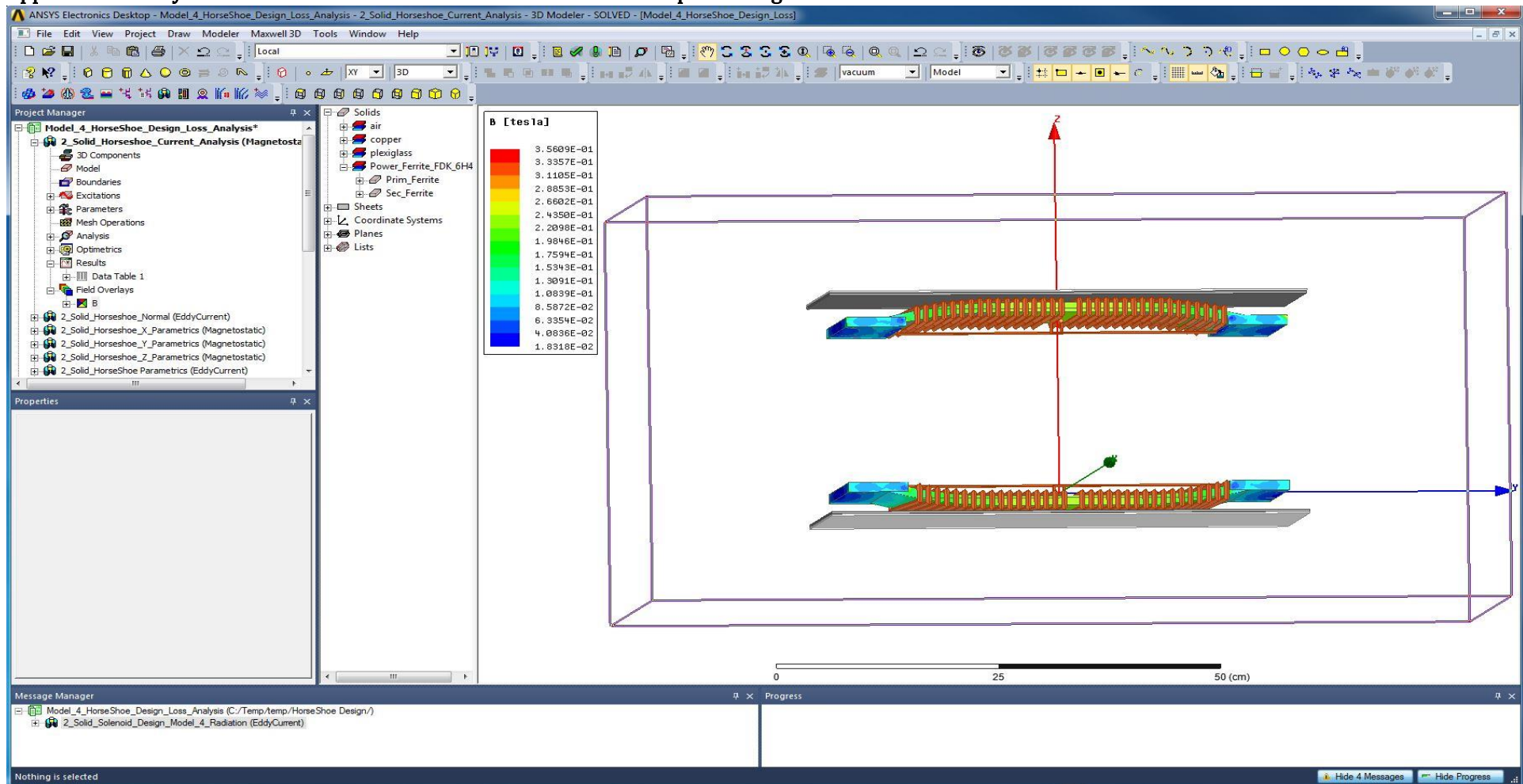
The Properties window at the bottom left shows the following parameters:

| Name | Value | Unit | Evaluated Value | Type |
|-----------|---------|------|-----------------|--------|
| frequency | 50 | kHz | 50kHz | Design |
| k | 0.36649 | | 0.36649 | Design |
| RL | 20 | ohm | 20ohm | Design |

The Message Manager at the bottom shows the simulation progress for the selected component:

- Model_4_HorseShoe_Design_Loss_Analysis (C:/Temp/temp/HorseShoe Design/)
 - 2_Solid_Solenoid_Design_Model_4_Radiation (EddyCurrent)

Appendix D5: Ansys Electronics Simulation Environment For the Flux-Pipe 3-D Magnetic Flux Distribution



Appendix D4: Ansys Electronics Simulation Environment for the Simplorer Circuit Simulations for S-P Compensation Scheme

The screenshot displays the ANSYS Electronics Desktop interface for a circuit simulation. The main workspace shows a schematic diagram of an S-P compensation scheme. The circuit consists of an AC voltage source (E1) connected to a network of components: a wattmeter (WM1), a capacitor (C1), a resistor (R1), a transformer, another resistor (R2), a capacitor (C2), a second wattmeter (WM2), and a resistor (R3). Ground terminals (gnd_term) are connected to the bottom of the circuit.

The Project Manager on the left shows a hierarchical tree of simulation models, including:

- Model_4_HorseShoe_Design_Loss_Analysis*
 - 2_Solid_HorseShoe_Current_Analysis (Magnetostatic)
 - 2_Solid_HorseShoe_Normal (EddyCurrent)
 - 2_Solid_HorseShoe_X_Parametrics (Magnetostatic)
 - 2_Solid_HorseShoe_Y_Parametrics (Magnetostatic)
 - 2_Solid_HorseShoe_Z_Parametrics (Magnetostatic)
 - 2_Solid_HorseShoe_Parametrics (EddyCurrent)
 - 2_Solid_Solenoid_Design_Model_4_Fer (EddyCurrent)
 - 2_Solid_Solenoid_Design_Model_4_Radiation (EddyCurrent)*
 - 0.0.1.Simplorer_Horse_S_P
 - 0.0.1.Simplorer_Horse_S_S
 - Definitions
- Opt_Model_4_HorseShoe_Design_Loss_Analysis*
 - 2_Solid_HorseShoe_Current_Analysis (Magnetostatic)
 - 2_Solid_HorseShoe_Gap_Analysis (EddyCurrent)
 - 2_Solid_HorseShoe_Normal (EddyCurrent)
 - 2_Solid_HorseShoe_X_Parametrics (Magnetostatic)
 - 2_Solid_HorseShoe_Y_Parametrics (Magnetostatic)
 - 2_Solid_HorseShoe_Z_Parametrics (Magnetostatic)
 - 2_Solid_HorseShoe_Parametrics (EddyCurrent)

The Properties window shows the following parameters:

| Name | Value | Unit | Evaluated Value | Type |
|-----------|---------|------|-----------------|--------|
| frequency | 50 | kHz | 50kHz | Design |
| k | 0.36649 | | 0.36649 | Design |
| RL | 50 | ohm | 50ohm | Design |

The Message Manager at the bottom shows simulation progress and completion messages, including: "Normal completion of simulation on server: Local Machine. (2:08:37 PM Mar 07, 2019)", "2_Solid_Solenoid_Design_Model_4_Radiation: Solutions have been invalidated. Undo to recover. (6:45:52 PM Mar 07, 2019)", and "The simulation: Model_4_HorseShoe_Design_Loss_Analysis : 2_Solid_Solenoid_Design_Model_4_Radiation : Setup1 has been added to the queue. (6:56:41 PM Mar 07, 2019)".

Appendix D4: Ansys Electronics Simulation Environment for the Gapped-core Model 4

The screenshot displays the Ansys Electronics Desktop environment for a simulation of a gapped-core solenoid. The main workspace shows a 3D model of the solenoid with a central gap, surrounded by a red bounding box. The model includes a central core with a gap, copper windings, and ferrite components. A coordinate system with X, Y, and Z axes is visible, along with a scale bar at the bottom right indicating 50 cm.

Project Manager

- Model_4_HorseShoe_Design_Loss_Analysis*
 - 2_Solid_HorseShoe_Current_Analysis (Magnetostatic)
 - 2_Solid_HorseShoe_Normal (EddyCurrent)
 - 2_Solid_HorseShoe_X_Parametrics (Magnetostatic)
 - 2_Solid_HorseShoe_Y_Parametrics (Magnetostatic)
 - 2_Solid_HorseShoe_Z_Parametrics (Magnetostatic)
 - 2_Solid_HorseShoe_Parametrics (EddyCurrent)
 - 2_Solid_Solenoid_Design_Model_4_Fer (EddyCurrent)
 - 2_Solid_Solenoid_Design_Model_4_Radiation (EddyCurrent)*
 - 0.0.1.Simplorer_Horse_S_P
 - 0.0.1.Simplorer_Horse_S_P
 - Definitions
- Opt_Model_4_HorseShoe_Design_Loss_Analysis*
 - 2_Solid_HorseShoe_Current_Analysis (Magnetostatic)
 - 2_Solid_HorseShoe_Gap_Analysis (EddyCurrent)
 - 2_Solid_HorseShoe_Normal (EddyCurrent)
 - 2_Solid_HorseShoe_X_Parametrics (Magnetostatic)
 - 2_Solid_HorseShoe_Y_Parametrics (Magnetostatic)
 - 2_Solid_HorseShoe_Z_Parametrics (Magnetostatic)
 - 2_Solid_HorseShoe_Parametrics (EddyCurrent)

Properties

| Name | Value | Unit | Evaluated Value | Type |
|------------------|------------|------|-----------------|--------|
| Airgap | 200 | mm | 200mm | Design |
| Orig_Pt | 0 | mm | 0mm | Design |
| Ang_Displ | 0 | deg | 0deg | Design |
| Offset_Y | (Airgap... | | 0mm | Design |
| Orig_X | 0 | mm | 0mm | Design |
| Fer_thickness | 12 | mm | 12mm | Design |
| coil_width | 441 | mm | 441mm | Design |
| XPositn | 227 | mm | 227mm | Design |
| Edge_width | 43 | mm | 43mm | Design |
| Offset_Z | Airgap* | | 0mm | Design |
| Slide_X | 0 | mm | 0mm | Design |
| Slide_Y | 0 | mm | 0mm | Design |
| coil_space | 10.35 | mm | 10.35mm | Design |
| Cur_inp | 50 | A | 50A | Design |
| Shield_thickness | 2 | mm | 2mm | Design |

Message Manager

- Model_4_HorseShoe_Design_Loss_Analysis (C:/Temp/temp/HorseShoe Design/)
 - 2_Solid_Solenoid_Design_Model_4_Radiation (EddyCurrent)
 - Normal completion of simulation on server: Local Machine. (2:08:37 PM Mar 07, 2019)
 - 2_Solid_Solenoid_Design_Model_4_Radiation: Solutions have been invalidated. Undo to recover. (6:45:52 PM Mar 07, 2019)
 - The simulation: Model_4_HorseShoe_Design_Loss_Analysis : 2_Solid_Solenoid_Design_Model_4_Radiation : Setup1 has been added to the queue. (6:56:41 PM Mar 07, 2019)

